Probing the Mycobacterial Cell Envelope: CRISPR interference-mediated investigation of two essential genes in the galactan biosynthetic pathway

Jesse Robin Conradie

CNRJES001

Molecular Mycobacteriology Research Unit

Division of Medical Microbiology

Department of Pathology

A master's dissertation

Submitted to the Faculty of Health Sciences, University of Cape Town

In fulfilment of the requirements for the degree

Master of Science in Medical Microbiology

Supervisor: Dr. Mandy Mason

Date of Submission: January 2025

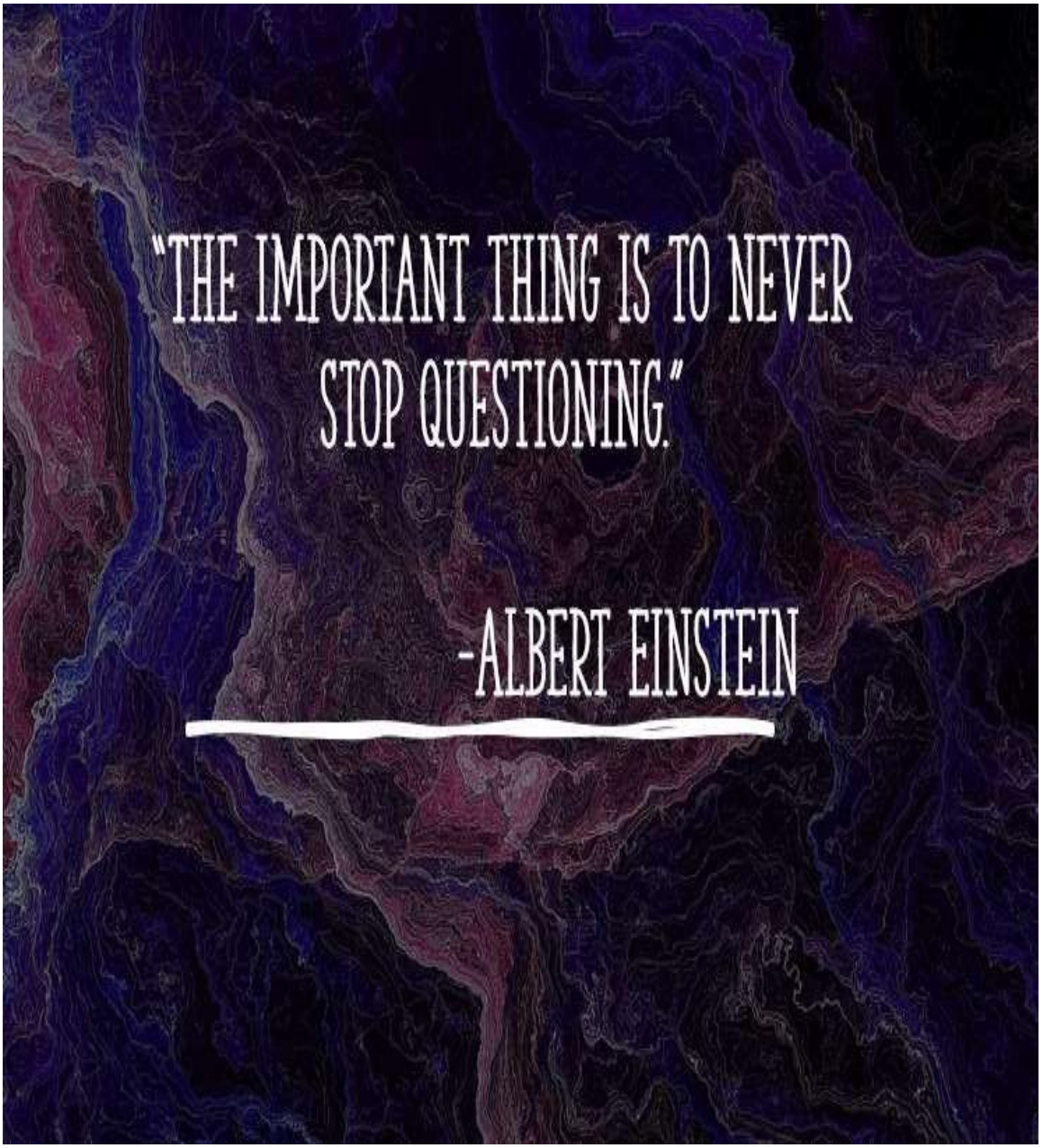
"THE IMPORTANT THING IS TO NEVER
STOP QUESTIONING."
-ALBERT EINSTEIN

Plagiarism declaration

1. I know that plagiarism is wrong. Plagiarism is to use another's work and pretend that it is one's own.

2. I have used the **Harvard** convention for citation and referencing. Each contribution to, and quotation in this **master's dissertation** from the work(s) of other people has been attributed and has been cited and referenced.

3. This **dissertation** is my own work.

4. I have not allowed and will not allow anyone to copy my work with the intention of passing it off as his or her own work.

Signature: Signed by candidate

Abstract

Tuberculosis (TB), caused by *Mycobacterium tuberculosis (Mtb),* is a global epidemic and one of the leading causes of death from an infectious organism. TB is treatable, however extended durations of treatment and the rise of multidrug resistant forms of TB contribute towards a health crisis that continues to hinder the global efforts in eradicating this disease. Shortening treatment regimens is a key objective in advancing TB therapy, with the aim of reducing the potential for antibiotic resistance. This highlights the need for the identification of essential cellular pathways in mycobacteria that can be targeted for novel drug development. A key feature of *Mtb* that confers intrinsic tolerance to many antibiotics is its complex cell envelope. The mycobacterial cell envelope is a dynamic compartment which serves as the interface between the pathogen and its host. It supports vital physiological processes and plays a key role in maintaining intracellular homeostasis. A unique and highly conserved structural component of the mycobacterial cell envelope is the heteropolysaccharide, arabinogalactan. This molecule is comprised of the galactan and Arabinan units, forming the characteristic cell wall core of mycobacterial species. Large scale drug screens have shown that arabinogalactan strains are sensitised to known anti-TB drugs.

The work presented in this dissertation aims to shine light on the functionality of the galactan component of arabinogalactan, examining its role in the sensitisation of mycobacteria to known antimycobacterial drugs and its impact on cell envelope characterisation and cell morphology. The CRISPR interference (CRISPRi) genome editing system was used to target genes involved in galactan biosynthesis and generate transcriptional knock down of *wecA* (also known as *rfe*, MSMEG_4947) and *rfbD* (MSMEG_6369) in *M. smegmatis,* a widely exploited modal for mycobacterial studies. We show that knockdown of both wecA and rfbD did not show hypersensitisation to first-line antibiotics rifampicin, ethambutol, vancomycin or linezolid. In addition, partial transcriptional silencing of *wecA* altered cell morphology, characterised by significant shortening and widening of cells, however partial transcriptional silencing of *rfbD* had no significant impact on cell shape. The *M. smegmatis* CRISPRi strains were finally stained with DMN-Tre, a fluorescent probe that selectively incorporates into the mycolic acid layer of the cell envelope. Morphological analyses revealed altered DMN-Tre signal along the medial axis of the cell, indicating a potential disruption of mycolic acid biosynthesis when galactan biosynthesis is compromised. Notably, loss of polar incorporation of DMN-Tre suggests issues with polar elongation. The findings of this study and its insights support the continuation of research into the role of galactan in maintaining cell envelope integrity and its role in supporting a robust mycolic acid leaflet.

Table of contents

List of Abbreviations and units

AG	Arabinogalactan
ATc	Ahydrotetracycline
ATP	Adenosine triphosphate
bp	Base pair
CAF	Central Analytical Facility
CRISPRi	Clustered regular short palindromic repeats interference
dCas9	Deactivated CRISPR associated protein 9
DMN-Tre	4-*N*,*N*-Dimethylamino-1,8-naphthalimide conjugate of trehalose
DMSO	Dimethyl sulfoxide
DNA	Deoxyribonucleic acid
EC	Effective concentration
EMB	Ethambutol
EtBr	Ethidium bromide
FOV	Field of View
FWD	Forward
GFP	Green fluorescent protein
INH	Isoniazid
Kan	Kanamycin
KanR	Kanamycin resistance
kb	Kilobase pair
L	Litres
LAM	Lipoarabinomannan
LB	Luria-bertani
LNZ	Linezolid
mAGP	Mycolyl-arabinogalactan
MDR-TB	Multidrug-resistant tuberculosis
MIC	Minimum inhibitory concentration
MIM	Mycobacterial inner membrane
Mins	Minutes
ml	Millilitres
mm	Millimetres
mM	Millimolar
MOM	Mycobacterial outer membrane
Msm/MSM	*Mycobacterium smegmatis*
Mtb/MTB	*Mycobacterium tuberculosis*

MTBC	Mycobacterium tuberculosis complex
NEB	New England biolabs
ng	Nanogram
NT	Non-targeting
OADC	Middlebrook Oleic Albumin Dextrose Catalase Growth Supplement.
OD	Optical density
PAM	Protospacer adjacent motif
PDIM	Phthiocerol dimycocerosate
PIM	Phosphatidylinositol mannosides
PBS	Phosphate buffered saline
PZA	Pyrazinamide
RCF	Relative centrifugal force
REV	Reverse
PCR	Polymerase chain reaction
PG	Peptidoglycan
RIF	Rifampicin
rpm	Revolutions per minute
RNA	Ribonucleic acid
sgRNA	Single guide RNA
STR	Streptomycin
TAE	Tris-acetate-EDTA buffer
TB	Tuberculosis
TMM	Trehalose monomycolate
v/v	Volume concentration
VAN	Vancomycin
UV	Ultraviolet
WHO	World Health Organisation
WT	Wild Type
XDR-TB	Extensively drug-resistant tuberculosis
°C	Degrees Celsius
µg	Micrograms
µl	Microlitres
µm	Micrometres
µM	Micromolar

List of figures

List of tables

Chapter 1: Introduction

1.1. Background: a curable infectious disease of global concern and local relevance

Tuberculosis (TB) is an ancient disease that has plagued humanity throughout known history (Daniel et al., 1994). TB is caused by the obligate intracellular pathogen *Mycobacterium tuberculosis (Mtb)* (Glickman and Jacobs, 2001, Jabir et al., 2018). TB is primarily a respiratory disease but can spread throughout the body including the lymph nodes (Ganchua et al., 2018), spine, bones and kidneys and can range from asymptomatic to life-threatening. Evidence of TB has been found in the bones of Egyptian mummies dating back to 8000 BC (Zink et al., 2003, Prabhu and Singh, 2019) and the disease was the leading cause of mortality in Europe during the 19th century where it was referred to as "consumption" due to significant weight loss and wasting of those infected with the disease. The current consensus is that just under one-third of the world's population is infected with TB (Lee, 2016, Houben and Dodd, 2016), with a majority of infected individuals described as having latent TB disease. Latent TB disease is defined as the immunoreactivity to TB antigens without the manifestation of active disease (Dartois and Rubin, 2022, Rao et al., 2019). Latently infected individuals are predominantly asymptomatic and do not require treatment (Rao et al., 2019). However, a minority of infected individuals do develop active TB and require treatment (Won et al., 2017). Despite modern interventions such as antibiotics, active TB remains one of the leading causes of death from an infectious organism worldwide (Peloquin and Davies, 2021), with an estimated 1.3 million deaths in 2022 attributed to the disease (WHO, 2023)

TB is traditionally considered a disease of poverty (Benatar and Upshur, 2010) with active TB prevalence being impacted by low socioeconomic status, such as overcrowding and undernutrition (Harling et al., 2008). Malnutrition and HIV-infection are among the strongest driving factors of TB worldwide (Getahun et al., 2015). A report published by the Food and Agriculture Organization in 2021 estimated that approximately 828 million people worldwide were undernourished, the majority living in South-East Asia (425 million) and Sub-Saharan Africa (278 million) (UNICEF, 2021). According to the World Health Organisation, low- to middle-income countries account for 87% of the world's TB burden: South-East Asia (46%), Africa (23%), Western Pacific (18%) (WHO, 2023). The TB crisis is aggravated by the global rise in resistance to known anti-TB drugs (Borgdorff et al., 2002, Ouattara et al., 2023). A multilevel analysis of TB infections in South Africa revealed that high levels of income inequality were associated with an increase in active TB infections on an individual-, community- and household level (Harling et al., 2008).

1.2. Tuberculosis (TB) treatment

One of the greatest impacts that medicine has had on society has been the development of antibiotics. The first step in understanding how to treat the causative agent of TB was through its discovery by Robert Koch in 1882 (Murray et al., 2015, Daniel, 2006). The discovery of antituberculosis drugs targeting the bacillus took place decades later during the golden age of antibiotics (1940s to 1960s), and in 1945 the benefits of streptomycin (STR) were announced (Rocha et al., 2021). Following the discovery of isoniazid (INH) in 1952 the antituberculosis effects of combining STR and INH became apparent (Murray et al., 2015, Cvetnić and Dugac, 2020). However, resistance to STR soon developed in a significant portion of TB patients (Murray et al., 2015, Rocha et al., 2021). In 1963, STR was substituted with a more effective regimen of drugs that combined ethambutol (EMB), rifampicin (RIF) and pyrazinamide (PZA) (Rocha et al., 2021). The introduction of RIF reduced the TB treatment regimen from 18-24 months to 9 months (Murray et al., 2015, Iseman, 2002). The introduction of PZA further reduced the treatment regimen to only 6 months for drug susceptible TB (Iseman, 2002).

Modern drug sensitive TB treatment in adults constitutes a 6-month multidrug regimen and consists of two main phases: (i) 2 months oral treatment combining INH, RIF, EMB and PZA, followed by (ii) a continuous phase of 4 months' treatment combining INH and RIF (Peloquin and Davies, 2021, Patil et al., 2018). Drugs to treat TB target various aspects of *Mtb* physiology **(Figure 1.1)**. Modern TB treatment, however, is not without side effects and difficulty in appropriately prescribing and adhering to this protocol has proven to be major factors driving drug resistance and threat to effective treatment (Iseman, 2002, Singh and Chibale, 2021). Second-line anti-TB drugs are administered in cases of resistance to first-line drugs (Khawbung et al., 2021) but are often more toxic than their first-line counterparts and require a longer period of treatment (Ramachandran and Swaminathan, 2015). Consequently, the global TB crisis is aggravated by the rise in resistance to established anti-TB drugs (Borgdorff et al., 2002, Ouattara et al., 2023). Drug resistance in TB can be broadly divided into 3 main categories: (i) mono-resistance is the least common form and is defined as *Mtb* strains resistant to a single first-line anti-TB drug, (ii) multi-drug resistance (MDR-TB) is the most common form of drug resistance and is defined as resistance to the main first-line anti-TB drugs INH and RIF and (iii) extensively drug-resistance (XDR-TB) refers to *Mtb* strains resistant to first-line drugs *as well as* at least one second line drug or injectable agent such as kanamycin (KAN) or amikacin (AMK) (Khawbung et al., 2021, Zumla et al., 2012).

Two recently emerged antitubercular candidates bedaquiline and delamanid have been approved and recommended by the WHO to treat MDR- and XDR-TB (D'Ambrosio et al., 2015). Bedaquiline and

delamanid function by inhibiting energy metabolism and mycolic acid synthesis, respectively (Bahuguna and Rawat, 2020). Despite evidence of the promising nature of both new drugs, there still exists a crucial need to discover novel drug targets within other essential pathways as potential resistance to these drugs remains a concern that may continue to hinder efforts in global TB eradication (Somoskovi et al., 2015).

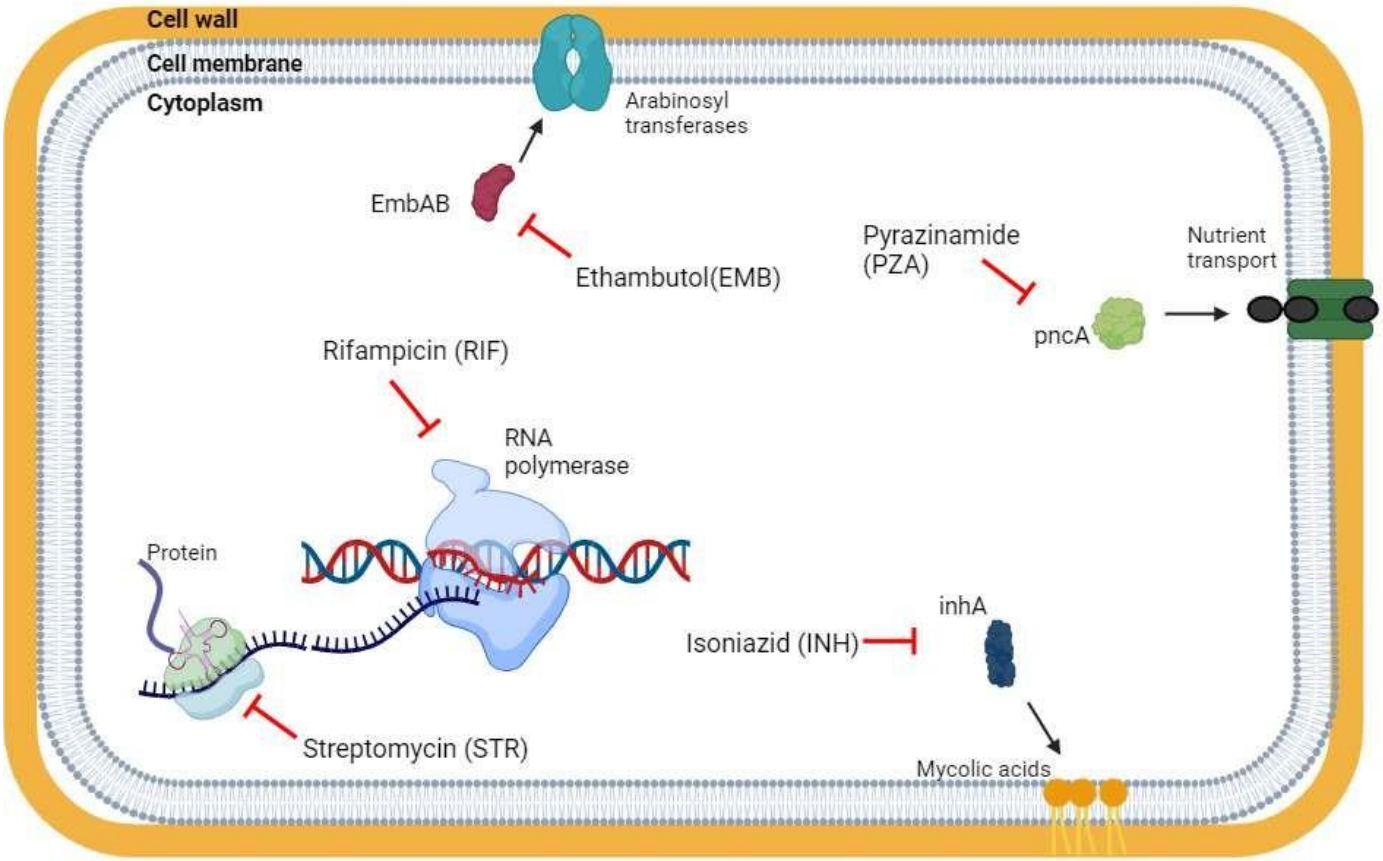

Figure 1.1. Schematic showing intracellular targets and mechanism of action of first-line anti-TB drugs. Ethambutol: inhibits the activity of the arabinosyltranferases, EmbA,B during arabinogalactan biosynthesis resulting in loss of arabinogalactan polymerisation; Rifampicin: inhibits the activity of DNA-dependent RNA synthesis; Isoniazid inhibits the activity of inhA in mycolic acid biosynthesis; Streptomycin: interferes with synthesis of ribosomal proteins; PPyrazinamide disrupts membrane potential via accumulation of pyrazinoic acid resulting in compromised nutrient uptake. In order to perform the illustrated functions, each drug needs to cross the barrier of the cell envelope. *Generated using* Bi*orender (*2025*).*

Although effective, antimycobacterial agents need to penetrate the cell envelope to reach their intracellular targets and perform their functions **(Figure 1.1)** (Lambert, 2002). This can be challenging as the cell envelopes of mycobacterial species are complex and rich in high molecular weight lipids (Christensen et al., 1999). This results in high hydrophobicity and restricted access to most antimycobacterial agents (Lambert, 2002). Relatively hydrophobic antibiotics, such as rifampicin can

diffuse across the hydrophobic bilayer, however hydrophilic compounds cannot easily cross the cell wall, and diffuse through porin proteins present in the cell wall (Danilchanka et al., 2008). Nevertheless, these porins are much less abundant in mycobacteria compared to other bacterial species, resulting in low rates of uptake of hydrophilic antibiotics (Niederweis, 2003). In addition, molecular weight of antibiotics plays a role in its exclusion and contributes to the difficulty many antibiotics encounter when crossing the physiochemically complex cell envelope structures (Lambert, 2002).

1.3. Origins and evolution of *M. tuberculosis*

During the 20th century, the traditional belief was that mycobacteria possessed animal and agricultural origins dating back approximately 10 000 years and the disease was subsequently transferred to humans due to close contact with cattle (Gagneux, 2012, Perrin, 2015). However molecular genetic studies by Gutierrez et al. (2005) have provided evidence that *Mycobacterium tuberculosis* complex (MTBC) may have emerged alongside early hominids in East Africa and share a common ancestor with other mycobacterial species dating back approximately 3 million years. Gutierrez's study supports evidence that *Mtb* may have coevolved alongside its human host for centuries, and subsequently spread and adapted as humans migrated (Brites and Gagneux, 2015, Uren et al., 2021, Correa-Macedo et al., 2019). This probable coevolution has resulted in the long-term intricate host-pathogen interactions between this bacterium and host immune defences (Gagneux, 2012, Correa-Macedo et al., 2019). Humans have co-evolved due to this relationship, adapting a complex immune response against this pathogen to form distinct granulomatous lesions in the majority of infected individuals (Zhai et al., 2019). *Mtb* has devoted a large portion of its genome towards successfully establishing latency or dormancy in these individuals (Ahmad, 2011, Khabibullina et al., 2022).

1.4. Pathogenesis of *M. tuberculosis* is dependent on key cell envelope virulence factors

In infectious disease, pathogenesis refers to the mechanism by which a pathogen infects, progresses and is resolved within its host (see Niederweis, 2003 for overview). In mycobacteria this includes the bacterium's ability to reside within macrophage cells and evade the antimicrobial responses of the host immune system (Echeverria-Valencia et al., 2018). *Mtb* has evolved to leverage a variety of its cellular components to facilitate growth and survival within the host (Sundararajan and Muniyan, 2021). These include genes and components of its unique and complex cell envelope that serve as key virulence factors (Al-Asady and Ali, 2023).

TB is primarily an air-borne disease spread via bio aerosols when an infected individual exhales, coughs or sneezes (Dinkele et al., 2024). Following inhalation of *Mtb*-containing aerosols by those in proximity

to the infected individual, the infection cycle of *Mtb*, in the case of pulmonary TB begins within the lung alveolar space (Pai et al., 2016). Here, the innate immune response to *Mtb* is characterised by the recruitment and accumulation of neutrophils, alveolar macrophages and dendritic cells (Bussi and Gutierrez, 2019). Phagocytosis of the bacilli by alveolar macrophages promotes the dissemination of *Mtb* to other immune cells and the lung interstitium (Cohen et al., 2018). Following phagocytosis of *Mtb* by alveolar macrophages, the particle is internalised by a membranous phagosome (Chandra et al., 2022). Standard phagosomal maturation occurs via sequential fusing with early and late endosome, a final fusion with a lysosome and the recruitment of vacuolar ATPases, ultimately forming a phagolysosome (Zhang et al., 2023). Conventionally the low pH within the phagolysosome releases reactive oxygen species and activates hydrolytic enzymes crucial to the destruction of the internalised bacterial cell (Dean et al., 2019). *Mtb* can traffic phagosomes and inhibit phagosomal maturation and evade destruction by escaping from the phagosome and disseminating to other immune cells (Echeverria-Valencia et al., 2018, Korb et al., 2016). Several cell envelope virulence factors have been implicated in this process, including surface lipids such as lipoarabinomannan (LAMs) (Welin et al., 2008) and phthiocerol dimycocerosates (PDIM) (Quigley et al., 2017). This immune evasion strategy allows *Mtb* to occupy an intracellular niche in which the bacilli can persist and replicate (Cohen et al., 2018), ultimately leading to the formation of granulomatous lesions **(Figure 1.2)**. Granulomas are characterised by a heterogenous population of immune cells surrounding the bacilli (Rao et al., 2019).

The majority of TB infections progress to latent disease (Chee et al., 2018). Approximately 5% to 15%, however, can progress to active TB disease (Kiazyk and Ball, 2017, Campbell et al., 2020). The risk of progression to active disease is typically affected by the integrity of the individual's immune system, such as those living with HIV, as well as environmental factors such as smoking, alcohol use and malnutrition (Getahun et al., 2015). The high prevalences of HIV and malnutrition in developing nations, such as South Africa, result in high active TB incidence. According to the WHO, South Africa is one of the 30 countries with the highest TB incidence rates worldwide. Although there has been a reported 50% decline in cases in South Africa between 2015 and 2022, TB incidence remains high with a reported 468 cases per 100 000 population and 54 000 deaths in 2022 (WHO 2023).

Mtb's remarkable success in subverting host immune responses and developing antibiotic resistance is largely due to its unique and waxy cell envelope (Dulberger et al., 2020). It structurally and functionally varies across the cell and may vary in comparison depending on the microenvironment and host immunity (reviewed by Dulberger et al., 2020).

A

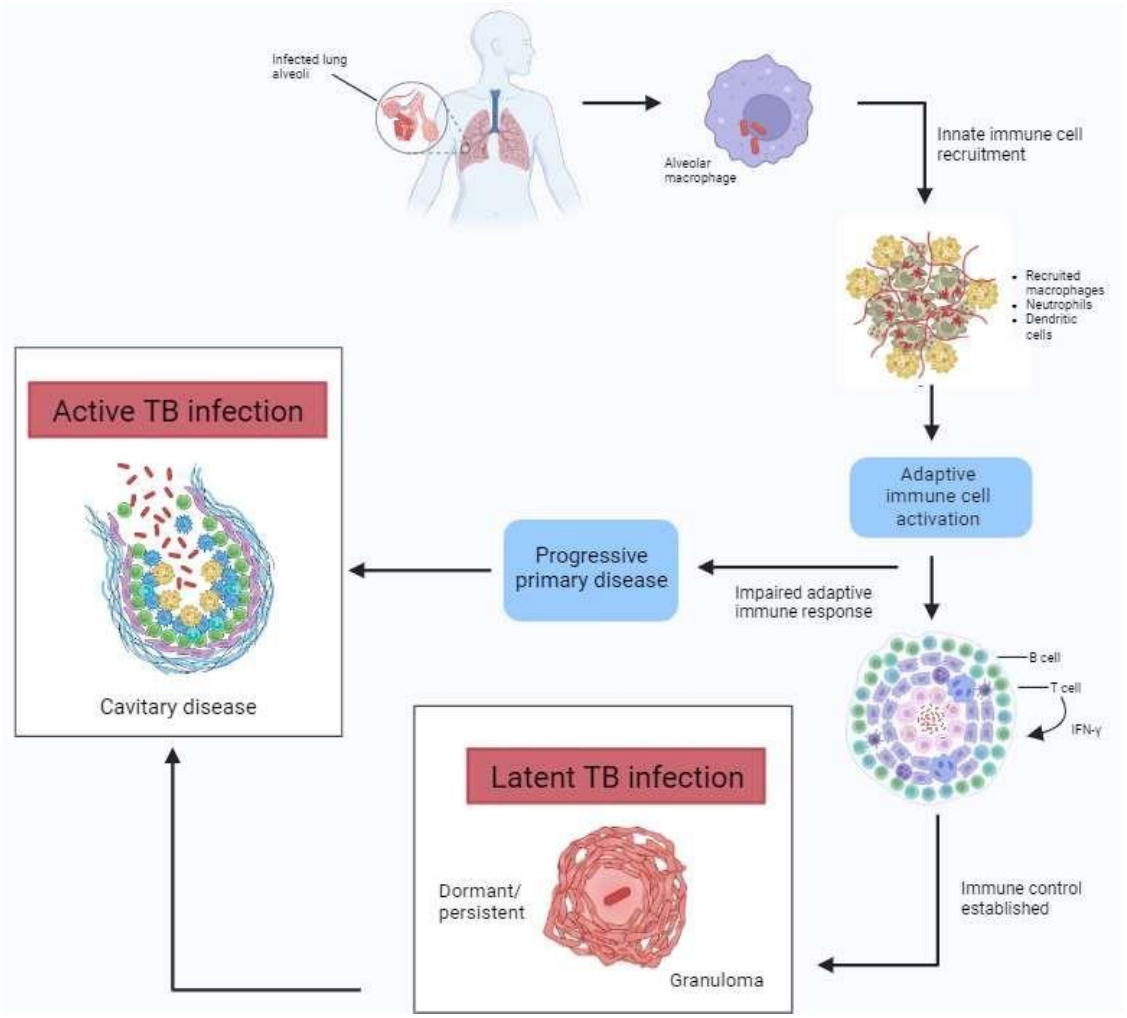

Figure 1.2. Summarised schematic of the life cycle of *M. tuberculosis*. Following inhalation of *Mtb*-containing aerosols, *Mtb* conventionally infects the lungs, leading to recruitment by macrophages and dendritic cells and the formation of granulomas characterised by a heterogenous population of immune cells surrounding the bacilli. A minority of infections progress to active disease characterised by the shedding and spread of the bacilli throughout the lungs. *Generated using* Biorender *(*2025*).*

1.5. The mycobacterial cell envelope

The mycobacterial cell envelope is a dynamic compartment which serves as the interface between the pathogen and its host. It supports vital processes involved in mycobacterial physiology and plays a role in preserving intracellular homeostasis (Garcia-Vilanova et al., 2019). The cell envelope is well studied and plays a role in mediating the intrinsic resistance of the bacterium towards the host and antimycobacterial drugs (Poulton and Rock, 2022). However, its high level of structural and molecular complexity has confounded our understanding of the mechanisms underlying its role as a barrier to drug

entry. Better knowledge of key enzymes involved in the biosynthesis of *Mtb*'s cell envelope may aid in the development of novel therapeutics against TB infection.

The evolutionary history that led to the development of the mycobacterial cell envelope is still not well understood (Vincent et al., 2018). *Mtb* belongs to a large group of bacteria in the Actinomycetes phylum within the *Coryenobacteriaceae* family (Rastogi et al., 2001, Vincent et al., 2018). Bacteria belonging to this group are characterised by their gram-positive single cell membrane and thick peptidoglycan (PG) layer (Pasquina-Lemonche et al., 2020, Sutcliffe, 2010). Gram-negative bacteria, in contrast, possess both inner and outer membranes surrounding a PG layer typically thinner than that of gram-positive species (Pasquina-Lemonche et al., 2020). However, the cell envelope of mycobacteria has a unique architecture and is more complex than typical gram-positive organisms, as it possesses aspects of both gram-negative, which possesses an outer membrane surrounding its PG layer, and gram-positive species (Brown et al., 2023, Dulberger et al., 2020, Fisher and Mobashery, 2020). In contrast to typical gram-positive bacteria, the cell envelope of mycobacteria is composed of a mycobacterial outer membrane (MOM) covalently linked to an arabinogalactan (AG) macromolecule which is in turn linked to the relatively thick PG layer sitting above the plasma membrane (also known as the mycobacterial inner membrane, MIM) (Brown et al., 2023). The presence of AG macromolecules is unique to species within the Actinomycetes phylum (Meyer and Bramkamp, 2024). In addition, MOM is surrounded by a matrix of polysaccharides, proteins and lipids which form the mycobacterial capsule. It is important to note that lipids are a defining feature of mycobacteria, making up approximately 40-60% of the cell envelope, significantly higher than the lipid composition of gram-negative species (Daffé and Marrakchi, 2019, Chiaradia et al., 2017).

The MOM can be divided into two compartments, namely the outer and inner leaflets **(Figure 1.3)**. The outer leaflet of the MOM is highly complex and heterogenous. It consists of glycolipids such as trehalose monomycolates (TMM) and a variety of phospholipids including phthiocerol dimycocerosates (PDIM), phosphatidylinositol mannosides (PIMs) and lipoarabinomannan (LAM) (Daffé and Marrakchi, 2019) providing shape and rigidity to the cell (Angala et al., 2014). Extracellular matrix experiments into the molecular composition of the mycobacterial capsule (Lemassu et al., 1996, Ortalo-Magne et al., 1995) revealed that pathogenic mycobacteria, such as *M. tuberculosis* and *M. kansasii* secrete an abundance of outer membrane materials compared to that of non-pathogenic mycobacteria such as *M. smegmatis* and *M.aurum.* These structures, therefore, may play an important role in the interactions between the pathogen and host, and aid in maintaining homeostasis and protecting the bacterium from environmental stress during the course of infection (Angala et al., 2014, Augenstreich and Briken, 2020).

The inner leaflet of the outer membrane consists of long chain α-alkyl-β-hydroxy fatty mycolic acids, consisting of 60-90 carbon molecules (Batt et al., 2020b). Mycolic acids are an integral part of the mycobacterial cell envelope and are largely responsible for the impermeability of the membrane to many drugs (Bhat et al., 2017). The first-line anti-TB drug, isoniazid inhibits the biosynthesis of mycolic acids by inhibiting the activity of the InhA enzyme (encoded by the *inhA* gene) **(Figure 1.1)** involved in the synthesis of fatty acids that form mycolic acids (Bhat et al., 2017, Timmins and Deretic, 2006). Experimental work by Chiaradia et al., 2017, revealed that mycolic acids are covalently attached to AG.

The branched AG macromolecule is unique to the *Coryenebacteriaceae* family of microorganisms (Vincent et al., 2018) comprising galactose (Gal) and arabinose (Ara) sugar residues, in the furanose (*f*) ring forms. These divide the molecule into two subunits: (1) three branched Arabinan chains of approximately 30 arabinose (Ara*f*) residues and (2) a linear galactan chain of 30 *Galf* residues (Daffe et al., 1990, Justen et al., 2020). The *Araf* sugars of the Arabinan subunit are linked to the 5-carbon unit of the *Galf* residues that make up the galactan chain, linking the two subunits (Bhat et al., 2017). The formation of linkages between the arabinose sugars and galactan chain can be inhibited via the action of the anti-TB drug ethambutol which interferes with the activity of the EmbB enzyme (encoded by the *embB* gene) (Telenti et al., 1997, Zhang et al., 2020).

Galactan serves as a linker unit tethering the arabinose unit to the PG layer, thereby anchoring this structure (Abrahams and Besra, 2018). This is structure is known as the mycolyl-arabinogalactan-peptidoglycan (mAGP) complex. The PG layer of *Mtb* is made up of a glycan backbone consisting of alternating units of *N*-acetylglucosamine (GlcNAc) and muramic acid linked by β(1→4) bonds (reviewed by Alderwick et al., 2015). PG is essential in maintaining cell shape and protection against changes in osmotic pressure (Angala et al., 2014).

Below the PG layer is the plasma membrane which forms the innermost layer of the cell envelope. The plasma membrane forms a barrier and is involved in the transport of cell envelope components across this lipid bilayer (Jackson et al., 2020). A key transmembrane protein mediating the transport of various lipids are the MmpL (mycobacterial membrane protein large) proteins (Melly and Purdy, 2019). The plasma membrane is therefore a vital component, not only in shaping the cell, but in the transport of lipids that contribute to the integrity of the cell envelope and its physiological functions (Daffé and Marrakchi, 2019). The mycolic acids, AG and PG link to form the mycolyl-arabinogalactan-peptidoglycan complex (mAGP) of the cell envelope **(Figure 1.3)** (Batt et al., 2020b, Liu et al., 2020).

Intrinsic resistance of *Mtb* to many antibiotics have largely been attributed to the low permeability of the cell envelope *as well as* the presence of several efflux systems which prevent drugs from crossing this barrier. This cell envelope is rich drug target space (Bhat et al., 2017, Li et al., 2021), and several

cell envelope features have been leveraged to develop antimycobacterial agents, such as ethambutol targeting arabinan biosynthesis, and isoniazid targeting mycolic acid biosynthesis (Lee et al., 2024). Furthermore, mAGP has been identified as a primary feature that serves as a barrier that mediates intrinsic resistance to anti-TB drugs (Batt et al., 2020a). Cell envelope features have therefore been validated as attractive targets for the development of novel therapeutic agents.

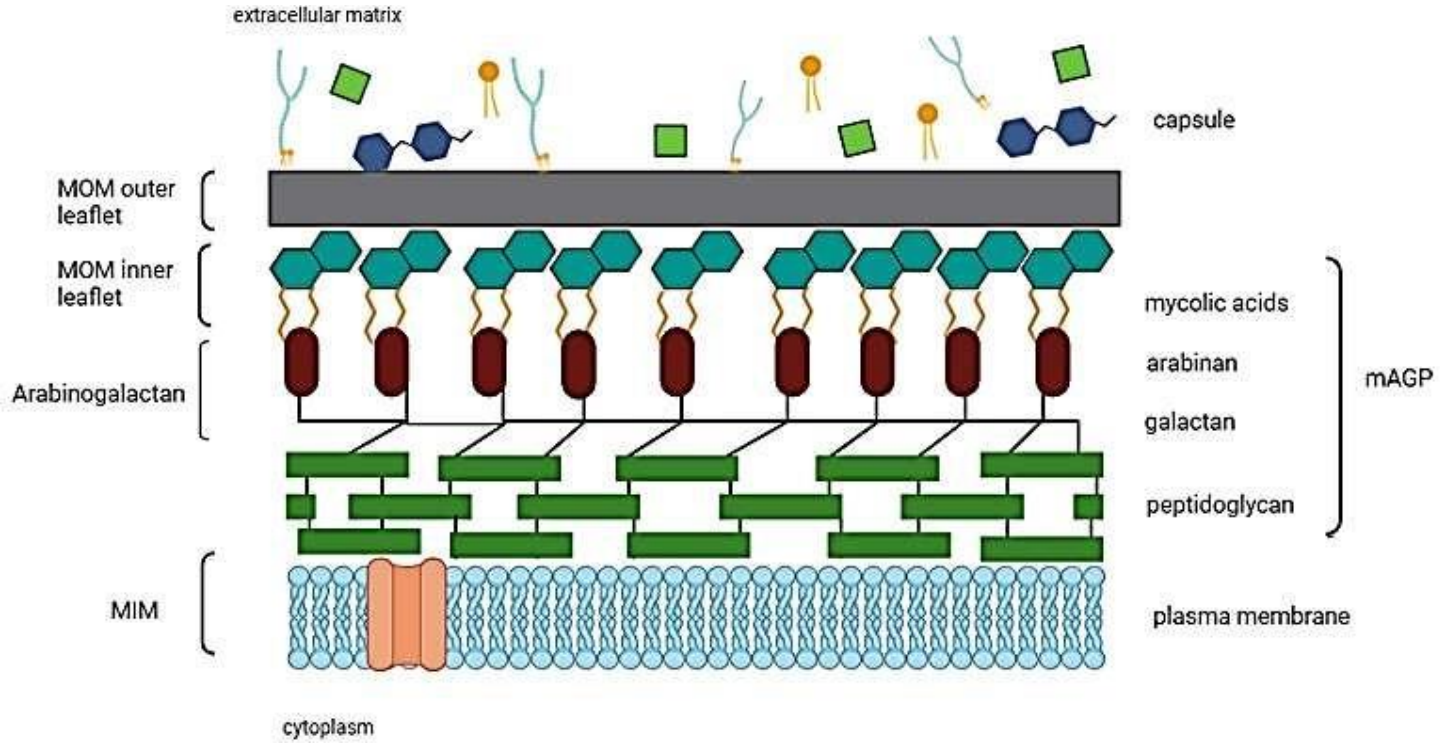

Figure 1.3. Schematic representation of the cell envelope of mycobacterial species. The cell envelope of mycobacteria consists of three layers: (1) the capsule, (2) the mycobacterial outer membrane (MOM) inner and outer leaflets and (3) the mycolyl-arabinogalactan layer and (4) the plasma membrane (mycobacterial inner membrane, MIM). The capsule and MOM outer leaflet are complex and contain various lipoproteins and polysaccharides non-covalently linked to the mycolic acids of the MOM inner leaflet. Arabinogalactan (AG) links the mycolic acid layer to peptidoglycan (PG), forming the mycolyl-arabinogalactan-peptidoglycan (mAGP) complex. The plasma membrane is the inner-most layer of the mycobacterial cell envelope and contains translocation proteins that transport cell envelope components to other outer-most layers. *Generated using Biorender (2025).*

1.6. A focus on arabinogalactan biosynthesis

The mycolyl-arabinogalactan-peptidoglycan complex (mAGP) is an atypical structure that differentiates the cell wall of *Corynebacteria* from other prokaryotes (Vincent et al., 2018). The presence of this heteropolymer is partially responsible for the low permeability of mycobacterial cells and plays a role in the development of intrinsic antibiotic resistance (Gao et al., 2003), posing a problem

for global TB control. Arabinogalactan plays a key role in anchoring mycolic acids to the peptidoglycan layer, securing the rigidity and robustness of the cell (Vincent et al., 2018). Disruption of arabinogalactan biosynthesis has been shown to result in increased cell envelope permeability (Bhat et al., 2017, Forbes et al., 1962), making this pathway an attractive target for development of novel anti-TB treatment (Al-Jourani et al., 2023).

Two processes are involved in the biosynthesis of arabinogalactan: (1) the formation of the galactan linker unit **(Figure 1.4)** and (2) the DPA pathway leading to the formation of arabinan. The synthesis of arabinogalactan is initiated in the cytoplasm starting with the generation of the galactan linker unit (Grzegorzewicz et al., 2016, Abrahams and Besra, 2018). The phosphoglycosyltransferase WecA (Rv1302) initiates this process by catalysing the addition of GlcNAc-P from the sugar donor UDP-GlcNAc to C_{50}-P, forming C_{50}-PP-GlcNAc (Huszár et al., 2017, Grzegorzewicz et al., 2016). This step is followed by the transfer of L-*Rha* from the sugar donor dTDP-rhamnose onto the 3-carbon position of the GlcNAc leading to C_{50}-PP-GlcNAc-*Rha*, catalysed by the activity of the rhamnosyl-transferase WbbL (Rv3265c) (Grzegorzewicz et al., 2008). The chain is finally elongated by the activity of two galactosyltransferases, GlfT1 (Rv3782) and GlfT2 (Rv3808c), catalysing the sequential transfer of two and twenty-eight *Galf* residues, respectively, from UDP-galactofuranose (UDP-Galf) (Poulin and Lowary, 2016). This completes the formation of the galactan linker unit. The remainder of arabinogalactan formation occurs in the periplasmic space between the plasma membrane and peptidoglycan (Grzegorzewicz et al., 2016). Studies in *M. smegmatis* have proposed that the ATP-binding cassette (ABC) transporter may be responsible for the translocation of the galactan precursor across the plasma membrane to the periplasmic space (Savková et al., 2021). This transporter consists of a membrane-spanning subunit, rfbD (Rv3781) and a nucleotide-binding subunit, rfbE (Rv3783) (Savková et al., 2021). Studies by Dianišková et al. (2011) showed the essentiality of the nucleotide-binding domain in *M. smegmtais.* Follow-up studies by Savková et al., 2021 revealed that the knockdown of the membrane-spanning subunit results in the accumulation of unusually long galactan chains in the cytoplasm. Following the translocation of the galactan chain across the plasma membrane, the arabinofuranosyltransferases, AftA, AftB, and AftC catalyze the addition of arabinose residues onto the galactan chain, via the transfer of several Ara*f* residues from the lipid donor decaprenylphosphoryl-D-arabinose (DPA) (Alderwick et al., 2015, Abrahams and Besra, 2018). The assembly of arabinans during the DPA pathway occurs via a linear pathway involving a collection of membrane-bound glycosyltransferases (Alderwick et al., 2015)

A promising caprazamycin derivative, CPZEN-45, is currently in the preclinical study phase (Ishizaki et al., 2013). Caprazamycins are nucleoside antibiotics that target peptidoglycan assembly (Patel et al.,

2019). In *Bacillus subtilis*, CPZEN-45 was shown to inhibit the activity of the wecA ortholog TagO (Ishizaki et al., 2013). However, no currently available anti-TB drugs target genes involved in galactan biosynthesis (Konyariková et al., 2020). The fundamental role of galactan in the cell envelope integrity of *Mtb* suggests a need to develop drugs that target enzymes essential to its biosynthesis (Justen et al., 2020).

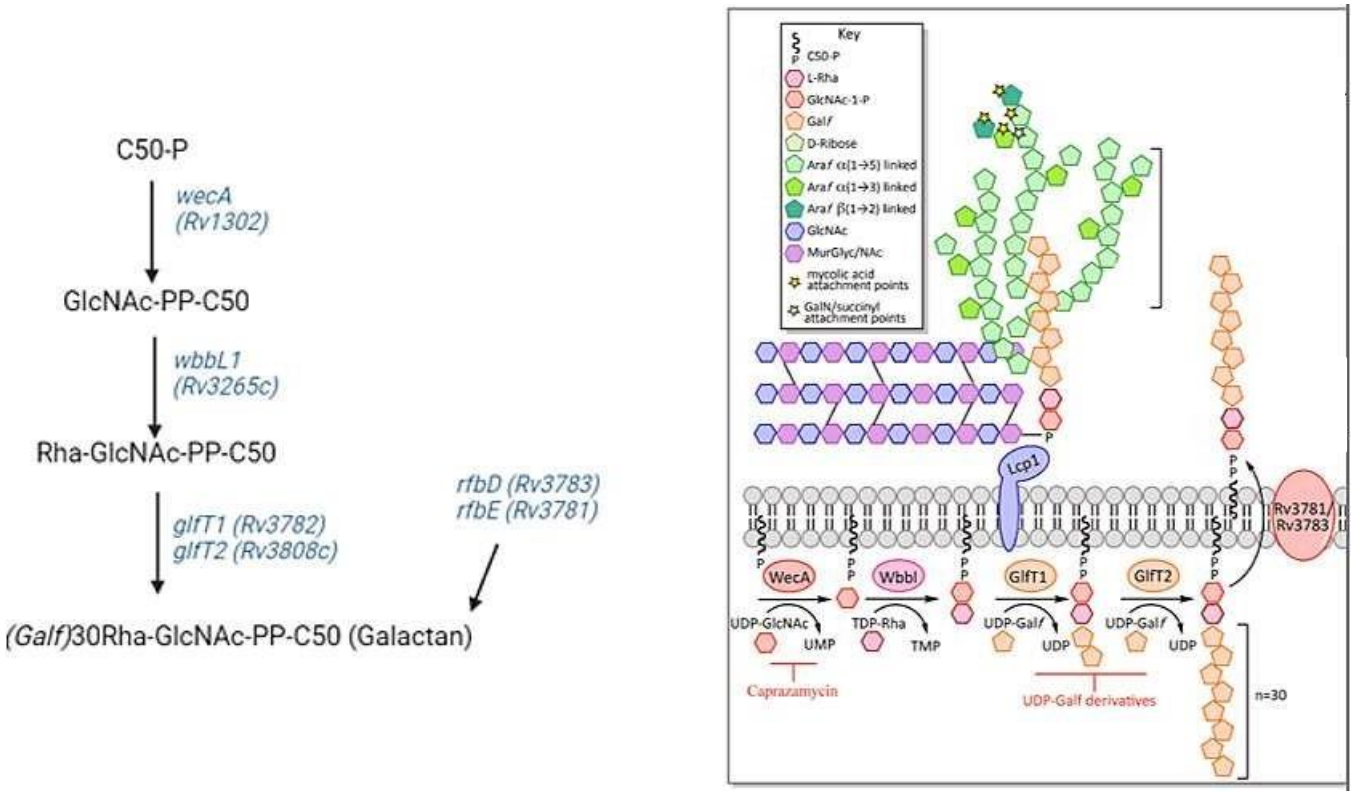

Figure 1.4. Galactan biosynthetic pathway. The formation of galactan begins on the cytosolic side of the cell envelope. wecA initiates this pathway via the transfer of GlcNAc-P onto a 50-carbon chain bounded to a phosphate group. wbbL1 then catalyses the transfer of a rhamnosyl group onto GlcNAc-PP-C50, followed by the transfer of 28 and 2 *galf* residues, catalysed by glfT1 and glfT2, respectively. *rfbD* encodes a membrane-spanning domain and *rfbE* encodes a nucleotide-binding domain of an ABC exporter present in the plasma membrane. The final step in this pathway involves the translocation of the galactan chain across the cell envelope via the ABC exporter. This is where the remainder of arabinogalactan biosynthesis takes place. *Retrieved from Batt et al. (2020a).*

1.7. Targeting galactan biosynthesis using CRISPR interference (CRISPRi)

The complete genome sequencing of mycobacteria by Cole et al., 1998 has led to the identification of genes involved in the biosynthesis of various cell envelope components, enabling for their targeted disruption and validation of their key roles in the pathogenesis of *Mtb* (Lai et al., 2020, Li et al., 2022). Genes involved in the biosynthesis of cell envelope components are attractive drug targets, and decades

of TB research has led to the discovery of antimycobacterial agents against active TB infection, including those currently being evaluated in both pre-clinical and clinical stages (Bhat et al., 2017). Although a compound targeting the synthesis of the arabinan component of arabinogalactan is available, no currently available drugs target genes involved in the biosynthesis of galactan (Konyariková et al., 2020). In addition, a compound targeting the activity of wecA has been identified and is currently in the preclinical phase (Ishizaki et al., 2013, Patel et al., 2019). However, the potential for antibiotic resistance remains a concern, and the fundamental role of galactan highlights the need for continued research into genes involved its biosynthesis (Konyariková et al., 2020).

The discovery of the CRISPR-Cas (Clustered regulatory interspaced short palindrome repeats-CRISPR associated proteins) system allowed for regulated gene silencing (Rock et al., 2017). CRISPR-Cas systems are a form of adaptive immunity in some bacteria and archaea, adapted as a defence mechanism against foreign forms of DNA (Hidalgo-Cantabrana et al., 2019). This technology offers a wide range of genome manipulation and transcription regulation tools (Hidalgo-Cantabrana et al., 2019). This system utilises a single endonuclease cas9 directed to the endogenous gene target by a single guide RNA (sgRNA) complementary to the target gene (Choudhary et al., 2015), cleaving the gene and preventing its transcription (Wright et al., 2016). The magnitude of gene silencing using the CRISPR-Cas system, however, is not tuneable and presents a challenge in achieving desired gene levels (Singh et al., 2016).

To circumvent this challenge, the CRISPR system has been re-purposed to mediate downregulated transcription of specific gene targets- a technology known as CRISPR interference (CRISPRi) **(Figure 1.5)** (Choudhary et al., 2015, Silveiro et al., 2023). In contrast to the traditional CRISPR system, the CRISPRi system utilises a catalytically inactive Cas9 protein, deactivated via point mutations in its endonuclease domains – this is known as dCas9 (Choudhary et al., 2015, Ghavami and Pandi, 2021, Zhang et al., 2021). Both the dCas9 and sgRNA genes are under the control of an anhydrotetracycline (ATc)-inducible promoter, enabling regulated expression of the target gene (Rock et al., 2017, Bosch et al., 2021). The co-transcription of dCas9 and sgRNA complementary to the target gene allows for the reduction or prevention of transcriptional progression through direct steric hindrance with the targeted dCas9 protein (Rock et al., 2017, Silveiro et al., 2023).

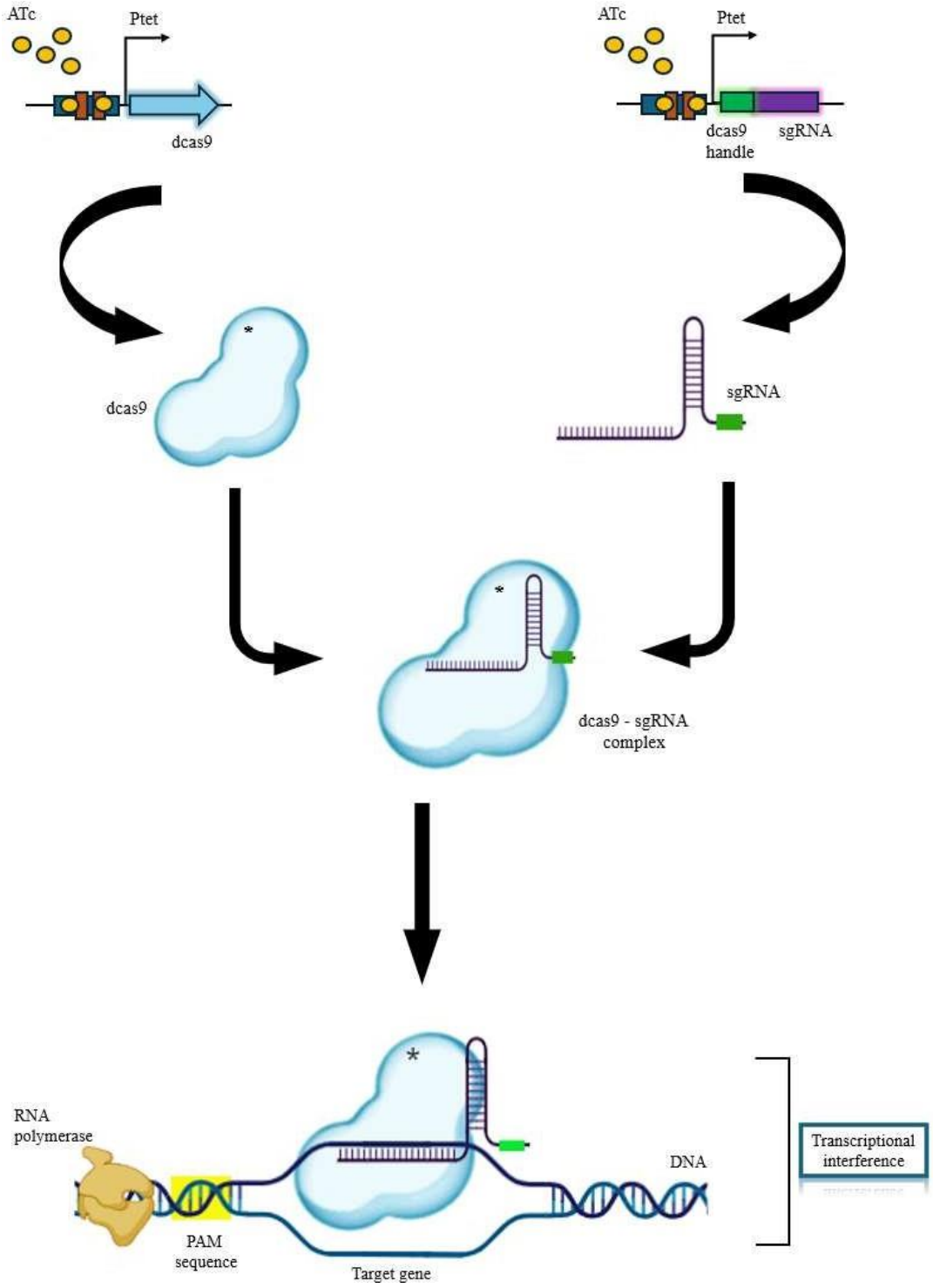

Figure 1.5. CRISPRi-mediated transcriptional interference of target gene. ATc-inducible sgRNA and dCas9 are transcribed and bind to form the dCas9-sgRNA complex. sgRNA guides dCas9 to the gene of interesting, obstructing and preventing RNA polymerase from transcribing the gene. *Adapted from Rock et al. (2017). Generated using Biorender.com (2025).*

1.8. Relevance of mycobacterial models for cell envelope studies

In TB studies, a range of experimental models are used in leu of the highly pathogenic clinical *Mtb* H37Rv strain (Altaf et al., 2010). Of these models, *M. smegmatis* (*Msm*) mc^{2}155 is most frequently utilised to investigate mycobacterial physiology (He and De Buck, 2010). *Msm* mc^{2}155 is non-pathogenic to humans and exhibits a fast-growing phenotype when compared to other mycobacterial species (Ranjitha et al., 2020). In addition, the *Msm* genome encodes thousands of highly conserved gene orthologs and shares many characteristics with pathogenic mycobacteria (Sparks et al., 2023). *Msm*'s non-pathogenic phenotype makes it an ideal model to conduct TB studies in the Biosafety level 2 (BSL2) laboratory for researchers not equipped with Biosafety Level 3 training (Sparks et al., 2023). Its fast growth also makes it an ideal organism in single cell studies.

Large genomic diversity between non-pathogenic and pathogenic mycobacterial species, however, does exist (Orgeur et al., 2024). Cell surface proteins are virulence factors involved in lipid metabolism and transport and play a key role in the pathogenicity of mycobacteria. Many of these proteins are absent in *Msm*, these include various glycolipids and phospholipids (Etienne et al., 2005). In addition, a screen of the LOPAC drug library for antimycobacterial agents was performed using *Msm* mc^{2}155 and *Mtb* H37Rv (Altaf et al., 2010). The authors discovered that 50% of inhibitors against *Mtb* H37Rv were missing in the library screening of *Msm* (Altaf et al., 2010). The same study found similar results when they performed screens with the NIH Diversity Set and Spectrum Collection. Overall, 30% of *Mtb* H37Rv proteins were missing conserved orthologs in *Msm* (Altaf et al., 2010). However, it is also important to note that antimycobacterial compounds that are effective against *Mtb* H37Rv, such as INH, PZN, EMB and Bedaquilines are also effective against *Msm* (Ranjitha et al., 2020). Although cell surface virulent factors are absent in *Msm*, it shares a similar physiology to *Mtb* H37Rv and still remains a useful model organism for *in vitro* studies (Sparks et al., 2023).

As mentioned, virulence factors of *Mtb* are a major determinant of pathogenesis (Echeverria-Valencia et al., 2018). Attenuated/avirulent strains of mycobacteria can be exploited to determine the roles of essential genes in a strain that more closely represents the clinical *Mtb* H37Rv strain (Målen et al., 2011). Zheng et al., 2008 determined the complete genome sequence of an avirulent *Mtb* H37Ra strain and found that the genome of this strain was vastly similar to the clinical strain, with 53 gene insertions and 21 gene deletions. These mutations included alterations to genes encoding cell envelope proteins involved in virulence, resulting in the attenuated virulence of this strain. Notably, proteomic studies have previously revealed that the vast majority of shared membrane proteins were present in similar relative abundance between the virulent and avirulent strains, with a minority of shared proteins present in distinct abundance (Målen et al., 2011, Verma et al., 2017).

Although the outer leaflet of the *Msm* mc^2155 and *Mtb* H37Ra model organisms differ from the virulent laboratory strain H37Rv and clinical strains, the mAGP structure is conserved across mycobacterial species (Alderwick et al., 2015). Both organisms are therefore relevant model organisms for galactan targeting and depletion studies. Targeting this structure in these organisms could aid in the understanding of the potential impact of this layer on drug penetration into the cell.

1.9. Problem statement and Rationale

This project was motivated by the ongoing global burden of TB and the need to understand underlying factors that contribute to *Mtb* pathogenesis and, more specifically, to elucidate the role of cell envelope components on the drug vulnerability of *Mtb.* The emergence of antibiotic resistance presents a challenge to global TB elimination. As a result, there exists an urgent need to develop novel drugs to treat the causative agent, *Mtb.* This imperative requires the identification of potential drug targets within essential cellular pathways.

CRISPRi chemical genetics screen enrichment analysis have highlighted that the depletion of mycolyl-arabinogalactan-peptidoglycan (mAGP) complex genes sensitises *Mtb* to a subset of drugs (Li et al., 2022). In our research group, arrayed *Msm* CRISPRi morphotyping screens of 263 essential gene knockdown *Msm* mutants revealed that disruption of genes involved in mAGP biosynthesis impacts cell morphology, resulting in distinct changes to cell shape (de Wet et al., 2020). In addition, disruption of the mAGP complex was previously shown to result in increased cell envelope permeability (Bhat et al., 2017, Forbes et al., 1962). Current first line drugs include the use of ethambutol, which targets the biosynthesis of the arabinan component of arabinogalactan (Telenti et al., 1997, Zhang et al., 2020). In line with this, the fundamental role of the galactan component in maintaining cell envelope integrity of mycobacteria makes it an attractive target for the development of anti-TB therapeutics (Weston et al., 1998).

The role of galactan in anchoring the MOM of mycobacteria positions it as a critical interface for maintaining cell envelope structure and integrity (Justen et al., 2020). Reduction in the length of this polysaccharide was shown to increase potency to hydrophobic antibiotics and result in changes to cell morphology (Justen et al., 2020). The galactan biosynthetic pathway comprises a highly desirable drug target for the development of new compounds (Konyariková et al., 2020).

It was hypothesised that silencing key genes involved in galactan biosynthesis would result in increased antibiotic sensitisation, linked to changes to cellular functions that disrupt the integrity of the cell wall, revealed via distinct changes to cell shape. The overall aim of the study was to confirm that known genetic vulnerabilities of this mycobacterial biosynthetic pathway could be translated into drug vulnerabilities. The essential requirement for galactan biosynthesis in both non-pathogenic *Msm* and attenuated *Mtb* H37Ra supports investigations of its role in these mycobacterial model strains.

1.10. Aims and objectives

AIM 1: CRISPRi hypomorph generation and verification in the mycobacterial model *M. smegmatis* mc^{2}155.

Objective 1: Generate *M. smegmatis* CRISPRi hypomorphs of two genes involved in the galactan biosynthesis pathway (5 strains with varying targeted gene knockdown of each gene):

a) The phosphoglycosyltransferase *wecA* (*rfe*, MSMEG_4947)
b) The gene encoding the membrane-spanning domain of the ABC Transporter *rfbD* (*wzm*, MSMEG_6369)

Objective 2: Verify knockdown of *M. smegmatis* wecA and rfbD by growth attenuation:

a) in both media (liquid)
b) on agar media (solid)

AIM 2: *M. smegmatis* CRISPRi hypomorph characterisation

Objective 1: Assess the effects of *wecA* and *rfbD* knockdown on the sensitisation of *M. smegmatis* to four antimycobacterial agents:

a) Linezolid (LNZ)
b) Rifampicin (RIF)
c) Ethambutol (EMB)
d) Vancomycin (VAN)

Objective 2: Examine the effects of *wecA* and *rfbD* knockdown on cell morphology and mycolic acid distribution in *M. smegmatis*

AIM 3: CRISPRi hypomorph generation and verification in mycobacterial model *M. tuberculosis* H37Ra

Objective 1: Generate *M. tuberculosis* H37Ra CRISPRi hypomorphs of the phosphoglycosyltransferase *wecA* (Rv1302) involved in the galactan biosynthesis pathway (5 strains with varying targeted gene knockdown).

Objective 2: Verify knockdown of *M. tuberculosis* H37Ra *wecA* by growth attenuation on agar media (solid).

Chapter 2: Methods and Materials

2.1. Bacterial strains and culture conditions

The reagents used and resources generated in this study are listed in the key resources table (**Table S1)** The *Escherichia coli* (*E. coli*) strain used in this study for molecular cloning is a derivative of DH5α (Thermofisher Scientific). Electrocompetent *E. coli* stocks were generated as lab resources by Lucas Raphela using the Rubidum chloride method described by Renzette, 2011. The *Mycobacterium smegmatis* (*Msm*) strain used in this study is mc^2155, an efficient transformation mutant that has been adapted as a tractable mycobacterial model (Snapper et al., 1990). To expand this work into a closer model of *Mycobacterium tuberculosis (Mtb)* an attenuated strain of *Mtb, Mtb* H37Ra, was selected for safe usage in the Biosafety Level (BSL) 2 laboratory. When handling *Mtb* H37Ra, work was performed with appropriate biosafety containment and standard operating procedures (SOPs) developed to reduce risk and hazards. All bacterial strains used in this study are listed in **Table 2.1.** Aligned with this project, work was performed in a virulent strain of *Mtb* (*Mtb* H37Rv). For this work *Mtb* plasmids generated within this project were utilised and the strains were generated and handled in the BSL3 laboratory by Dr Mandy Mason.

E. coli strains were cultured in Luria-Bertani (LB) broth, a nutrient rich medium comprising; 1% tryptone, 0.5% (v/v) yeast extract and 0.5% (v/v) NaCl, and incubated at 37°C in a shaking incubator (IncoShake incubator, Labotec) at an orbital of 100 *rpm*. *E. coli* colonies were grown on solid media comprising LB agar and incubated at 37°C in a stationary incubator (IncoCool incubator, Labotec). For molecular cloning work, the *E. coli* strains were transformed to carry plasmids containing the kanamycin resistance gene (*KanR*) as a selective marker (see **Chapter 7: Appendix Figure 1 & 2**). The agar and media were supplemented with 50 µg/ml kanamycin (Kan50) to maintain selection pressure and ensure plasmid retention. Post transformation, *E. coli* glycerol stocks were generated from single picked colonies that were inoculated and expanded in LB broth and stored at -80°C in 33% (v/v) glycerol. Glycerol stocks were thawed on ice prior to culturing and usage.

Mycobacterial strains were grown in 7H9/OADC media comprising: Middlebrook 7H9 (Difco™), 10% (v/v) OADC, 0.2% (v/v) glycerol, and 0.05% Tween 80 and incubated at 37°C in a shaking incubator (orbital at 100 *rpm*). Genetically modified strains able to express *KanR* were supplemented with 25 µg/ml kanamycin (Kan25) to maintain selection pressure during propagation steps **(Figure 2.1**). Mycobacterial colonies were grown on solid media comprising Middlebrook 7H10 agar; 0.2% (v/v) glycerol and 10% (v/v) OADC, supplemented with Kan25 and incubated at 37°C in a stationary incubator. Mycobacterial stocks were generated from single colonies that were picked, inoculated and expanded in 7H9/OADC and stored at -80°C in 33% (v/v) glycerol. Glycerol stocks were thawed on ice prior to culturing and usage.

Recovery of glycerol stocks, growth and passaging of mycobacterial strains were performed as illustrated in **Figure 2.1**. The glycerol stocks were thawed on ice and 1 ml of the glycerol stock added to 7H9/OADC with (for recombinant strains) or without (for non-recombinant strains) Kan25 and incubated at 37°C while shaking. This was generally performed overnight or for 16-24 hours for *Msm* and 5 days for *Mtb*. Following this incubation period the optical density of the cultures was measured; this was used to determine the portion of culture that was added to fresh 7H9/OADC (with or without Kan25) and these sub-cultures were incubated at 37°C prior to usage.

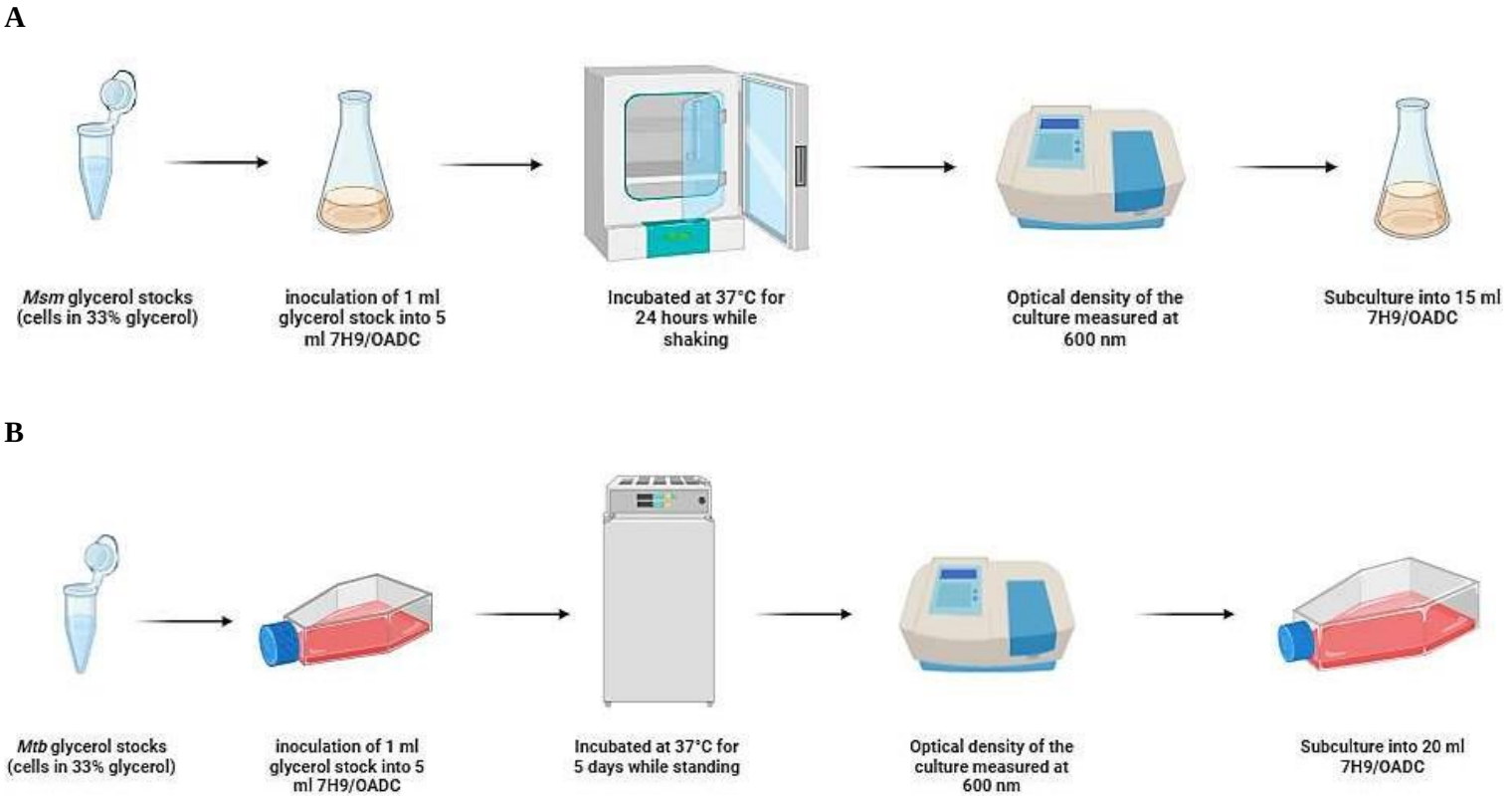

Figure 2.1. Diagram illustrating preparation of mycobacterial strains. Stationary phase glycerol stocks of ***A,*** *Msm* were thawed and inoculated into 5 ml 7H9/OADC and incubated for up to 24 hours at 37°C while shaking. Optical density (OD_{600}) of the stationary phase culture was taken and the culture was passaged into 15 ml 7H9/OADC and incubated for 6 hours at 37°C while shaking to reach a final OD_{600} of 0.4-0.5; ***B,*** *Mtb* were thawed and inoculated into 5 ml 7H9/OADC and incubated for 5 days at 37°C while stationary. OD_{600} of the culture was taken and the culture passaged in 20 ml 7H9/OADC and incubated at 37°C for 3 days while stationary to reach a final OD_{600} of 0.4-0.5. In the case of CRISPRi hypomorph strains, the 7H9/OADC was supplemented with Kan25. *Image generated using* Bi*orender (*2025*).*

Table 2.1. Bacterial strains used and generated in this study. The strain name, genotype composition and reference or source (where appropriate) is given.

Strain	Genotype composition	Reference
***Escherichia coli (E. coli)* DH5α**	F– φ80lacZΔM15 Δ(lacZYAargF)U169 recA1 endA1 hsdR17(rK–, mK+) phoA supE44 λ–thi-1 gyrA96 relA1	Thermofisher Scientific
***Mycobacterium smegmatis (Msm)* MSM_WT**	High frequency transformation laboratory strain mc^2155	(Snapper et al., 1990)
MSM_NT	*Msm* strain harbouring the plRL117_NT recombinant plasmid	Gift from Dr Melissa Chengalroyen (MMRU, UCT)
MSM_*clpP2*	*Msm* strain harbouring the plRL117_*clpP2* recombinant plasmid	This study
MSM_*wecA*01	*Msm* strain harbouring the plRL117_*wecA*01 recombinant plasmid	This study
MSM_*wecA*02	*Msm* strain harbouring the plRL117_*wecA*02 recombinant plasmid	This study
MSM_*wecA*03	*Msm* strain harbouring the plRL117_*wecA*03 recombinant plasmid	This study
MSM_*wecA*05	*Msm* strain harbouring the plRL117_*wecA*04 recombinant plasmid	This study
MSM_*wecA*05	*Msm* strain harbouring the plRL117_*wecA*05 recombinant plasmid	This study
MSM_*rfbD*01	*Msm* strain harbouring the plRL117_*rfbD*01 recombinant plasmid	This study
MSM_*rfbD*02	*Msm* strain harbouring the plRL117_*rfbD*02 recombinant plasmid	This study
MSM_*rfbD*03	*Msm* strain harbouring the plRL117_*rfbD*03 recombinant plasmid	This study
MSM_*rfbD*05	*Msm* strain harbouring the plRL117_*rfbD*04 recombinant plasmid	This study
MSM_*rfbD*05	*Msm* strain harbouring the plRL117_*rfbD*05 recombinant plasmid	This study
***Mycobacterium tuberculosis (*MTB*)* H37Ra MTB_Ra_WT**	*Mycobacterium tuberculosis* (Zopf) Lehmann and Neumann attenuated genome sequenced strain	NCBI Taxonomy ID: 419947 ATCC®25177™
MTB_Ra_NT	MTB_Ra carrying a non-targeting guide	This study
MTB_Ra_*wecA*01	*Msm* strain harbouring the plRL2-*wecA*01 recombinant plasmid	This study
MTB_Ra_*wecA*02	*Msm* strain harbouring the plRL2-*wecA*02 recombinant plasmid	This study
MTB_Ra_*wecA*03	*Msm* strain harbouring the plRL2-*wecA*03 recombinant plasmid	This study
MTB_Ra_*wecA*05	*Msm* strain harbouring the plRL2-*wecA*04 recombinant plasmid	This study
MTB_Ra_*wecA*05	*Msm* strain harbouring the plRL2-*wecA*05 recombinant plasmid	This study

2.2. Plasmid DNA extractions from *Escherichia coli*

To generate project stocks of CRISPRi plasmids, *E. coli* DH5α glycerol stocks carrying the plasmids of interest (provided by Dr Mandy Mason), plRL117 (plasmid#163635, addgene) and plRL2 (plasmid#163631, addgene) were inoculated from microbank beads in 50 ml LB broth and cultured overnight at 37°C in a shaking incubator. Plasmid DNA was extracted using the Zyppy™ plasmid miniprep kit as per manufacturer's instructions as follows: approximately 1.5 ml of the overnight culture was added to a 2 ml Eppendorf tube and centrifuged (Beckman Coulter centrifuge Allegra) at 14 000 *rcf* (relative centrifugal force) for 30 seconds. Following centrifugation, the supernatant was discarded, and an additional 1.5 ml of the same culture was added to the bacterial pellet, to increase biomass, and centrifuged as previously described. The pellet was then resuspended in 600 µl MilliQ water (dH_2O). Next, 100 µl of 7X Lysis Buffer was added to the resuspended cells and the tube gently inverted 6 times. Within 2 minutes, 350 µl of cold Neutralization Buffer was added and the tube gently inverted 2-3 times. The culture was then centrifuged at 14 000 *rcf* for 4 minutes. The supernatant was transferred into a Zymo-Spin™ IIN column, while ensuring that the cell debris was not disturbed. The column containing the sample was then transferred into a collection tube and centrifuged at 11 000 *rcf* for 20 seconds. Thereafter, 200 µl of Endo-Wash Buffer was added to the sample, and the column centrifuged at 11 000 *rcf* for 30 seconds. Finally, 400 µl of Zyppy™ Wash Buffer was added to the column and centrifuged at 11 000 *rcf* for 1 min. The column was placed into a clean 1.5 ml microcentrifuge tube and 50 µl of Zyppy™ Elution Buffer was added directly into the column. The column was allowed to stand at room temperature for approximately 1 min and was finally centrifuged at 11 000 *rcf* for 30 seconds to collect the plasmid DNA in the clean tube. The elution containing plasmid DNA was assessed for purity and quantified using the NanoDrop ND-2000 Spectrophotometer (Thermo Scientific).

2.3. Preparation of electrocompetent wild-type (WT) *mycobacterium smegmatis* and *Mycobacterium tuberculosis*

All standardised DNA manipulation and molecular cloning techniques were adapted from Sambrook, 1989 and Parish and Stoker, 1998.

Glycerol stocks of stationary phase cultures of MSM_WT were thawed on ice and added to 100 ml 7H9/OADC and grown for approximately 16 hours in a 37°C shaking incubator to reach mid to late log phase (OD of 0.4-0.8). Next, 2x 50 ml aliquots of the culture were centrifuged at 4 000 *rcf* for 10 mins at 4°C (Allegra™ X-22R Centrifuge, Beckman Coulter) and the supernatant discarded. The bacterial pellet was gently resuspended in 40 ml of 10% (v/v) glycerol and centrifuged as described above. The supernatant was discarded, and the pellet gently resuspended in 30 ml of 10% (v/v) glycerol and

centrifuged as above. The supernatant was discarded, and the pellet resuspended in 20 ml of 10% (v/v) glycerol and centrifuged as above. The final supernatant was discarded, and the bacterial pellet gently resuspended in 2 ml of 10% (v/v) glycerol. The electrocompetent cells were dispensed as 800 µl aliquots into 1.5 ml Eppendorf tubes and stored at -80°C.

2.4. Design and assembly of CRISPRi constructs targeting specific genes

2.4.1. CRISPRi targeting sgRNA assessment and selection

Two genes essential to mycobacterial galactan biosynthesis, *wecA* (MSMEG_4947; also known as *rfe*) and *rfbD* (MSMEG_6369; also known as *wzm*) were selected for this study with the objective of knocking down their expression using the CRISPRi system, utilising the CRISPRi plasmids and protocols developed by the Rock Laboratory (Rockefeller University, US) (Rock et al., 2017).

The features of each gene, including its function and the genomic and transcriptional organisation (potential operonic structure) **(Supplementary Figure S1)** were assessed using Mycobrowser and the relevant literature (see **Section 1.6**). The target genes and their enzymatic products are listed in **Table 2.2**. As these are essential genes, full knockdown of the gene product was not desirable as the bacteria would not survive in the absence of the essential functions of these genes, which would prohibit an interrogation of the bacterium's phenotype. Instead, we aimed to generate CRISPRi hypomorphs (strains with partial transcriptional silencing of the target gene).

To achieve this, the Pebble database was used for sgRNA selection. This database is the Rock lab's portal for sharing information on CRISPRi gene vulnerabilities in mycobacteria (Bosch et al., 2021) The database also contains a sgRNA Design Tool that enables researchers to select sgRNAs complementary to a gene of interest to be targeted. Notably, each sgRNA has a distinct predicted knockdown strength ranging from weak (0) to strong (1). Five sgRNAs with varying vulnerability profiles were selected for each target gene **(**see **Results, Figure 3.2).** Features and design choices used for selection included predicted strength of the guide as determined by the PAM site, and the length of its top and bottom oligonucleotides constrained to be between 20-25 bp.

The sgRNA oligos used in this study were synthesised by Inqaba Biotec (Cape Town); each sgRNA was synthesised at a scale of 0.01 µmol using standard (desalted) purification. The sgRNA designed to target the gene encoding the ATP-dependent CLP protease proteolytic subunit 2 (*clpP2*) was supplied by Lucas Raphela and used as a positive knockdown control with strong transcriptional silencing of the gene (data not shown, personal communication with Lucas Raphela). A plasmid containing a sgRNA which had no homology to the *Msm* genome (non-targeting sgRNA) was designed and generated by Dr.

Melissa Chengalroyen and served as a negative knockdown control (no expected transcriptional knockdown). The *Mtb* non targeting plasmid was designed and generated by Dr. Melissa Chengalroyen. The *Msm* oligo sequences are presented in **Results, Table 3.1** and **Table 3.2**. The *Mtb* oligo sequences are presented in **Results, Table 3.3.** Each oligo comprises a 'top' and 'bottom' sequence that can be annealed to form double stranded DNA that is suited to be integrated into a linearised CRISPRi plasmid.

Table 2.2. List of genes targeted in this study with information given regarding their Gene IDs, Uniprot references, enzymatic product and their functions which were taken directly from the Mycobrowser (Release 5) annotation for *Mtb* H37Rv

Gene name	***Msm* Gene ID (Unitprot Reference)**	***Mtb* Gene ID (Unitprot Reference)**	**Enzymatic product (Mycobrowser, *Mtb* H37Rv)**	**Function (Mycobrowser, *Mtb* H37Rv)**
***wecA* (*rfe*)**	MSMEG_4947 (A0R211)	Rv1302 (P9WMW5)	Probable undecapaprenyl-phosphate alpha-N-acetylglucosaminyltransferase Rfe (UDP-GlcNAc transferase)	Thought to be involved in AG biosynthesis, catalyzing the synthesis of GlcNAc-pyrophosphorylundecaprenol (lipid I).
***rfbD* (*wzm*)**	MSMEG_6369 (A0R5Z3)	Rv3265c (P72049)	Probable O-antigen/lipopolysaccharide transport integral membrane protein ABC transporter RfbD	May form an ATP-driven O-antigen/lipopolysaccharide export apparatus, in association with RFBE|Rv3781. Responsible for the translocation of the substrate across the membrane.
clpP2	MSMEG_4672 (A0R197)	Rv2460c (P9WPC3)	Probable ATP-dependent CLP protease proteolytic subunit 2 ClpP2 (endopeptidase CLP 2)	CLP cleaves peptides in various proteins in a process that requires ATP hydrolysis. CLP may be responsible for a general and central housekeeping function rather than for the degradation of specific substrates.

2.4.2. Plasmid restriction enzyme digestion

To allow for the incorporation of the sgRNA oligo into the CRISPRi backbone, the extracted circular plasmid DNA was linearised. Linearisation of the plRL117 and plRL2 plasmids from **Section 2.2** was performed by cleaving two *Bsm*BI sites in the multiple cloning site (MCS) of the plasmid (**Figure 2.2**). To achieve this, 2 µg of the extracted plasmid DNA was added to a reaction mixture that included 4 µl *Bsm*BI restriction enzyme (40 units) (NEB), 5 µl *Bsm*BI buffer (NEB) and nuclease-free water was added to yield a final reaction mixture volume of 20 µl. Two undigested control (no *Bsm*BI restriction enzyme) reactions were run alongside the digestion reactions: (1) the undigested plasmid in *Bsm*BI buffer and nuclease free water and (2) the undigested plasmid in nuclease-free water only. These were included to compare the migration of the plasmid post digestion with that of the undigested plasmid in

different buffer conditions. The reactions were gently mixed and spun down at low speed to collect at the bottom of the tube. The reaction mixtures were incubated at 55°C overnight (18-20 hours) in a MyCycler™ thermal cycler (Bio-Rad). A portion (5 µl) of these digestion reactions were run on a 1% TAE agarose gel alongside the undigested controls to confirm the linearisation of the plasmid.

2.4.3. Agarose gel electrophoresis

The reaction mixtures were run on a 1% TAE agarose gel (**Figure 2.2**) comprising 0.2 g agarose powder (Sigma-Aldrich) in 20 ml 1 x TAE buffer (40mM Tris-acetic acid, 1 mM Na_2EDTA). The agarose gel was solubilised by heating in a microwave, it was left to cool and then supplemented with 0.5 µg/ml ethidium bromide (EtBr). For each sample loaded, approximately 3 µl loading dye (0.025% bromophenol-blue in 30% (v/v) glycerol) was combined with 5 µl of the digested plasmid DNA. To allow for fragments sizes to be assessed, the Quick-Load Purple 1 kb DNA ladder (Roche Applied Science, Germany) was loaded into lane 1. Gels were run in a Mini-Sub GT mini horizontal submarine unit (Bio-Rad) at 80 volts for 60 mins. The bands were visualized under UV-light using the Gel Doc (WealTech Keta Imaging System).

A

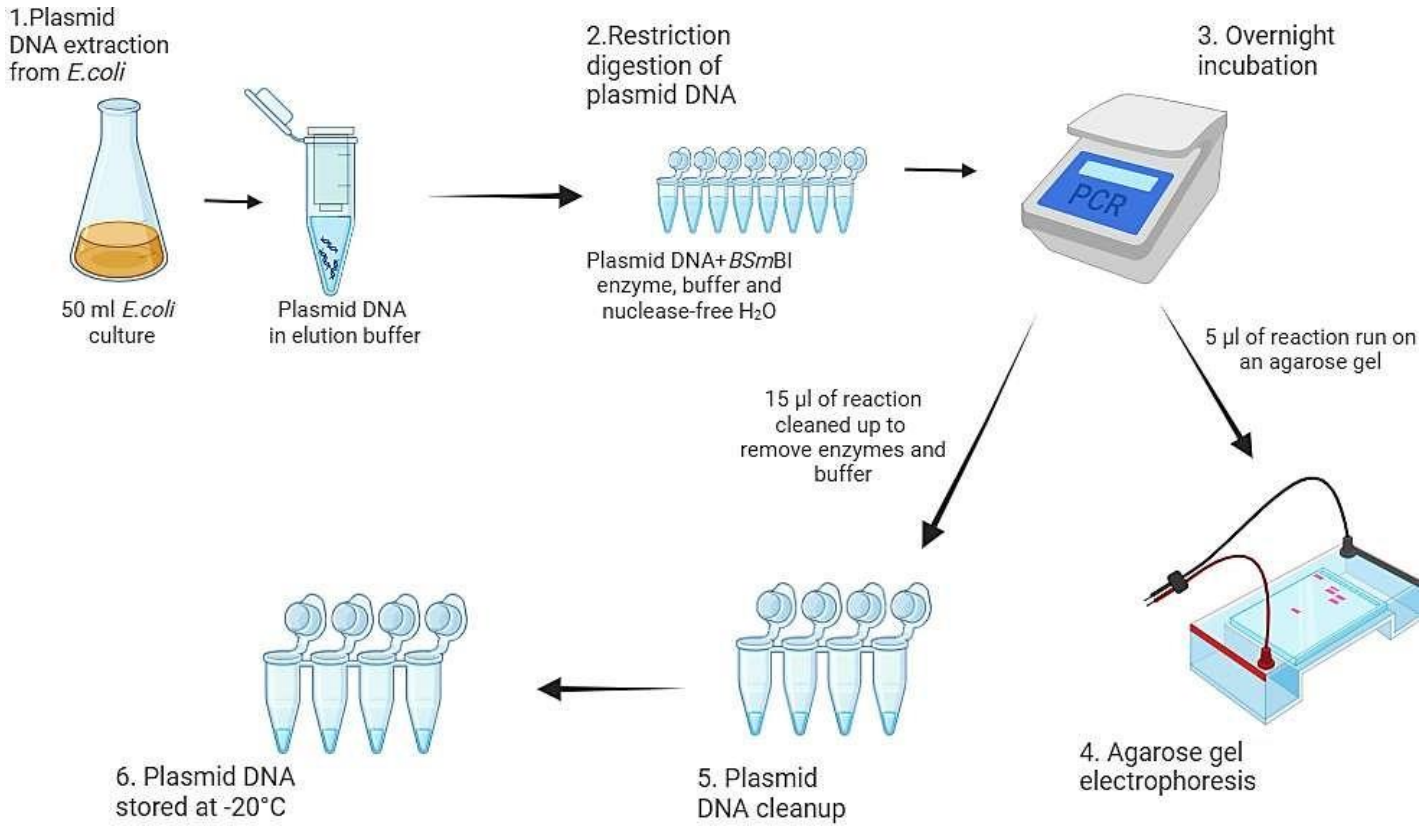

Figure 2.2. Illustration of restriction enzyme digestion and agarose gel electrophoresis. (1) The plRL117 and plRL2 plasmid DNA were extracted from *E. coli* DH5α cells, and (2) restriction digested using *Bsm*BI restriction enzymes. (3) The plasmid reactions were incubated overnight at 55°C, and (4) 5 µl of the reaction mixture run on an agarose gel to confirm successful restriction digestion. (5) The remaining 15 µl of the reaction mixture was cleaned up using the Gel and PCR clean up kit to remove enzymes and buffers, and (6) the plasmid DNA stored ar-20°C. *Generated using Biorender (2025).*

2.4.4. Plasmid DNA clean up

To ensure the plasmid DNA used for downstream experiments were not exposed to UV damage, the remaining 15 µl digested samples were used for ligation with the oligos **(Figure 2.2)**. The digestion enzymes and buffer were removed from the samples using the NucleoSpin® Gel and PCR Clean-up kit as per manufacturer's instructions. The plasmid DNA was mixed with Buffer NTI to a ratio of 1:2. The sample was placed into a 2 ml collection tube and centrifuged at 11 000 *rcf* for 30 seconds. The flow-through was discarded and 700 µl Buffer NT3 was added to the column and centrifuged as previous described. The flow-through was discarded and the column centrifuged for an additional 60 seconds as previously described. Finally, the column was placed into a clean 1.5 ml microcentrifuge tube and 30 µl Buffer NE added to the sample. The sample was allowed to incubate at room temperature for 1 min

and centrifuged at 11 000 *rcf* for 1 min to elute the linearised plasmid DNA. The plasmid DNA in Buffer NE was stored at -20°C. These were stored at -20°C prior to usage.

2.4.5. sgRNA oligo annealing

To incorporate the sgRNA insert into the linearised double stranded plasmid (**Figure 2.3**), the sgRNA must be double stranded. To achieve this, the top and bottom oligos for each sgRNA (see **Results Section 3.1**) were centrifuged at 11 000 *rcf* for 1 minute and diluted in nuclease-free water to a final working stock concentration of 100 µM. For each oligo pair, 46 µl oligo annealing buffer (50 mM Tris, 1 mM EDTA, 50 mM NaCl, pH 7.5) was added to a PCR tube and 2 µl of the top and 2 µl of the corresponding bottom oligo were added to the tube. Annealing reactions were run in the MyCycler™ thermal cycler at a denaturation step of 95°C for 2 mins, followed by an annealing phase comprising declining temperature increments of 0.1°C per second, until the temperature reached 4°C. This was repeated for each oligo pair, generating a total of 5 double stranded sgRNAs per gene. This process was repeated for each gene, generating a total of 15 double stranded sgRNAs. The sgRNAs were then stored at -20°C prior to usage.

2.4.6. Ligations

Following the annealing of the complementary oligos, the process of ligating the annealed oligos into the linearised plasmid was performed (**Figure 2.3**). Briefly, 1 µl of the annealed oligo was added to a reaction mixture containing 9 ng of the purified linearised plasmid from **Section 2.4.4**, 1 µl Quick-ligase enzyme (NEB) and 10 µl Quick-ligase buffer (NEB) (50 mM Tris-HCl, 10 mM $MgCl_2$, 10 mM DTT, pH 7.5). The reaction was made up to a final volume of 20 µl using nuclease-free water. The reaction mixtures were incubated at 25°C for 15 mins in the MyCycler™ thermal cycler. The ligated circular plasmids were then stored at -20°C prior to usage.

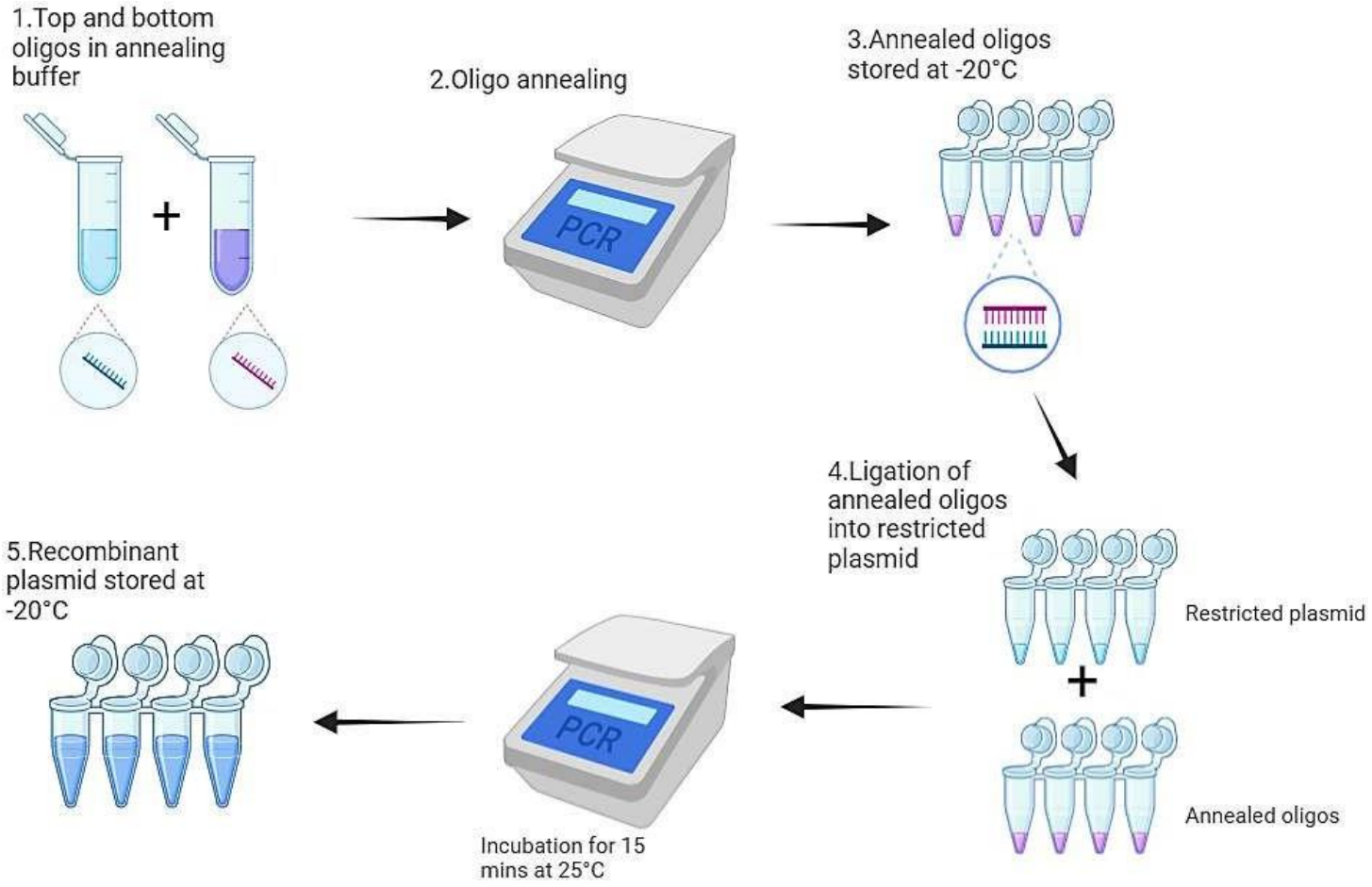

Figure 2.3. Generation of recombinant CRISPRi plasmids. (1) The top and bottom oligonucleotides were mixed and (2) annealed in annealing buffer. (3) The annealed oligos were stored at -20°C prior to ligation. (4) The annealed oligos were then ligated into the linearised plasmid and incubated at 25°C for 15 mins. (5) The resulting recombinant plasmids were stored at -20°C prior to usage. *Generated using Biorender (*2025*).*

2.5. Plasmid transformation and electroporation methods

2.5.1. Transformation into *Escherichia coli* for cloning and propagation

E. coli DH5α competent cells were thawed on ice for 10 mins and aliquoted in volumes of 100 µl into 1.5 ml Eppendorf tubes after which 2 µl of the ligation reactions (recombinant plasmids) were added. The mixtures were then incubated on ice for 30 mins. The competent cells were briefly heated at 42°C for 30 seconds and placed back on ice for an additional 5 mins. The competent cells were added to 900 µl LB broth and incubated at 37°C for 1 hour while shaking. Following incubation, the cultures were centrifuged at 11 000 *rcf* for 1 min and the supernatant discarded. The cell pellets were resuspended in 100 µl LB broth. Two different dilutions of the cultures were plated on LB agar supplemented with

Kan50 as follows: 1:1 and 1:10. As a control, DH5α competent cells that were not transformed were plated onto LB agar plates with Kan50 to confirm that kanamycin was effective as a selective marker. LB agar plates with no Kan50 were used as controls to confirm that the transformed cells were viable. The plates were incubated overnight in a 37°C stationary incubator. Individual transformant colonies were picked from the Kan50 plates using a plastic loop and inoculated into 10 ml LB agar supplemented with Kan50 and incubated overnight at 37°C while shaking. Extra transformant colonies were picked to allow subsequent screening and sequencing; these were streaked onto LB agar plates supplemented with Kan50 and incubated for 2 days at 37°C in a standing incubator to ensure outgrowth, and stored at 4°C. The plasmid DNA was extracted from the 10 ml overnight cultures using the Zyppy™ miniprep kit (described in **Section 2.2)** and the purified recombinant plasmids were quantified using the NanoDrop ND-2000 Spectrophotometer. The purified recombinant plasmids were sent for sanger sequencing (CAF. Stellenbosch University) to confirm successful ligation of the desired oligo pair (see **Section 2.6**). The plasmids generated are shown in **Table 2.3** and **Table 2.4**.

Table 2.3. List of *Mycobacterium smegmatis* plasmids used and generated in this study

Plasmid	**Composition**	**Reference**
plRL117	ATc-inducible (1) Tet^R-regulated promoter expressing Sth1 dcas9 containing a modified Shine-Dalgardo motif, (2) kanamycin-selectable maker and (3) a single-copy L5 integrase	Addgene plasmid #163635
plRL117_NT	Non-targeting construct ligated into the plRL117 plasmid	This study
plRL117_*clpP2*	*clpP2* knockdown construct made by ligating *clpP2* sgRNA oligo into the plRL117 plasmid	This study
plRL117_*wecA*01	*wecA* knockdown construct made by ligating *wecA*_01 sgRNA oligo into the plRL117 plasmid	This study
plRL117_*wecA*02	*wecA* knockdown construct made by ligating *wecA*_02 sgRNA oligo into the plRL117 plasmid	This study
plRL117_*wecA*03	*wecA* knockdown construct made by ligating *wecA*_03 sgRNA oligo into the plRL117 plasmid	This study
plRL117_*wecA*04	*wecA* knockdown construct made by ligating *wecA*_04 sgRNA oligo into the plRL117 plasmid	This study
plRL117_*wecA*05	*wecA* knockdown construct made by ligating *wecA*_05 sgRNA oligo into the plRL117 plasmid	This study
plRL117_*rfbD*01	*rfbD* knockdown construct made by ligating *rfbD*_01 sgRNA oligo ligated into the plRL117 plasmid	This study
plRL117_*rfbD*02	*rfbD* knockdown construct made by ligating *rfbD*_02 sgRNA oligo ligated into the plRL117 plasmid	This study

plRL117_*rfbD*03	*rfbD* knockdown construct made by ligating *rfbD*_03 sgRNA oligo ligated into the plRL117 plasmid	This study
plRL117_*rfbD*04	*rfbD* knockdown construct made by ligating *rfbD*_04 sgRNA oligo ligated into the plRL117 plasmid	This study
plRL117_*rfbD*05	*rfbD* knockdown construct made by ligating *rfbD*_05 sgRNA oligo ligated into the plRL117 plasmid	This study
plRL117_*clPp2*	*clpP2* knockdown construct made by ligating *clpP2* sgRNA oligo ligated into the plRL117 plasmid	This study

Table 2.4. List of *Mycobacterium tuberculosis* plasmids used in this study

Plasmid	**Composition**	**Reference**
plRL2	ATc-inducible (1) Tet^R -regulated promoter expressing Sth1 dcas9, (2) kanamycin-selectable marker and (3) a single-copy L5 integrase	Addgene plasmid #163631
plRL2_NT	Non-targeting construct ligated into the plRL2 plasmid	This study
plRL2_*wecA*01	*wecA* knockdown construct made by ligating *wecA*_01 sgRNA oligo into the plRL2 plasmid	This study
plRL2_*wecA*02	*wecA* knockdown construct made by ligating *wecA*_02 sgRNA oligo into the plRL2 plasmid	This study
plRL2_*wecA*03	*wecA* knockdown construct made by ligating *wecA*_03 sgRNA oligo into the plRL2 plasmid	This study
plRL2_*wecA*04	*wecA* knockdown construct made by ligating *wecA*_04 sgRNA oligo into the plRL2 plasmid	This study
pIRL2_*wecA*05	*wecA* knockdown construct made by ligating *wecA*_05 sgRNA oligo into the plRL2 plasmid	This study

2.5.2. Electroporation into WT *Mycobacterium smegmatis*

Once confirmation of the ligation, transformation and purification of the generated CRISPRi plasmid construct had been performed, these were electroporated into electrocompetent *Msm* and *Mtb* (**Figure 2.4**).

Electrocompetent stationary cultures of MSM_WT were thawed on ice for 15 mins and aliquoted (400 µl) into 2 ml Eppendorf tubes. Gene pulser Electroporation cuvettes (2 mm electrode gap, Bio-Rad) were pre-chilled on ice. Next, for each plasmid 2000 ng sgRNA-pIL117 recombinant vector was added to 400 µl electrocompetent MSM_WT and transferred to the pre-chilled 2 mm cuvettes. A no plasmid control was used to show the amount of background in the transformations. The cultures were pulsed in a GenePulser™ (Bio-Rad) using the following Exponential Protocol settings: 2500 V, 1000 Ω, 25µF.

The electroporated cells were then recovered by adding them to 1.5 ml Eppendorf tubes containing 600 µl 7H9/OADC. The cells were incubated at 37°C for 6 hours while shaking. Following the incubation period, the cultures were centrifuged at 11 000 *rcf* for 1 min and diluted to 1:1, 1:20 and 1:80 suspensions in 100 µl 7H9/OADC. The dilutions were plated on 7H10 agar plates supplemented with Kan25 and incubated at 37°C for 3 days in a stationary incubator. The cultures were also plated on 7H10 agar with no Kan25 to confirm that the cells remained viable throughout the electroporation process. Following the incubation period, single colonies of each transformant were picked from the Kan25 plate as previously described, and each colony was added to 5 ml 7H9/OADC supplemented with Kan25 and incubated at 37°C for 24 hours while shaking to yield a final OD_{600} of 0.8-1.0 (stationary phase). The OD_{600} of the stationary phase cultures were measured and the cultures resuspended in 15 ml fresh 7H9/OADC supplemented with Kan25. The cultures were incubated for 6 hours at 37°C while shaking, to yield a final OD_{600} of ~0.4-0.8 (mid to late log phase). Following the incubation period, freezer stocks of each of the cultures (12 strains in total) were made by adding 1 ml of the culture to 500 µl of 33% (v/v) glycerol, and stored at -80°C. To allow for the large number of strains to be generated without cross contamination, this process was handled in small batches (gene sets) and repeated.

2.5.3. Electroporation into WT *Mycobacterium tuberculosis* H37Ra

The electroporation of electrocompetent stationary cultures of MTB_Ra_WT was performed with the same steps performed in **Section 2.5.2** with the following amendments. Approximately, 500 ng of sgRNA-plRL2 recombinant vector was added to 300 µl MTB_Ra_WT prior to pulsing as described in **Section 2.5.2**. The cells were then recovered in 700 µl 7H9/OADC and incubated overnight in a 37°C shaking incubator. The cells were plated on 7H10 agar supplemented with Kan25 as 1:10, 1:100 and 1:1000 dilutions and incubated in a 37°C stationary incubator for 3-4 weeks. The cells were also plated on 7H10 agar with no Kan25 to confirm that the cells were viable. Following this incubation period, single colonies were picked from the Kan25 plate as described and added to 50 ml culture flasks containing 5 ml 7H9/OADC supplemented with Kan25 and incubated in a 37°C stationary incubator for 5 days. The cultures were then resuspended in a 200 ml culture flask containing 15 ml fresh 7H9/OADC supplemented with Kan25 and incubated for 3 days as described. Freezer stocks of the cultures (6 strains in total) were made by adding 1 ml of the culture to 500 µl of 33% (v/v) glycerol and stored at -80°C.

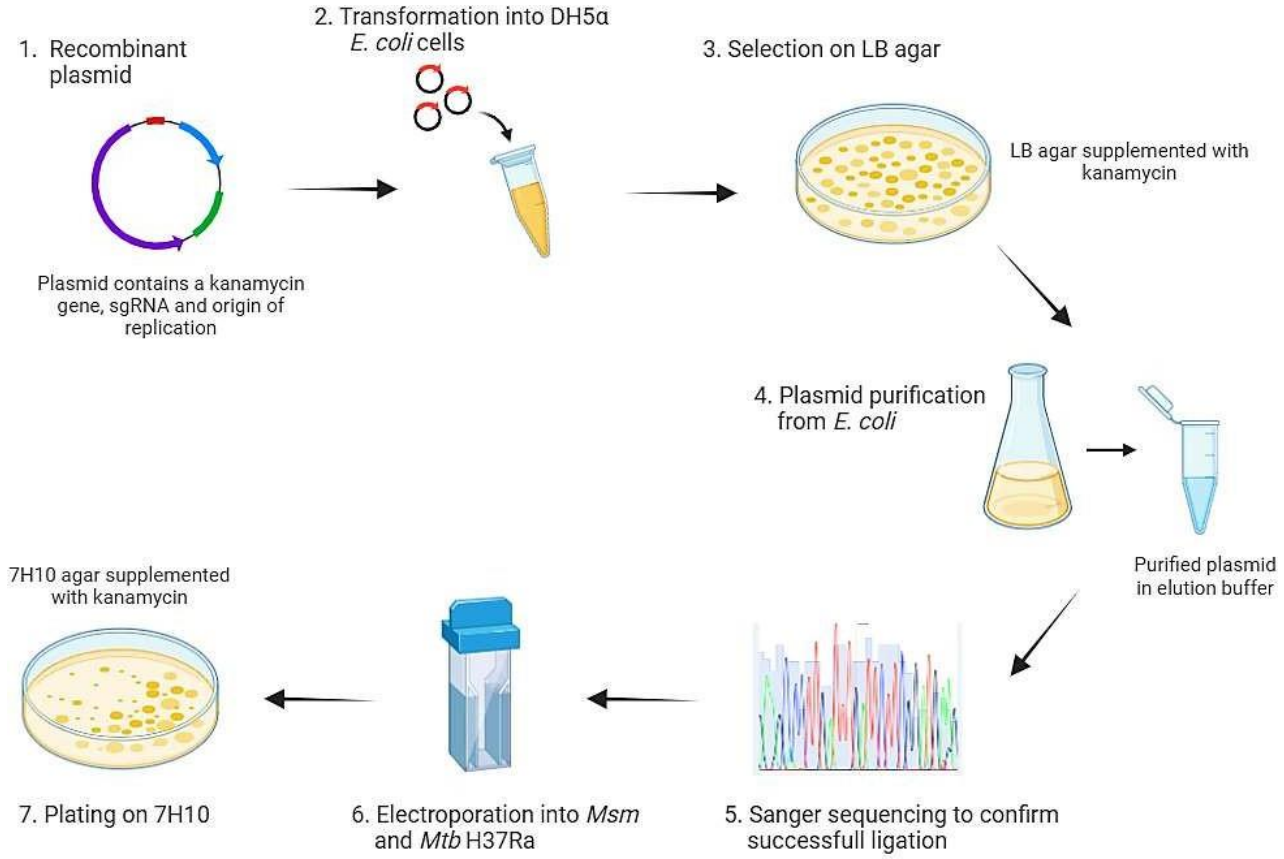

Figure 2.4. Electroporation of the recombinant plasmids into *Mycobacterium smegmatis* and *Mycobacterium tuberculosis*. (1) The recombinant plasmids were (2) transformed into DH5α *E. coli* cells and (3) successfully transformed cells were selected on LB agar supplemented with Kan25. Following (4) purification of the plasmids, (5) successful ligation of the oligos were confirmed by sanger sequencing and (6) the recombinant pIRL117 and pIRL2 plasmids electroporated into *M. smegmatis* and *M. tuberculosis* cells, respectively. (7) Successfully electroporated cells were selected on 7H10 agar supplemented with Kan25. *Generated using Biorender (2025).*

2.6. Sanger sequencing of plasmid DNA

All sanger sequencing reactions were performed by the Central Analytic Sequencing Facility (CAF) at the University of Stellenbosch using the Primer 1834 (5'-TTCCTGTGAAGAGCCATTGATAATG-3') (Rock et al., 2017) Sequencing data were analysed using Benchling Sequence Alignment Tool (Benchling, San-Francisco) to confirm the presence of the expected oligo sequence insert within the MCS of each plasmid.

2.7. Validation of CRISPRi knockdowns

2.7.1. Spotting assays to assess growth inhibition on solid media.

Mycobacterium smegmatis

To inoculate strains, 1 ml of the stationary phase *Msm* hypomorph glycerol freezer stock was added to 5 ml 7H9/OADC supplemented with Kan25 and incubated to late log phase for 24 hours at 37°C while shaking. The OD_{600} measurements of these late log phase cultures were determined, and the cultures resuspended in 10 ml fresh 7H9/OADC supplemented with Kan25 and incubated overnight at 37°C while shaking to reach a final OD of 0.4-0.6. The OD_{600} of these overnight cultures was used to standardised (by either diluting or concentrating in 7H9/OADC) to a final OD_{600} of 0.4 to ensure equal optical densities of bacterial cells among cultures. A 10 µl aliquot of each culture was sequentially added to 90 µl 7H9/OADC to form six 10-fold serial dilutions, and 5 µl of each 10-fold dilution was spotted on 7H10 agar plates **(Figure 2.5)**. These were spotted on two agar media plates, one that had been supplemented with 100 ng/ml anhydrotetracycline (ATc) and one without ATc. The dilution spots were allowed to dry and be absorbed into the agar. The plates were lidded, inverted and covered in foil to protect the ATc from light. The plates were then placed in a 37°C stationary incubator for 3 days. On outgrowth of the cells into spots, images of each plate were captured using the WealTech Ketagalan Imaging Gel doc.

Mycobacterium tuberculosis

To inoculate strains, 1 ml of the stationary phase *Mtb* hypomorph glycerol freezer stocks were added to 5 ml 7H9/OADC supplemented with Kan25 and incubated to late log phase for 5 days at 37°C while stationary. The OD_{600} of these late log phase cultures were determined, and the cultures were resuspended into 15 ml 7H9/OADC supplemented with Kan25 and incubated for 3 days at 37°C while stationary to yield a final OD of 0.4-0.6. The OD_{600} of these overnight cultures were used to standardise (by either diluting or concentrating in 7H9/OADC) to a final OD_{600} of 0.5 to ensure equal optical densities of bacterial cells among culture. A 10 µl aliquot of each culture was sequentially added to 90 µl 7H9/OADC to form six 10-fold serial dilutions, and 10 µl of each dilution was spotted onto 7H10 agar **(Figure 2.5)** plates, one was supplemented with 100 ng/ml ATc, and one without. The plates were prepared for incubation as described above and placed in a 37°C stationary incubator for 2 weeks. The images were then captured and exported as described above.

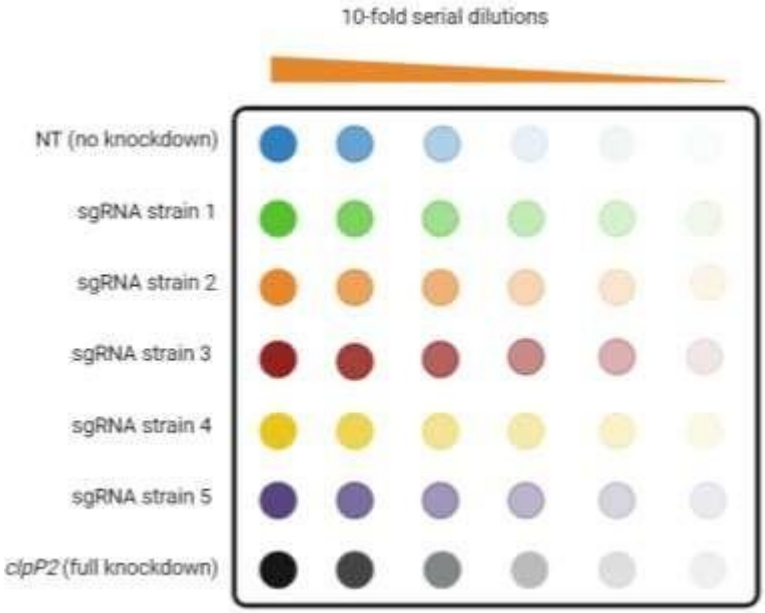

Figure 2.5. Spotting assay plate format showing CRISPRi strains and dilution series. *Generated using Biorender (2025).*

2.7.2. Growth dynamics to assess growth inhibition of *Mycobacterium smegmatis* in liquid media

To inoculate strains, 1 ml of the stationary phase *Msm* hypomorph glycerol stocks was added to 5 ml 7H9/OADC supplemented with Kan25 and incubated for 24 hours at 37°C while shaking. The OD_{600} of the cultures were determined and the cultures resuspended, into 10 ml 7H9/OADC supplemented with Kan25 and incubated overnight at 37°C while shaking to yield a final OD_{600} of 0.4-0.6. The overnight cultures were diluted or concentrated in 7H9/OADC to a final OD_{600} of 0.4 to ensure equal optical densities of bacterial cells amongst strains. Approximately 10 µl of each culture was added to 90 µl 7H9/OADC in a 96-well microtiter clear flat-bottom plate (Greiner bio-one. CELLSTAR®) with or without 100 ng/ml ATc. The OD_{600} of each well was measured every 5 minutes without shaking over a 24-hour period in a plate reader (FLUOstar Optima, BMG LabTech) in technical replicates of 4 **(Figure 2.6)**. Graphs were generated as OD_{600} vs time (minutes) with the hourly data plotted.

		1	2	3	4	5	6	7	8	9	10	11	12
-ATc	A	NT	*wecA*01	*wecA*02	*wecA*03	*wecA*04	*wecA*05	*rfbD*01	*rfbD*02	*rfbD*03	*rfbD*05	*rfbD*05	*clpP2*
	B	NT	*wecA*01	*wecA*02	*wecA*03	*wecA*04	*wecA*05	*rfbD*01	*rfbD*02	*rfbD*03	*rfbD*05	*rfbD*05	*clpP2*
	C	NT	*wecA*01	*wecA*02	*wecA*03	*wecA*04	*wecA*05	*rfbD*01	*rfbD*02	*rfbD*03	*rfbD*05	*rfbD*05	*clpP2*
	D	NT	*wecA*01	*wecA*02	*wecA*03	*wecA*04	*wecA*05	*rfbD*01	*rfbD*02	*rfbD*03	*rfbD*05	*rfbD*05	*clpP2*
	E	NT	*wecA*01	*wecA*02	*wecA*03	*wecA*04	*wecA*05	*rfbD*01	*rfbD*02	*rfbD*03	*rfbD*05	*rfbD*05	*clpP2*
	F	NT	*wecA*01	*wecA*02	*wecA*03	*wecA*04	*wecA*05	*rfbD*01	*rfbD*02	*rfbD*03	*rfbD*05	*rfbD*05	*clpP2*
+ATc	G	NT	*wecA*01	*wecA*02	*wecA*03	*wecA*04	*wecA*05	*rfbD*01	*rfbD*02	*rfbD*03	*rfbD*05	*rfbD*05	*clpP2*
	H	NT	*wecA*01	*wecA*02	*wecA*03	*wecA*04	*wecA*05	*rfbD*01	*rfbD*02	*rfbD*03	*rfbD*05	*rfbD*05	*clpP2*

Figure 2.6. Layout of growth curve plate with the *M. smegmatis* hypomorph strains

2.8. Phenotype characterisation

2.8.1. Determining reference Minimum Inhibitory Concentrations (MICs) of known antimycobacterial drugs in wild-type *Mycobacterium smegmatis*

A 1 ml aliquot of MSM_WT glycerol stock was thawed on ice and added to 5 ml 7H9/OADC and incubated for 24 hours at 37°C while shaking. The culture was then resuspended in 15 ml 7H9/OADC and incubated overnight at 37°C while shaking. The cultures were standardised in 7H9/OADC to a final OD_{600} of 0.4. The culture was then diluted 1:1000 in 7H9/OADC (50 µl culture into 50 ml media). Working stocks of the drugs of interest were made in 7H9/OADC as follows: 1024 µg/ml rifampicin (RIF), 32 µg/ml ethambutol (EMB), 80 µg/ml vancomycin (VAN), 64 µg/ml linezolid (LNZ). Using a clear flat-bottom 96 well microtiter plates (Greiner bio-one, CELLSTAR®), four MIC assays were set up as follows: 100 µl 7H9/OADC added to row A, column 1-12; 50 µl 7H9/OADC added to all remaining wells. Next, 50 µl working stock of the drug was added to wells in column 1 rows B-G, and 50 µl of media added to well 1H to give a total volume of 100 µl all wells of column 1 **(Figure 2.7).** Two-fold serial dilutions of the drug of interest were carried out, using an 8-channel multichannel pipette, by transferring the 50 ul from the wells of column 1 (drug) into those of column 2, pipetting up and down 5 times to mix the contents, and subsequently transferring 50 µl from column 2 into the following column and repeating until all 12 columns have been serially diluted and contain a portion the drug of interest. The final 50 µl from column 12 was discarded to ensure that all columns contained 50 µl of liquid. Using a 12-channel multichannel pipette, 50 µl of the 1:1000 diluted culture was added

to the entire plate, apart from row A, columns 1-12 which was not inoculated with cells (these serve as media only control wells). All wells contained a final volume of 100 µl of liquid. The plates were covered in foil and incubated at 37°C in a stationary incubator for 48 hours. Following the incubation period, 10 µl of resazurin (0.01%) was added to each well and plates re-incubated at 37°C for an additional 8 hours. Alamar blue functions by penetrating cells and incorporates an oxidative-reduction function by reducing the redox dye resazurin (blue) to a fluorescent product resorufin (pink) in living cells (Dinh et al., 2023, Franzblau et al., 1998).

Fluorescent readings were taken using the FLUOstar Optima, BMG LabTech plate reader using a fluorescence protocol containing an excitation and emission wavelength of 544 nm and 590 nm, respectively. The raw data derived were pre-processed in Microsoft Excel. The data from each plate were analysed independently. The average reading of the media control wells was calculated (average background fluorescence value). Each sample well was then background corrected by subtracting the average background fluorescence value from each sample well reading. Following this, the background corrected value for the no drug wells (expected to be the maximum growth achieved) was calculated (average 100% growth). The proportion of growth of each well was then calculated by dividing each sample well by the average 100% growth value for that strain and plate. Finally, the proportion growth value was multiplied by 100 to generate a percentage growth value. The percentage inhibition for each well was then determined by subtracting the percentage growth value of each sample well from 100. Data of percentage inhibition was visualized using Graphpad Prism 10.2.0 (GraphPad Inc.). The inhibition data were graphed on an XY plot, with the drug concentration on the X axis and the percentage (%) inhibition on the Y axis. Due to the drug concentrations being represented by 2-fold dilution series, the X-axis was converted to a log10 scale. A dose-response (non-linear regression analysis) was run using GraphPad Prism and the MIC_{90} of each drug against WT *Msm* mc^2155 determined. The determined MIC_{90} was compared to previously published data (see **Results Section 3.4.1**).

A

Decreasing drug concentration

	1	2	3	4	5	6	7	8	9	10	11	12
A	7H9	7H9	7H9	7H9	7H9	7H9	7H9	7H9	7H9	7H9	7H9	7H9
B	Drug+ Cells	Drug+ Cells	Drug+ cells	Drug+ cells	Drug+ cells	Drug+ cells	Drug+ cells	Drug+ cells	Drug+ cells	Drug+ cells	Drug+ cells	Drug+ cells
C	Drugs+ Cells	Drugs+ Cells	Drugs+ cells	Drugs+ cells	Drugs+ cells	Drugs+ cells	Drugs+ cells	Drugs+ cells	Drugs+ cells	Drugs+ cells	Drugs+ cells	Drugs+ cells
D	Drug+ Cells	Drug+ cells	Drug+ cells	Drug+ cells	Drug+ cells	Drug+ cells	Drug+ cells	Drug+ cells	Drug+ cells	Drug+ cells	Drug+ cells	Drug+ cells
E	Drug+ Cells	Drug+ cells	Drug+ cells	Drug+ cells	Drug+ cells	Drug+ cells	Drug+ cells	Drug+ cells	Drug+ cells	Drug+ cells	Drug+ cells	Drug+ Cells
F	Drug+ cells	Drug+ cells	Drug+ cells	Drug+ cells	Drug+ cells	Drug+ cells	Drug+ cells	Drug+ cells	Drug+ cells	Drug+ cells	Drug+ cells	Drug+ cells
G	Drug+ Cells	Drug+ cells	Drug+ cells	Drug+ cells	Drug+ cells	Drug+ cells	Drug+ cells	Drug+ cells	Drug+ cells	Drug+ cells	Drug+ cells	Drug+ cells
H	Cells+ 7H9	Cells+ 7H9	Cells+ 7H9	Cells+ 7H9	Cells+ 7H9	Cells+ 7H9	Cells+ 7H9	Cells+ 7H9	Cells+ 7H9	Cells+ 7H9	Cells+ 7H9	Cells+ 7H9

B

	1	2	3	4	5	6	7	8	9	10	11	12
A	100µl	100µl	100µl	100µl	100µl	100µl	100µl	100µl	100µl	100µl	100µl	100µl
B	50µl	50µl	50µl	50µl	50µl	50µl	50µl	50µl	50µl	50µl	50µl	50µl
C	50µl	50µl	50µl	50µl	50µl	50µl	50µl	50µl	50µl	50µl	50µl	50µl
D	50µl	50µl	50µl	50µl	50µl	50µl	50µl	50µl	50µl	50µl	50µl	50µl
E	50µl	50µl	50µl	50µl	50µl	50µl	50µl	50µl	50µl	50µl	50µl	50µl
F	50µl	50µl	50µl	50µl	50µl	50µl	50µl	50µl	50µl	50µl	50µl	50µl
G	50µl	50µl	50µl	50µl	50µl	50µl	50µl	50µl	50µl	50µl	50µl	50µl
H	50µl	50µl	50µl	50µl	50µl	50µl	50µl	50µl	50µl	50µl	50µl	50µl

Figure 2.7. Wild-type *M. smegmatis* MIC plate layout. *A,* Final plate layout, drug concentration decreasing 2-fold along the plate; ***B,*** final volume of 7H9/OADC media in each well. Final volume of contents in each well after addition of cells is 100 µl.

2.8.2. Antimycobacterial drug susceptibility assays of CRISPRi *Mycobacterium smegmatis* strains

To inoculate strains, 1 ml of the stationary phase *Msm* hypomorph glycerol stocks were added to 5 ml 7H9/OADC supplemented with Kan25 and incubated for 24 hours at 37°C while shaking. The cultures were resuspended in 15 ml 7H9/OADC supplemented with Kan25 with or without 100 ng/ml ATc and incubated for 15 hours at 37°C while shaking. The cultures were then diluted to a final OD_{600} of 0.4, in 7H9/OADC supplemented with Kan25, to ensure comparable optical density of cells between cultures. The cultures were finally diluted 1:1000 in 7H9/OADC with or without 100 ng/ml ATc. Using flat-bottom 96 well microtiter plates, four MIC assays for each CRISPRi strain pair were set up as follows: 100 µl 7H9/OADC without ATc into row A columns 1-6; 50 µl 7H9/OADC without ATc into row A columns 7-12; 50 µl 7H9/OADC without ATc into all wells of rows B-D. Next, 100 µl 7H9/OADC with 100 ng/ml ATc was added to row H columns 1-6; 50 µl 7H9/OADC with 100 ng/ml ATc into row H column 7-12; 50 µl 7H9/OADC with 100 ng/ml ATc into all wells of rows E-G **(Figure 2.8).** The WT MICs determined in **Section 2.8.1 (**see **Results Section 3.4)** were used as references to determine the working concentration of the drugs against our CRISPRi hypomorph strains. Working stocks of the drugs of interests were made in 7H9/OADC as follows: 256 µg/ml rifampicin (RIF), 4 µg/ml ethambutol (EMB), 10 µg/ml vancomycin (VAN), 16 µg/ml linezolid (LNZ). Briefly, 50 µl of the drug of interest was added to the wells of column 1 rows B-G. Two-fold serial dilutions of the drug (rows B-G only) were carried out, using 6 tips loaded on an 8-channel multichannel pipette by transferring the contents from the wells of column 1 into those of column 2, pipetting up and down 5 times to mix the contents, and subsequently transferring 50 µl from column 2 into the following column and repeating until all columns have been diluted. The final 50 µl from column 12 was discarded to ensure that all columns contained 50 µl of liquid. The plate was loaded with ATc treated and untreated cells, using a 12-channel multichannel pipette as follows: First, 50 µl of the 1:1000 diluted untreated culture was added to the row A, columns 7-12 and to all wells of rows B-D. Second, 50 µl of the 1:1000 diluted treated culture was added to the row H, columns 7-12 and to all wells of rows E-G. All wells contained a final volume of 100 µl of liquid. The plates were covered in foil and incubated at 37°C in a stationary incubator for 1.5 days. Finally, 20 µl of resazurin (0.01%) was added to each well and plates re-incubated at 37°C for an additional 4 hours. Images of each plate was captured, fluorescent readings taken and inhibition vs log concentration graphs generated as described in **Section 2.8.1**.

A

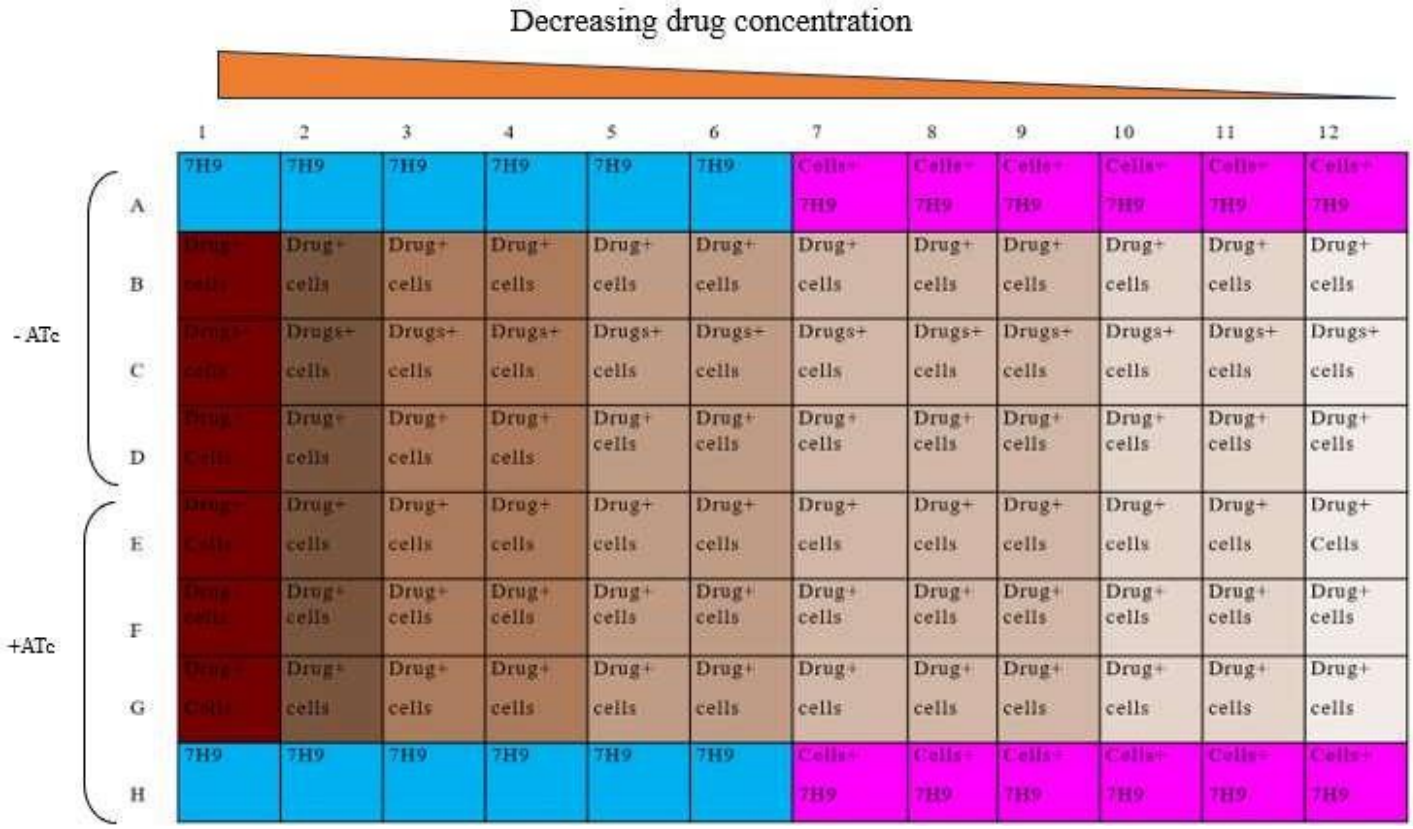

B

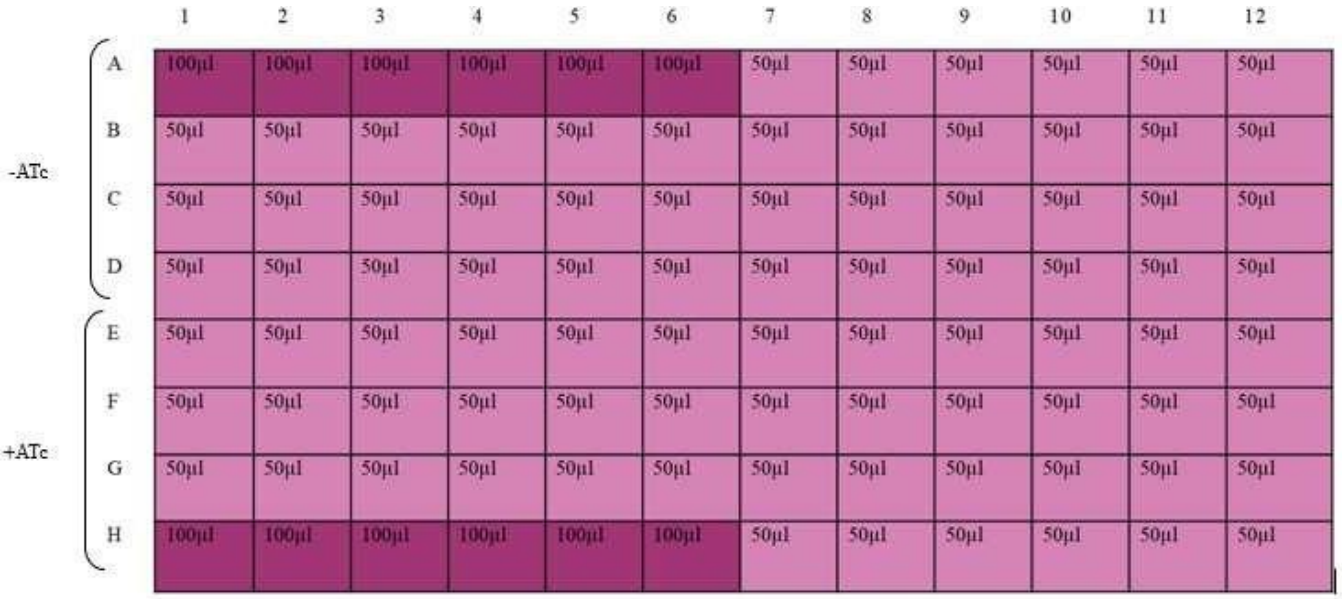

Figure 2.8. ***M. smegmatis*** **hypomorph MIC plate layout.** ***A,*** Final plate layout, drug concentration decreasing 10-fold across the plate; ***B,*** final volume of 7H9/OADC media in each well. Final volume of contents in each well 100 µl.

2.9. Morphotype characterisation

2.9.1. Metabolic labelling of *Mycobacterium smegmatis* with DMN-Trehalose fluorescent probe

To inoculate strains, 1 ml of stationary phase *Msm* hypomorph glycerol stocks of strains were added to 5 ml 7H9/OADC supplemented with Kan25 and incubated for 24 hours at 37°C while shaking, to yield final OD_{600} of ~1.0. Following the incubation period, the OD_{600} of the cultures were determined and the cells resuspended in 15 ml 7H9/OADC supplemented with Kan25 and incubated at 37°C in a shaking incubator to an expected OD_{600} of 0.4. Paired cultures (one with the addition of 100 ng/ml ATc and one without ATc) were incubated for 15 hours at 37°C while shaking. Next, 100 µl of the exponentially replicating bacterial cells were mixed with 1 µl of 1 mM DMN-Tre (final concentration of 10 µM) and incubated at 37°C while shaking for 2 hours. The cells were then centrifuged at 11 000 *rcf* for 5 mins and resuspended in 100 µl Phosphate Buffered Saline supplemented with 0.05% Tween80 (PBST). The cells were prepped and visualised by microscopy as described below in **Section 2.9.2**.

2.9.2. Fluorescence microscopy

To visualise mycobacterial cells by microscopy, the cells were prepared on agarose pad-based slides. A 2% agarose solution was made by melting 2 g low gelling temperature agarose (Sigma) in 100 ml Milli-Q dH_2O. Melted agarose was pipetted onto a rectangular glass slide (LASEC) allowing the volume of agarose to spread across the slide, this was capped by another rectangular glass slide to create a smooth surface. The agarose was then allowed to solidify at room temperature. After cooling of the agarose, the second glass slide was gently removed by sliding across the solidified agarose layer. Approximately 3 µl of the labelled mycobacterial cells from **Section 2.9.1** were spotted onto the agar surface and allowed to airdry on the agarose and coverslips placed over the sample. Samples were imaged using a Zeiss Axio Observer fluorescent microscope (Carl ZEISS) using the settings listed in **Table 2.5**. The images and data retrieved were analysed using ImageJ-Fiji (Shivanandan et al., 2013) and the MicrobeJ plugin (see **Supplementary Table S3** for list of settings) (Ducret et al., 2016).

Table 2.5. Microscope settings

Data	**Setting**
Type of microscope	Inverted
Objective settings	1000X Oil Immersion
Brightfield channel settings	Acquisition Mode= Widefield Fluor= TL Brightfield Illumination type= Transmitted

DMN-Tre fluorescent channel settings	Acquisition Mode= Widefield Fluor= EGFP Illumination type= Epifluorescence Emission Wavelength= 509.0 nm Excitation Wavelength= 488.0 nm

Chapter 3: Results

3.1 Selection and design of sgRNAs and plasmids

The CRISPRi/dcas9 system has previously been utilised to study essential genes in many bacterial species, including *Escherichia coli* (Qi et al., 2013), *Staphylococcus aureus* (Zhao et al., 2017), *Bacillus subtilis* (Peters et al., 2016) and *Corynebacterium glutamicum* (Cleto et al., 2016). Additionally, several papers have demonstrated the use of this system for knocking down essential genes in mycobacteria such as *M. abscessus* (Gupta and Rohde, 2023) and *M. smegmatis* (Xiao et al., 2019).

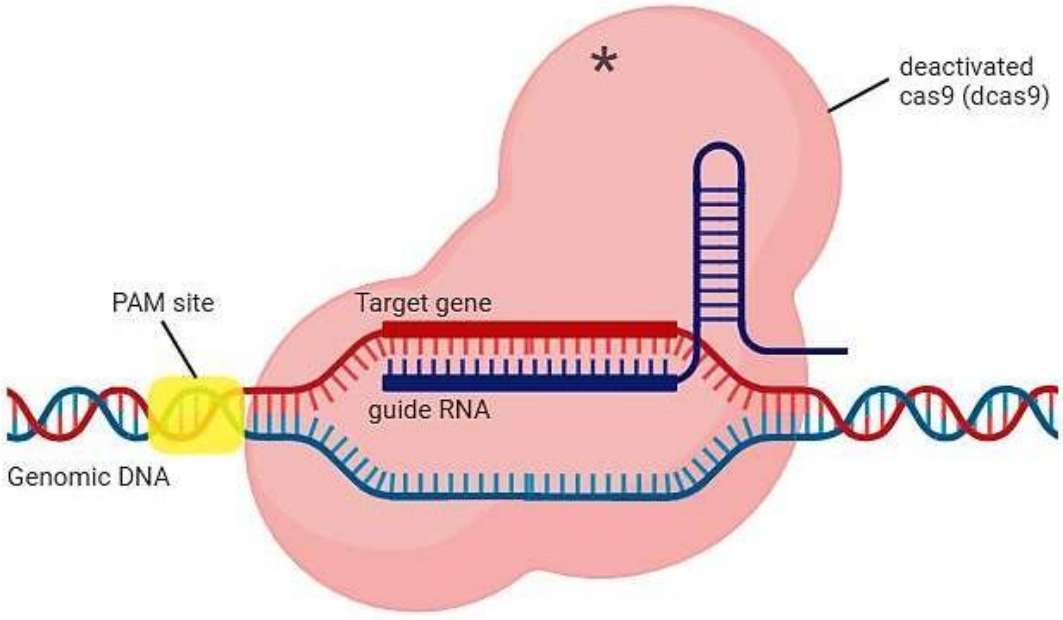

Figure 3.1. Mechanism of sgRNA-dCas9 recognition of target gene regions of genomic DNA. The sgRNA forms a complex with the deactivated Cas9 (dCas9) protein. This sgRNA-dCas9 complex scans the genomic DNA and recognises the PAM site. The complex encounters then a homologous region of the DNA and binds tightly to this region to form a stable complex, blocking RNA polymerase, resulting in transcriptional silencing of the target gene. *Generated using Biorender (2025).*

To generate CRISPRi strains, the design of targeting guide sequences needs to be considered and undertaken. Single guide RNAs (sgRNAs) contain short forward and reverse oligonucleotides (oligos) and in this project the length of each oligo was confined to 23-26 base pairs. When transcribed the sgRNAs are designed to be complementary to the desired target sequence region of the bacterial chromosomal DNA, and adjacent to a specific sequence called a protospacer adjacent motif (PAM), and requires Watson-Crick base-pairing between the sgRNA and the gene target (Rock et al., 2017) A catalytically inactive dCas9 (deactivated dCas9) is expressed from the integrated CRISPRi system and binds to the sgRNA molecule. This complex is then guided along the DNA by the sgRNA until it matches with the target region in the gene of interest, binding tightly to this region resulting in the

complex sterically hindering transcription of the target gene (Rock et al., 2017, Larson et al., 2013) **(Figure 3.1).** With the rise in the employment of the CRISPRi system to knock down expression of target genes and validate their functional activity, several computational tools exist to assist in the design and identification of sgRNA sequences (Gooden et al., 2021). For this study, the Pebble Database (Rockerfeller University), specifically the sgRNA Design Tool, was used to select oligos for sgRNA targeting of both *M. smegmatis* and *M. tuberculosis* strains. This database is a portal created by the Rock Lab and is used for sharing sgRNA designs and CRISPRi genomic experiments in mycobacteria (Rock et al., 2017). The selected CRISPRi sgRNAs for each gene in this study were derived from the Pebble database's sgRNA Design Tool which identifies multiple sgRNAs that target each gene of interest. The tool supplies information relating to the potential knockdown efficacy of each sgRNA and, for this study, the predicated strength of each guide and its target sequence length was utilised to select guides.

The selected sgRNA oligos were required to:

1) Target the region of interest
2) Encode 5' and 3' *Bsm*BI compatible sticky end restriction sites for ligation into the CRISPRi plasmids
3) Have a region of target sequence homology that is 20-26 base pairs
4) Have the same PAM site strength

We designed *M. smegmatis* CRISPRi plasmids using the backbone plasmid plRL117 (Addgene plasmid #163635), with the aim of targeting two essential genes, *wecA* (also known as *rfe*, MSMEG_4947) and *rfbD* (also known as *wzm*, MSMEG_6369). For each gene, five sgRNAs with varying predicted strengths and vulnerability profiles were selected **(Figure 3.2A & B; Table 3.1).** *M. tuberculosis* CRISPRi plasmids were designed to target *wecA* (*rfe*, Rv1302) using the plasmid pIRL2 (Addgene plasmid #163631). Five sgRNAs with varying predicted strengths vulnerability profiles were selected, each approximately 26 nucleotides long **(Figure 3.2C; Table 3.2).**

Non-targeting sgRNAs with no homology to genomic DNA regions (gift of Dr. Melissa Chengalroyen) were used as non-targeting (negative) controls for both *M. smegmatis* and *M. tuberculosis* studies. It is noted that these were generated using the original mycobacterial CRISPRi plasmid pLJR962 (Addgene plasmid #115162). A sgRNA targeting the essential *clpP2* gene, possessing a high vulnerability profile, was used as a positive control for *M. smegmatis* studies, using the plRL117 plasmid **(Table 3.3)**.

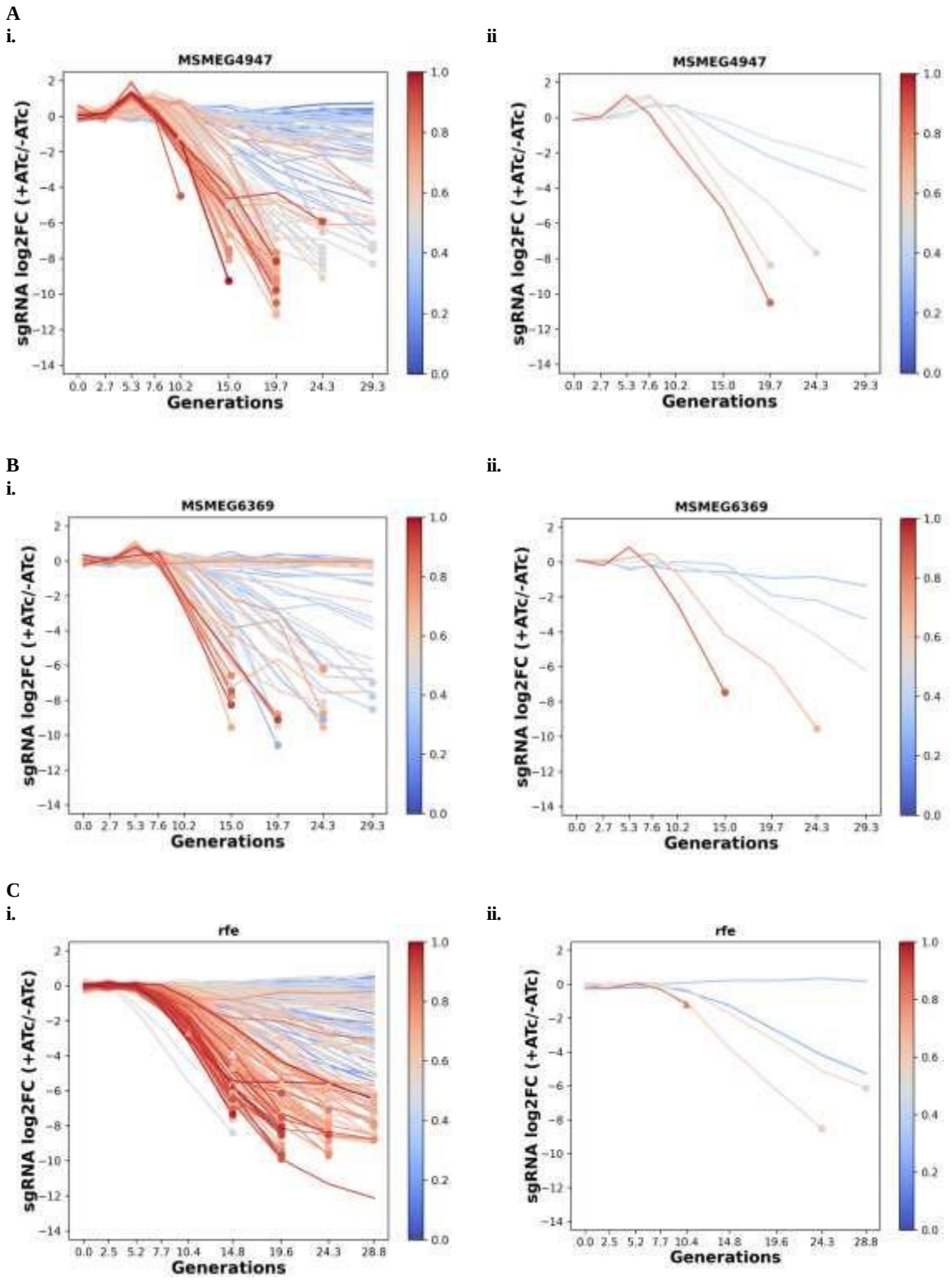

Figure 3.2. Overview of sgRNAs and final selection of guides for each gene and strain. ***A,*** MSM_*wecA*; ***B,*** MSM_*rfbD;* ***C,*** MTB_Ra_*wecA.* Index of all Pebble Database guides given on the left (i); index of the predicted guide strength of the selected guides is given on the right (ii). Weaker guides indicated by blue and stronger guides indicated by red. *Graphs generated by Pebble Database (https://pebble.rockefeller.edu/).*

Table 3.1. List of sgRNA oligos selected to construct *M. smegmatis* CRISPRi knockdown strains of the genes of interest. The oligo length, sequence and its sgRNA predicted knockdown strength, ranging from weak (0) to strong (1), were obtained from the Pebble sgRNA Design Tool.

CRISPRi primer set	**Sequence**	**Length (bp)**	**Predicted knockdown strength**	**Expected knockdown strength**
MSM_*wecA*01_FWD MSM_*wecA*01_REV	5'-GGGAATCGCGGTCTGGCCCGGATC-3' 5'-AAACGATCCGGGCCAGACCGCGAT-3'	24	0.86	Strong
MSM_*wecA*02_FWD MSM_*wecA*02_REV	5'-GGGAGGCGGTGGTCGAGGCCGCGC-3' 5'- AAACGCGCGGCCTCGACCACCGCC-3'	24	0.58	Intermediate
MSM_*wecA*03_FWD MSM_*wecA*03_REV	5'-GGGAGCGCGGTGGAAGTTGTGCG-3' 5'-AAACCGCACAACTTCCACCGCGC-3'	23	0.53	Intermediate
MSM_*wecA*05_FWD MSM_*wecA*05_REV	5'-GGGAGATCGTGCCCACTCCCCCGA-3' 5'-AAACTCGGGGGAGTGGGCACGATC-3'	24	0.45	Weak
MSM_*wecA*05_FWD MSM_*wecA*05_REV	5'-GGGAGATCACCGCGGGCGGGTAGA-3' 5'-AAACTCTACCCGCCCGCGGTGATC-3'	24	0.35	Weak
MSM_*rfbD*01_FWD MSM_*rfbD*01_REV	5'-GGGAGTTCCAGATGATCGGCGTCAT-3' 5'-AAACATGACGCCGATCATCTGGAAC-3'	25	0.86	Strong
MSM_*rfbD*02_FWD MSM_*rfbD*02_REV	5'-GGGAGATGATGATGTTGTGGGCGA-3' 5'-AAACTCGCCCACAACATCATCATC-3'	24	0.65	Intermediate
MSM_*rfbD*03_FWD MSM_*rfbD*03_REV	5'-GGGAAGATGATCGGCGTCATGAAGA-3' 5'-AAACTCTTCATGACGCCGATCATCT-3'	25	0.51	Intermediate
MSM_*rfbD*05_FWD MSM_ *rfbD*05_REV	5'-GGGAATGATCGGCGTCATGAAGA-3' 5'-AAACTCTTCATGACGCCGATCAT-3'	23	0.35	Weak
MSM_*rfbD*05_FWD MSM_*rfbD*05_REV	5'-GGGAATGATCAGGCCCAGCGTCACAT-3' 5'-AAACATGTGACGCTGGGCCTGATCAT-3'	26	0.30	Weak

Table 3.2. List of sgRNA oligos selected to construct *M. tuberculosis* CRISPRi knockdown strains of the genes of interest. The oligo length, sequence and its sgRNA predicted knockdown strength, ranging from weak (0) to strong (1), were obtained from the Pebble sgRNA Design Tool

CRISPRi primer set	**Sequence**	**Length (bp)**	**Predicted knockdown strength**	**Expected knockdown strength**
MTB_*wecA*01_FWD MTB_*wecA*01_REV	5'-GGGAGCACCGGCCACCAGCACCG-3' 5'-AAACCGGTGCTGGTGGCCGGTGC-3'	23	0.25	Weak
MTB_*wecA*02_FWD MTB_*wecA*02_REV	5'-GGGAGACCAGCGCAAGCTCACGCA-3' 5'-AAACTGCGTGAGCTTGCGCTGGTC-3'	24	0.30	Weak
MTB_*wecA*03_FWD MTB_*wecA*03_REV	5'-GGGAGCAGCGGGACACCGGCGCCGCG-3' 5'-AAACCGCGGCGCCGGTGTCCCGCTGC-3'	26	0.56	Intermediate
MTB_*wecA*05_FWD MTB_*wecA*05_REV	5'-GGGAACATGACCGCCACCACCAG -3' 5'-AAACCTGGTGGTGGCGGTCATGT-3'	23	0.58	Intermediate
MTB_*wecA*05_FWD MTB_*wecA*05_REV	5'-GGGAGCCGCGGTGTCGCGCGGGTT-3' 5'-AAACAACCCGCGCGACACCGCGGC-3'	24	0.84	Strong

Table 3.3. List of sgRNA oligos selected to construct CRISPRi control strains used in this study. The oligo length, sequence and its sgRNA expected knockdown strength are listed.

CRISPRi primer set	**Sequences**	**Length (bp)**	**Predicted knockdown strength**	**Expected knockdown strength**
Non-targeting_FWD Non-targeting_REV	5'-GGGAGCATCCGGAGCCCGTCCGTTAA-3' 5'-AAACTTAACGGACGGGCTCCGGATGC-3'	26	No knockdown	None (Negative control)
MSM_*clpP2*_FWD MSM_*clpP2*_REV	5'-GGGAATGTCGTCGTCCACTTGGGAACC-3' 5'-AAACGGTTCCCAAGTGGACGACGACAT-3'	23	Strong knockdown	Strong (Positive control)

3.2 Generation of CRISPRi constructs

To generate CRISPRi hypomorphs for the genes of interest, the oligo sets were used to generate specific CRISPRi plasmids. Briefly, *E. coli* glycerol stocks of the plasmid plRL117 and plRL2 were obtained (gift of Dr. Mandy Mason) and used to inoculate LB cultures and grown overnight. Amplified purified plasmids were extracted, and *Bsm*BI double digestion reactions performed to yield linear plasmids. Two restriction enzyme reactions were performed and a portion of each were run on an agarose gel to visualise the plRL117 and plRL2 digestion reactions resulted in clear single bands that approximately corresponded to the expected sizes of 8580 base pairs (bp) **(Figure 3.3A)** and 8621 bp, respectively **(Figure 3.3B)**. The sizes of the digested plasmids were determined by subtracting the region of the MCS cut out from the plasmid and the original plasmid size. In addition, two control reactions were run alongside the digestion reactions. These include the undigested plRL117 and plRL2 plasmids in *Bsm*BI buffer as well as the undigested plasmids in nuclease-free water, neither in the presence of *Bsm*BI restriction enzyme. The plRL117 plasmid was visualised alongside the Quick-load 1 kb DNA Ladder **(Supplementary Figure S3A)**, while the plRL2 plasmid was visualised alongside the Quick-load 1 kb Plus DNA Ladder **(Supplementary Figure S3B)**.

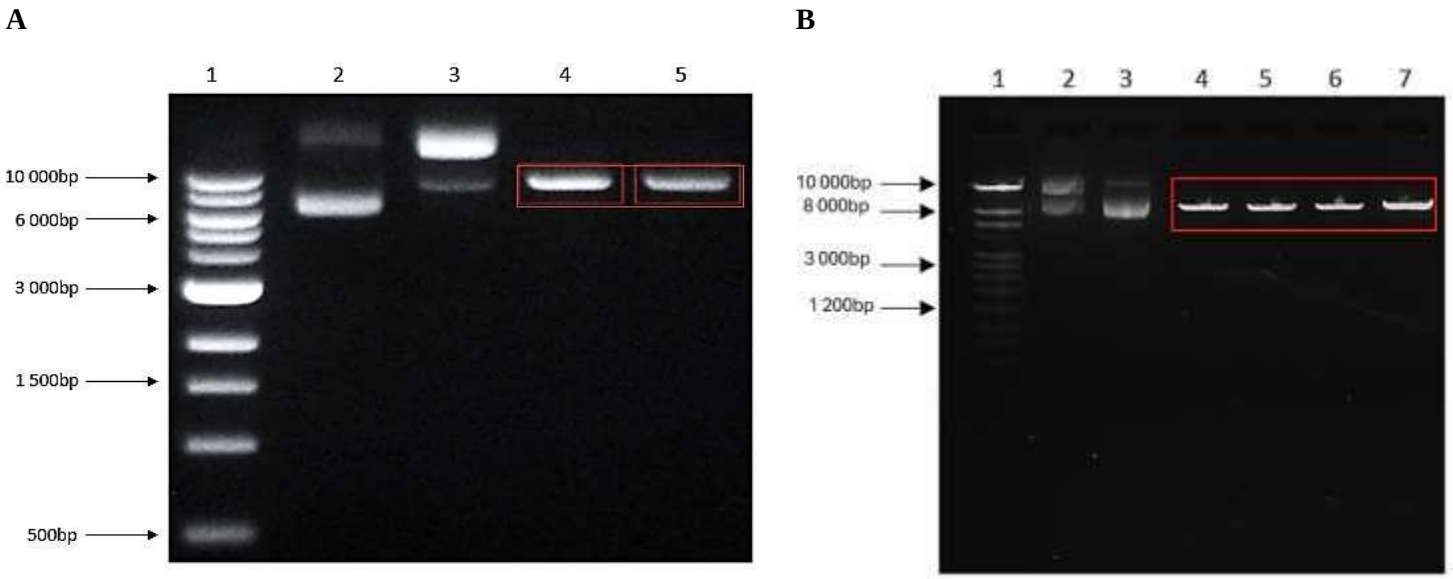

Figure 3.3. *A,* Agarose gel electrophoresis confirming successful restriction digest of the plRL117 and plRL2 CRISPRi plasmid backbones. ***A,*** Agarose gel electrophoresis confirming digestion of plRL117 CRISPRi plasmid backbone. Lane 1: Quick-Load Purple 1 kb DNA Ladder I; Lane 2: uncut plasmid in *Bsm*BI NEB buffer; Lane 3: uncut plasmid in nuclease-free H_2O; Lane 4 & 5: digest reactions resulting in the 8 600 bp linearized plasmid backbone. ***B,*** Agarose gel electrophoresis confirming digestion of plRL2 CRISPRi plasmid backbone. Lane 1: Quick-Load Purple 1 kb Plus DNA Ladder; Lane 2: uncut plasmid in nuclease-free H_2O; Lane 3: uncut plasmid in *Bsm*BI NEB buffer; Lane 4-7: digest reactions resulting in the 8631 bp linearized plasmid backbone. *(Poulton and Rock, 2022).*

The FWD and REV sgRNA oligos for each set were annealed and subsequently cloned into the linearized plasmids **(Figure 3.4)**. The resulting recombinant plasmids were transformed into DH5α *E. coli* cells for cloning and propagation, and the cells plated on LB agar supplemented with selection antibiotic Kan50. Colonies were observed on all transformant plates while no colonies were observed on the untransformed MSM_WT no-plasmid control plates (data not shown), indicating successful transformation of the plasmid. Incorporation of the guide RNAs into the plasmids were confirmed by sanger sequencing of purified plasmids **(Supplementary Figures S2, S3 & S4)**.

The resulting plRL117 and plRL2 recombinant plasmids were then electroporated independently into MSM_WT and MTB_Ra_WT electrocompetent cells. Following electroporation, the recombinant plasmids integrate into the attB site (Armianinova et al., 2022) on the bacterial chromosome where it expresses the sgRNA and dCas9 under the control of an ATc inducible promoter (Rock et al., 2017) The cells were plated on 7H10 agar supplemented with Kan25 to select for successful transformants. Colonies were observed on the transformant plates, while no colonies were observed on the untransformed MSM_WT no-plasmid control plate (data not shown). Random transformant colonies were picked from the transformant plates and grown to stationary phase in 7H9/OADC supplemented with Kan25. Finally, 1 ml of the stationary phase cultures were added to 33% (v/v) glycerol and the glycerol stocks stored at -80°C.

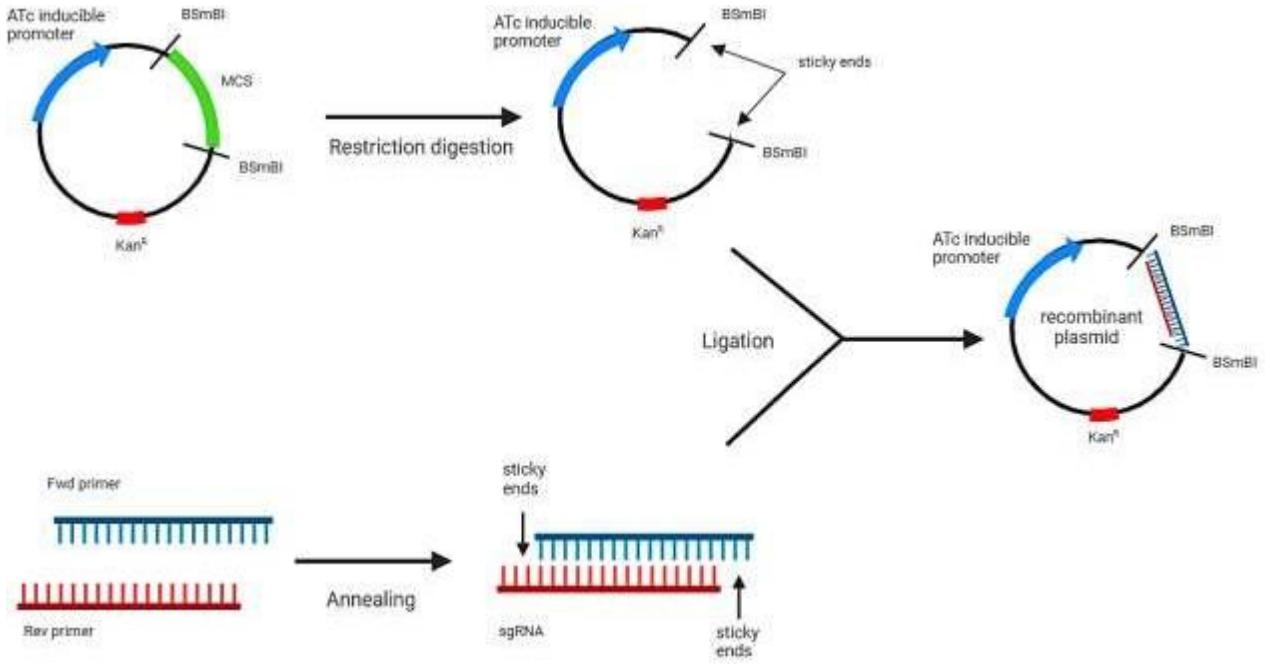

Figure 3.4. Diagram showing the generation of CRISPRi recombinant plasmid. Cloning approach used to generate the sgRNA-CRISPRi backbone construct. The plasmid contains an ATc regulated promoter, a kanamycin resistance gene, and a multiple cloning site (MCS) located between two *Bsm*BI restriction sites. The FWD and REV oligos were annealed and subsequently ligated into the digested plasmid. *Generated using Biorender (*2025*).*

3.3. Validation and selection of *M. smegmatis* and *M. tuberculosis* hypomorphs

The genes targeted in this study are essential, meaning that these are necessary for the survival or growth of the bacterium, therefore generating knockout mutants would not be feasible for this study as the total loss of these genes would render the bacteria nonviable. We thus generated knockdown mutants with the aim to reduce the transcription of the genes of interest (partial silencing). Investigating the impact of the use of sgRNAs with different predicted strengths on the *in vitro* growth of each hypomorph is a vital check to establish whether the knockdown profile correlates to the predicted sgRNA strength. Growth attenuation phenotypes were used to show the direct impact of the transcriptional knockdown of each sgRNA on a whole cell level and can be leveraged to select for the most optimal guide for downstream experiments. For this work, the most optimal sgRNA would be determined as the guide demonstrating strong to intermediate knockdown on solid media and in liquid media. To test this, spotting assays were performed on solid media and growth kinetics (absorbance vs time) determined in liquid media. This was done both in the in the absence (uninduced) and presence (induced) of 100 ng/ml anhydrotetracycline (ATc) to induce CRISPRi-mediated transcriptional silencing of the target gene. Two control strains were used throughout the study: (i) a strong positive control strain targeting *clpP2* (MSM_*clpP2)*, an essential protease required for housekeeping and the degradation of prematurely terminated peptides (Raju et al., 2012) which was used to confirm efficient gene silencing by the CRISPRi system and (ii) a non-targeting negative control strain (MSM_NT) with no gene target which was used to demonstrate that the induction of the CRISPRi system has no impact on cell growth and viability, a condition that should phenocopy the wild-type strain.

3.3.1. Growth consequences of partial silencing of target genes on solid media

To determine the impact of each sgRNA on the growth of our strains, exponential phase cultures were spotted as ten-fold serial dilutions on 7H10 agar either with or without 100 ng/ml ATc. The strains exhibited distinct knockdown profiles upon induction of the CRISPRi system. In these assays strong growth inhibition is defined as no to slight evidence of growth (spots) in any of the dilutions (including the 10^0 and 10^{-1} dilutions), intermediate growth inhibition is defined as spots on 10^0, 10^{-1} and 10^{-2} dilutions or evidence of some outgrowth (faint spots) in all dilutions, while weak growth inhibition refers to spots with no discernible difference between their No ATc and ATc phenotypes or (spots in all dilutions).

As expected, the MSM_NT control spots were evident in all dilutions in both uninduced and induced conditions, displaying negligible growth attenuation in the presence of ATc **(Figure 3.5)**. Based on this

lack of attenuation in the MSM_NT strain, we can confirm that the addition of ATc did not impact growth of the *Msm* CRISPRi strains. For all spotting assays, the growth of the positive knockdown control, MSM_*clpP2*, showed growth in all dilutions in the uninduced condition but showed no growth in the induced condition, indicating potent inhibition of *Msm* when transcription of this gene is strongly knocked down. This confirmed that an ATc concentration of 100 ng/ml was sufficient to impact the growth of a strong CRISPRi sgRNA strain (MSM_*clpP2*) under the assay conditions performed. It was notable that in the wecA experimental agar plates **(Figure 3.5A)**, the control MSM_*clpP2* showed growth of a relatively large colony in dilution 10^{-1}. This was not seen in the rfbD assay which was relatively clean of growth **(Figure 3.5B).** This was determined to be likely due to some level of cross contamination and is attributed to the use of 12-channel multichannel pipettes, which are less precise when handling, allowing the rare occurrence of aerosolised droplets from an MSM_*wecA* strain falling onto the plate.

Based on the guide strength we expected the *Msm* strains with the lower numbers to have greater growth attenuation than the guides with the higher numbers **(Table 3.1).** MSM_*wecA*01 displayed strong attenuation showing slight evidence of growth in the 10^{0} dilution and no growth from the 10^{-1} dilutions when induced with ATc. Again, a single colony was noted in the 10^{-3} dilution, potentially attributable to cross contamination from co-spotting with the MSM_NT strain. MSM_*wecA*02 and MSM_*wecA*03 elicited intermediate growth inhibition, each with spots evident in the 10^{0} dilution, and clear growth of colonies seen in 10^{-1} and 10^{-2} dilutions in the induced condition; MSM_*wecA*05 and MSM_*wecA*05 demonstrated no growth attenuation in the presence of ATc, with growth of spots visible across all dilutions in the induced condition that were relatively indistinguishable from the non-induced comparison **(Figure 3.5A)**. While for MSM_wecA05 some spots did appear smaller than expected (uninduced: dilution 10^{-4}; induced: 10^{-1}) this did not reflect attenuation of the strain and could be attributed to slight pipetting error with the use of a multichannel pipette.

MSM_*rfbD*01 displayed intermediate growth inhibition with spots in the 10^{0}, 10^{-1} dilution and a colony in the 10^{-2} dilution when induced with ATc. MSM_*rfbD*02 was notable in that clear spots were evident in all dilutions, however these appeared distinct from that of the uninduced condition, being smaller and having the appearance of smoother edges. MSM_rfbD03, MSM_rfbD04 and MSM_*rfbD*05 had no growth attenuation in the induced conditions, with no discernible difference between all dilutions in the uninduced and induced conditions and growth on all spots **(Figure 3.5B)**.

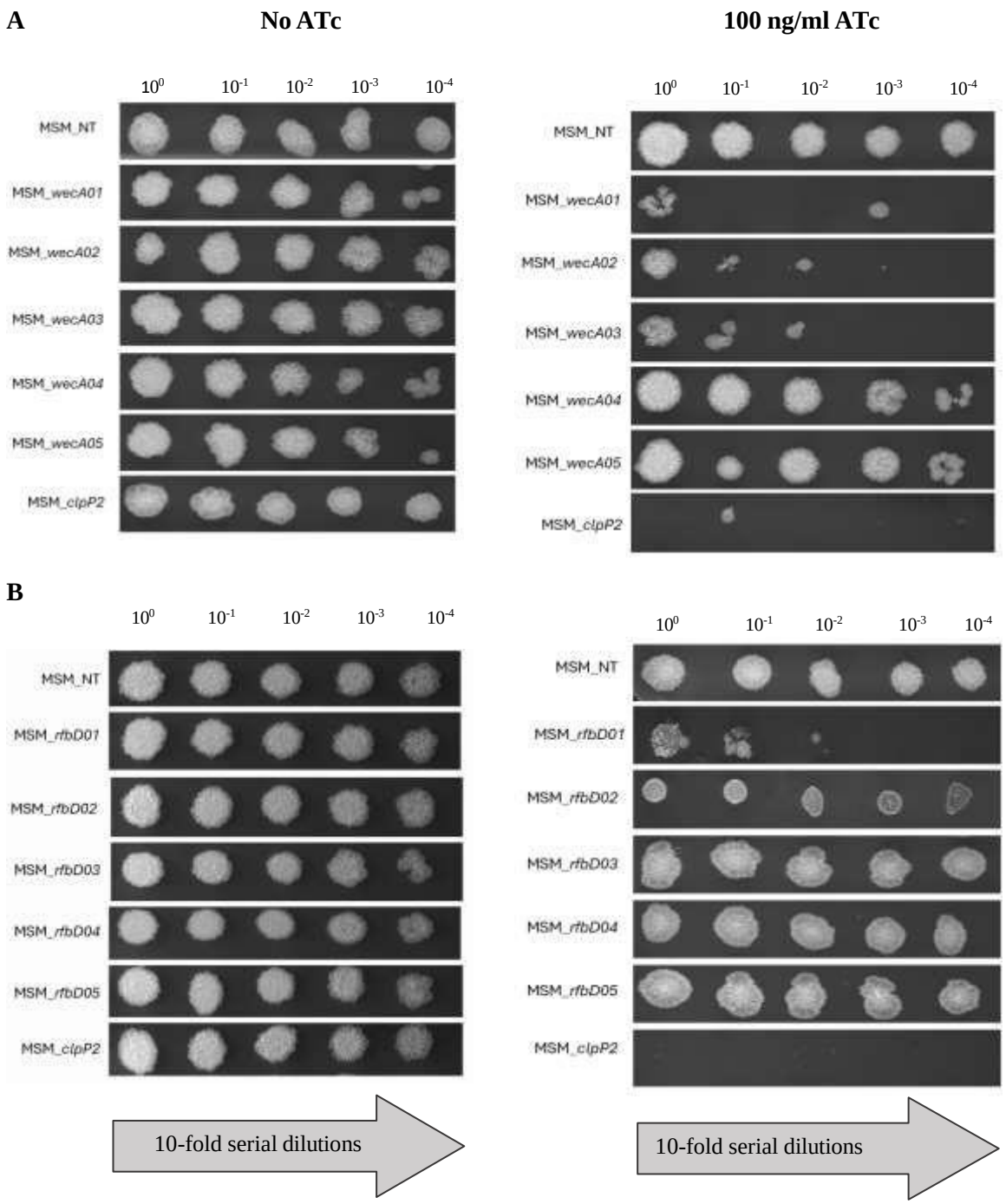

Figure 3.5. Assessment of *wecA* and *rfbD* sgRNA knockdown impact in *M. smegmatis* strains. *A,* *wecA and* ***B,*** *rfbD k*nockdown impact on growth of *Msm* was determined using a spotting assay with ten-fold serial dilution spotted on solid 7H10 agar supplemented with Kan25. Growth of *Msm* strains in the uninduced condition are shown in the left panel; growth of *Msm* strains in the induced condition are given in the right panel.

The spotting assay phenotypes of the MTB_Ra hypomorphs in the absence and presence of 100 ng/ml ATc are shown in **Figure 3.6**. Based on the guide strength we expected the *Mtb* strains with the higher

numbers to have greater growth attenuation than the guides with the lower numbers (Table 3.2). All MTB_Ra CRISPRi strains demonstrated some level of growth attenuation when induced with ATc. Briefly, MTB_Ra_*wecA*02 showed the least impact on growth (weak attenuation) with spots evident in all dilutions, though these were reduced in size as compared to its non-induced comparison. MTB_Ra_*wecA*01 and then MTB_Ra_*wecA*03 showed intermediate attenuation with clear spots evident in dilutions 10^0 and 10^{-1} and some colonies seen in further dilutions. MTB_Ra_*wecA*05 showed strong attenuation of growth when induced, colonies could be seen in the 10^0 dilutions with low to no evidence of outgrowth in further dilutions. The strongest attenuation was seen in MTB_Ra_*wecA*05 which only had very small colonies evident in 10^0 and 10^{-1} dilutions when induced. Interestingly, an attenuation of the growth of MTB_Ra_NT was observed in the induced condition with attenuation of growth (relative decrease in spot size) seen in the 10^{-1} to 10^{-4} conditions. Based on this phenotype, we cannot confirm that the addition of ATc did not impact growth of MTB_Ra strains that contain the non-targeting sgRNA (MTB_Ra_NT). This could point to a potential sensitisation of MTB_Ra to the CRISPRi system. Alternatively, the non-targeting guide may be having some impact to the *Mtb* genome. A summary of the spotting assay shifts of each strain is shown in **Table 3.4.**

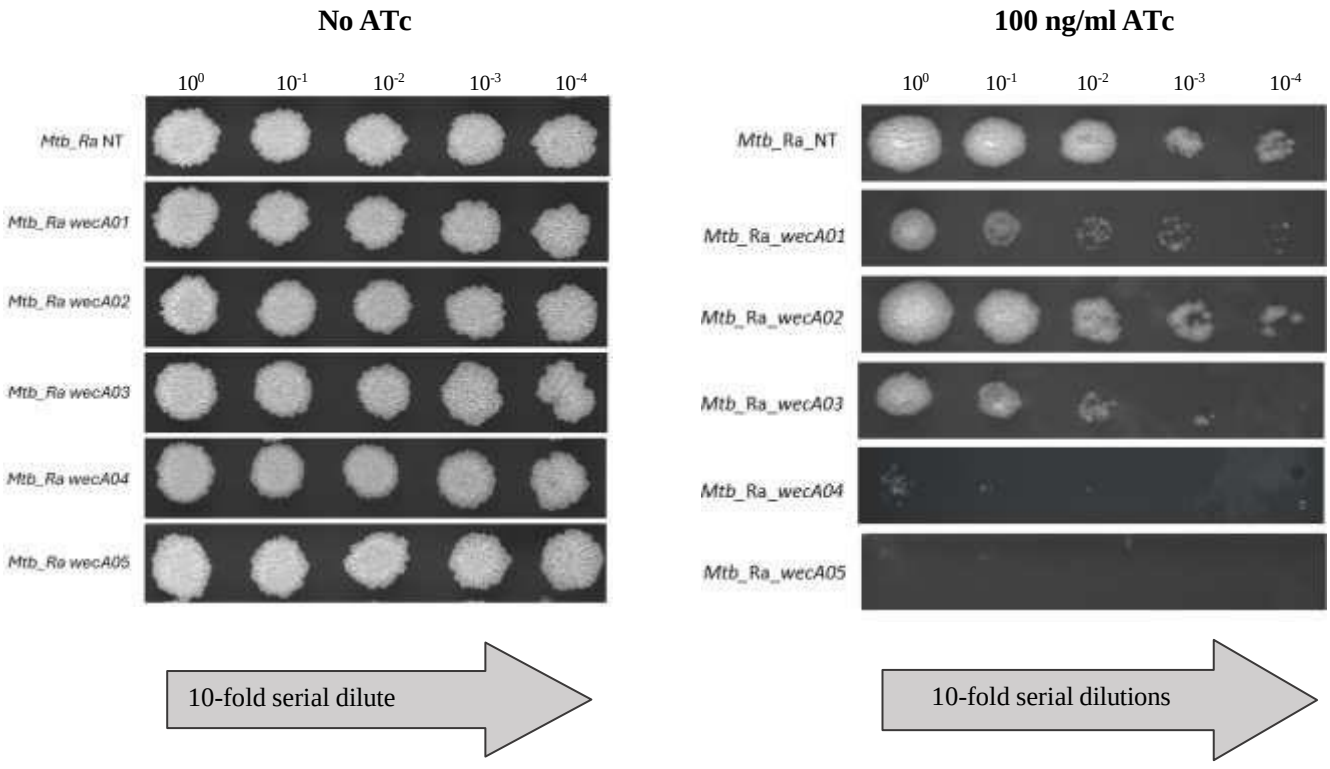

Figure 3.6. Assessment of *wecA* sgRNA knockdown impact in *M. tuberculosis* strains. ***w****ecA k*nockdown impact on growth of MTB_Ra was determined using a spotting assay with ten-fold serial dilution spotted on solid 7H10 agar supplemented with Kan25. Growth of MTB_Ra strains in the uninduced condition are shown in the left panel; growth of MTB_Ra strains in the induced condition are given in the right panel.

3.3.2. Outgrowth phenotype of *M. smegmatis* hypomorphs in liquid media

Characterisation of growth attenuation was also performed in liquid media in which the absorbances of cultures were measured at 600 nm in a plate reader over a 24-hour period, in technical replicates of 4. During the period of outgrowth, the strains were either not exposed to (uninduced) or exposed to (induced) to 100 ng/ml ATc. As expected, for the negative control, the growth of MSM_NT was not impacted by the ATc **(Figure 3.7A)**, while the positive control, MSM_*clpP2* showed a decline in the growth upon CRISPRi induction **(Figure 3.7B).** In terms of outgrowth, both MSM_NT negative control and MSM_*clpP2* positive control displayed steady comparable growth during the first 10 hours of incubation (approximately 4 generations). This was followed by exponential growth of MSM_NT, while in contrast, after 10 hours, MSM_*clpP2* displayed a substantial decline in growth rate in the presence of ATc. Based on the liquid media phenotype results we can confirm that the addition of ATc did not impact growth of strains that contained the CRISPRi system expressing a non-targeting sgRNA (MSM_NT). In addition, we determined that an ATc concentration of 100 ng/ml was sufficient to impact the growth of a strong CRISPRi sgRNA strain (MSM_*clpP2*) under the assay conditions performed.

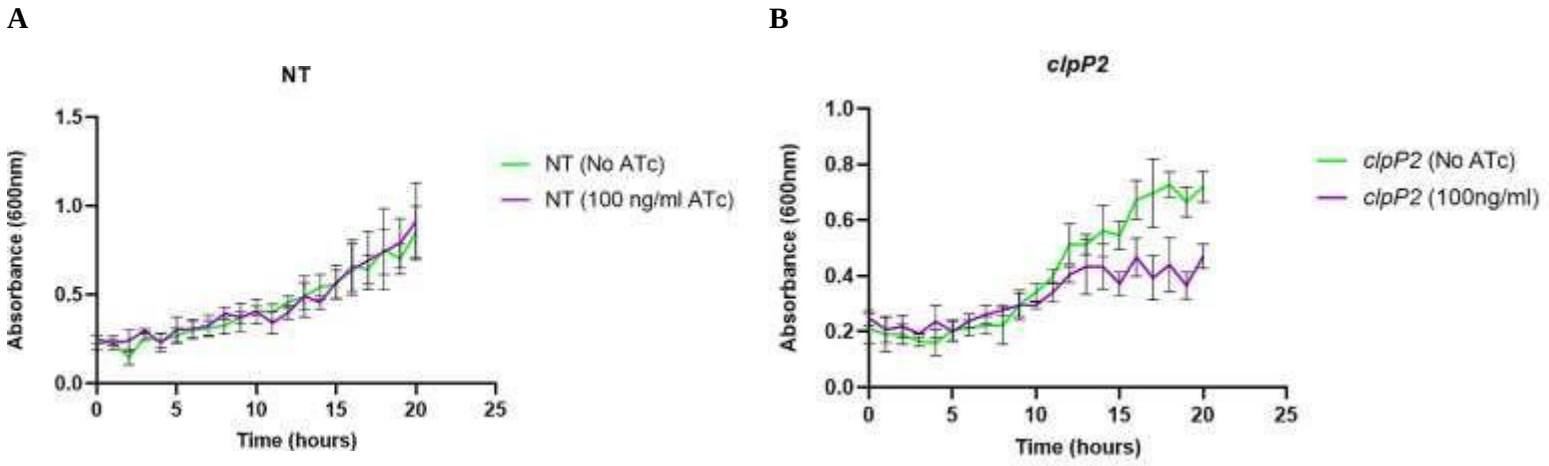

Figure 3.7. CRISPRi-mediated growth kinetics of *M. smegmatis* control strains under uninduced and non-induced conditions. *A,* growth dynamics of MSM_NT in the absence (green) and presence (purple) of 100 ng/ml ATc and ***B,*** growth dynamics of MSM_*clpP2* in the absence (green) and presence (purple) of 100 ng/ml ATc. Error bars represent standard deviations for technical repeats of 3.

The culture outgrowth kinetics of the *wecA* targeting CRISPRi strains, MSM_*wecA*01 to MSM_*wecA*05 are shown in **Figure 3.8**. Growth of all strains in the absence of ATc were similar to that seen in MSM_NT, characterised by slightly slower growth rates (lag phase) over the first 10 hours of growth, followed by higher rates of growth. After 20 hours, the average OD_{600} tended to reach an OD_{600} of 1.0 with the exception of MSM_*wecA*03, which only reached an OD_{600} of 0.8 after 20 hours **(Figure 3.8C)**. The technical variation of absorbance readings in the uninduced experiment was averaged at 0.14

ranging from 0.04 and 0.26. Upon induction of the CRISPRi system, MSM_*wecA*01-03 showed a decline in growth rate following the 10-hour lag period **(Figure 3.8A, B & C)**. This was not observed in MSM_*wecA*05 and 05 which showed comparable growth over this period as the uninduced condition **(Figure 3.8D & E)**. The technical variation in the induced experiment was similar to that of the uninduced experiment, averaged at 0.15 ranging from 0.038 and 0.26.

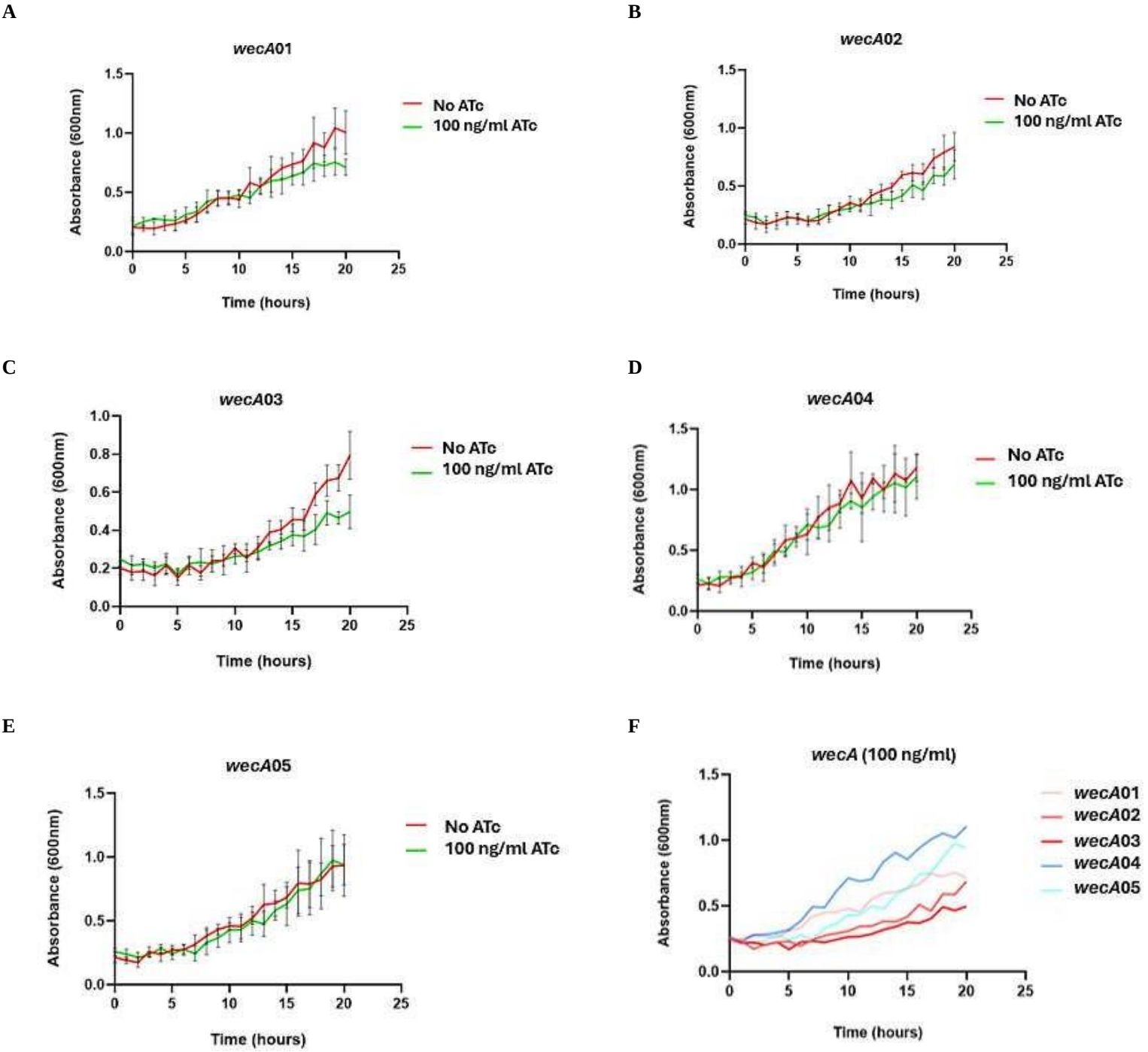

Figure 3.8. CRISPRi-mediated growth kinetics of *M. smegmatis* of *wecA* CRISPRi strains under uninduced and non-induced conditions. ***A,*** MSM_*wecA*01, ***B,*** MSM_*wecA*02*;* ***C,*** MSM_*wecA*03*;* ***D,*** MSM_*wecA*04*;* ***E,*** MSM_*wecA*05 growth in the absence (red) and presence (green) of 100 ng/ml ATc. ***F,*** Comparison of selected guides in the presence of 100 ng/ml ATc. Growth attenuation ranges from strong (dark red), intermediate (light pink/dark blue) to weak (light blue). Error bars represent standard deviation for technical repeats of 3.

A comparison of the growth curves of each strain under the induced condition is illustrated by **Figure 3.8F.** Strong growth attenuation in this assay is defined as strains reaching an end point OD_{600} of ≤0.5 after a growth period of 20 hours; intermediate growth attenuation is defined as strains reaching an OD_{600} of 0.5-0.7 after 20 hours and weak growth attenuation defined as strains reaching an OD_{600} of ≥0.7 after 20 hours. The results showed that MSM_*wecA*01 and MSM_*wecA*02 showed intermediate growth attenuation, MSM_*wecA*03 showed strong growth attenuation, while MSM_*wecA*04 and MSM_*wecA*05 displayed weak growth attenuation.

The outgrowth phenotypes of the *rfbD* targeting CRISPRi strains, MSM_*rfbD*01 to MSM_*rfbD*02 are shown in **Figure 3.9**. Similarly to the MSM_*wecA* results, the growth of the MSM_*rfbD* strains in the uninduced conditions are similar as that of MSM_NT, with a slower growth rate (lag phase) over the first 10 hours of growth followed by increased growth rates. All strains except for MSM_*rfbD*01 and MSM_*rfbD*02 reached an endpoint OD_{600} of 1.0 after 20 hours of growth. The technical variation in the uninduced experiment was averaged at 0.11 ranging from 0.04 and 0.21 Under ATc induction, MSM_*rfbD*01 and MSM_*rfbD*02 showed a relatively reduced growth rate following the 10-hour lag phase (**Figure 3.9A & B**), while no discernible difference in growth rate is seen in MSM_*rfbD*03 to MSM_*rfbD*05 presence of ATc **(Figure 3.9C, D & E)**. The technical variation in the induced condition was similar to that of the uninduced and averaged at 0.11 ranging from 0.04 and 0.25.

A comparison of the growth curves of each strain under the induced condition is illustrated in **Figure 3.9F.** The results showed that MSM_*rfbD*01 showed strong growth attenuation after 20 hours of growth; MSM_*rfbD*02 showed intermediate growth attenuation after 20 hours, while MSM_*rfbD*03 to MSM_*rfbD*05 showed weak growth attenuation after 20 hours of growth. A summary of the growth curves slopes of each strain is shown in **Table 3.4.** An overlay of the growth trajectory of the controls and hypomorphs are presented as log10 absorbance vs time (hours) is shown in **supplementary Figure S5.**

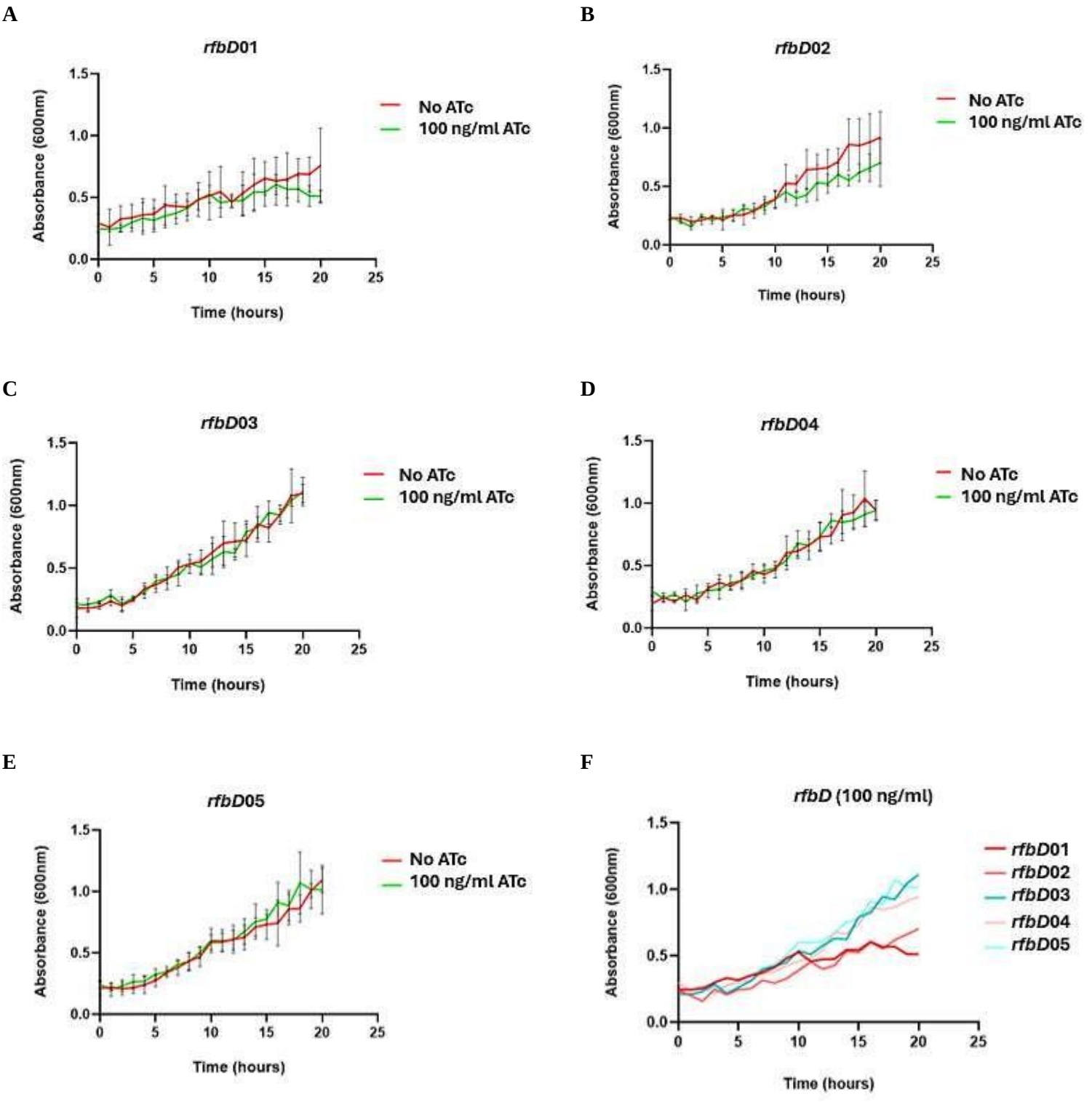

Figure 3.9. CRISPRi -mediated growth kinetics of *M. smegmatis* following *rfbD* under uninduced and non-induced conditions. ***A,*** MSM_*rfbD*01 ***B,*** MSM_*rfbD*02*;* ***C,*** MSM_*rfbD*03*;* ***D,*** MSM_*rfbD*05*;* ***E,*** MSM_*rfbD*05 growth in the absence (red) and presence (green) of 100 ng/ml ATc). ***F,*** Comparison of selected guides in the presence of 100 ng/ml ATc. Growth attenuation ranges from strong (dark red), intermediate (light pink/dark blue) to weak (light blue Error bars represent standard deviation for technical repeats of 3.

Table 3.4. Summary of the *Msm* and *Mtb* spotting assays shifts, and *Msm* growth curve slopes. Based on these data, an assessment of the suitability of each hypomorph for downstream assays was made

Strain name	**Predicted strength**	**Spotting assay shift**	***Growth curve slope**	**Suitability**
MSM_NT	None	Negligible	0.054	Negative control
MSM_*clpP2*	Strong	Strong	0.009	Positive control
MSM_*wecA*01	Strong	Strong	0.029	Yes
MSM_*wecA*02	Intermediate	Intermediate	0.035	Yes
MSM_*wecA*03	Intermediate	Intermediate	0.025	Yes
MSM_*wecA*05	Weak	Weak	0.043	No
MSM_*wecA*05	Weak	Weak	0.059	No
MSM_*rfbD*01	Strong	Intermediate	0.006	Yes
MSM_*rfbD*02	Intermediate	Weak	0.03	Yes
MSM_*rfbD*03	Intermediate	Weak	0.062	No
MSM_*rfbD*05	Weak	Weak	0.051	No
MSM_*rfbD*05	Weak	Weak	0.044	No
MTB_Ra_NT	None	Intermediate	Not performed	
				Negative control
MTB_Ra_*wecA*01	Weak	Intermediate	Not performed	No
MTB_Ra_*wecA*02	Weak	Weak	Not performed	No
MTB_Ra_*wecA*03	Intermediate	Intermediate	Not performed	No
MTB_Ra_*wecA*05	Intermediate	Strong	Not performed	No
MTB_Ra_*wecA*05	Strong	Strong	Not performed	Yes

*Slope of the growth curve in the induced condition was determined between 10 and 20 hours of growth. Slopes were calculated in GraphPad Prism 10.2.0.

Based on the solid and liquid media hypomorph phenotypes three of the *Msm wecA* CRISPRi strains and two of the *Msm rfbD* strain could be considered suited for further experimentation **(Table 3.4)**. When strains showed no attenuation of growth on solid media these were excluded from consideration. Downstream assays (MIC assays and single-cell phenotyping) were to be performed in liquid culture and for this purpose the strongest guides of the set were considered to be the most appropriate for use. MSM_*wecA*01 (hereafter referred to as MSM_*wecA*) and MSM_*rfbD*01 (hereafter referred to as MSM_*rfbD*) were selected for all further *Msm* mc^2155 experiments.

Due to the unexpected intermediate growth attenuation observed when MTB_Ra_NT (control non-targeting strain) was treated with ATc, we could not confirm that ATc did not impact the growth of the

MTB_Ra hypomorphs. These assays were deprioritised and the *wecA* targeting CRISPRi strains were not assessed in liquid media. In conjunction with this work, we aimed to extend our *Msm* work into a strain of MTB which did have an appropriate non-targeting control strain for comparison. Therefore, the plRL2_*wecA*05 recombinant plasmid (see **Methods Table 2.4**), displaying strong knockdown strength, was selected and electroporated into a virulent *Mtb* H37Rv (MTB_Rv) strain, in the BSL3 by Dr. Mandy Mason. Growth attenuation of the non-targeting strain had previously been confirmed in another project by Dr. Mason (data not shown) and an assessment of growth attenuation was performed in liquid culture and subsequent microscopy experiments performed on this strain as a pilot study aligned with this work (see **supplementary Section 6.6**).

3.4. Antimycobacterial drug susceptibility assays

Previous studies have shown that disruption of mycobacterial arabinogalactan, an essential component of the mycobacterial cell wall, results in increased cell envelope permeability (Rombouts et al., 2012, Justen et al., 2020). The unique architecture of the mycobacterial cell envelope makes it relatively impermeable to most drugs, therefore, an increase in cell envelope permeability can be denoted by an increase in drug uptake (de Keijzer et al., 2016). Hypomorph strains with partial transcriptional silencing have proven a useful tool to infer vulnerability of mycobacterial cells to potential drugs (Evans and Mizrahi, 2015). Dose-response studies are often used to investigate potency of a drug against bacterial cells (Jiang and Kopp-Schneider, 2014). To evaluate the effect of disruption of *wecA* and *rfbD* on susceptibility of *Msm* to known antimycobacterial compounds, microtiter alamar blue assays (MABA) (Franzblau et al., 1998) were used to assess drug sensitivity as a consequence of disruption in the galactan biosynthetic pathway. A small set of compounds with distinct physiochemical properties and mechanisms of action were used in this study; these include rifampicin (RIF), ethambutol (EMB), vancomycin (VAN) and linezolid (LNZ). Compounds and their mechanisms of action are listed in **Table 3.5** below. These comprise compounds with a range of molecular weights, with two being relatively smaller and less complex compounds (EMB and LNZ) with EMB being slightly hydrophilic while LNZ is both hydrophilic and lipophilic and two being relatively larger and more complex lipophilic compounds (RIF and VAN) with RIF being highly hydrophobic and VAN being highly hydrophilic.

Table 3.5. Antimycobacterial compounds used in this study. Mechanisms of action, key physiochemical properties (molecular weight, complexity and hydrophobicity) and PubChem CID for each compound is given.

Compound name	Molecular weight	Complexity	Hydrophobic/ Hydrophilic (XLogP3*)	Mechanism of action	PubChem CID
Ethambutol (EMB)	204.31 g/mol	109	Slightly hydrophilic (-0.1)	Inhibits activity of arabinosyl transferase during arabinogalactan biosynthesis (Zhu et al., 2018)	14052
Linezolid (LNZ)	337.35 g/mol	472	More hydrophobic (0.7)	Inhibits initial phase of protein synthesis (Liu et al., 2020)	441401
Rifampicin (RIF)	822.9 g/mol	1620	Highly hydrophobic (4.9)	Inhibition of DNA-dependent RNA synthesis (Mosaei and Zenkin, 2020)	135398735
Vancomycin (VAN)	1449.2 g/mol	2960	Highly hydrophilic (-2.6)	Inhibits biosynthesis of peptidoglycan (WILHELM, 1991)	14969

*Negative values indicate that compound is more hydrophilic, and positive values indicate compound is more hydrophobic with values between -1 and 1 indicating that the compound has properties that favour both states.

EMB is a first-line drug that is administered for the treatment of active pulmonary active TB (Lee et al., 2024) (see **Figure 1.1**). It functions by inhibiting the activity of *Mtb* membrane associated arabinotransferases, EmbA and EmbB which are essential to the synthesis of arabinogalactan (Telenti et al., 1997, Zhang et al., 2020). Previous studies have demonstrated that mycobacterial strains with mAGP knockdown showed sensitisation when challenged with EMB (Li et al., 2021). With this in mind, we aimed to assess whether galactan plays a role in sensitisation to this drug by examining the effect of exposure to this drug on galactan compromised *Msm* strains.

LNZ is a synthetic compound typically used in the treatment of gram-positive bacterial infections, including pneumonia caused by methicillin-resistant *Streptococcus pneumoniae* and vancomycin-resistant Enterococci (Hashemian et al., 2018). It functions by binding to the rRNA on both the 30S and 50S ribosomal subunits, thereby inhibiting the initiation of protein synthesis (see **Figure 1.1**). LNZ was shown to be effective against both MDR- and XDR-TB but its use in the treatment of TB is generally restricted due to its toxicity and the potential for development of resistance to the compound. However, it is a useful compound to probe mycobacterial physiology. In large scale CRISPRi chemical-genetic screens investigating drug sensitisation, it was shown that targeting the mAGP complex did not result in sensitisation to LNZ (Li et al., 2022). Therefore, this feature was used as a control to assess a compound that does not appear to be impacted by changes to the mAGP layer.

RIF is a large semisynthetic compound derived from rifamycin and is a potent first-line antibiotic in the treatment of active pulmonary TB (Lee et al., 2017). It functions by inhibiting the activity of RNA polymerase's β-subunit, effectively blocking the elongation step during RNA synthesis (Mosaei and Zenkin, 2020) (see **Figure 1.1**). RIF was shown to be sensitised by the depletion of key enzymes involved in the synthesis of mAGP components, including those involved in arabinogalactan biosynthesis (Li et al., 2022). RIF's efficacy is however compromised by its size and ability to cross the cell envelope (Lambert, 2002). We therefore aimed to examine whether knocking down the synthesis of galactan results in sensitisation to this compound.

VAN is a compound derived from *Streptococcus orientalis* and used in the treatment of severe infections caused by gram-positive bacteria, such as methicillin-resistant and methicillin-susceptible *Staphylococcus aureus* (Stogios and Savchenko, 2020, Patel et al., 2017) but is also effective against *Clostridium difficile* as well as streptococci and enterococci (Patel et al., 2017). It functions by inhibiting the polymerisation of peptidoglycan onto the bacterial cell envelope (Soetaert et al., 2015). VAN was shown to be sensitised by the depletion of key enzymes involved in mAGP components (Li et al., 2022). In this study we assessed whether this drug was sensitised to mycobacterial strains with depleted galactan.

3.4.1 Determining reference Minimum Inhibitory Concentration (MIC) in WT *M. smegmatis* mc^{2}155

Minimum inhibitory concentration (MIC) is the level of susceptibility of a bacterial population to an applied antibiotic and is defined as the lowest concentration of an antibiotic that inhibits the detectable growth of a bacterial population after a period of incubation under defined *in vitro* conditions (Kowalska-Krochmal and Dudek-Wicher, 2021). MIC is a critical research measure to assess the *in vitro* activity of drugs and confirm resistance (Andrews, 2001). The MIC_{90} refers to the concentration of antibacterial agent required to visibly inhibit the growth of approximately 90% of a bacterial population. In these assays, dose responses are characterized by no to low inhibition at low drug concentrations, followed by substantial growth inhibition at increased drug concentrations.

To determine the reference MIC of each compound, dilutions of each drug were tested against MSM_WT strains. Pre-cultured exponential phase cultures were inoculated at low density into flat-bottom 96-well microtiter plates containing two-fold serial dilutions of each compound. Inhibition was determined both calorimetrically **(Supplementary Figure S9 & S10)** and fluorometrically via alamar blue reduction. Fluorometric measurements were plotted (**Figure 3.10**) and the reference MIC_{90} of VAN, LNZ and RIF calculated using GraphPad Prism (see **Methods Section 2.8.1**). When treated with drug, we see low growth inhibition at low drug concentrations, thereafter a rapid increase in the level of

inhibition is observed at higher drug concentrations. The growth inhibition plateaus at 100% inhibition as the drug reaches a maximal effective concentration. Comparing the MIC_{90} of each drug against *Msm* WT to that of previously published data (**Table 3.6**) demonstrated that the majority of these were within the range of previously published MIC_{90} data in *Msm* mc^2155. However, the determined MIC_{90} of EMB obtained for the MSM_WT strain used in this project was 2-fold lower than that of the minimum MIC_{90} reported in the literature (**Table 3.6**). An experimental repeat was performed utilising the same plate layout and drug concentrations. The experimental repeat yielded the same MIC_{90} values for all drugs tested, confirming the reproducibility of the data (**supplementary Figure S6, Table 3.6**).

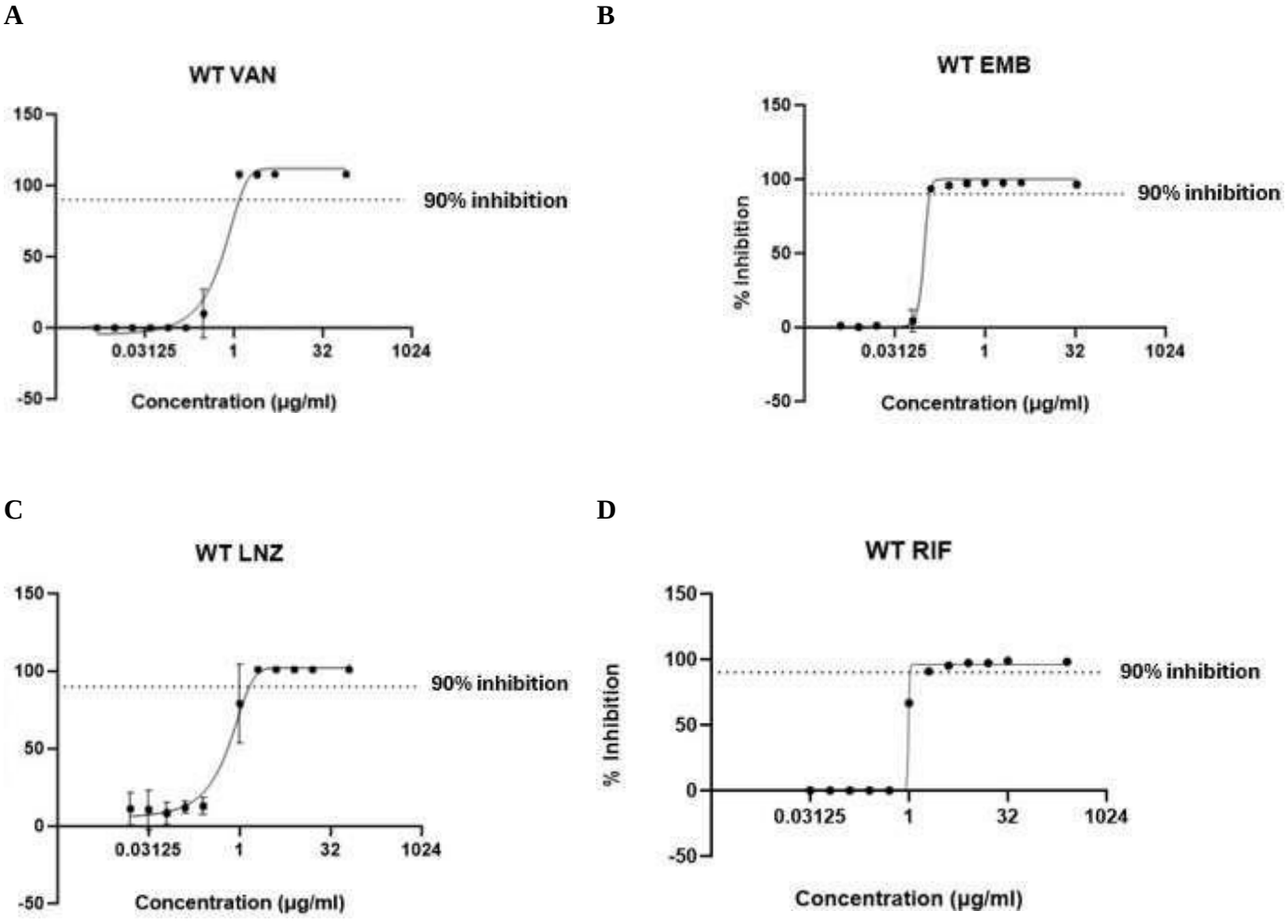

Figure 3.10. Determination of reference Minimum Inhibitory Concentrations (MIC) of MSM_WT strains. Dose-response curves modelling growth inhibition of MSM_WT following ***A,*** vancomycin (VAN); ***B,*** ethambutol (EMB); ***C,*** linezolid (LNZ) and ***D,*** rifampicin (RIF) treatment. Dotted line represents the 90% inhibition and indicates where this intersects with the dose response curve. Error bars represent standard deviation of 3 technical repeats, and 2 experimental repeats were performed (see **Supplementary Figure S6**).

Table 3.6. Comparison of reference MIC_{90} of each compound against our MSM_WT strain to the range of MIC_{90} data obtained for *Msm* mc^2155 in published literature

Compound name	**Published MIC_{90} (µg/ml)**	**Determined M I C $_{90}$ (µg/ml)**	**Determined MIC_{90} (µg/ml)**	**Reference for published *Msm* mc^2155 MIC_{90}**
	***Msm* mc^2155**	**MSM_WT**	**MSM_NT**	
Rifampicin (RIF)	1.32-2.57	2 *2	2 *2	(Faulkner et al., 2021)
Ethambutol (EMB)	0.25-2	0.125 *0.125	2 *1	(Khoo et al., 1996, Lechner et al., 2008)
Vancomycin (VAN)	0.625-5	1.25 *1.25	1.25 *1.25	(Danilchanka et al., 2008, Stephan et al., 2004)
Linezolid (LNZ)	0.5-4	1 *1.25	1 *2	(Wallace Jr et al., 2001)

*Determined MIC_{90} from repeat experiment (see supplementary data 7.3)

3.4.2. Effect of galactan depletion on the MIC90 of *M. smegmatis* mc^2155

The determination of the reference MIC_{90} in our MSM_WT strains allowed for the assessment of the effect of *wecA* and *rfbD* partial transcriptional silencing on the susceptibility of *Msm* to antimycobacterial agents. In addition, a second measure of dose-response curves, the half maximal effective concentration (EC_{50}) was also made. The EC_{50} is an alternative parameter used for evaluating dose-response relationships (Jiang and Kopp-Schneider, 2014) and is defined as the concentration of compound that gives half-maximal response (Noel et al., 2018, Sebaugh, 2011). To do this, the MABA assays described in **Section 3.4.1** were performed on the CRISPRi strains that were not induced with ATc or pre-depleted with ATc for 18 hours (see **Methods Section 2.8.2**). The strains were pre-depleted to ensure the hypomorph phenotype was present on first exposure to the drug.

As a control, the MSM_NT strain, expressing a sgRNA with no homology to the *Msm* genome, included in this assay and was not exposed (uninduced) or exposed (induced) to 100 ng/ml ATc (**Figure 3.11**). This negative control is expected to display no differences in drug susceptibility between the uninduced and induced conditions. As expected, for each drug no shifts in the MIC_{90} (**Figure 3.11**) or EC_{50} of the MSM_NT control was observed in the presence of ATc. These results confirm that integration of the CRISPRi system into the mycobacterial genome and induction of ATc does not impact drug susceptibility. For most of the drugs, the MSM_NT strain phenotype closely resembles the WT phenotype, with the MIC_{90} of LNZ, RIF and VAN being comparable to that of the WT MIC_{90} values. The MIC_{90} of EMB was higher than that of the MSM_WT, however this is within the range of the published MIC_{90}. An experiment repeat was performed utilising the same plate layout and drug

concentrations against the MSM_NT strain. The experimental repeats showed the same MIC_{90} values for LNZ, RIF and VAN, while the MIC_{90} of EMB was two-fold lower than the first experiment, but within the range of the published MIC_{90} (**Supplementary Figure S7, Table 3.6**).

The EC_{50} values of each drug had less than two-fold difference between uninduced and induced conditions and are presented in **Supplementary Table S2**. The colorimetric data for the MSM_NT assays do not show a shift in the visible MIC and are presented in **Supplementary Figure S9.**

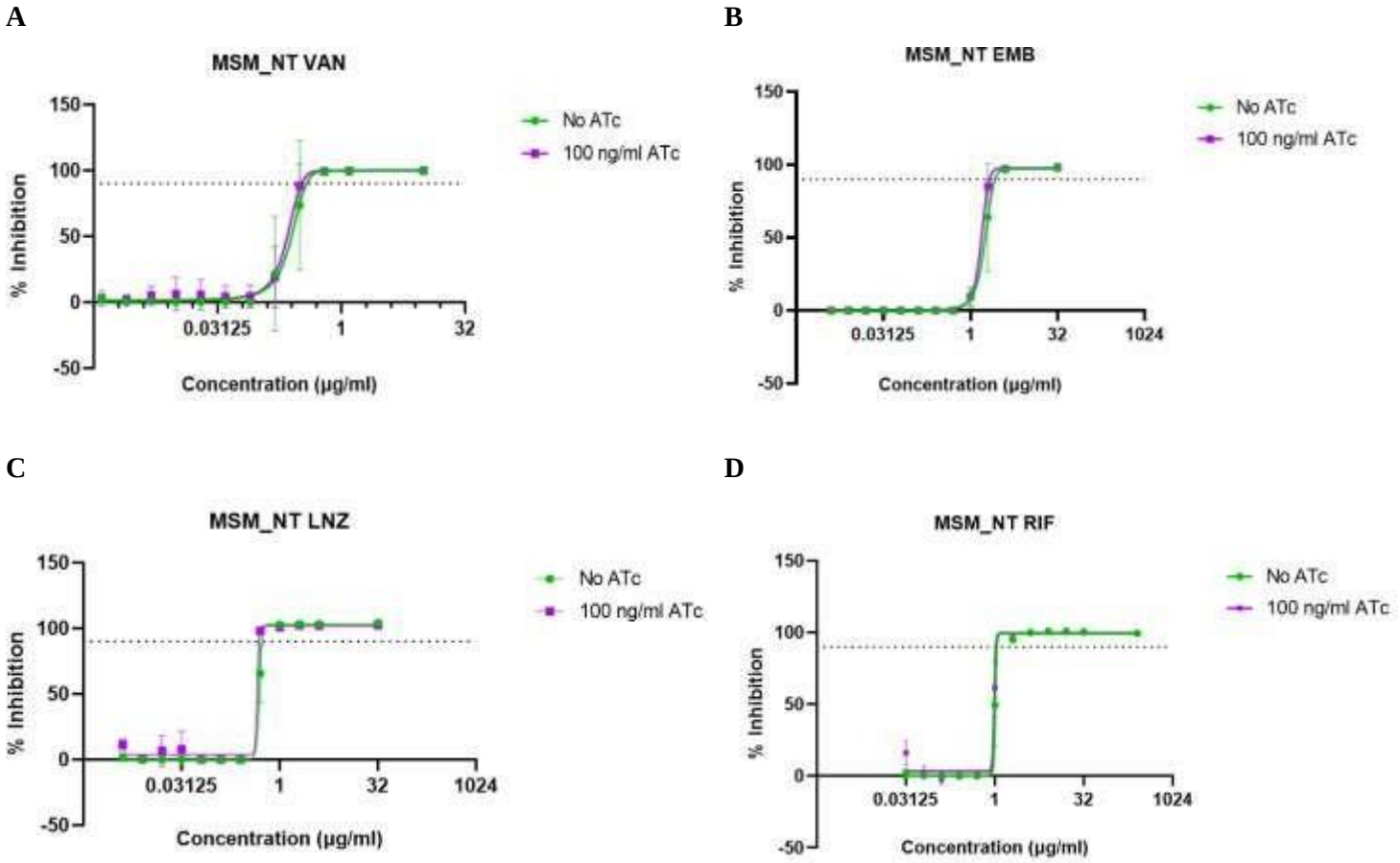

Figure 3.11. Determination of MIC_{90} in MSM_NT negative control. Dose responses of MSM_NT following exposure to a range of drug concentrations of ***A,*** vancomycin (VAN); ***B,*** ethambutol (EMB); ***C,*** linezolid (LNZ) and ***D,*** rifampicin (RIF) without (green) and with (pink) induction of the CRISPRi system. Dotted line represents the 90% inhibition. Error bars represent standard deviation for 3 technical repeats, and 2 experimental repeats were performed (see **Supplementary Figure S7**). Some error bars not visible due to low standard deviation.

The *clpP2* gene is essential and was utilised as a positive transcriptional knockdown control for spotting assays (see **Section 3.3.1**). This gene encodes a caseinolytic protease that plays a critical role in proteome homoeostasis and is responsible for the degradation of misfolded or damaged proteins (Yang et al., 2023). Considering the *clpP2* gene is not directly involved in cell envelope biosynthesis, we did not expect depletion of enzyme products that compromise the cell envelope structure. Therefore, we

expected no observed increase in sensitisation to drugs targeting cell envelope biosynthesis (specifically EMB) upon depletion of this enzyme, nor would there be an observed increase in sensitisation to drugs that have difficulty crossing the cell envelope (specifically VAN and RIF) as compared to those that do not (LNZ). These expectations were partially fulfilled (**Figure 3.12**). When treated with VAN, there was no observed shift in MIC_{90} (**Figure 3.12A**) and a slight shift in EC_{50} of 1.27-fold. When treated with EMB there was no shift in either MIC_{90} (**Figure 3.12B**) or EC_{50}. However, a shift was observed when MSM_*clpP2* was challenged with protein synthesis inhibitor LNZ (**Figure 3.12C**), corresponding to an EC_{50} fold-change of 2.8. Unexpectedly, a substantial shift in MIC_{90} is observed when MSM_*clpP2* is challenged with the RNA synthesis inhibitor RIF (**Figure 3.12D**), with an EC_{50} shift of 38-fold. The EC_{50} values are presented in **Supplementary Table S2**. The colorimetric data of MSM_*clpP2* support these results and are presented in **Supplementary Figure S9.** The experimental repeats performed against the MSM_*clpP2* strain showed similar MIC_{90} for VAN, EMB and LNZ, while RIF showed a higher MIC_{90} than the first experiment (**Supplementary Figure S7, Table 3.6**).

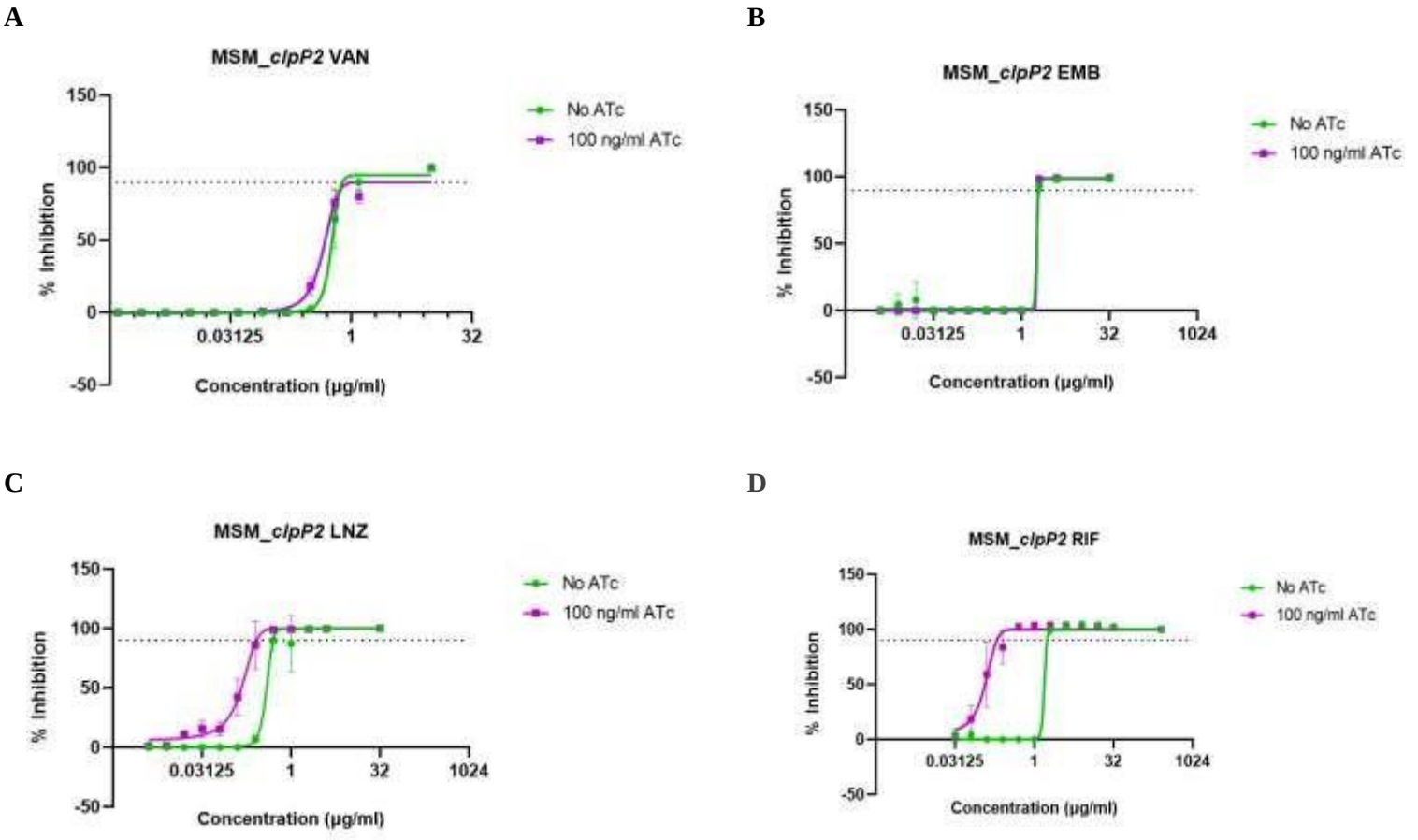

Figure 3.12. Determination of MIC_{90} in MSM_*clpP2* positive control. Dose responses of MSM_*clpP2* following exposure to a range of drug concentrations of ***A,*** vancomycin (VAN); ***B,*** ethambutol (EMB); ***C,*** linezolid (LNZ) and ***D,*** rifampicin (RIF) without (green) and with (pink) induction of the CRISPRi system. Dotted line represents the 90% inhibition. Error bars represent standard deviation for 3 technical repeats, and 2 experimental repeats were performed (see **Supplementary Figure S7**). Some error bars not visible due to low standard deviation.

Determination of sensitisation of wecA hypomorphs

The dose-responses of MSM_*wecA* when exposed to increasing concentrations of compound are shown in **Figure 3.13** below. As expected, the growth inhibition of all strains without ATc induction was similar to that of the MSM_NT strain, characterized by a typical dose-response curve **(Figure 3.13)**. The MIC_{90} of MSM_*wecA* in the uninduced (no ATc) condition was comparable to that of MSM_NT strain when challenged with LNZ, RIF and VAN (**Table 3.6)**. The MIC_{90} of this uninduced strain when challenged with EMB was two-fold lower than that of MSM_NT, but similar to that of MSM_WT (**Table 3.6**). These results confirm that the phenotype of MSM_*wecA* closely resembles that of MSM_NT when the CRISPRi system is not induced. The two-fold difference of EMB is notable but within the range of variation that has been observed, and which is tolerated for these assays.

After induction of the CRISPRi system (18 hours of pre-depletion with 100 ng/ml ATc), no shift in MIC_{90} is observed when MSM_*wecA* was exposed to VAN (**Figure 3.13A**). However, there was a slight difference in EC_{50} corresponding to a 1.9-fold change. When exposed to EMB, slight shifts in MIC_{90} with a minor decrease of that of the induced condition were seen (**Figure 3.13B**), with differences in EC_{50} corresponding to a 1.8-fold shift were noted. This slight sensitisation was also within the range of technical variation observed for this assay. Similar shifts (with minor decreases of the induced condition) were noted when this strain was challenged with either LNZ or RIF with EC_{50} differences of 1.7- and 2-fold, respectively. This indicates slight sensitisation, which was also within the range of technical variation observed for this assay. While slight increases in sensitisation did appear to occur in the induced condition only, this did not appear to be specific to the cell envelope targeting drugs nor to a potentiation of the larger molecules. The experimental repeats performed against the MSM_*wecA* strain showed similar MIC_{90} for all drugs, however, in contrast to the first experiment, no shifts in MIC_{90} were observed when the CRISPRi system was induced (**Supplementary Figure S7, Table 3.6**). The EC_{50} values are presented in **Supplementary Table S2**. The colorimetric data of MSM_*wecA* support these results and are presented in **Supplementary Figure S10.**

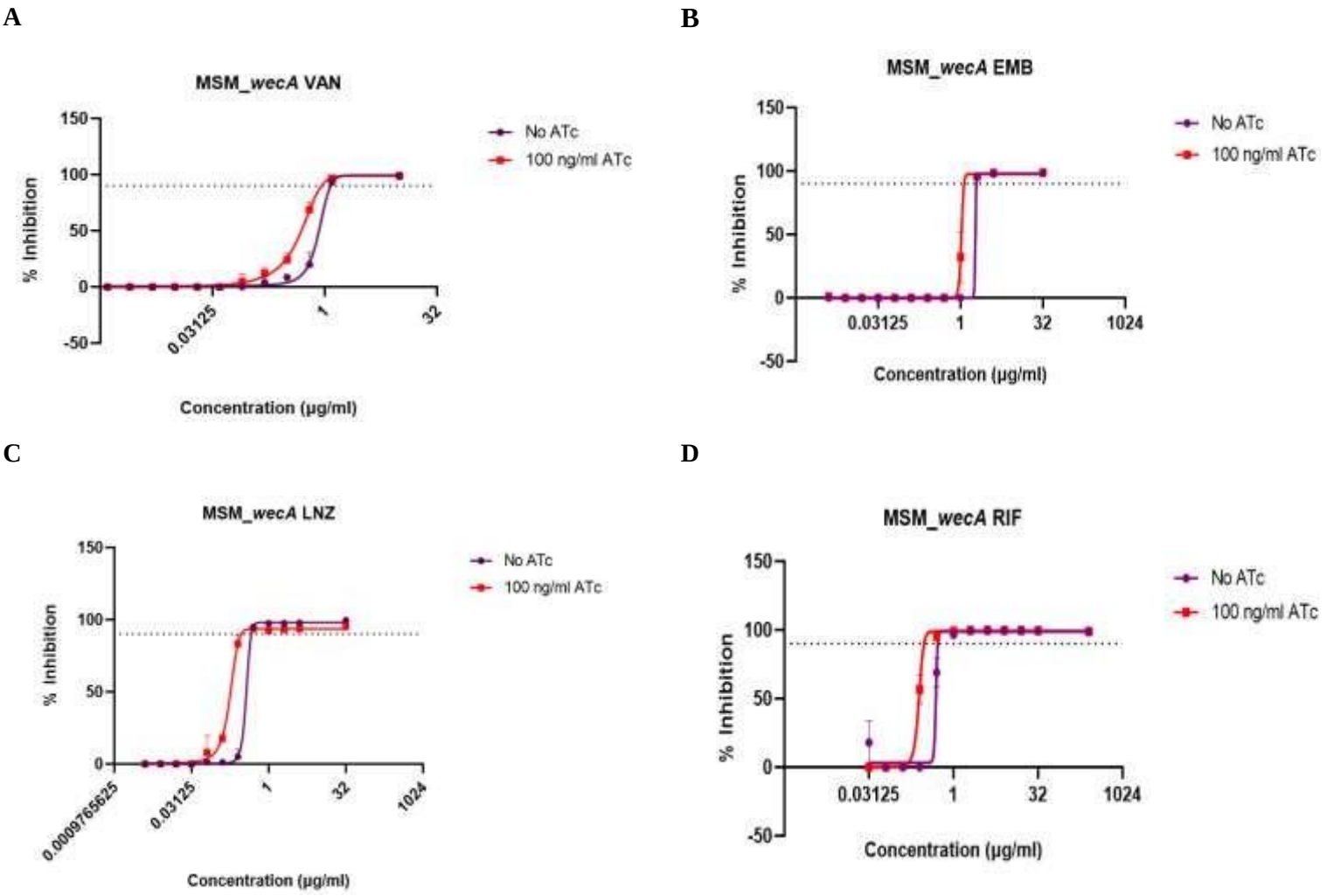

Figure 3.13. Determination of MIC_{90} in MSM_*wecA* hypomorphs. Dose responses of MSM_*wecA* following exposure to a range of drug concentrations of ***A,*** vancomycin (VAN); ***B,*** ethambutol (EMB); ***C,*** linezolid (LNZ) and ***D,*** rifampicin (RIF) without (purple) and with (red) induction of the CRISPRi system. Dotted line represents the 90% inhibition. Error bars represent standard deviation for 3 technical repeats, and 2 experimental repeats were run (see **Supplementary Figure S8**). Some error bars not visible due to low standard deviation.

Determination of sensitisation of rfbD hypomorphs

The dose-responses when MSM_*rfbD* was challenged with 2-fold increases in drug concentrations are shown in **Figure 3.14.** The MIC_{90} of MSM_*rfbD* without ATc induction was demonstrated to be 2-fold lower than that of MSM_NT when exposed to LNZ and RIF, but 3-fold higher when exposed to VAN (**Table 3.6**). Interestingly, the MIC_{90} when MSM_*rfbD* was challenged with EMB was lower when compared to MSM_NT and MSM_WT.

After induction of the CRISPRi system (18 hours of pre-depletion with 100 ng/ml ATc), no shift in MIC_{90} was observed when MSM_*rfbD* was challenged with either VAN or EMB (**Figure 3.14A & B**), with each of the drugs resulting of in a EC_{50} difference of 1.33 and 1.42-fold, respectively. Similarly, no shift in MIC_{90} (**Figure 3.14C**), and 1.29 shifts in EC_{50} observed when challenged with LNZ. When treated with RIF, no MIC_{90} shift is seen (**Figure 3.14D**), but interestingly in this assay the uninduced condition appeared slightly sensitised with a 0.77-fold shift in EC_{50} observed. This slight sensitisation was within the range of technical variation observed for this assay. The experimental repeats performed against the MSM_*rfbD* strain showed similar MIC_{90} for EMB and LNZ, however, the MIC_{90} of VAN was determined to be lower than the first experiment while the MIC_{90} of RIF was higher (**Supplementary Figure S8**). The EC_{50} values are presented in **Supplementary Table S2.** The colorimetric data of MSM_*rfbD* support these results and are presented in **Supplementary Figure S10.**

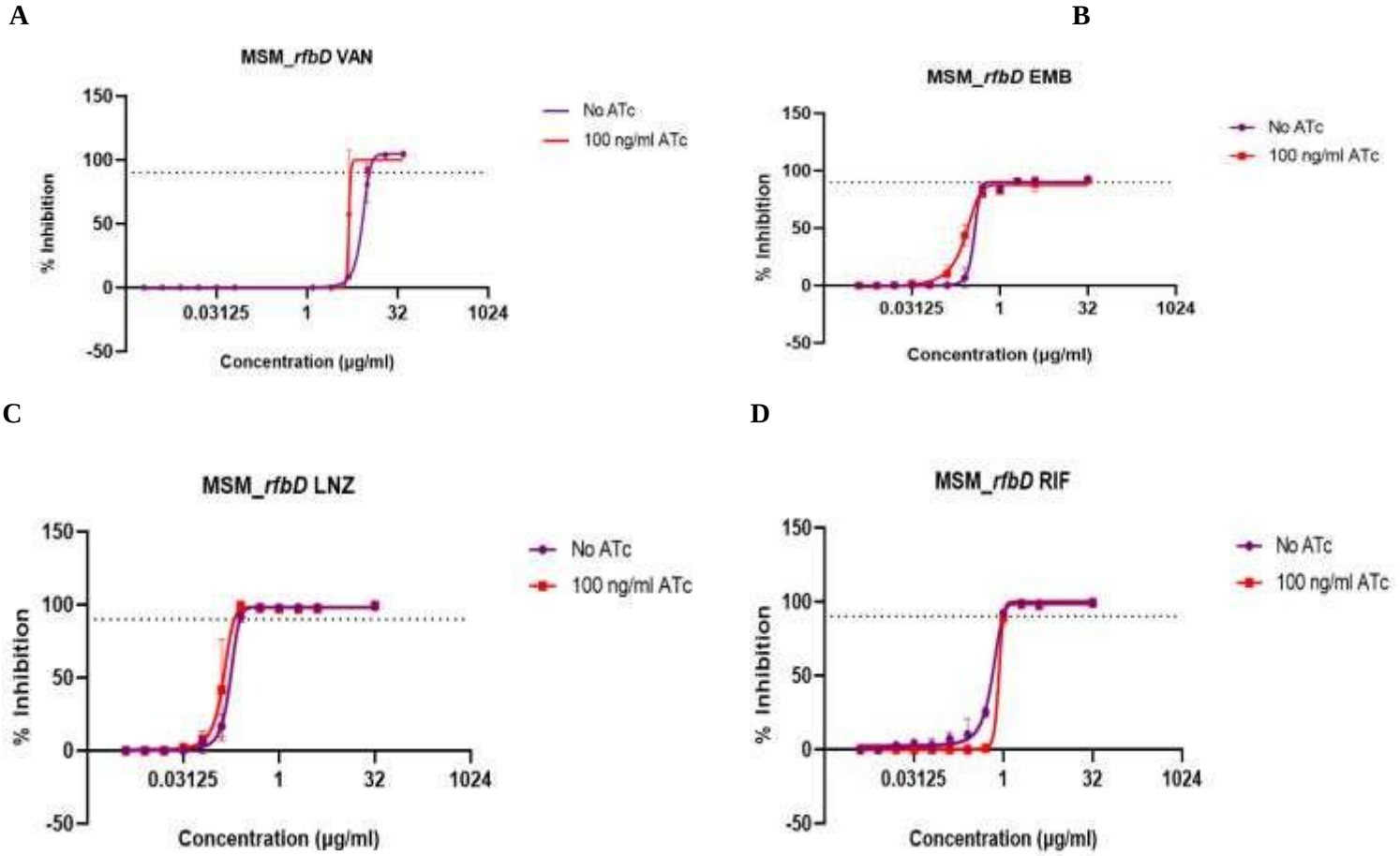

Figure 3.14. Determination of MIC_{90} in MSM_*rfbD* hypomorphs. Dose responses of MSM_*rfbD* following exposure to a range of drug concentrations of ***A,*** vancomycin; ***B,*** ethambutol; ***C,*** linezolid and ***D,*** rifampicin without (purple) and with (red) induction of the CRISPRi system. Dotted line represents the 90% inhibition. Error bars represent standard deviation for 2 technical repeats, and experimental repeats of 2 were run (see **Supplementary Figure S8**). Some error bars not visible due to low standard deviation.

3.5. Morphological profiling

3.5.1. DMN-Tre labelling of *M. smegmatis* hypomorphs

Decrease in cell replication and abundance is just one metric that reflects changes to cellular function brought upon by the repression of essential genes. Single-cell morphological profiling is a method used to assess how individual bacteria respond to perturbations, such as genetic alterations, through analysing changes in cell shape and the organisation of other spatial features (de Wet et al., 2020). We used quantitative imaging studies to further characterise the impact of disrupting galactan biosynthesis on cellular functions using single cell image and analysis and examining cell-to-cell variation following incorporation of a metabolic probe. 4-*N*,*N*-Dimethylamino-1,8-naphthalimide (DMN) is a solvatochromic dye conjugated to a trehalose molecule to form DMN-Tre (Sahile et al., 2020) **(Figure 3.15B)**. DMN-Tre is taken up by live mycobacterial cells and metabolically processed through the activity of the mycobacterial Ag85 enzyme, which mycolates the molecule to mycolic acids. This mycolated DMN-Tre molecule is then transported and incorporated into the mycomembrane, where it undergoes fluorescence enhancement within this lipophilic environment **(Figure 3.15A)**, allowing for the rapid visualisation of mycobacterial strains without the need for multiple wash steps (Kamariza et al., 2018).

A

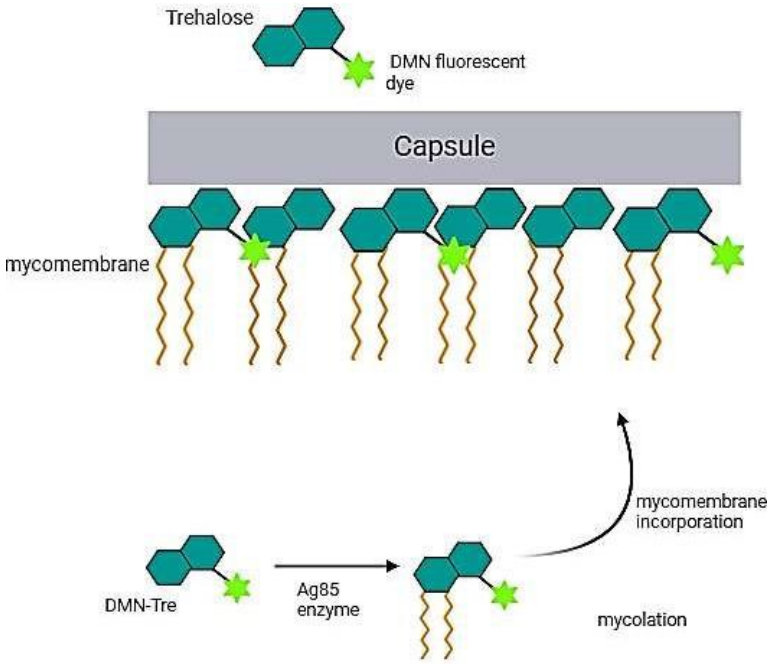

B

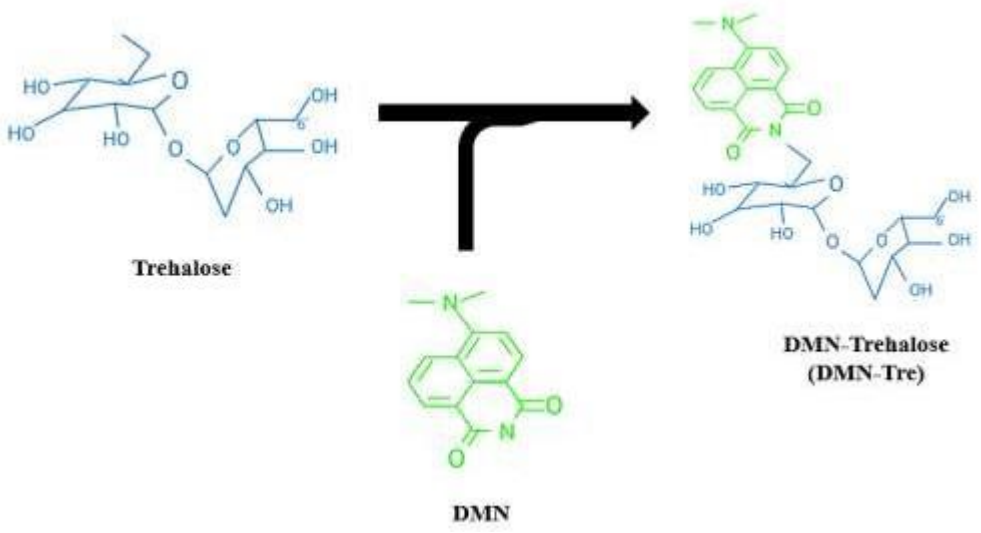

Figure 3.15. DMN-Tre incorporation into the outer leaflet of the mycomembrane and molecular structure. ***A***, Schematic showing DMN-Tre penetrating the mycobacterial cell envelope and the mycolation of trehalose by the Ag85 enzyme. The mycolated DMN-Tre molecule is subsequently incorporated into the mycomembrane where it undergoes enhanced fluorescence. ***B***, the molecular structure of DMN-Tre probe showing the DMN dye (green) and the trehalose molecule (blue). *Adapted from Kamariza et al. (2018) and generated using Biorender (2025).*

A study by Sahile et al., 2020 assessed the suitability of DMN-Tre to label mycobacterial strains for high-content drug screening, comparing this to a traditional red fluorescent protein read-out system. They showed that the probe was able to successfully label with no toxicity to the host cell or alterations to *Mtb*'s intracellular growth or other virulence features, demonstrating the potential of this metabolic probe for use in drug discovery.

To determine the impact of partially knocking down the process of galactan biosynthesis on cellular functions that impact cell morphology and cell envelope composition, suspensions of bacterial cultures were probed through the metabolic incorporation of DMN-Tre, and single-cells were examined by microscopy to determine cellular dimensions and DMN-Tre signatures.

3.5.2. Cell shape is not impacted by experimental conditions

To confirm that addition of ATc does not impact the cellular dimensions of the strains used in this study, exponentially growing cultures of MSM_NT were tested either in the absence or presence of 100 ng/ml ATc. As a comparator MSM_WT strains were cultured in the absence of ATc. These uninduced and induced cultures were mixed with 100 µM DMN-Tre and incubated for 2 hours to allow time to probe the cell envelope. The cells were washed and subsequently visualised using fluorescence microscopy. Single cells of the MSM_WT and MSM_NT cultures were observed and exhibited clear and distinct fluorescence in the DMN-Tre fluorescence channel (**Figure 3.16A**). No difference in cell length or width were observed in the uninduced MSM_NT CRISPRi control cell population compared to that of the parental MSM_WT strain, indicating that the morphology of the CRISPRi negative control was equivalent to the WT strain **(Supplementary Figure S11).** In addition, no differences in cell length (p-value= 0.23) or width (p-value= 0.67) were evident between the uninduced and induced MSM_NT conditions (**Figure 3.16A**), demonstrating that the addition of ATc did not impact these cellular dimensions. As expected, higher DMN-Tre signals were observed at the poles (**Figure 3.16B**). These DMN-Tre profile signals are quantified in **Section 3.5.5**.

A

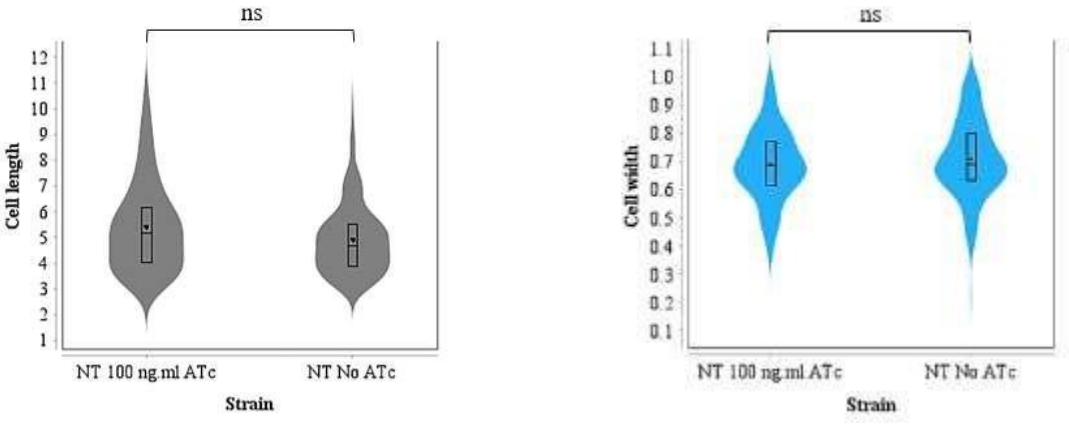

B

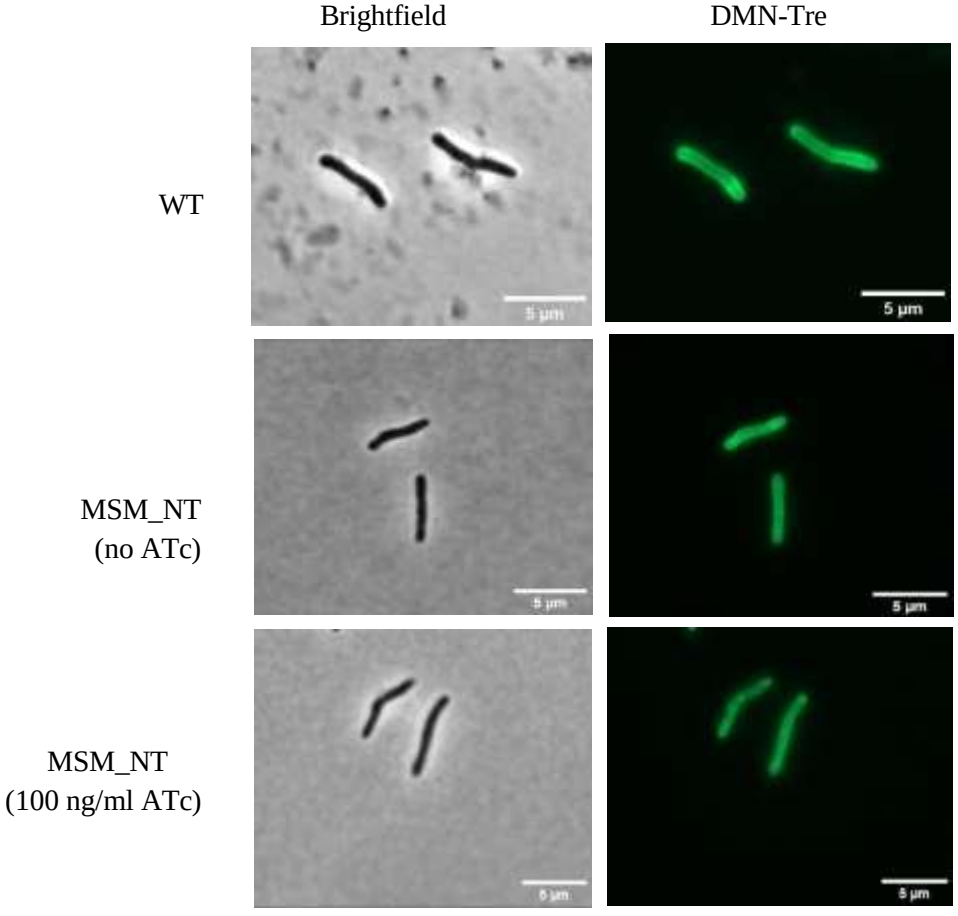

Figure 3.16. Visualisation of DMN-Tre staining in control strains MSM_WT and MSM_NT. ***A***, Violin graphs showing MSM_NT cellular dimensions. Comparison of cell lengths, and cell widths of MSM_NT strains with and without ATc treatment. Approximately 100 cells analysed per strain. ***B***, Visualisation of MSM_WT and MSM_NT cellular dimensions and DMN-Tre localisation, with and without ATc treatment in representative single cells. MSM_WT with no ATc is indicated on the top row, untreated MSM_NT is indicated in the middle row while treated MSM_NT are indicated on the bottom row. Left

panel illustrates bacilli under brightfield channel; right panel illustrates bacilli under DMN-Tre fluorescence signal (GFP channel). Scale bar 5 µm. Cellular dimensions compared using a paired t-test. Comparison of MSM_NT and MSM_WT lengths and widths are shown in **Supplementary Figure S11.**

3.5.3. Morphological analyses of M. smegmatis CRISPRi control strains

Previous high-throughput screening of 263 essential *Msm* mc^2155 genes revealed that disruption of cell envelope components resulted in distinct alterations to bacterial single cell morphology (de Wet et al., 2020).

Following confirmation that cell shape was not impacted by experimental conditions and that the addition of ATc did not impact cell morphology in the CRISPRi MSM_NT strain, the cellular dimensions of *Msm* hypomorph strains were analysed under the same experimental conditions.

Studies by (Raju et al., 2012) demonstrated that the absence of *clpP2* in mycobacteria results in the accumulation of non-functioning misfolded proteins. Additionally, genetically altered *Msm* strains with disruption to components of DNA translation, including a CRISPRi *Msm* strain targeting the partner protein in the clpP1/clpP2 complex **(Supplementary Figure S13)**, *clpP1* is known to have an elongated cell morphology that is distinct from that of the WT strain (de Wet et al., 2020) Based on this information, we expected to see increases in cell length upon depletion of *clpP2,* and thus this strain was used as a positive control in this assay to detect single cell morphological alterations. The DMN-Tre-stained single cell phenotypes of this strain with or without induction of CRISPRi system are shown in **Figure 3.17**.

The morphological alterations in this control strain demonstrate that disruption of the essential protease, *clpP2* results in cellular elongation and variations in cell widths (**Figure 3.17A**). An uneven distribution of DMN-Tre resembling the formation of foci, was noted (**Figure 3.17B**). No foci were observed in the absence of ATc, and the DMN-Tre signal appeared as expected with a higher signal at the poles (similar to that of the MSM_WT and MSM_NT described in **Section 3.5.2**). These DMN-Tre profile signals are quantified in **Section 3.5.5**. The results of the MSM_*clpP2* positive control confirms that ATc induction of the CRISPRi system was successful, resulting in a significant difference in cell length (p-value= 0.016). While the average cell width remained unchanged (p-value= 0.49) upon induction **(Figure 3.17A)** the single cell widths did appear to change across the cell.

A

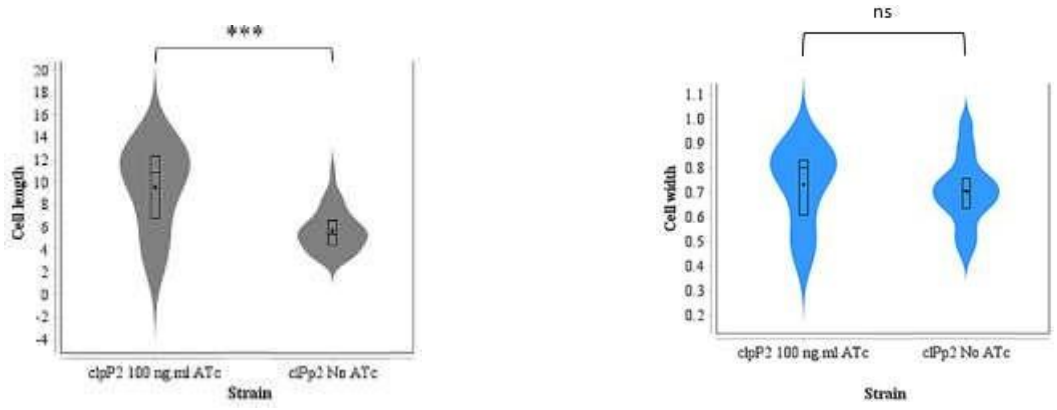

B

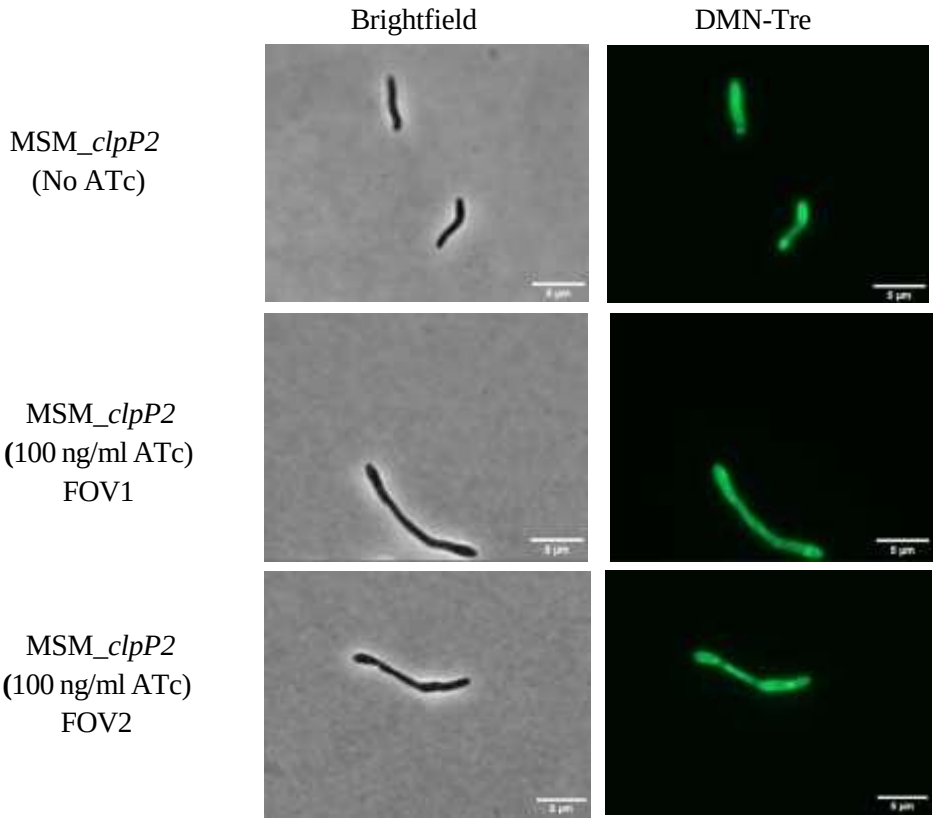

Figure 3.17. Visualisation of MSM_*clpP2* cellular dimensions. ***A***, Violin plot showing cellular dimensions of MSM_*clpP2* positive control. Comparison of MSM_*clpP2* cell lengths and average cell width with and without ATc treatment. Approximately 50 cells analysed under ATc induction; 100 cells analysed under untreated condition. ***B***, Visualisation of MSM_*clpP2* cellular dimensions and DMN-Tre localisation, with and without ATc treatment in representative single cells. Untreated MSM_*clpP2* are indicated in the top row, while ATc treated MSM_*clpP2* are indicated in the middle and bottom rows. Left panel illustrates bacilli under the brightfield channel; right panel illustrates bacilli under DMN-Tre fluorescence signal (GFP channel). Scale bar 5 µm. Cellular dimensions compared using a paired t-test. FOV = Field of View.

3.5.4 Morphological profiling of galactan-compromised *M. smegmatis* strains

Disruption of wecA results in distinct cell morphology

Mycobacterial CRISPRi strains targeting the mAGP layer were shown to have distinct cell morphology (de Wet et al., 2020). To further our understanding of galactan's role in maintaining cell morphology, the MSM_*wecA* strains were pre-cultured without or with ATc and then were mixed with DMN-Tre as described in **Section 3.5.2.** The cells were visualised under the same experimental conditions as those described above and are presented in **Figure 3.18**. Shortened cell lengths were observed in the induced condition when compared to the uninduced condition (p-value= 0.004) (**Figure 3.18A)**. In addition, increased average cell widths were seen when the CRISPRi system was induced (p-value= 0.036) (**Figure 3.18A)**. These cellular dimensions were compared to MSM_NT and MSM_*clpP2* controls and are presented in **Supplementary Figure S12A.**

The DMN-Tre signature in the uninduced condition was shown to be similar to that of the MSM_WT and MSM_NT strains with higher signals seen at the poles (see **Figure 3.18B**). In the induced condition, however, a uniform DMN-Tre signal is seen along the medial axis of the cell, with a few cells showing a higher signal at the septum **(Figure 3.18B**). The DMN-Tre profile signals are quantified in **Section 3.5.5**.

A

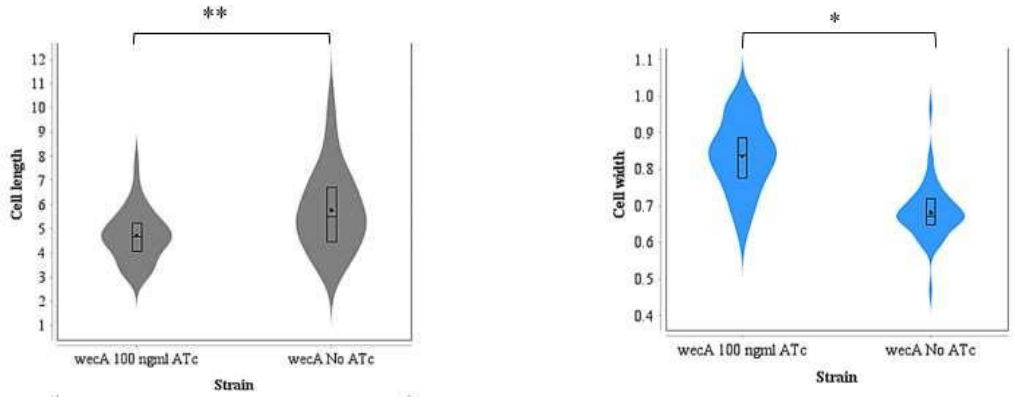

B

Brightfield

DMN-Tre

MSM_*wecA* (No ATc) FOV1

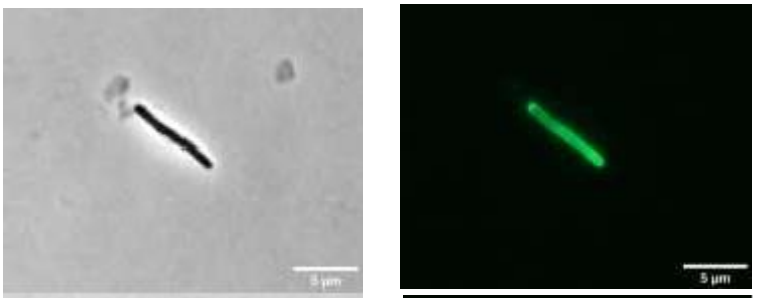

MSM_*wecA* (No ATc) FOV2

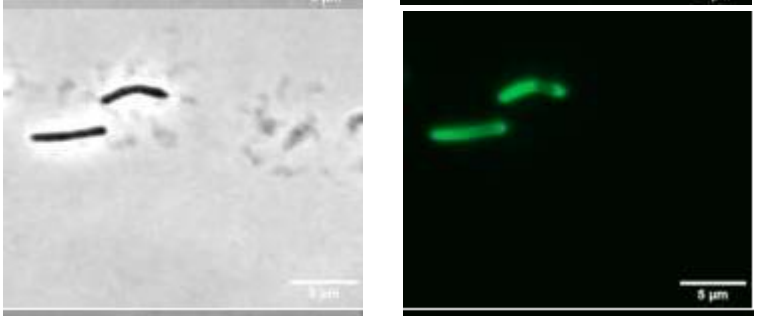

MSM_*wecA* (100 ng/ml ATc) FOV1

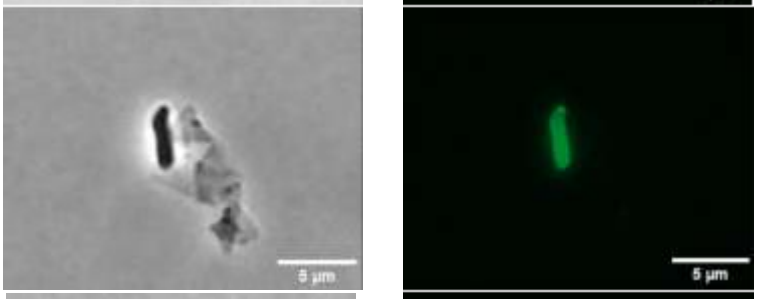

MSM_*wecA* (100 ng/ml ATc) FOV2

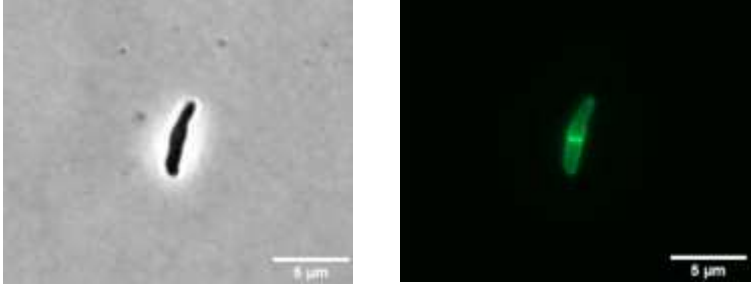

Figure 3.18. Visualisation of MSM_*wecA* cellular dimensions. ***A***, Violin plot showing cellular dimensions of MSM_*wecA* hypomorphs. Approximately 150 cells analysed per untreated condition; approximately 130 cells analysed under treated condition. Scale bar 5 µm. Comparison of cell length, and width with and without ATc treatment. ***B***, Visualisation of MSM_*wecA* strains and localisation of DMN-Tre**.** Untreated MSM_*wecA* strains are indicated on the top two rows, while ATc treated MSM_*wecA* strains are indicated on the bottom two rows. Left panel shows bacilli under the brightfield channel; right panel illustrates bacilli under DMN-Tre fluorescence signal. Cellular dimensions compared using a paired t-test. MSM_*wecA* cellular dimensions were compared to MSM_NT and MSM_*clpP2* controls and are presented in **Supplementary Figure S12A.** FOV= field of view

Disruption of rfbD does not impact cell morphology

We examined the effect of disrupting galactan's translocation across the cell membrane on cell morphology. MSM_*rfbD* strains that had either been cultured without (uninduced) or with (induced) ATc were mixed with DMN-Tre as described in **Section 3.5.2**. The cells were visualised under the same experimented conditions as described above. No change in cell lengths is observed when the induced condition was compared to the uninduced condition (p-value= 0.4) **(Figure 3.19A)**. In addition, no changed in the average cell widths was observed between the induced and uninduced conditions (p-value= 0.62) **(Figure 3.19A).** The cellular dimensions of MSM_*rfbD* were compared to MSM_NT and MSM_*clpP2* controls and are presented in **Supplementary Figure S12B**.

The DMN-Tre signal in the MSM_*rfbD* strains are similar to that seen in the MSM_*wecA* strains **(Figure 3.19B)**. The DMN-Tre in the uninduced condition was shown to be similar to that of the MSM_WT and MSM_NT strains with higher signals seen at the poles (see **Figure 3.19B**). In the induced condition, however, a uniform DMN-Tre signal is seen along the medial axis of the cell, with a few cells showing a higher signal at the septum **(Figure 3.19B**). The DMN-Tre profile signals are quantified in **Section 3.5.5**.

A

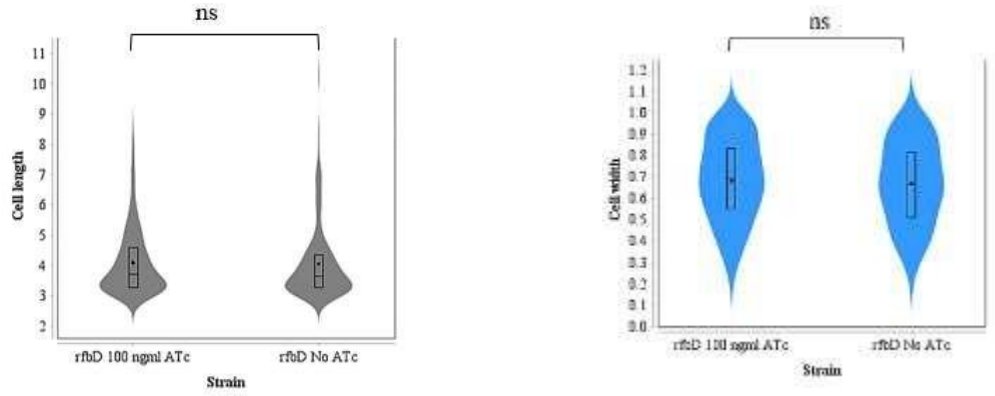

B

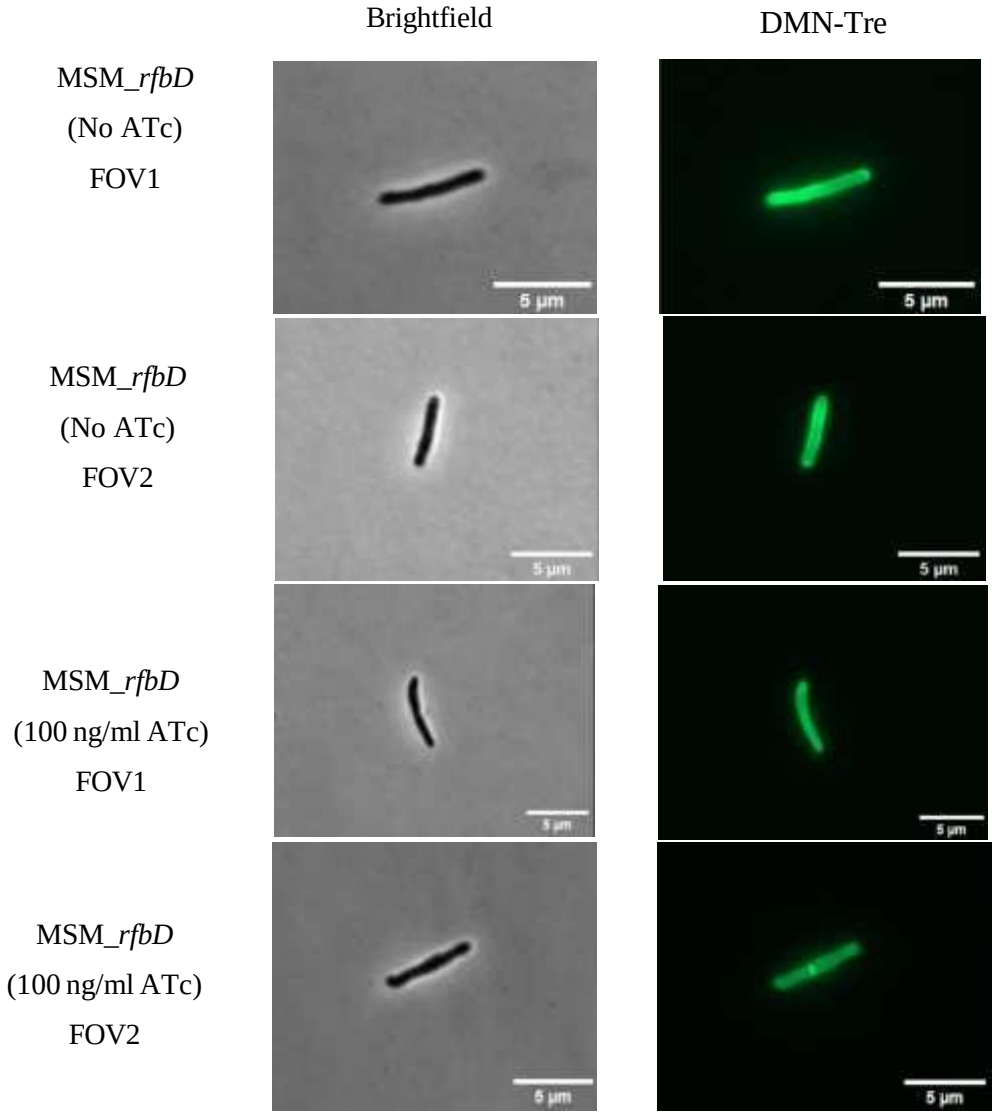

Figure 3.19. Visualisation of MSM_*rfbD* cellular dimensions. *A,* Quantitation of cellular dimensions of MSM_*rfbD* hypomorphs. Approximately 150 cells analysed per untreated condition; approximately 130 cells analysed under treated

condition. Scale bar 5 µm. Comparison of cell length, and width with and without ATc treatment. ***B,*** Visualisation of MSM_*rfbD* strains and localisation of DMN-Tre**.** Untreated MSM_*rfbD* strains are indicated on the top two rows, while ATc treated MSM_*rfbD* strains are indicated on the bottom two rows. Left panel shows bacilli under the brightfield channel; right panel illustrates bacilli under DMN-Tre fluorescence signal. Cellular dimensions compared using a paired t-test. MSM_*rfbD* cellular dimensions were compared to MSM_NT and MSM_*clpP2* controls and are presented in **Supplementary Figure S12B.** FOV= field of view

3.5.5. DMN-Tre fluorescent signal and sub-cellular localisation

To quantify DMN-Tre localisation patterns and spatial distribution, a X Stat Profile visualisation was performed in the MicrobeJ plugin of Fiji-ImageJ (Ducret et al., 2016). DMN-Tre fluorescent signals along the medial axis of each cell were detected to plot intensity profiles of the pixels in the fluorescent image. The DMN-Tre fluorescent signals of 100-150 cells were averaged for 11 regions along the medial axis of the cells with 0 and 1.0 representing the poles and 0.5 representing the midline of the cell, and the standard deviations calculated.

MSM_NT demonstrated comparable average fluorescent intensity profiles in the absence and presence of ATc (**Figure 3.20A**). MSM_NT under both conditions displayed higher signal at the poles at 4500, with the lowest average signal observed at the mid-cell at 4000 for the untreated condition and 3000 for the treated condition **(Figure 3.20A)**.

No discernible difference in average fluorescent signal is observed between MSM_*clpP2* and MSM_NT in the absence of ATc (**Figure 3.20A & 3.20B**). The highest average DMN-Tre fluorescent signal at 4500 is observed at the poles of the MSM_*clpP2* positive control, with the lowest average signal at the septum at 3000 **(Figure 3.20B)**. Notably, upon induction of the MSM_*clpP2* strain with ATc, distinct DMN-Tre fluorescent intensities are observed at each pole: one pole has an average intensity of 3500 while the other pole has an average intensity of 5000, while the mid-line region has a lower average intensity of 1500. This indicates that the addition of ATc had an effect on the MSM_*clpP2* strain.

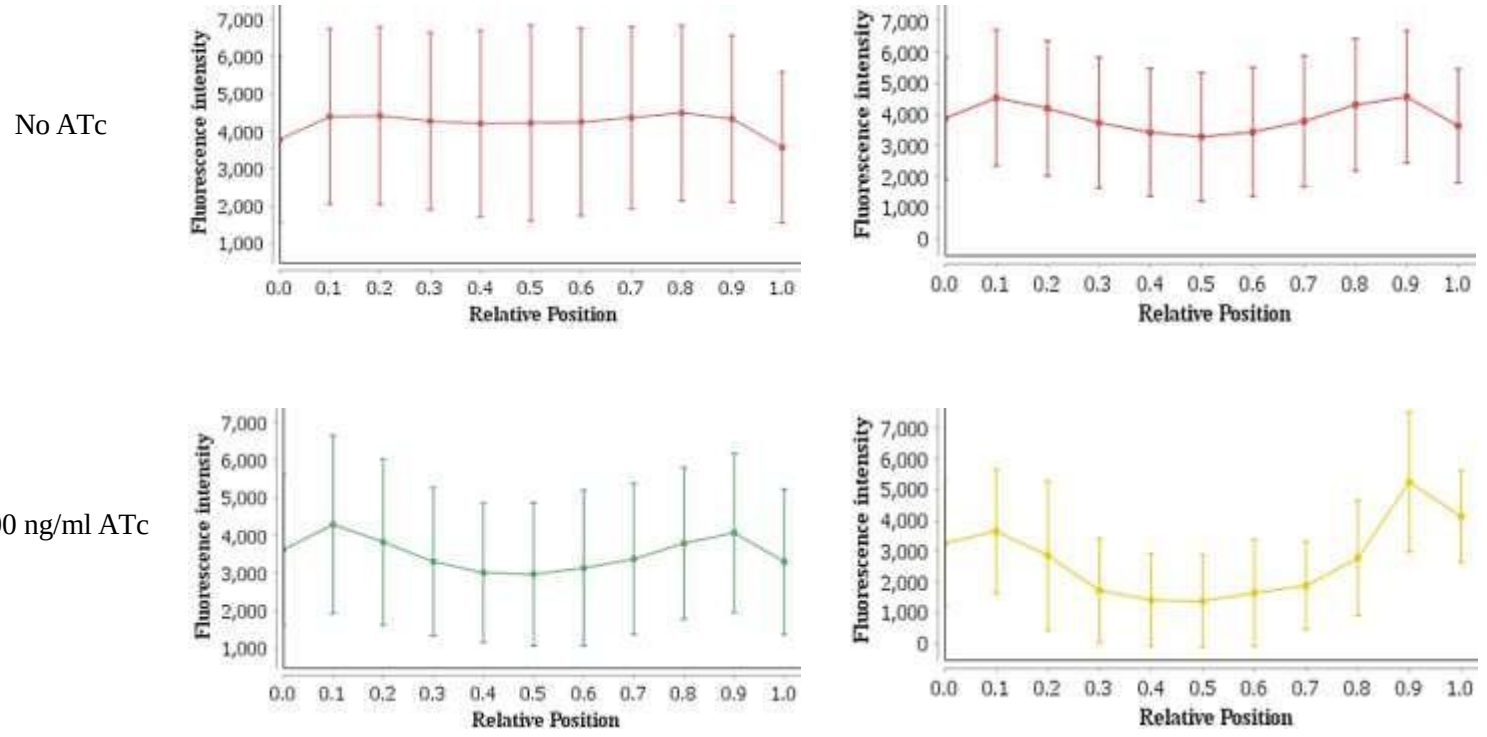

Figure 3.20. Cellular intensity profiles of DMN-Tre signal in *M. smegmatis* control strains. Intensity distribution of the DMN-Tre stain across ***A,*** MSM_NT negative control when uninduced and induced with ATc. ***B,*** MSM_*clpP2* control when uninduced and induced with ATc. The X-axis represents the relative position along the cell length where 0.5 represents the mid-cell and 0 or 1.0 represent each cell pole. The Y-axis represents the average fluorescence intensity of the DMN-Tre stain. Error bars represent standard deviation of multiple cells measured. Approximately 100 of the MSM_NT cells analysed under both ATc untreated and treated strains. Approximately 100 of the MSM_*clpP2* cells analysed under untreated condition; 50 of the MSM_*clpP2* cells analysed under treated condition.

The average DMN-Tre fluorescence intensities along the medial axis of our MSM_*wecA* strain are shown in **Figure 3.21A**. When this strain remained uninduced, the average DMN-Tre fluorescence intensity was measured as 3500 at the poles and 2500 at the mid-line. Upon induction with ATc, a distinct fluorescence intensity was observed: a unform distribution of average DMN-Tre intensities along the cell of 4000. Notably, a lower average intensity was seen at the poles with average fluorescent intensities of 3000.

A similar phenomenon was observed in the MSM_*rfbD* strain (**Figure 3.21B**), with average DMN-Tre fluorescence intensities similar to that seen in MSM_*wecA*. The distribution of DMN-Tre along the medial axis of the MSM_*rfbD* strain was comparable to that of the MSM_NT strain without ATc (uninduced), with an average intensity of 3700 at the poles and an average intensity of 3000 at the septum. In the presence of ATc (induced), a uniform distribution of DMN-Tre was observed along the

cell at an average fluorescence intensity of 4000 with the lowest signals seen at the poles with average fluorescent intensities of 3500.

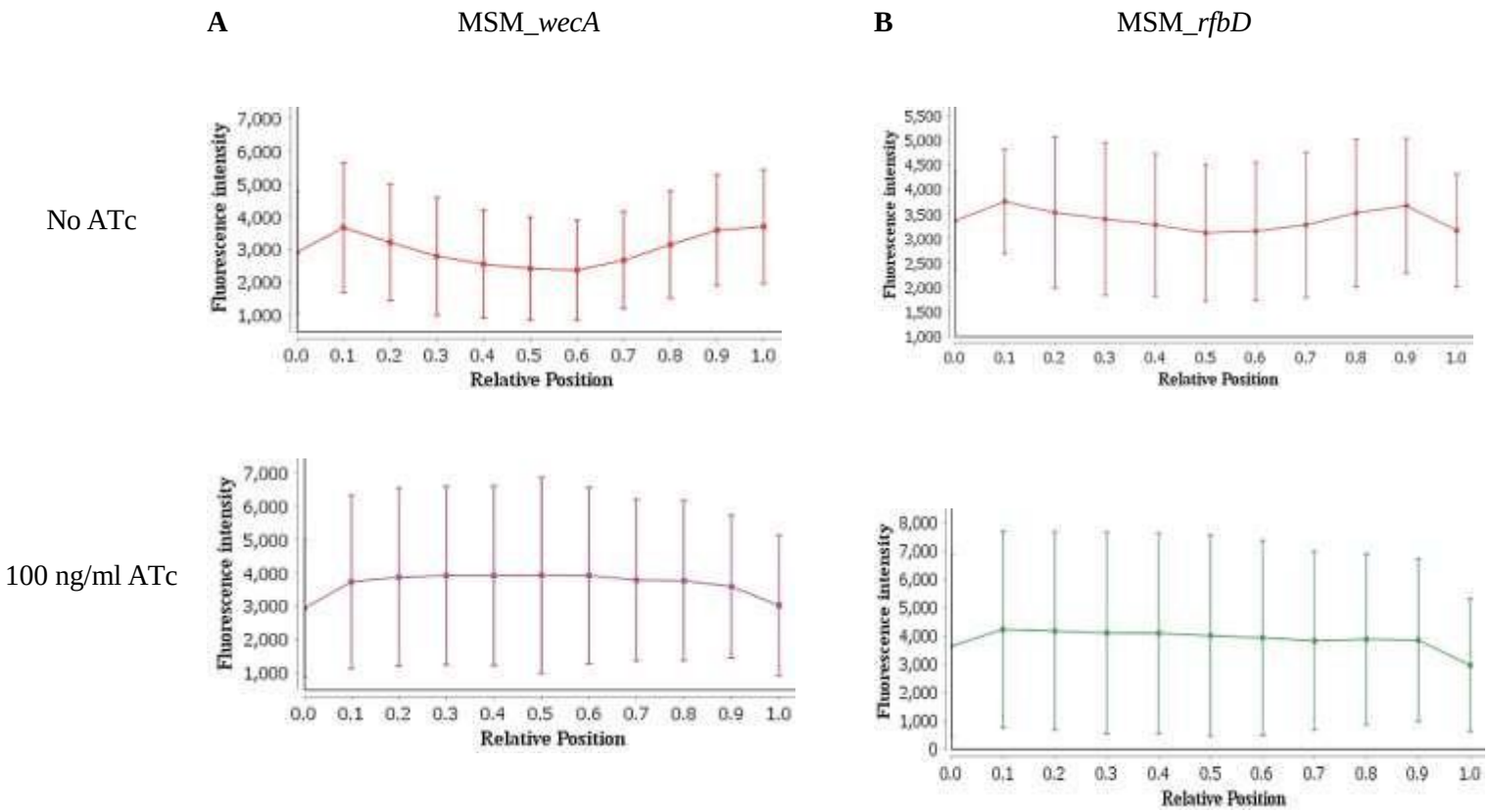

Figure 3.21. Quantification of the sub-cellular localisation of DMN-Tre in *M. smegmatis* hypomorphs. Intensity distribution of DMN-Tre stain across A, MSM_wecA when uninduced and induced with ATc; ***B,*** MSM_rfbD when uninduced and induced with ATc. Approximately 100-150 cells analysed per MSM_*wecA* and MSM_*rfbD* strain. The X-axis represents the relative position along the cell length where 0.5 represents the mid-cell and 0 or 1.0 represents each cell pole. The Y-axis represents the average fluorescence intensity of the DMN-Tre stain. Background fluorescence not subtracted for localisation data. Error bars represent standard deviation of multiple cells measured. Approximately 150 of the MSM_*wecA* cells analysed under untreated condition; 130 MSM_*wecA* cells analysed under treated condition. Approximately 130 of the MSM_*rfbD* cells analysed under untreated condition; approximately 50 of the MSM_*rfb* cells analysed under treated condition.

3.5.6. Notable formation of cell aggregates upon disruption of galactan biosynthesis

Previous studies have demonstrated that nontubercular mycobacterial species form various types of aggregates under stressful conditions in order to survive and persist in both nonhost and host environments (DePas et al., 2019). An additional observation made during the single cell morphological analyses was the consistent and notable formation of aggregates in liquid culture following galactan biosynthesis disruption. The cultures were grown to exponential phase in 0.05% Tween80 detergent to minimise clumping and 0.2% glycerol as a carbon source. A close examination of our MSM_*wecA*

(**Figure 3.22**) and MSM_*rfbD* (**Figure 3.23**) strains induced by ATc showed a high prevalence of small clumps when compared to non-induced samples. This feature was not observed in the WT or MSM_NT strains (data not shown).

A

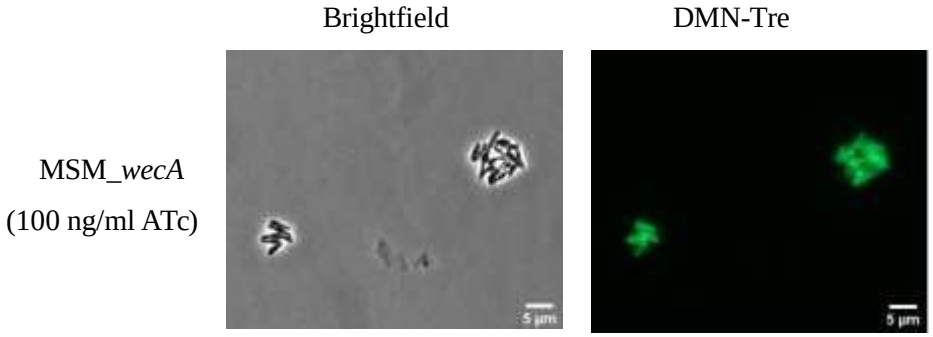

Figure 3.22. Visualisation of MSM_*wecA* cell aggregates. ATc treated MSM_*wecA* strains with left panel showing bacilli under the brightfield channel and right panel showing DMN-Tre fluorescence under the green GFP fluorescence channel. Scale bar 5 µm.

B

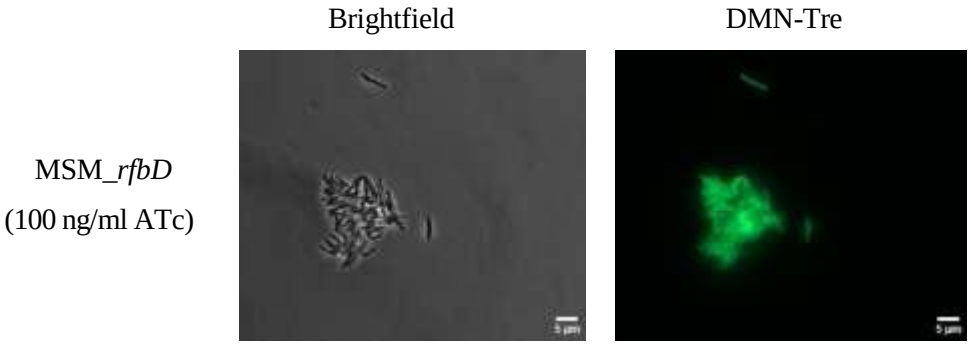

Figure 3.23. Visualisation MSM_*rfbD* cell aggregates. ATc treated MSM_*rfbD* strains with left panel showing bacilli under the brightfield channel and right panel showing DMN-Tre fluorescence under the green GFP fluorescence channel. Scale bar 5 µm.

Chapter 4: Discussion

Background

The ongoing emergence of drug-resistant *M. tuberculosis* (*Mtb*) strains requires attention for the development of new TB drugs and the elimination of this disease (Tiberi et al., 2022). Current TB treatment regimens are often compromised by their long durations, high toxicity, sub-optimal treatment and risk of relapse due to the rise in resistant strains (Tiberi et al., 2018). Newly approved drugs against TB are currently in the pre-clinical and clinical phases and are being integrated into experimental drug regimens (Angula et al., 2021). These include bedaquiline and delamanid which respectively target ATP synthase proton pumping mechanisms (Koul et al., 2007, Hards et al., 2015) and biosynthesis of keto- and methoxy mycolic acids (Fujiwara et al., 2018). Resistance to these compounds, however, has already been reported in *in vitro* studies and clinical settings (Gler et al., 2012, Pang et al., 2017, Nguyen et al., 2020). These findings emphasise the need to identify novel drug targets in essential components of *Mtb* physiology to prime the drug discovery pipeline (reviewed by Evans and Mizrahi, 2018).

The mycobacterial cell envelope structural and biosynthetic components have been identified as virulence factors playing a key role in the pathogenesis of *Mtb* as well as contributing to its intrinsic resistance to antibiotics (Al-Asady and Ali, 2023, Poulton and Rock, 2022). Targeting genes in the biosynthesis of specific mycobacterial cell envelope components may compromise this barrier's function and aid in the development of future *Mtb*-specific TB treatment strategies (Bhat et al., 2017). Biosynthesis of the galactan linker unit is an essential pathway in mycobacteria (Mikusová et al., 1996). Galactan serves as a component of the arabinogalactan molecule which is an essential component of mAGP. It gives the cell envelope structural integrity and impermeability against host antimicrobial agents and acts as a barrier to drug influx across the cell envelope (Konyariková et al., 2020). Galactan biosynthesis has remained an attractive target for novel TB drug development since the characterisation of this enzymatic pathway (Mikušová et al., 2000), with these essential proteins involved in its biosynthesis representing potentially useful drug targets (Konyariková et al., 2020). However, essentiality alone is not sufficient to prioritise a drug target. With this in mind, this study aimed to further characterise genes involved in this pathway and examine their potential as drug targets. Given the conservation of essential cell envelope components across mycobacterial species (Vincent et al., 2018), the role of *Mtb* cell envelope proteins may be investigated through interrogation of their orthologues in related mycobacterial species, such as *M. smegmatis* (*Msm*).

In vitro characterisation and validation of CRISPRi hypomorph strains

Interrogation of essential genes and their functions remains a vital tool to identify possible drug targets for the development of novel anti-TB therapeutics (de Wet et al., 2020). Conventional tools to characterise phenotypes of genes, such as transposon insertion and gene-deletion methods (Wiedenheft, Sternberg et al. 2012, Volke, Orsi et al. 2023) were inadequate for this study as the bacteria would not

survive the loss of the essential functions of galactan biosynthetic genes. However, new tools have been developed to generate genetically altered strains that exhibit conditional or partial transcriptional silencing and allow for loss-of-function studies of essential genes (Gilbert et al., 2014). In this study, we utilise the CRISPRi/dCas9 transcriptional interference system (Choudhary et al., 2015) optimised for mycobacteria (Rock et al., 2017) to produce *Msm* conditional hypomorphs with partial silencing of genes involved in the biosynthesis of galactan. CRISPRi is tuneable and can be adjusted using the length of the of sgRNA-target complementarity region or through the choice of PAM motif (Rock et al., 2017). In addition, the strength of gene knockdown can be adjusted by optimising the concentration of the anhydrotetracycline (ATc) inducer (Peters et al., 2016). By evaluating several sgRNAs complementary to the target gene, we produced inducible transcriptional knockdowns of wecA and rfbD, that exhibited attenuation of growth which varied depending on the computationally predicted guide strength of the sgRNA that each strain carried (see **Section 3.1**).

ATc is a derivative of the tetracycline family which does not exhibit any antibiotic activity and is used to control gene expression systems in mycobacteria (Ehrt et al., 2005). ATc is leveraged in the CRISPRi system to induce expression of both the exogenous dCas9 protein and the sgRNA at high levels (Rock et al., 2017). Various studies, where CRISPRi *Msm* strains were challenged with varying ATc concentrations (Raphela, 2020, McNeil et al., 2021), have demonstrated that concentrations of 100 ng/ml were sufficient to elicit potent and efficient transcriptional knockdown. A study by Choudhary et al., 2015 showed that ATc concentrations of up to 50 ng/ml does not affect the *in vitro* growth of *Msm* CRISPRi mutants, and that increasing the concentration of the inducer does not affect or enhance the expression of the dCas9 protein. As expected, at an ATc concentration of 100 ng/ml, the growth of MSM_NT (*Msm* strain harbouring a sgRNA with no gene target) did not display any growth attenuation with the addition of ATc in liquid or on solid media. This confirms that the addition of ATc at this saturating concentration had no negative impact on the viability or replication of *Msm* as compared to the non-expressed CRISPRi strain, either directly by exposure to ATc or indirectly by the expression of high levels of dCas9 and the non-targeting sgRNA molecules.

In contrast to MSM_NT, the growth of our positive control, MSM_*clpP2* (*Msm* strain harbouring a sgRNA that targets the essential *clpP2* gene), with the selected guide having strong predicted knockdown. This strong growth attenuation was expected as the essentiality of *clpP2* in both *Msm* and *Mtb* has been demonstrated by Transposon insertion sequencing (DeJesus et al., 2017, Kester et al., 2021) and using CRISPRi sequencing (Bosch et al., 2021). The *clpP2* targeting CRISPRi strain was potently inhibited by the addition of ATc. This phenotype was seen both on solid and in liquid media and was used to confirm that the ATc induction of the mycobacterial CRISPRi system was activated within this assay.

When assessing the knockdown phenotypes of the CRISPRi hypomorphs, a minority of the tested strains displayed a degree of knockdown that did not correspond to the predicted knockdown efficiencies of the guide (see **Section 3.3**). Some of the strains demonstrated differing growth attenuation in liquid media when compared to their growth attenuation on solid media, showing strong growth attenuation on solid media while displaying intermediate growth attenuation in liquid media. As all downstream experiments were performed in liquid media, we selected the guides that showed intermediate growth attenuation in liquid culture. This was done to ensure the cells remain viable for subsequent experiments and did demonstrate some partial growth attenuation. When utilising CRISPRi, additional validation of the efficacy of transcriptional knockdown, through the quantification and direct assessment of transcriptional silencing is often undertaken via qRT-PCR (Larson et al., 2013). This gives insight into the relative level of molecular knockdown that has been achieved for the selected gene and could potentially serve as a direct quantitative comparison of the strains. However, degree of transcriptional knockdown of essential genes may not always have a direct relationship to a growth attenuated phenotype. We, therefore prioritised measuring the growth of our strains to evaluate their suitability for downstream assays. In addition, the molecular quantification of gene expression levels is costly and requires specialist reagents and equipment to perform and while necessary to assess impact of CRISPRi silencing on non-essential genes, this is not explicitly needed to assess this impact on essential genes. In this study, we relied on growth attenuation as a tractable and informative approach for the selection of suitable sgRNAs of interest. With only one of a set of five being utilised in the downstream microbiological assays. While this did not fall within the scope of this current research, the quantification of the level of transcriptional silencing of these strains would be informative to undertake in further studies into the interrogation of the genes selected in this study.

Altogether, these results show that relying on computationally predicted guide strengths is informative, but not sufficient to determine growth attenuation, and empirical testing of multiple guides is required to select the most suitable sgRNAs hypomorph for downstream gene disruption and the generation of an appropriate hypomorph phenotype for assays. The use of growth attenuation to select of guides is a suitable method to select hypomorph strains that are suited to the conditions of each assay.

Determination of the reference Minimum Inhi*bitory *Concentration (MIC) of WT M. smegmatis

Antimycobacterial agents exhibit potent killing of mycobacteria and exhibit a range of minimum inhibitory concentrations (MIC). A review by Mouton et al., 2018 found that MIC values within the same organism may differ due to several factors. Individual strains within the same species harbour individual characteristics (strain-to-strain variations); assay variations may arise due to differences in medium and inoculum preparation influenced by the technical skills of the researcher and degree of training (inter- and intra-laboratory variations). As such, the MICs of antimicrobial agents can often be interpreted as a range rather than a 'true' MIC value. The MIC_{90} values of rifampicin (RIF), vancomycin

(VAN), ethambutol (EMB) and linezolid (LNZ) were, therefore, determined in our WT *Msm* (MSM_WT) strains prior to testing in the CRISPRi hypomorphs. The MIC_{90} values refer to the minimum drug concentration required to inhibit the detectable growth of 90% of a bacterial population.

For this study, a set of antibiotics were selected and assessed for their sensitisation in our *Msm* CRISPRi hypomorphs. RIF is a hydrophobic compound and a potent first-line drug against active TB and functions by inhibiting the activity of DNA-dependent RNA polymerase β-subunit, blocking the elongation step during transcription (Mosaei and Zenkin, 2020). Mycobacterial strains with compromised mycolyl-arabinogalactan-peptidoglycan (mAGP) have previously been shown to be sensitised to RIF (Li et al., 2022), proving support for testing the sensitisation of our strains to this drug. The MIC_{90} of RIF in our MSM_WT strains was found to be 2 µg/ml, within the previously published range of 1.32-2.57 µg/ml (Faulkner et al., 2021). VAN is a large hydrophilic compound that inhibits the biosynthesis of peptidoglycan (Soetaert et al., 2015), and, similar to RIF, mycobacterial species with mAGP knockdown were shown to be sensitised to VAN treatment (Li et al., 2022). As expected, the MIC_{90} of VAN in our MSM_WT strains was found to be 1.25 µg/ml, within the range previously shown to be between 0.625 µg/ml and 5 µg/ml (Stephan et al., 2004, Danilchanka et al., 2008). EMB is a first-line drug against active TB and functions by inhibiting the addition of arabinose residues onto the galactan chain during arabinogalactan biosynthesis (Zhu et al., 2018). Surprisingly, the MIC_{90} of EMB was determined to be 0.125 µg/ml, half that of the lowest value within the determined MIC range of 0.25-2 µg/ml (Khoo et al., 1996, Lechner et al., 2008). LNZ, an antimycobacterial compound that inhibits the initial phase of protein synthesis (Liu et al., 2020), served as a negative control in this study as it was shown to not be sensitised by compromising the mAGP (Li et al., 2022). LNZ's MIC_{90} was determined to be 1 µg/ml, within the MIC range of 0.5-4 µg/ml (Wallace Jr et al., 2001). The data from our experimental repeat supports these MIC_{90} values. Altogether, these results suggest that the use of a single MIC value is likely inappropriate, and to optimise for drug treatment, inherent variations in the MIC determinant should be accounted for.

Investigation of the MIC_{90} of M. smegmatis CRISPRi non-targeting control

The selected CRISPRi hypomorph strains targeting each gene (including the MSM_*clpP2* strain previously used as a positive control), were then challenged with RIF, VAN, LNZ and EMB, with the determined MIC_{90} values in the MSM_WT used as a reference. The MSM_NT strain was used as a negative control to serve as a CRISPRi negative control and was expected to be non-responsive. The MSM_NT was confirmed to closely resemble the MSM_WT strain with the MIC_{90} of most drugs, with the exception being EMB, being comparable to that of the MSM_WT reference MIC_{90} value. The MIC_{90} when MSM_NT was challenged with EMB was 4-fold higher than that seen in the WT reference. The CRISPRi strains used in this assay were derived from the MSM_WT parental strain with minimal handling and passaging in the lab. It is known that laboratory mycobacterial strains may undergo genetic

alterations due to extended cultivation in the lab setting, resulting in genomic and phenotypic variation (Ioerger et al., 2010). Although our strains had not been handled or cultivated for an extended period, the rise of subtle genetic variations among strains cannot be excluded as a possibility and may be resolved through the use of whole genome sequencing (WGS) of both the parental and genetically altered strains. It is important to also note that the MIC assays were performed at different times, therefore technical issues may arise (such as slight variations of initial drug working stock concentrations or pipetting errors) which might impact the observed growth of the strains within the experimental set up. Within the hypomorph MIC assays the growth of the MSM_NT control strain was determined to be the comparator. While differences in EMB MIC_{90} were observed between the MSM_WT and MSM_NT strains, no shift in the MIC_{90} was observed due to the induction of the CRISPRi system in MSM_NT, a strain that carried a sgRNA that had no homology to the *Msm* genome. Therefore, we could conclude that the addition of ATc and the induction of the CRISPRi system alone did not impact sensitivity to any of the four drugs tested within these assay conditions.

Investigation of the MIC_{90} of M. smegmatis wecA CRISPRi hypomorph

The *wecA* gene is essential in mycobacterial species, catalysing the transfer of GlcNAc-P onto a lipid carrier molecule, undecaprenyl phosphate to initiate galactan biosynthesis. We reasoned that disruption of this gene would disrupt galactan biosynthesis resulting in alterations to cell envelope permeability, facilitating an increase in susceptibility to antibiotics. The drugs tested in study, LNZ (MW= 337.35) and RIF (MW= 822.9), are compounds that target cytoplasmic pathways which are not directly involved in the biosynthesis of cell envelope components. In contrast, EMB (MW= 204.31) and VAN (MW= 1449.2) directly target components of the mAGP complex. Importantly, RIF, VAN and EMB have been shown to be sensitised by depletion of mAGP in mycobacteria, while sensitivity of LNZ had not been impacted (Li et al., 2022). Selection of antibiotics with various cellular targets may provide an informative panel to probe the phenotype of *wecA* depletion against a range of drugs with both intracellular and cell envelope targets, and different physiochemical properties some of which have been validated as drug targets through large scale CRISPRi screens.

When MSM_*wecA* was challenged with RIF, a 2-fold decrease in MIC_{90} was observed in the induced strain. These findings correspond to a previous study by Justen et al., 2020 where it was revealed that *Msm glfT2* mutant strains with truncated galactan chains developed enhanced susceptibility to hydrophobic antibiotics, rifampicin and novobiocin. However, in contrast, no shift is seen when MSM_*wecA* was exposed to VAN. Results from the same study showed that hydrophilic compounds, streptomycin and meropenem, exhibited no change in activity in mutants with decreased galactan lengths. However, depletion of WecA showed slight hypersensitisation to EMB, a hydrophilic compound. The authors of this study hypothesized that their mutant with truncated galactan likely had

an intact mycolic acid outer layer as this layer serves a major barrier to hydrophilic compounds. As expected, no shift in MIC_{90} is observed when MSM_*wecA* was challenged with LNZ, consistent with that observed by Li et al., 2022. In addition, approximately 2-fold decreases are observed in the EC_{50} of all drugs tested against MSM_*wecA*. Often in these assays, 2-fold shifts are not considered meaningful, and due to these shifts not being supported by the experimental repeats, we consider these shifts as technical variations within the assay. In addition, the possibility of polar effects, when targeting *wecA*, is low as the target gene was the most downstream gene in its operon (see **Supplementary Figure S1**).

Investigation of the MIC_{90} of M. smegmatis rfbD CRISPRi hypomorph

Mycobacteria possess 28 genes that encode ABC Exporters involved in peptide transport across the cell envelope (Cassio Barreto de Oliveira and Balan, 2020). Of these, *rfbD* and *rfbE* were identified as transporters of membrane components and liposaccharides (Braibant et al., 2000, Cassio Barreto de Oliveira and Balan, 2020). The *rfbD* gene (encoding the membrane-spanning domain of the ABC Exporter), and the *rfbE* gene (encoding the nucleotide-binding domain) and are co-transcribed under a single promoter (Cassio Barreto de Oliveira and Balan, 2020). Studies into the inactivation of *rfbD* and *rfbE* in *M. smegmatis* have suggested their involvement in the biosynthesis of arabinogalactan (Cuthbertson et al., 2010). Disruption of *rfbD* did not confer sensitivity to any of the tested compounds, which are supported by the experimental repeats. These findings are interesting, as disruption of this gene was shown to affect *in vitro* galactan synthesis (Dianišková et al., 2011), and the results from our *in vitro* growth attenuation experiments confirmed the essentiality of this gene in mycobacteria. Drug sensitisation studies in *Mtb* strains with *rfbD* sgRNAs found that significant sensitisation in *Mtb* is seen when challenged with high doses of RIF and LNZ (Li et al., 2022).

Phenotypic characterisation of this gene by Dianišková et al., 2011 suggests that the functionality of rfbD in *Msm* might be medium dependent: growth of Δ*rfbD* did not reveal cell envelope changes when grown in Sauton media and, interestingly, growth of Δ*rfbD* in GAS media produces an unknown compound when analysed via thin layer chromatography. In addition, *rfbD* and *rfbE* are co-transcribed in mycobacteria (Cassio Barreto de Oliveira and Balan, 2020), and in our study *rfbE,* the upstream gene in this operon, was still functional, therefore the possibility of polar effects is low as the target gene was the most downstream gene in this operon (see **Supplementary Figure S1** for operon). However, we cannot exclude the possibility the nucleotide-binding domain potentially binding to another membrane-spanning domain to compensate for the partial loss of *rfbD.*

Investigation of the MIC_{90} of M. smegmatis clpP2 CRISPRi positive control

Caseinolytic proteases (Clp) are highly conserved, and essential proteases present in many organisms, including bacteria, mammals and plants (Porankiewicz et al., 1999). Mycobacteria possess two *clpP* genes, *clpP1* and *clpP2*, which are co-transcribed under a single promoter to form the ClpP1P2 complex

(Li et al., 2016). These genes are responsible for the degradation of mis-folded or damaged proteins, critical to maintain protein homeostasis (Yang et al., 2023) The ClpP1 protein was shown to be responsible for nearly all peptidase activity that breaks down proteins, while the coupling of ClpP1 and ClpP2 is required for protein degradation (Barik et al., 2010) with ClpP2 serving as a scaffold for chaperone binding and substrate delivery by ClpC1 (Lee, 2016) (see **Supplementary Figure S13**). Depletion of ClpP2 protein would impair proteolytic activity resulting in the accumulation of undesirable protein products and has been shown to reduce growth in the presence of drugs that produce errors in protein translation (amikacin and streptomycin) (d'Andrea et al., 2022).

A strong *clpP2* mutant was used in this study as a positive control of the CRISPRi system's induction, and as this gene is the most downstream gene in its operon (**Supplementary Figure S1**), we expect no polar effects. We were curious to determine the effects of strong *clpP2* knockdown on the susceptibility of *Msm* to RIF, VAN, EMB and LNZ, as this strain does not directly target cell envelope biosynthesis, and depletion of both *clpP1* and *clpP2* rather shows decreased sensitisation to the higher concentrations of EMB assayed in CRISPRi screens in *Mtb* (Li et al., 2022). CRISPRi screens in *Mtb* strains with *clpP2* sgRNAs found that significant sensitisation in *Mtb* is seen when challenged with high doses of RIF and LNZ, but not when treated with EMB (Li et al., 2022).

No alterations in sensitivity to EMB and VAN were observed in MSM_*clpP2* in our assays. In our study, *clpP1* was still expected to be transcribed and translated into an enzyme with functional peptidase activity. Barik et al., 2010 demonstrated that the *clgR* gene homologue in *M. smegmatis*, MSMEG_2694, was involved in the upregulation of the Clp regulon in *M. smegmatis*, and when challenged with VAN, resulting in an increase in the activity of this system.

Interestingly, as shown in the CRISPRi screens of *Mtb* mentioned above, in our study substantial decreases in both MIC_{90} and EC_{50} were observed when MSM_*clpP2* was exposed to RIF (see **Section 3.4.2**), while a smaller decrease was seen when exposed to LNZ. In a study by Duc et al., 2020 the ATPase activity of ClpC1 was shown to increase with a gradual increase in the concentrations of drugs that include EMB, RIF and pyrazinamide (PZA), but these activities were less potent than Ecumicins, which are known to target the activity of Clp genes. Overall, the investigation of the drug sensitisation of a CRISPRi strain that was not directly involved in arabinogalactan biosynthesis revealed some insights regarding the interactions between various genes in maintaining cellular integrity.

Investigation of the morphology of M. smegmatis CRISPRi hypomorphs by microscopy

The mycobacterial cell envelope plays an important role in maintaining cell shape, rigidity and osmotic regulation, as well as protection from environmental harm (Abrahams and Besra, 2018). Screening of essential mycobacterial cell envelope knockdown mutants of *Msm* revealed that disruption of essential cell envelope components, including components of mAGP, resulted in distinct changes to cell shape

(de Wet et al., 2020). This prompted us to examine the effects of galactan depletion on the architecture of the mycobacterial cell envelope and its impact on cell morphology at a population level.

Microscopic analyses from our study showed that disruption of the first step in galactan biosynthesis, catalysed by WecA, resulted in distinct shortening and widening of cells when compared to non-depleted strains. Studies by Shen et al., 2020 indicated that dynamic remodelling of AG occurs in the periplasmic space and work by Justen et al., 2020 showed that galactan dictates periplasm size, with cryo-TEM visualisations of *Msm* strains revealing reduced periplasm size when galactan was compromised. The presence of galactan, therefore may have a direct impact on how mycobacteria respond to osmotic pressure and environmental stress, with the depletion of this structure affecting cell envelope properties and potentially disrupting cell integrity.

Silencing the gene encoding the membrane-spanning domain of the exporter responsible for translocation of galactan, *rfbD* however, showed regionalised bulging of the cells, but cell length and average width were not significantly affected. A study by Savková et al., 2021 demonstrated that silencing the transcription of *rfbD* (named *wzm* in this study) resulted in the accumulation of lipid-linked galactan within *Msm* cells, confirming its function in the transport of the galactan polymer across the cell membrane. The same study found that silencing both *rfbD* and *rfbE* caused growth defects and resulted in drastic changes to *Msm* cell morphology, these being swelling of the bacteria. However, this swelling was not seen in our *Msm* cells. However, we did see localised bulging, which was also seen in the above-mentioned study.

Examination of MSM_*clpP2*, not directly targeting galactan biosynthesis, revealed that silencing of this gene resulted in significant elongation of the cells. Mycobacterial strains harbouring the *clpP1* gene contain peptidase activity, however the absence of the protein degradation activity of *clpP2* likely results in accumulation of protein peptides. Silencing the activity of ClpP2 may lead to an accumulation of protein peptides and substrates that interfere with the cell cycle, delaying septum formation leading to elongated cells. A large scale CRISPRi screen demonstrated that silencing of *clpP1* resulted in similar cell morphology (de Wet et al., 2020). The morphological results of our MSM_*clpP2* positive control confirm that the induction of the CRISPRi system by ATc was successful.

Investigating the cell envelope composition of M. smegmatis CRISPRi hypomorphs by fluorescence microscopy

The galactan chain serves as a linkage between peptidoglycan and the mycolic acid layer of the mycomembrane. As such, disrupting galactan biosynthesis may disrupt the mycomembrane of the cell envelope. To examine this hypothesis, the cells were stained with DMN-Tre, a solvatochromic probe that selectively incorporates into the mycolic acid layer as trehalose monomycolates (Kamariza et al.,

2017). The change in polarity from an aqueous to lipophilic environment results in enhanced fluorescence of this metabolic probe (Sahile et al., 2020).

Fluorescent microscopy analyses of our MSM_NT negative control showed high DMN-Tre signals at the poles as expected (Kamariza et al., 2018), indicating the incorporation of mycolic acids in a CRISPRi strain that does not impact galactan biosynthesis. These results confirm that the cells are dividing and forming a robust mycomembrane, and that the metabolic probe is incorporating and is able to be detected. Upon examination of the MSM_*clpP2* strain, which targeted protein homeostasis, we see the formation of foci, which we could speculate are possible lipid bodies formed as a result of the accumulation of damaged and misfolded proteins. The results also show that incorporation of DMN-Tre was not distinctly polar and appeared irregular, caused by the formation of foci.

Both MSM_*wecA* and MSM_*rfbD* hypomorphs showed a similar sub-cellular localisation of DMN-Tre along the length of the cell. Similar to that seen in the MSM_NT strain, when the CRISPRi system was uninduced, the DMN-Tre fluorescent signal in both MSM_*wecA* and MSM_*rfbD* appeared highest at the poles, with the lowest signal present at the mid-cell. When expression of either *wecA* or *rfbD* were compromised, the DMN-Tre signal appeared uniform along the length of the cell with a reduction of signal observed at the poles. The addition of new cell envelope material in discrete zones at the poles are a defining feature of mycobacterial growth (Hannebelle et al., 2020, Uhía et al., 2015). The data presented here point toward obstruction in the addition of trehalose monomycolates at the poles when galactan is compromised, implying that there has been some disruption in apical growth and polar elongation. It has previously been reported that preventing the addition of AG onto the cell envelope leads to a loss of the mycolic acid layer (Telenti et al., 1997). A study by Schubert et al., 2017 showed that mycobacterial cells treated with EMB, blocking the polymerisation of arabinan onto galactan, resulted in a loss of mycolic acids at the poles and specifically blocked cellular elongation at these regions. This suggests that galactan formation and translocation across the cell envelope is essential to the formation of a robust mycomembrane. In addition, it was interesting to note that disruption of both genes resulted in clumping which were not observed in the WT or no target control strain. We could speculate that this is due to defects in the cell division process or alterations to the cell envelope lipid structure and hydrophobicity. Future work could resolve this using fluorescent probes that target various components of the cell envelope (see **Section 5.2**).

Chapter 5

Limitations and future work

Due to time constraints, qRT-PCR to quantify targeted gene expression was not conducted in either *Msm* or *Mtb*. This could be performed in further studies using a SYBR Green fluorescent dye where the fluorescent signal correlates to PCR product concentration (Chengalroyen et al., 2024). This could quantify the level of transcriptional silencing of each sgRNA and could be extended to confirm that there were no polar effects (transcriptional alterations of downstream genes and, more rarely upstream genes) that contribute towards strain phenotypes. To get full insight into potential impact of the CRISPRi system at the level of the genome, transcriptomics could be leveraged to determine not only target and neighbouring gene silencing, but also the global impact of the depletion of the target protein. A small set of antimycobacterial compounds were tested in this study as informed by previous work (Li et al 2022). However, this could be extended to additional drugs been found to be effective against mycobacteria. Two drugs assayed by CRISPRi screening in our research group are promising candidates showing sensitisation of the mAGP components. Griselimycin is a preclinical anti-TB candidate that was shown to be effective against *Mtb* (Kling et al., 2015). Nargenicin is a bactericidal compound that binds to DnaE1 and was shown to inhibit replication and induce DNA damage in *Mtb* (Chengalroyen et al., 2022). The sensitisation of mAGP strains to these drugs are yet to be validated and should be explored in further studies. The drug susceptibility assays were informative regarding the effects of galactan disruption on the susceptibility of *Msm* to a small set of compounds, however it does not confirm increased permeability of the cell envelope. To test this, cell envelope permeability assays could be conducted in future studies by assessing the rate of influx of Ethidium bromide across the cell envelope (Rodrigues et al., 2011).

The use of only one probe (DMN-Tre) may limit our understanding of the effects of galactan disruption on the composition of the cell envelope. In future studies, probes that label various regions of the cell envelope could be used to inform about the effects of disrupting the galactan linker on the integrity of the cell envelope. Probes such as sCy5DA (Zhang and Manley, 2023), RADA (García-Heredia et al., 2018) and HADA (Hsu et al., 2017) are fluorescent probes used for labelling peptidoglycan. These probes could also be utilised to image mycobacterial cell and assess the effects of galactan disruption on polar cell growth.

Chapter 6

Concluding remarks

In this study, the utility of CRISPRi gene silencing allowed for the interrogation of two essential genes in the galactan biosynthetic pathway. A set of CRISPRi knockdown mutants of *wecA* and *rfbD* were successfully generated and characterised in *M. smegmatis* and that of *wecA* was characterised in *M. tuberculosis*. Silencing of these genes resulted in *in vitro* growth defects and selection of sgRNA suited for downstream experimental interrogation was done. *Msm* strains with wecA and rfbD knockdown both did not show sensitisation to first-line antibiotics rifampicin, ethambutol, vancomycin and linezolid. Evidently, depletion of *wecA* had detrimental effects on the morphology of *M. smegmatis* with a decrease in cell length, and cell swelling. In contrast, depletion of *rfbD* had no impact on cell length but resulted in cell envelope bulging. Disruption of galactan biosynthesis via depletion of both genes appeared to disrupt the integrity of the mycomembrane and impact polar growth, evidenced by the loss of DMN-Tre signal at the polar regions of the cell. The relatively higher signal at the mid-cell region that apical incorporation is compromised. The findings of this study and its insights support the continuation of research into the role of galactan in maintaining cell envelope integrity and its role in supporting the generation of a robust mycolic acid leaflet.

References

ABRAHAMS, K. A. & BESRA, G. S. 2018. Mycobacterial cell wall biosynthesis: a multifaceted antibiotic target. *Parasitology,* 145**,** 116-133.

AHMAD, S. 2011. Pathogenesis, immunology, and diagnosis of latent Mycobacterium tuberculosis infection. *Clinical and Developmental Immunology,* 2011.

AL-ASADY, I. N. & ALI, J. F. 2023. Review Article: Virulence Factors of Mycobacterium Tuberculosis. *Journal for Research in Applied Sciences and Biotechnology,* 2**,** 221-237.

AL-JOURANI, O., BENEDICT, S. T., ROSS, J., LAYTON, A. J., VAN DER PEET, P., MARANDO, V. M., BAILEY, N. P., HEUNIS, T., MANION, J. & MENSITIERI, F. 2023. Identification of D-arabinan-degrading enzymes in mycobacteria. *Nature Communications,* 14**,** 2233.

ALDERWICK, L. J., HARRISON, J., LLOYD, G. S. & BIRCH, H. L. 2015. The mycobacterial cell wall—peptidoglycan and arabinogalactan. *Cold Spring Harbor perspectives in medicine,* 5**,** a021113.

ALTAF, M., MILLER, C. H., BELLOWS, D. S. & O'TOOLE, R. 2010. Evaluation of the Mycobacterium smegmatis and BCG models for the discovery of Mycobacterium tuberculosis inhibitors. *Tuberculosis,* 90**,** 333-337.

ANDREWS, J. M. 2001. Determination of minimum inhibitory concentrations. *Journal of antimicrobial Chemotherapy,* 48**,** 5-16.

ANGALA, S. K., BELARDINELLI, J. M., HUC-CLAUSTRE, E., WHEAT, W. H. & JACKSON, M. 2014. The cell envelope glycoconjugates of Mycobacterium tuberculosis. *Critical reviews in biochemistry and molecular biology,* 49**,** 361-399.

ANGULA, K. T., LEGOABE, L. J. & BETECK, R. M. 2021. Chemical classes presenting novel antituberculosis agents currently in different phases of drug development: A 2010–2020 review. *Pharmaceuticals,* 14**,** 461.

ARMIANINOVA, D., KARPOV, D., KOTLIAROVA, M. & GONCHARENKO, A. 2022. Genetic Engineering in Mycobacteria. *Molecular Biology,* 56**,** 830-841.

AUGENSTREICH, J. & BRIKEN, V. 2020. Host cell targets of released lipid and secreted protein effectors of Mycobacterium tuberculosis. *Frontiers in Cellular and Infection Microbiology,* 10**,** 595029.

BAHUGUNA, A. & RAWAT, D. S. 2020. An overview of new antitubercular drugs, drug candidates, and their targets. *Medicinal research reviews,* 40**,** 263-292.

BARIK, S., SUREKA, K., MUKHERJEE, P., BASU, J. & KUNDU, M. 2010. RseA, the SigE specific anti-sigma factor of Mycobacterium tuberculosis, is inactivated by phosphorylation-dependent ClpC1P2 proteolysis. *Molecular microbiology,* 75**,** 592-606.

BATT, S. M., BURKE, C. E., MOOREY, A. R. & BESRA, G. S. 2020a. Antibiotics and resistance: the two-sided coin of the mycobacterial cell wall. *The Cell Surface,* 6**,** 100044.

BATT, S. M., MINNIKIN, D. E. & BESRA, G. S. 2020b. The thick waxy coat of mycobacteria, a protective layer against antibiotics and the host's immune system. *Biochemical Journal,* 477**,** 1983-2006.

BENATAR, S. & UPSHUR, R. 2010. Tuberculosis and poverty: what could (and should) be done?[Unresolved issues]. *The International Journal of Tuberculosis and Lung Disease,* 14**,** 1215-1221.

BHAT, Z. S., RATHER, M. A., MAQBOOL, M., LAH, H. U., YOUSUF, S. K. & AHMAD, Z. 2017. Cell wall: A versatile fountain of drug targets in Mycobacterium tuberculosis. *Biomedicine & Pharmacotherapy,* 95**,** 1520-1534.

BORGDORFF, M. W., FLOYD, K. & BROEKMANS, J. F. 2002. Interventions to reduce tuberculosis mortality and transmission in low-and middle-income countries. *Bulletin of the World Health Organization,* 80**,** 217-227.

BOSCH, B., DEJESUS, M. A., POULTON, N. C., ZHANG, W., ENGELHART, C. A., ZAVERI, A., LAVALETTE, S., RUECKER, N., TRUJILLO, C. & WALLACH, J. B. 2021. Genome-wide gene expression tuning reveals diverse vulnerabilities of M. tuberculosis. *Cell,* 184**,** 4579-4592. e24.

BRAIBANT, M., GILOT, P. & CONTENT, J. 2000. The ATP binding cassette (ABC) transport systems of Mycobacterium tuberculosis. *FEMS microbiology reviews,* 24**,** 449-467.

BRITES, D. & GAGNEUX, S. 2015. Co-evolution of M ycobacterium tuberculosis and H omo sapiens. *Immunological reviews,* 264**,** 6-24.

BROWN, T., CHAVENT, M. & IM, W. 2023. Molecular modeling and simulation of the mycobacterial cell envelope: from individual components to cell envelope assemblies. *The Journal of Physical Chemistry B,* 127**,** 10941-10949.

BUSSI, C. & GUTIERREZ, M. G. 2019. Mycobacterium tuberculosis infection of host cells in space and time. *FEMS microbiology reviews,* 43**,** 341-361.

CAMPBELL, J. R., WINTERS, N. & MENZIES, D. 2020. Absolute risk of tuberculosis among untreated populations with a positive tuberculin skin test or interferon-gamma release assay result: systematic review and meta-analysis. *bmj,* 368.

CASSIO BARRETO DE OLIVEIRA, M. & BALAN, A. 2020. The ATP-binding cassette (ABC) transport systems in Mycobacterium tuberculosis: Structure, function, and possible targets for therapeutics. *Biology,* 9**,** 443.

CHANDRA, P., GRIGSBY, S. J. & PHILIPS, J. A. 2022. Immune evasion and provocation by Mycobacterium tuberculosis. *Nature Reviews Microbiology,* 20**,** 750-766.

CHEE, C. B., REVES, R., ZHANG, Y. & BELKNAP, R. 2018. Latent tuberculosis infection: Opportunities and challenges. *Respirology,* 23**,** 893-900.

CHENGALROYEN, M. D., MASON, M. K., BORSELLINI, A., TASSONI, R., ABRAHAMS, G. L., LYNCH, S., AHN, Y.-M., AMBLER, J., YOUNG, K. & CROWLEY, B. M. 2022. DNA-dependent binding of nargenicin to DnaE1 inhibits replication in Mycobacterium tuberculosis. *ACS Infectious Diseases,* 8**,** 612-625.

CHENGALROYEN, M. D., MEHAFFY, C., LUCAS, M., BAUER, N., RAPHELA, M. L., OKETADE, N., WARNER, D. F., LEWINSOHN, D. A., LEWINSOHN, D. M. & DOBOS, K. M. 2024. Modulation of riboflavin biosynthesis and utilization in mycobacteria. *Microbiology Spectrum,* 12**,** e03207-23.

CHIARADIA, L., LEFEBVRE, C., PARRA, J., MARCOUX, J., BURLET-SCHILTZ, O., ETIENNE, G., TROPIS, M. & DAFFÉ, M. 2017. Dissecting the mycobacterial cell envelope and defining the composition of the native mycomembrane. *Scientific reports,* 7**,** 12807.

CHOUDHARY, E., THAKUR, P., PAREEK, M. & AGARWAL, N. 2015. Gene silencing by CRISPR interference in mycobacteria. *Nature communications,* 6**,** 6267.

CHRISTENSEN, H., GARTON, N. J., HOROBIN, R. W., MINNIKIN, D. E. & BARER, M. R. 1999. Lipid domains of mycobacteria studied with fluorescent molecular probes. *Molecular microbiology,* 31**,** 1561-1572.

CLETO, S., JENSEN, J. V., WENDISCH, V. F. & LU, T. K. 2016. Corynebacterium glutamicum metabolic engineering with CRISPR interference (CRISPRi). *ACS synthetic biology,* 5**,** 375-385.

COHEN, S. B., GERN, B. H., DELAHAYE, J. L., ADAMS, K. N., PLUMLEE, C. R., WINKLER, J. K., SHERMAN, D. R., GERNER, M. Y. & URDAHL, K. B. 2018. Alveolar macrophages provide an early Mycobacterium tuberculosis niche and initiate dissemination. *Cell host & microbe,* 24**,** 439-446. e4.

COLE, S., BROSCH, R., PARKHILL, J., GARNIER, T., CHURCHER, C., HARRIS, D., GORDON, S., EIGLMEIER, K., GAS, S. & BARRY III, C. 1998. Deciphering the biology of Mycobacterium tuberculosis from the complete genome sequence. *Nature,* 396**,** 190-190.

CORREA-MACEDO, W., CAMBRI, G. & SCHURR, E. 2019. The interplay of human and mycobacterium tuberculosis genomic variability. *Frontiers in Genetics,* 10**,** 865.

CUTHBERTSON, L., KOS, V. & WHITFIELD, C. 2010. ABC transporters involved in export of cell surface glycoconjugates. *Microbiology and Molecular Biology Reviews,* 74**,** 341-362.

CVETNIĆ, Ž. & DUGAC, Ž. 2020. History of tuberculosis-from tuberculin to antituberculotics (Part II).
D'AMBROSIO, L., CENTIS, R., SOTGIU, G., PONTALI, E., SPANEVELLO, A. & MIGLIORI, G. B. 2015. New anti-tuberculosis drugs and regimens: 2015 update. *ERJ Open Research,* 1.
D'ANDREA, F. B., POULTON, N. C., FROOM, R., TAM, K., CAMPBELL, E. A. & ROCK, J. M. 2022. The essential M. tuberculosis Clp protease is functionally asymmetric in vivo. *Science Advances,* 8**,** eabn7943.
DAFFE, M., BRENNAN, P. J. & MCNEIL, M. 1990. Predominant structural features of the cell wall arabinogalactan of Mycobacterium tuberculosis as revealed through characterization of oligoglycosyl alditol fragments by gas chromatography/mass spectrometry and by 1H and 13C NMR analyses. *Journal of Biological Chemistry,* 265**,** 6734-6743.
DAFFÉ, M. & MARRAKCHI, H. 2019. Unraveling the structure of the mycobacterial envelope. *Microbiology spectrum,* 7**,** 10.1128/microbiolspec. gpp3-0027-2018.
DANIEL, T. M. 2006. The history of tuberculosis. *Respiratory medicine,* 100**,** 1862-1870.
DANIEL, T. M., BATES, J. H. & DOWNES, K. A. 1994. History of tuberculosis. *Tuberculosis: pathogenesis, protection, and control***,** 13-24.
DANILCHANKA, O., PAVLENOK, M. & NIEDERWEIS, M. 2008. Role of porins for uptake of antibiotics by Mycobacterium smegmatis. *Antimicrobial agents and chemotherapy,* 52**,** 3127-3134.
DARTOIS, V. A. & RUBIN, E. J. 2022. Anti-tuberculosis treatment strategies and drug development: challenges and priorities. *Nature Reviews Microbiology,* 20**,** 685-701.
DE KEIJZER, J., MULDER, A., DE HAAS, P. E., DE RU, A. H., HEERKENS, E. M., AMARAL, L., VAN SOOLINGEN, D. & VAN VEELEN, P. A. 2016. Thioridazine alters the cell-envelope permeability of Mycobacterium tuberculosis. *Journal of proteome research,* 15**,** 1776-1786.
DE WET, T. J., WINKLER, K. R., MHLANGA, M., MIZRAHI, V. & WARNER, D. F. 2020. Arrayed CRISPRi and quantitative imaging describe the morphotypic landscape of essential mycobacterial genes. *Elife,* 9**,** e60083.
DEAN, P., HEUNIS, T., HÄRTLOVA, A. & TROST, M. 2019. Regulation of phagosome functions by post-translational modifications: a new paradigm. *Current Opinion in Chemical Biology,* 48**,** 73-80.
DEJESUS, M. A., GERRICK, E. R., XU, W., PARK, S. W., LONG, J. E., BOUTTE, C. C., RUBIN, E. J., SCHNAPPINGER, D., EHRT, S. & FORTUNE, S. M. 2017. Comprehensive essentiality analysis of the Mycobacterium tuberculosis genome via saturating transposon mutagenesis. *MBio,* 8**,** 10.1128/mbio. 02133-16.
DEPAS, W. H., BERGKESSEL, M. & NEWMAN, D. K. 2019. Aggregation of nontuberculous mycobacteria is regulated by carbon-nitrogen balance. *MBio,* 10**,** 10.1128/mbio. 01715-19.
DIANIŠKOVÁ, P., KORDULÁKOVÁ, J., ŠKOVIEROVÁ, H., KAUR, D., JACKSON, M., BRENNAN, P. J. & MIKUŠOVÁ, K. 2011. Investigation of ABC transporter from mycobacterial arabinogalactan biosynthetic cluster. *General physiology and biophysics,* 30**,** 239.
DINH, M. N., HITOMI, M., AL-TURAIHI, Z. A. & SCOTT, J. G. 2023. Alamar Blue assay optimization to minimize drug interference and inter-assay viability. *Biorxiv*.
DINKELE, R., KHAN, P. Y. & WARNER, D. F. 2024. Mycobacterium tuberculosis transmission: the importance of precision. *The Lancet Infectious Diseases,* 24**,** 679-681.
DUC, N. M., LEE, H., SUH, J. W., THUY, V. T. B., MINH, N. N. & HONG, N. P. L. 2020. The high-throughput screening system for inhibitor Mycobacterium tuberculosis compounds based on ATP hydrolysis activity of recombinant protein ClpC1. *Vietnam Journal of Biotechnology,* 18**,** 239-247.
DUCRET, A., QUARDOKUS, E. M. & BRUN, Y. V. 2016. MicrobeJ, a tool for high throughput bacterial cell detection and quantitative analysis. *Nature microbiology,* 1**,** 1-7.
DULBERGER, C. L., RUBIN, E. J. & BOUTTE, C. C. 2020. The mycobacterial cell envelope—a moving target. *Nature Reviews Microbiology,* 18**,** 47-59.
ECHEVERRIA-VALENCIA, G., FLORES-VILLALVA, S. & ESPITIA, C. I. 2018. *Virulence factors and pathogenicity of Mycobacterium*, InTech Rijeka.

EHRT, S., GUO, X. V., HICKEY, C. M., RYOU, M., MONTELEONE, M., RILEY, L. W. & SCHNAPPINGER, D. 2005. Controlling gene expression in mycobacteria with anhydrotetracycline and Tet repressor. *Nucleic acids research,* 33**,** e21-e21.

ETIENNE, G., LAVAL, F., VILLENEUVE, C., DINADAYALA, P., ABOUWARDA, A., ZERBIB, D., GALAMBA, A. & DAFFE, M. 2005. The cell envelope structure and properties of Mycobacterium smegmatis mc2155: is there a clue for the unique transformability of the strain? *Microbiology,* 151**,** 2075-2086.

EVANS, J. C. & MIZRAHI, V. 2015. The application of tetracyclineregulated gene expression systems in the validation of novel drug targets in Mycobacterium tuberculosis. *Frontiers in microbiology,* 6**,** 154795.

EVANS, J. C. & MIZRAHI, V. 2018. Priming the tuberculosis drug pipeline: new antimycobacterial targets and agents. *Current opinion in microbiology,* 45**,** 39-46.

FAULKNER, V., COX, A. A., GOH, S., VAN BOHEMEN, A., GIBSON, A. J., LIEBSTER, O., WREN, B. W., WILLCOCKS, S. & KENDALL, S. L. 2021. Re-sensitization of Mycobacterium smegmatis to rifampicin using CRISPR interference demonstrates its utility for the study of non-essential drug resistance traits. *Frontiers in microbiology,* 11**,** 619427.

FISHER, J. F. & MOBASHERY, S. 2020. Constructing and deconstructing the bacterial cell wall. *Protein science,* 29**,** 629-646.

FORBES, M., KUCK, N. & PEETS, E. 1962. Mode of action of ethambutol. *Journal of bacteriology,* 84**,** 1099-1103.

FRANZBLAU, S. G., WITZIG, R. S., MCLAUGHLIN, J. C., TORRES, P., MADICO, G., HERNANDEZ, A., DEGNAN, M. T., COOK, M. B., QUENZER, V. K. & FERGUSON, R. M. 1998. Rapid, low-technology MIC determination with clinical Mycobacterium tuberculosis isolates by using the microplate Alamar Blue assay. *Journal of clinical microbiology,* 36**,** 362-366.

FUJIWARA, M., KAWASAKI, M., HARIGUCHI, N., LIU, Y. & MATSUMOTO, M. 2018. Mechanisms of resistance to delamanid, a drug for Mycobacterium tuberculosis. *Tuberculosis,* 108**,** 186-194.

GAGNEUX, S. 2012. Host–pathogen coevolution in human tuberculosis. *Philosophical Transactions of the Royal Society B: Biological Sciences,* 367**,** 850-859.

GANCHUA, S. K. C., CADENA, A. M., MAIELLO, P., GIDEON, H. P., MYERS, A. J., JUNECKO, B. F., KLEIN, E. C., LIN, P. L., MATTILA, J. T. & FLYNN, J. L. 2018. Lymph nodes are sites of prolonged bacterial persistence during Mycobacterium tuberculosis infection in macaques. *PLoS pathogens,* 14**,** e1007337.

GAO, L. Y., LAVAL, F., LAWSON, E. H., GROGER, R. K., WOODRUFF, A., MORISAKI, J. H., COX, J. S., DAFFE, M. & BROWN, E. J. 2003. Requirement for kasB in Mycobacterium mycolic acid biosynthesis, cell wall impermeability and intracellular survival: implications for therapy. *Molecular microbiology,* 49**,** 1547-1563.

GARCÍA-HEREDIA, A., POHANE, A. A., MELZER, E. S., CARR, C. R., FIOLEK, T. J., RUNDELL, S. R., LIM, H. C., WAGNER, J. C., MORITA, Y. S. & SWARTS, B. M. 2018. Peptidoglycan precursor synthesis along the sidewall of pole-growing mycobacteria. *Elife,* 7**,** e37243.

GARCIA-VILANOVA, A., CHAN, J. & TORRELLES, J. B. 2019. Underestimated manipulative roles of Mycobacterium tuberculosis cell envelope glycolipids during infection. *Frontiers in immunology,* 10**,** 2909.

GETAHUN, H., MATTEELLI, A., ABUBAKAR, I., AZIZ, M. A., BADDELEY, A., BARREIRA, D., DEN BOON, S., GUTIERREZ, S. M. B., BRUCHFELD, J. & BURHAN, E. 2015. Management of latent Mycobacterium tuberculosis infection: WHO guidelines for low tuberculosis burden countries. *European Respiratory Journal,* 46**,** 1563-1576.

GHAVAMI, S. & PANDI, A. 2021. CRISPR interference and its applications. *Progress in molecular biology and translational science,* 180**,** 123-140.

GILBERT, L. A., HORLBECK, M. A., ADAMSON, B., VILLALTA, J. E., CHEN, Y., WHITEHEAD, E. H., GUIMARAES, C., PANNING, B., PLOEGH, H. L. & BASSIK, M. C. 2014. Genome-scale CRISPR-mediated control of gene repression and activation. *Cell,* 159**,** 647-661.

GLER, M. T., SKRIPCONOKA, V., SANCHEZ-GARAVITO, E., XIAO, H., CABRERA-RIVERO, J. L., VARGAS-VASQUEZ, D. E., GAO, M., AWAD, M., PARK, S.-K. & SHIM, T. S. 2012. Delamanid for multidrug-resistant pulmonary tuberculosis. *New England Journal of Medicine,* 366**,** 2151-2160.

GLICKMAN, M. S. & JACOBS, W. R. 2001. Microbial pathogenesis of Mycobacterium tuberculosis: dawn of a discipline. *Cell,* 104**,** 477-485.

GOODEN, A. A., EVANS, C. N., SHEETS, T. P., CLAPP, M. E. & CHARI, R. 2021. dbGuide: a database of functionally validated guide RNAs for genome editing in human and mouse cells. *Nucleic Acids Research,* 49**,** D871-D876.

GRZEGORZEWICZ, A. E., DE SOUSA-D'AURIA, C., MCNEIL, M. R., HUC-CLAUSTRE, E., JONES, V., PETIT, C., KUMAR ANGALA, S., ZEMANOVÁ, J., WANG, Q. & BELARDINELLI, J. M. 2016. Assembling of the Mycobacterium tuberculosis cell wall core. *Journal of Biological Chemistry,* 291**,** 18867-18879.

GRZEGORZEWICZ, A. E., MA, Y., JONES, V., CRICK, D., LIAV, A. & MCNEIL, M. R. 2008. Development of a microtitre plate-based assay for lipid-linked glycosyltransferase products using the mycobacterial cell wall rhamnosyltransferase WbbL. *Microbiology,* 154**,** 3724-3730.

GUPTA, R. & ROHDE, K. H. 2023. Implementation of a mycobacterial CRISPRi platform in Mycobacterium abscessus and demonstration of the essentiality of ftsZMab. *Tuberculosis,* 138**,** 102292.

GUTIERREZ, M. C., BRISSE, S., BROSCH, R., FABRE, M., OMAÏS, B., MARMIESSE, M., SUPPLY, P. & VINCENT, V. 2005. Ancient origin and gene mosaicism of the progenitor of Mycobacterium tuberculosis. *PLoS pathogens,* 1**,** e5.

HANNEBELLE, M. T., VEN, J. X., TONIOLO, C., ESKANDARIAN, H. A., VUARIDEL-THURRE, G., MCKINNEY, J. D. & FANTNER, G. E. 2020. A biphasic growth model for cell pole elongation in mycobacteria. *Nature communications,* 11**,** 452.

HARDS, K., ROBSON, J. R., BERNEY, M., SHAW, L., BALD, D., KOUL, A., ANDRIES, K. & COOK, G. M. 2015. Bactericidal mode of action of bedaquiline. *Journal of Antimicrobial Chemotherapy,* 70**,** 2028-2037.

HARLING, G., EHRLICH, R. & MYER, L. 2008. The social epidemiology of tuberculosis in South Africa: a multilevel analysis. *Social science & medicine,* 66**,** 492-505.

HASHEMIAN, S. M. R., FARHADI, T. & GANJPARVAR, M. 2018. Linezolid: a review of its properties, function, and use in critical care. *Drug design, development and therapy***,** 1759-1767.

HE, Z. & DE BUCK, J. 2010. Cell wall proteome analysis of Mycobacterium smegmatis strain MC2 155. *BMC microbiology,* 10**,** 1-10.

HIDALGO-CANTABRANA, C., GOH, Y. J. & BARRANGOU, R. 2019. Characterization and repurposing of type I and type II CRISPR–Cas systems in bacteria. *Journal of molecular biology,* 431**,** 21-33.

HOUBEN, R. M. & DODD, P. J. 2016. The global burden of latent tuberculosis infection: a re-estimation using mathematical modelling. *PLoS medicine,* 13**,** e1002152.

HSU, Y.-P., RITTICHIER, J., KURU, E., YABLONOWSKI, J., PASCIAK, E., TEKKAM, S., HALL, E., MURPHY, B., LEE, T. K. & GARNER, E. C. 2017. Full color palette of fluorescent d-amino acids for in situ labeling of bacterial cell walls. *Chemical science,* 8**,** 6313-6321.

HUSZÁR, S., SINGH, V., POLČICOVÁ, A., BARÁTH, P., BARRIO, M. B., LAGRANGE, S., LEBLANC, V., NACY, C. A., MIZRAHI, V. & MIKUŠOVÁ, K. 2017. N-acetylglucosamine-1-phosphate transferase, WecA, as a validated drug target in Mycobacterium tuberculosis. *Antimicrobial agents and chemotherapy,* 61**,** 10.1128/aac. 01310-17.

IOERGER, T. R., FENG, Y., GANESULA, K., CHEN, X., DOBOS, K. M., FORTUNE, S., JACOBS JR, W. R., MIZRAHI, V., PARISH, T. & RUBIN, E. 2010. Variation among genome sequences of H37Rv

strains of Mycobacterium tuberculosis from multiple laboratories. *Journal of bacteriology,* 192**,** 3645-3653.
ISEMAN, M. 2002. Tuberculosis therapy: past, present and future. *European Respiratory Journal,* 20**,** 87S-94s.
ISHIZAKI, Y., HAYASHI, C., INOUE, K., IGARASHI, M., TAKAHASHI, Y., PUJARI, V., CRICK, D. C., BRENNAN, P. J. & NOMOTO, A. 2013. Inhibition of the first step in synthesis of the mycobacterial cell wall core, catalyzed by the GlcNAc-1-phosphate transferase WecA, by the novel caprazamycin derivative CPZEN-45. *Journal of Biological Chemistry,* 288**,** 30309-30319.
JABIR, R. A., RUKMANA, A., SALEH, I. & KURNIAWATI, T. 2018. The existence of Mycobacterium tuberculosis in microenvironment of bone. *Mycobacterium Res. Dev*.
JACKSON, M., STEVENS, C. M., ZHANG, L., ZGURSKAYA, H. I. & NIEDERWEIS, M. 2020. Transporters involved in the biogenesis and functionalization of the mycobacterial cell envelope. *Chemical reviews,* 121**,** 5124-5157.
JIANG, X. & KOPP-SCHNEIDER, A. 2014. Summarizing EC50 estimates from multiple dose-response experiments: A comparison of a meta-analysis strategy to a mixed-effects model approach. *Biometrical Journal,* 56**,** 493-512.
JUSTEN, A. M., HODGES, H. L., KIM, L. M., SADECKI, P. W., PORFIRIO, S., ULTEE, E., BLACK, I., CHUNG, G. S., BRIEGEL, A. & AZADI, P. 2020. Polysaccharide length affects mycobacterial cell shape and antibiotic susceptibility. *Science Advances,* 6**,** eaba4015.
KAMARIZA, M., SHIEH, P., EALAND, C. S., PETERS, J. S., CHU, B., RODRIGUEZ-RIVERA, F. P., BABU SAIT, M. R., TREUREN, W. V., MARTINSON, N. & KALSCHEUER, R. 2018. Rapid detection of Mycobacterium tuberculosis in sputum with a solvatochromic trehalose probe. *Science translational medicine,* 10**,** eaam6310.
KAMARIZA, M., SHIEH, P., RODRIGUEZ-RIVERA, F. P., EALAND, C. S., CHU, B., MARTINSON, N., KANA, B. D. & BERTOZZI, C. R. 2017. Detection of live mycobacteria with a solvatochromic trehalose probe for point-of-care tuberculosis diagnosis. *bioRxiv***,** 171553.
KAPOPOULOU, A., LEW, J. M. & COLE, S. T. 2011. The MycoBrowser portal: a comprehensive and manually annotated resource for mycobacterial genomes. *Tuberculosis,* 91**,** 8-13.
KESTER, J. C., KANDROR, O., AKOPIAN, T., CHASE, M. R., ZHU, J., RUBIN, E. J., GOLDBERG, A. L. & FORTUNE, S. M. 2021. ClpX is essential and activated by single-strand DNA binding protein in mycobacteria. *Journal of Bacteriology,* 203**,** 10.1128/jb. 00608-20.
KHABIBULLINA, N. F., KUTUZOVA, D. M., BURMISTROVA, I. A. & LYADOVA, I. V. 2022. The biological and clinical aspects of a latent tuberculosis infection. *Tropical Medicine and Infectious Disease,* 7**,** 48.
KHAWBUNG, J. L., NATH, D. & CHAKRABORTY, S. 2021. Drug resistant Tuberculosis: A review. *Comparative immunology, microbiology and infectious diseases,* 74**,** 101574.
KHOO, K.-H., DOUGLAS, E., AZADI, P., INAMINE, J. M., BESRA, G. S., MIKUŠOVÁ, K., BRENNAN, P. J. & CHATTERJEE, D. 1996. Truncated structural variants of lipoarabinomannan in ethambutol drug-resistant strains of Mycobacterium smegmatis: inhibition of arabinan biosynthesis by ethambutol. *Journal of Biological Chemistry,* 271**,** 28682-28690.
KIAZYK, S. & BALL, T. 2017. Tuberculosis (TB): Latent tuberculosis infection: An overview. *Canada Communicable Disease Report,* 43**,** 62.
KLING, A., LUKAT, P., ALMEIDA, D. V., BAUER, A., FONTAINE, E., SORDELLO, S., ZABURANNYI, N., HERRMANN, J., WENZEL, S. C. & KÖNIG, C. 2015. Targeting DnaN for tuberculosis therapy using novel griselimycins. *Science,* 348**,** 1106-1112.
KONYARIKOVÁ, Z., SAVKOVÁ, K., KOZMON, S. & MIKUŠOVÁ, K. 2020. Biosynthesis of galactan in Mycobacterium tuberculosis as a viable TB drug target? *Antibiotics,* 9**,** 20.
KORB, V. C., CHUTURGOON, A. A. & MOODLEY, D. 2016. Mycobacterium tuberculosis: manipulator of protective immunity. *International journal of molecular sciences,* 17**,** 131.

KOUL, A., DENDOUGA, N., VERGAUWEN, K., MOLENBERGHS, B., VRANCKX, L., WILLEBRORDS, R., RISTIC, Z., LILL, H., DORANGE, I. & GUILLEMONT, J. 2007. Diarylquinolines target subunit c of mycobacterial ATP synthase. *Nature chemical biology,* 3**,** 323-324.

KOWALSKA-KROCHMAL, B. & DUDEK-WICHER, R. 2021. The minimum inhibitory concentration of antibiotics: Methods, interpretation, clinical relevance. *Pathogens,* 10**,** 165.

LAI, Y., BABUNOVIC, G. H., CUI, L., DEDON, P. C., DOENCH, J. G., FORTUNE, S. M. & LU, T. K. 2020. Illuminating host-mycobacterial interactions with genome-wide CRISPR knockout and CRISPRi screens. *Cell systems,* 11**,** 239-251. e7.

LAMBERT, P. 2002. Cellular impermeability and uptake of biocides and antibiotics in Gram-positive bacteria and mycobacteria. *Journal of applied microbiology,* 92**,** 46S-54S.

LARSON, M. H., GILBERT, L. A., WANG, X., LIM, W. A., WEISSMAN, J. S. & QI, L. S. 2013. CRISPR interference (CRISPRi) for sequence-specific control of gene expression. *Nature protocols,* 8**,** 2180-2196.

LECHNER, D., GIBBONS, S. & BUCAR, F. 2008. Modulation of isoniazid susceptibility by flavonoids in Mycobacterium. *Phytochemistry Letters,* 1**,** 71-75.

LEE, C.-Y., HUANG, C.-H., LU, P.-L., KO, W.-C., CHEN, Y.-H. & HSUEH, P.-R. 2017. Role of rifampin for the treatment of bacterial infections other than mycobacteriosis. *Journal of Infection,* 75**,** 395-408.

LEE, N., PATEL, P. & NGUYEN, H. 2024. Ethambutol. *StatPearls [Internet].* StatPearls Publishing.

LEE, S. H. 2016. Tuberculosis infection and latent tuberculosis. *Tuberculosis and respiratory diseases,* 79**,** 201-206.

LEMASSU, A., ORTALO-MAGNE, A., BARDOU, F., SILVE, G., LANÉELLE, M.-A. & DAFFÉ, M. 1996. Extracellular and surface-exposed polysaccharides of non-tuberculous mycobacteria. *Microbiology,* 142**,** 1513-1520.

LI, M., KANDROR, O., AKOPIAN, T., DHARKAR, P., WLODAWER, A., MAURIZI, M. R. & GOLDBERG, A. L. 2016. Structure and functional properties of the active form of the proteolytic complex, ClpP1P2, from Mycobacterium tuberculosis. *Journal of Biological Chemistry,* 291**,** 7465-7476.

LI, S., POULTON, N. C., CHANG, J. S., AZADIAN, Z. A., DEJESUS, M. A., RUECKER, N., ZIMMERMAN, M. D., ECKARTT, K., BOSCH, B. & ENGELHART, C. 2021. A chemical-genetic map of the pathways controlling drug potency in Mycobacterium tuberculosis. *BioRxiv***,** 2021.11. 27.469863.

LI, S., POULTON, N. C., CHANG, J. S., AZADIAN, Z. A., DEJESUS, M. A., RUECKER, N., ZIMMERMAN, M. D., ECKARTT, K. A., BOSCH, B. & ENGELHART, C. A. 2022. CRISPRi chemical genetics and comparative genomics identify genes mediating drug potency in Mycobacterium tuberculosis. *Nature microbiology,* 7**,** 766-779.

LIU, B.-G., YUAN, X.-L., HE, D.-D., HU, G.-Z., MIAO, M.-S. & XU, E.-P. 2020. Research progress on the oxazolidinone drug linezolid resistance. *European Review for Medical & Pharmacological Sciences,* 24.

MÅLEN, H., DE SOUZA, G. A., PATHAK, S., SØFTELAND, T. & WIKER, H. G. 2011. Comparison of membrane proteins of Mycobacterium tuberculosis H37Rv and H37Ra strains. *BMC microbiology,* 11**,** 1-10.

MCNEIL, M. B., KEIGHLEY, L. M., COOK, J. R., CHEUNG, C. Y. & COOK, G. M. 2021. CRISPR interference identifies vulnerable cellular pathways with bactericidal phenotypes in Mycobacterium tuberculosis. *Molecular microbiology,* 116**,** 1033-1043.

MELLY, G. & PURDY, G. E. 2019. MmpL proteins in physiology and pathogenesis of M. tuberculosis. *Microorganisms,* 7**,** 70.

MEYER, F. M. & BRAMKAMP, M. 2024. Cell wall synthesizing complexes in Mycobacteriales. *Current Opinion in Microbiology,* 79**,** 102478.

MIKUSOVÁ, K., MIKUS, M., BESRA, G. S., HANCOCK, I. & BRENNAN, P. J. 1996. Biosynthesis of the Linkage Region of the Mycobacterial Cell Wall (∗). *Journal of Biological Chemistry,* 271**,** 7820-7828.

MIKUŠOVÁ, K. N., YAGI, T., STERN, R., MCNEIL, M. R., BESRA, G. S., CRICK, D. C. & BRENNAN, P. J. 2000. Biosynthesis of the galactan component of the mycobacterial cell wall. *Journal of Biological Chemistry,* 275**,** 33890-33897.

MOSAEI, H. & ZENKIN, N. 2020. Inhibition of RNA polymerase by rifampicin and rifamycin-like molecules. *EcoSal Plus,* 9**,** 10.1128/ecosalplus. ESP-0017-2019.

MOUTON, J. W., MULLER, A. E., CANTON, R., GISKE, C. G., KAHLMETER, G. & TURNIDGE, J. 2018. MIC-based dose adjustment: facts and fables. *Journal of Antimicrobial Chemotherapy,* 73**,** 564-568.

MURRAY, J. F., SCHRAUFNAGEL, D. E. & HOPEWELL, P. C. 2015. Treatment of tuberculosis. A historical perspective. *Annals of the American Thoracic Society,* 12**,** 1749-1759.

NGUYEN, T. V. A., ANTHONY, R. M., CAO, T. T. H., BAÑULS, A.-L., NGUYEN, V. A. T., VU, D. H., NGUYEN, N. V. & ALFFENAAR, J.-W. C. 2020. Delamanid resistance: update and clinical management. *Clinical Infectious Diseases,* 71**,** 3252-3259.

NIEDERWEIS, M. 2003. Mycobacterial porins–new channel proteins in unique outer membranes. *Molecular microbiology,* 49**,** 1167-1177.

NOEL, Z. A., WANG, J. & CHILVERS, M. I. 2018. Significant influence of EC50 estimation by model choice and EC50 type. *Plant Disease,* 102**,** 708-714.

ORGEUR, M., SOUS, C., MADACKI, J. & BROSCH, R. 2024. Evolution and emergence of Mycobacterium tuberculosis. *FEMS Microbiology Reviews,* 48**,** fuae006.

ORTALO-MAGNE, A., DUPONT, M.-A., LEMASSU, A., ANDERSEN, A. B., GOUNON, P. & MAMADOU, D. 1995. Molecular composition of the outermost capsular material of the tubercle bacillus. *Microbiology,* 141**,** 1609-1620.

OUATTARA, C. A., PODA, A. G., MÉDA, Z. C., SAWADOGO, Y., KABORE, O., BIRBA, E., SOURABIÉ, A., ZOUNGRANA, J., TRAORE, I. T. & SANGARÉ, I. 2023. Evaluation of the impact of COVID-19 in people coinfected with HIV and/or tuberculosis in low-income countries: study protocol for mixed methods research in Burkina Faso. *BMC Infectious Diseases,* 23**,** 1-8.

PAI, M., BEHR, M., DOWDY, D., DHEDA, K., DIVANGAHI, M., BOEHME, C., GINSBERG, A., SWAMINATHAN, S., SPIGELMAN, M. & GETAHUN, H. 2016. Tuberculosis Nat Rev Dis Primers, 2 (2016). *View in Scopus***,** 16076.

PANG, Y., ZONG, Z., HUO, F., JING, W., MA, Y., DONG, L., LI, Y., ZHAO, L., FU, Y. & HUANG, H. 2017. In vitro drug susceptibility of bedaquiline, delamanid, linezolid, clofazimine, moxifloxacin, and gatifloxacin against extensively drug-resistant tuberculosis in Beijing, China. *Antimicrobial agents and chemotherapy,* 61**,** 10.1128/aac. 00900-17.

PARISH, T. & STOKER, N. G. 1998. *Mycobacteria protocols*, Springer.

PASQUINA-LEMONCHE, L., BURNS, J., TURNER, R., KUMAR, S., TANK, R., MULLIN, N., WILSON, J., CHAKRABARTI, B., BULLOUGH, P. & FOSTER, S. 2020. The architecture of the Gram-positive bacterial cell wall. *Nature,* 582**,** 294-297.

PATEL, B., RYAN, P., MAKWANA, V., ZUNK, M., RUDRAWAR, S. & GRANT, G. 2019. Caprazamycins: Promising lead structures acting on a novel antibacterial target MraY. *European Journal of Medicinal Chemistry,* 171**,** 462-474.

PATEL, S., PREUSS, C. V. & BERNICE, F. 2017. Vancomycin.

PATIL, K., BAGADE, S., BONDE, S., SHARMA, S. & SARAOGI, G. 2018. Recent therapeutic approaches for the management of tuberculosis: Challenges and opportunities. *Biomedicine & pharmacotherapy,* 99**,** 735-745.

PELOQUIN, C. A. & DAVIES, G. R. 2021. The treatment of tuberculosis. *Clinical Pharmacology & Therapeutics,* 110**,** 1455-1466.

PERKEL, J. M. 2020. The software that powers scientific illustration. *Nature,* 582**,** 137-139.

PERRIN, P. 2015. Human and tuberculosis co-evolution: An integrative view. *Tuberculosis,* 95**,** S112-S116.

PETERS, J. M., COLAVIN, A., SHI, H., CZARNY, T. L., LARSON, M. H., WONG, S., HAWKINS, J. S., LU, C. H., KOO, B.-M. & MARTA, E. 2016. A comprehensive, CRISPR-based functional analysis of essential genes in bacteria. *Cell,* 165**,** 1493-1506.

PORANKIEWICZ, J., WANG, J. & CLARKE, A. K. 1999. New insights into the ATP-dependent Clp protease: Escherichia coli and beyond. *Molecular microbiology,* 32**,** 449-458.

POULIN, M. B. & LOWARY, T. L. 2016. Chemical insight into the mechanism and specificity of GlfT2, a bifunctional galactofuranosyltransferase from mycobacteria. *The Journal of Organic Chemistry,* 81**,** 8123-8130.

POULTON, N. C. & ROCK, J. M. 2022. Unraveling the mechanisms of intrinsic drug resistance in Mycobacterium tuberculosis. *Frontiers in cellular and infection microbiology,* 12**,** 997283.

PRABHU, R. & SINGH, V. 2019. The history of tuberculosis: past, present, and future. *Advances in Microbiology,* 9**,** 931-942.

QI, L. S., LARSON, M. H., GILBERT, L. A., DOUDNA, J. A., WEISSMAN, J. S., ARKIN, A. P. & LIM, W. A. 2013. Repurposing CRISPR as an RNA-guided platform for sequence-specific control of gene expression. *Cell,* 152**,** 1173-1183.

QUIGLEY, J., HUGHITT, V. K., VELIKOVSKY, C. A., MARIUZZA, R. A., EL-SAYED, N. M. & BRIKEN, V. 2017. The cell wall lipid PDIM contributes to phagosomal escape and host cell exit of Mycobacterium tuberculosis. *MBio,* 8**,** 10.1128/mbio. 00148-17.

RAJU, R. M., UNNIKRISHNAN, M., RUBIN, D. H., KRISHNAMOORTHY, V., KANDROR, O., AKOPIAN, T. N., GOLDBERG, A. L. & RUBIN, E. J. 2012. Mycobacterium tuberculosis ClpP1 and ClpP2 function together in protein degradation and are required for viability in vitro and during infection. *PLoS pathogens,* 8**,** e1002511.

RAMACHANDRAN, G. & SWAMINATHAN, S. 2015. Safety and tolerability profile of second-line anti-tuberculosis medications. *Drug safety,* 38**,** 253-269.

RANJITHA, J., RAJAN, A. & SHANKAR, V. 2020. Features of the biochemistry of Mycobacterium smegmatis, as a possible model for Mycobacterium tuberculosis. *Journal of infection and public health,* 13**,** 1255-1264.

RAO, M., IPPOLITO, G., MFINANGA, S., NTOUMI, F., YEBOAH-MANU, D., VILAPLANA, C., ZUMLA, A. & MAEURER, M. 2019. Latent TB Infection (LTBI)–Mycobacterium tuberculosis pathogenesis and the dynamics of the granuloma battleground. *International journal of infectious diseases,* 80**,** S58-S61.

RAPHELA, M. L. 2020. Targeted depletion of RibF, a putative bifunctional FAD synthetase/flavokinase in Mycobacterium smegmatis using CRISPR interference.

RASTOGI, N., LEGRAND, E. & SOLA, C. 2001. The mycobacteria: an introduction to nomenclature and pathogenesis. *Revue Scientifique Et Technique-Office International Des Epizooties,* 20**,** 21-54.

RENZETTE, N. 2011. Generation of transformation competent E. coli. *Current Protocols in Microbiology,* 22**,** A. 3L. 1-A. 3L. 5.

ROCHA, D. M., VIVEIROS, M., SARAIVA, M. & OSÓRIO, N. S. 2021. The neglected contribution of streptomycin to the tuberculosis drug resistance problem. *Genes,* 12**,** 2003.

ROCK, J. M., HOPKINS, F. F., CHAVEZ, A., DIALLO, M., CHASE, M. R., GERRICK, E. R., PRITCHARD, J. R., CHURCH, G. M., RUBIN, E. J. & SASSETTI, C. M. 2017. Programmable transcriptional repression in mycobacteria using an orthogonal CRISPR interference platform. *Nature microbiology,* 2**,** 1-9.

RODRIGUES, L., RAMOS, J., COUTO, I., AMARAL, L. & VIVEIROS, M. 2011. Ethidium bromide transport across Mycobacterium smegmatis cell-wall: correlation with antibiotic resistance. *BMC microbiology,* 11**,** 1-10.

ROMBOUTS, Y., BRUST, B., OJHA, A. K., MAES, E., CODDEVILLE, B., ELASS-ROCHARD, E., KREMER, L. & GUERARDEL, Y. 2012. Exposure of mycobacteria to cell wall-inhibitory drugs decreases production of arabinoglycerolipid related to mycolyl-arabinogalactan-peptidoglycan metabolism. *Journal of Biological Chemistry,* 287**,** 11060-11069.

SAHILE, H. A., RENS, C., SHAPIRA, T., ANDERSEN, R. J. & AV-GAY, Y. 2020. DMN-Tre labeling for detection and high-content screening of compounds against intracellular mycobacteria. *ACS omega,* 5**,** 3661-3669.
SAMBROOK, J. 1989. Molecular cloning: a laboratory manual. *Cold Spring Habor Laboratory*.
SAVKOVÁ, K., HUSZÁR, S., BARÁTH, P., PAKANOVÁ, Z., KOZMON, S., VANCOVÁ, M., TESAŘOVÁ, M., BLAŠKO, J., KALIŇÁK, M. & SINGH, V. 2021. An ABC transporter Wzm–Wzt catalyzes translocation of lipid-linked galactan across the plasma membrane in mycobacteria. *Proceedings of the National Academy of Sciences,* 118**,** e2023663118.
SCHINDELIN, J., ARGANDA-CARRERAS, I., FRISE, E., KAYNIG, V., LONGAIR, M., PIETZSCH, T., PREIBISCH, S., RUEDEN, C., SAALFELD, S. & SCHMID, B. 2012. Fiji: an open-source platform for biological-image analysis. *Nature methods,* 9**,** 676-682.
SCHUBERT, K., SIEGER, B., MEYER, F., GIACOMELLI, G., BÖHM, K., RIEBLINGER, A., LINDENTHAL, L., SACHS, N., WANNER, G. & BRAMKAMP, M. 2017. The antituberculosis drug ethambutol selectively blocks apical growth in CMN group bacteria. *MBio,* 8**,** 10.1128/mbio. 02213-16.
SEBAUGH, J. 2011. Guidelines for accurate EC50/IC50 estimation. *Pharmaceutical statistics,* 10**,** 128-134.
SHEN, L., VILJOEN, A., VILLAUME, S., JOE, M., HALLOUM, I., CHÊNE, L., MÉRY, A., FABRE, E., TAKEGAWA, K. & LOWARY, T. L. 2020. The endogenous galactofuranosidase GlfH1 hydrolyzes mycobacterial arabinogalactan. *Journal of Biological Chemistry,* 295**,** 5110-5123.
SHIVANANDAN, A., RADENOVIC, A. & SBALZARINI, I. F. 2013. MosaicIA: an ImageJ/Fiji plugin for spatial pattern and interaction analysis. *BMC bioinformatics,* 14**,** 1-10.
SILVEIRO, C., MARQUES, M., OLIVENÇA, F., PIRES, D., MORTINHO, D., NUNES, A., PIMENTEL, M., ANES, E. & CATALÃO, M. J. 2023. CRISPRi-mediated characterization of novel anti-tuberculosis targets: Mycobacterial peptidoglycan modifications promote beta-lactam resistance and intracellular survival. *Frontiers in Cellular and Infection Microbiology,* 13**,** 1089911.
SINGH, A. K., CARETTE, X., POTLURI, L.-P., SHARP, J. D., XU, R., PRISIC, S. & HUSSON, R. N. 2016. Investigating essential gene function in Mycobacterium tuberculosis using an efficient CRISPR interference system. *Nucleic acids research,* 44**,** e143-e143.
SINGH, V. & CHIBALE, K. 2021. Strategies to combat multi-drug resistance in tuberculosis. *Accounts of chemical research,* 54**,** 2361-2376.
SNAPPER, S., MELTON, R., MUSTAFA, S., KIESER, T. & JR, W. J. 1990. Isolation and characterization of efficient plasmid transformation mutants of Mycobacterium smegmatis. *Molecular microbiology,* 4**,** 1911-1919.
SOETAERT, K., RENS, C., WANG, X.-M., DE BRUYN, J., LANÉELLE, M.-A., LAVAL, F., LEMASSU, A., DAFFÉ, M., BIFANI, P. & FONTAINE, V. 2015. Increased vancomycin susceptibility in mycobacteria: a new approach to identify synergistic activity against multidrug-resistant mycobacteria. *Antimicrobial Agents and Chemotherapy,* 59**,** 5057-5060.
SOMOSKOVI, A., BRUDERER, V., HÖMKE, R., BLOEMBERG, G. V. & BÖTTGER, E. C. 2015. A mutation associated with clofazimine and bedaquiline cross-resistance in MDR-TB following bedaquiline treatment. *European Respiratory Journal,* 45**,** 554-557.
SPARKS, I. L., DERBYSHIRE, K. M., JACOBS JR, W. R. & MORITA, Y. S. 2023. Mycobacterium smegmatis: the vanguard of mycobacterial research. *Journal of bacteriology,* 205**,** e00337-22.
STEPHAN, J., MAILAENDER, C., ETIENNE, G., DAFFÉ, M. & NIEDERWEIS, M. 2004. Multidrug resistance of a porin deletion mutant of Mycobacterium smegmatis. *Antimicrobial agents and chemotherapy,* 48**,** 4163-4170.
STOGIOS, P. J. & SAVCHENKO, A. 2020. Molecular mechanisms of vancomycin resistance. *Protein Science,* 29**,** 654-669.
SUNDARARAJAN, S. & MUNIYAN, R. 2021. Latent tuberculosis: interaction of virulence factors in Mycobacterium tuberculosis. *Molecular Biology Reports,* 48**,** 6181-6196.

SUTCLIFFE, I. C. 2010. A phylum level perspective on bacterial cell envelope architecture. *Trends in microbiology,* 18**,** 464-470.
TELENTI, A., PHILIPP, W. J., SREEVATSAN, S., BERNASCONI, C., STOCKBAUER, K. E., WIELES, B., MUSSER, J. M. & JACOBS JR, W. R. 1997. The emb operon, a gene cluster of Mycobacterium tuberculosis involved in resistance to ethambutol. *Nature medicine,* 3**,** 567-570.
TIBERI, S., MUÑOZ-TORRICO, M., DUARTE, R., DALCOLMO, M., D'AMBROSIO, L. & MIGLIORI, G.-B. 2018. New drugs and perspectives for new anti-tuberculosis regimens. *Pulmonology,* 24**,** 86-98.
TIBERI, S., UTJESANOVIC, N., GALVIN, J., CENTIS, R., D'AMBROSIO, L., VAN DEN BOOM, M., ZUMLA, A. & MIGLIORI, G. B. 2022. Drug resistant TB–latest developments in epidemiology, diagnostics and management. *International Journal of Infectious Diseases,* 124**,** S20-S25.
TIMMINS, G. S. & DERETIC, V. 2006. Mechanisms of action of isoniazid. *Molecular microbiology,* 62**,** 1220-1227.
UHÍA, I., WILLIAMS, K. J., SHAHREZAEI, V. & ROBERTSON, B. D. 2015. Mycobacterial growth. *Cold Spring Harbor Perspectives in Medicine,* 5**,** a021097.
UNICEF 2021. The state of food security and nutrition in the world 2021.
UREN, C., HOAL, E. G. & MÖLLER, M. 2021. Mycobacterium tuberculosis complex and human coadaptation: a two-way street complicating host susceptibility to TB. *Human Molecular Genetics,* 30**,** R146-R153.
VERMA, R., PINTO, S. M., PATIL, A. H., ADVANI, J., SUBBA, P., KUMAR, M., SHARMA, J., DEY, G., RAVIKUMAR, R. & BUGGI, S. 2017. Quantitative proteomic and phosphoproteomic analysis of H37Ra and H37Rv strains of Mycobacterium tuberculosis. *Journal of Proteome Research,* 16**,** 1632-1645.
VINCENT, A. T., NYONGESA, S., MORNEAU, I., REED, M. B., TOCHEVA, E. I. & VEYRIER, F. J. 2018. The mycobacterial cell envelope: a relict from the past or the result of recent evolution? *Frontiers in microbiology,* 9**,** 2341.
WALLACE JR, R., BROWN-ELLIOTT, B., WARD, S., CRIST, C., MANN, L. & WILSON, R. 2001. Activities of linezolid against rapidly growing mycobacteria. *Antimicrobial agents and chemotherapy,* 45**,** 764-767.
WELIN, A., WINBERG, M. E., ABDALLA, H., SÄRNDAHL, E., RASMUSSON, B., STENDAHL, O. & LERM, M. 2008. Incorporation of Mycobacterium tuberculosis lipoarabinomannan into macrophage membrane rafts is a prerequisite for the phagosomal maturation block. *Infection and immunity,* 76**,** 2882-2887.
WESTON, A., STERN, R., LEE, R., NASSAU, P., MONSEY, D., MARTIN, S., SCHERMAN, M., BESRA, G., DUNCAN, K. & MCNEIL, M. 1998. Biosynthetic origin of mycobacterial cell wall galactofuranosyl residues. *Tubercle and Lung Disease,* 78**,** 123-131.
WHO 2023. *Global tuberculosis report 2023*, WHO.
WILHELM, M. P. Vancomycin. Mayo Clinic Proceedings, 1991. Elsevier, 1165-1170.
WON, E.-J., CHOI, J.-H., CHO, Y.-N., JIN, H.-M., KEE, H. J., PARK, Y.-W., KWON, Y.-S. & KEE, S.-J. 2017. Biomarkers for discrimination between latent tuberculosis infection and active tuberculosis disease. *Journal of Infection,* 74**,** 281-293.
WRIGHT, A. V., NUÑEZ, J. K. & DOUDNA, J. A. 2016. Biology and applications of CRISPR systems: harnessing nature's toolbox for genome engineering. *Cell,* 164**,** 29-44.
XIAO, J., JIA, H., PAN, L., LI, Z., LV, L., DU, B., ZHANG, L., DU, F., HUANG, Y. & CAO, T. 2019. Application of the CRISPRi system to repress sepF expression in Mycobacterium smegmatis. *Infection, Genetics and Evolution,* 72**,** 183-190.
YANG, Y., ZHAO, N., XU, X., ZHOU, Y., LUO, B., ZHANG, J., SUI, J., HUANG, J., QIU, Z. & ZHANG, X. 2023. Discovery and mechanistic study of novel Mycobacterium tuberculosis ClpP1P2 inhibitors. *Journal of Medicinal Chemistry,* 66**,** 16597-16614.

ZHAI, W., WU, F., ZHANG, Y., FU, Y. & LIU, Z. 2019. The immune escape mechanisms of Mycobacterium tuberculosis. *International journal of molecular sciences,* 20**,** 340.
ZHANG, C. & MANLEY, S. 2023. Super-Resolution Microscopy of the Bacterial Cell Wall Labeled by Fluorescent D-Amino Acids. *The Bacterial Cell Wall: Methods and Protocols.* Springer.
ZHANG, L., ZHAO, Y., GAO, Y., WU, L., GAO, R., ZHANG, Q., WANG, Y., WU, C., WU, F. & GURCHA, S. S. 2020. Structures of cell wall arabinosyltransferases with the anti-tuberculosis drug ethambutol. *Science,* 368**,** 1211-1219.
ZHANG, Q.-A., MA, S., LI, P. & XIE, J. 2023. The dynamics of Mycobacterium tuberculosis phagosome and the fate of infection. *Cellular Signalling,* 108**,** 110715.
ZHANG, R., XU, W., SHAO, S. & WANG, Q. 2021. Gene silencing through CRISPR interference in bacteria: current advances and future prospects. *Frontiers in Microbiology,* 12**,** 635227.
ZHAO, C., SHU, X. & SUN, B. 2017. Construction of a gene knockdown system based on catalytically inactive ("dead") Cas9 (dCas9) in Staphylococcus aureus. *Applied and environmental microbiology,* 83**,** e00291-17.
ZHENG, H., LU, L., WANG, B., PU, S., ZHANG, X., ZHU, G., SHI, W., ZHANG, L., WANG, H. & WANG, S. 2008. Genetic basis of virulence attenuation revealed by comparative genomic analysis of Mycobacterium tuberculosis strain H37Ra versus H37Rv. *PloS one,* 3**,** e2375.
ZHU, C., LIU, Y., HU, L., YANG, M. & HE, Z.-G. 2018. Molecular mechanism of the synergistic activity of ethambutol and isoniazid against Mycobacterium tuberculosis. *Journal of Biological Chemistry,* 293**,** 16741-16750.
ZINK, A. R., SOLA, C., REISCHL, U., GRABNER, W., RASTOGI, N., WOLF, H. & NERLICH, A. G. 2003. Characterization of Mycobacterium tuberculosis complex DNAs from Egyptian mummies by spoligotyping. *Journal of clinical microbiology,* 41**,** 359-367.
ZUMLA, A., ABUBAKAR, I., RAVIGLIONE, M., HOELSCHER, M., DITIU, L., MCHUGH, T. D., SQUIRE, S. B., COX, H., FORD, N. & MCNERNEY, R. 2012. Drug-resistant tuberculosis—current dilemmas, unanswered questions, challenges, and priority needs. *Journal of Infectious Diseases,* 205**,** S228-S240.

Acknowledgements

First and foremost, I'd like to thank the **Lord Almighty** for granting me the opportunity to pursue my master's degree and giving me the mental and physical capabilities to get this far.

I would like to thank the **National Research Foundation (NRF)** for the financial assistance throughout the course of my degree.

To my supervisor, **Dr. Mandy Mason**, I would like to express my gratitude for the opportunity to pursue my degree alongside you, and for the patience and support that you have offered me. I have learned a lot over the course of my degree, and I am grateful to you for it.

Thank you to **Dr. Melisa Chengalroyen** and **Lucas Raphela** for providing me with control strains. I am grateful for your generosity.

Thank you to **Dharanidharan Ramamurthy** for taking time out to help by offering training in the attenuated hood. You have been a great help.

I would like to extend my thanks to **Audrey Jordaan** for being a friend to confide in during times of confusion and when times felt overwhelming.

Lastly, thank you to **Prof. Valerie Mizrahi, Prof. Digby Warner** and the rest of the **Molecular Mycobacteriology Research Unit (MMRU)** for being so welcoming and allowing me the opportunity to learn from all of you, and for the insightful meetings.

Chapter 7: Supplementary data

7.1. Generation of CRISPRi constructs

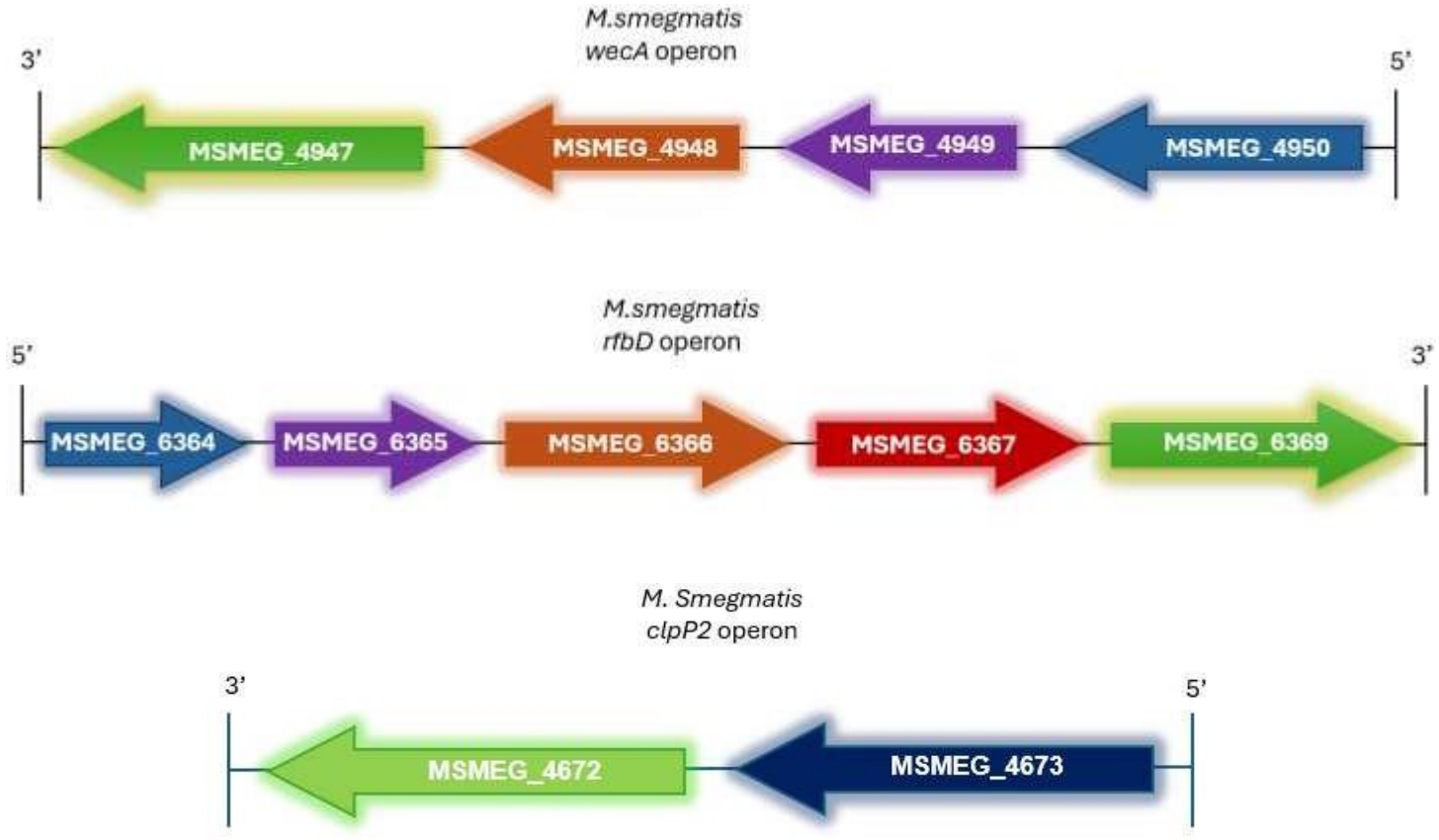

Figure S1. Representation of the genomic organisation genes relative to *Msm wecA* (MSMEG_4947), *Msm rfbD* (MSMEG_6369) and *Msm clpP2* (MSMEG_4672) showing the order of each gene and their operonic regions. Green genes represent the target gene. *Mtb wecA* gene is not part of an operon. *Adapted from Mycobrowser.*

Table S1. Key Resources Table

REAGENT or RESOURCE	SOURCE	IDENTIFIER
Bacterial strains		
Escherichia coli DH5α	Thermofisher Scientific	Cat#18265017
Mycobacterium smegmatis mc^2155	(Snapper et al., 1990)	N/A
Mycobacterium tuberculosis H37Ra	*Mycobacterium tuberculosis* (Zopf) Lehmann and Neumann American Type Culture Collection (ATCC)	ATCC 25177
Mycobacterium tuberculosis H37Rv	H37Ra MA. A gift from Dr Chris Ssseti, UMass Chan Medical School, USA (Ioerger et al., 2010)	ATCC 2729
Biological samples		
Chemicals and proteins		
Rifampicin, Antibiotic agent	Sigma-Aldrich (Merck)	Cat# R3501-25G
Ethambutol, Antibiotic agent	Sigma-Aldrich (Merck)	Cat# E4630-25G
Vancomycin, Antibiotic agent	Sigma-Aldrich (Merck)	Cat# V34850
Linezolid, Antibiotic agent	Biotechnology Hub Africa	Cat# HY-10394
Kanamycin, Antibiotic agent	Sigma-Aldrich (Merck)	Cat# K1377-5G
DMN-Tre fluorescent probe	Olilux Biosciences, INC	Cat# DMN-010
RADA fluorescent probe	Whitehead Scientific (Pty) Ltd.	Cat# 6649/5
ATc	Sigma-Aldrich (Merck)	Cat# 37919-100MG-R
Alamar Blue/Resazurin	Celtic Molecular Diagnostics (Pty)Ltd	Cat# BUF012B
Enzymes		
BSmBI-v2 enzyme	New England Biolabs (NEB)	Cat# R0580
Quick-ligase enzyme	Inqaba biotec	Cat# NEB M2200S
Media and supplements		
LB media	Sigma-Aldrich (Merck)	Cat# L2897-1KG
LB agar	Sigma-Aldrich (Merck)	Cat# L2897-1KG
7H9	BD DIFCO™	Cat# 271310
7H10	BD DIFCO™	Cat# 262710
Glycerol	Sigma-Aldrich (Merck)	Cat# G5516-500ML
Tween80	Sigma-Aldrich (Merck)	Cat# P4780-500ML
OADC	BD DIFCO™	Cat# 212240
Commercial assays		
Zyppy™ Plasmid MiniPrep Kit	Inqaba Biotech	Cat# ZR D4037
NucleoSpin® Gel and PCR Clean-up kit	Sigma Aldrich	Item# 750 609.50
Oligonucleotides		
See Table 3.1, 3.2 and 3.3 for information on primers and other oligonucleotides used in this study	Inqaba Biotech	Cat# IB OL0001
Recombinant plasmid DNA		
plRL117	Addgene (Rock et al., 2017)	Plasmid# 163635
plRL117_NT_sgRNA	Gift from Dr. Melissa Chengaloroyen	N/A
plRL117_*wecA*_sgRNA 1	This paper	N/A
plRL117_*wecA*_sgRNA 2	This paper	N/A
plRL117_*wecA*_sgRNA 3	This paper	N/A
plRL117_*wecA*_sgRNA 4	This paper	N/A
plRL117_*wecA*_sgRNA 5	This paper	N/A
plRL117_*rfbD*_sgRNA 1	This paper	N/A
plRL117_*rfbD*_sgRNA 2	This paper	N/A

plRL117_*rfbD*_sgRNA 3	This paper	N/A
plRL117_*rfbD*_sgRNA 4	This paper	N/A
plRL117_*rfbD*_sgRNA 5	This paper	N/A
plRL117_*clpP2*_sgRNA	Gift from Lucas Raphela	N/A
plRL2	Addgene (Bosch et al., 2021)	Plasmid #163631
plRL2_NT_sgRNA	Gift from Dr. Melissa Chengaloroyen	N/A
plRL2_*wecA*_sgRNA 1	This paper	N/A
plRL2_*wecA*_sgRNA 2	This paper	N/A
plRL2_*wecA*_sgRNA 3	This paper	N/A
plRL2_*wecA*_sgRNA 4	This paper	N/A
plRL2_*wecA*_sgRNA 5	This paper	N/A
Experimental models: Organisms/strains		
Mycobacterium smegmatis mc^2155 *wecA* sgRNA 1	This paper	N/A
Mycobacterium smegmatis mc^2155 *wecA* sgRNA 2	This paper	N/A
Mycobacterium smegmatis mc^2155 *wecA* sgRNA 3	This paper	N/A
Mycobacterium smegmatis mc^2155 *wecA* sgRNA 4	This paper	N/A
Mycobacterium smegmatis mc^2155 *wecA* sgRNA 5	This paper	N/A
Mycobacterium smegmatis mc^2155 *rfbD* sgRNA 1	This paper	N/A
Mycobacterium smegmatis mc^2155 *rfbD* sgRNA 2	This paper	N/A
Mycobacterium smegmatis mc^2155 *rfbD* sgRNA 3	This paper	N/A
Mycobacterium smegmatis mc^2155 *rfbD* sgRNA 4	This paper	N/A
Mycobacterium smegmatis mc^2155 *rfbD* sgRNA 5	This paper	N/A
Mycobacterium tuberculosis H37Ra *wecA* sgRNA 1	This paper	N/A
Mycobacterium tuberculosis H37Ra *wecA* sgRNA 1	This paper	N/A
Mycobacterium tuberculosis H37Ra *wecA* sgRNA 1	This paper	N/A
Mycobacterium tuberculosis H37Ra *wecA* sgRNA 1	This paper	N/A
Mycobacterium tuberculosis H37Ra *wecA* sgRNA 1	This paper	N/A
Web applications, Software and algorithms		
Microsoft Excel	Microsoft	Version 2411 (Build 16.0.18227.20082)
FLUOstar Optima plate reader	BMG LabTech plate reader	https://www.bmglabtech.com/en/fluostar-omega/
Biorender	(Perkel, 2020)	Biorender (2025)
Pebble	(Rock et al., 2017)	sgRNA design 2.0
Mycobrowser	(Kapopoulou et al., 2011)	©2018-2025 EPFL, 1015 Lausanne
GraphPad Prism 10	GraphPad	Version 10.2.0
ZEN (blue) Imaging Software	Carl ZEISS AG (https:www.zeiss.com)	Version ZEN 3.11
FIJI (ImageJ)	Fiji/ImageJ Development (Schindelin et al., 2012)	Java 1.8.0_322
Microbe J Plugin	MicrobeJ Contributors (Ducret et al., 2016)	Version 5.13p

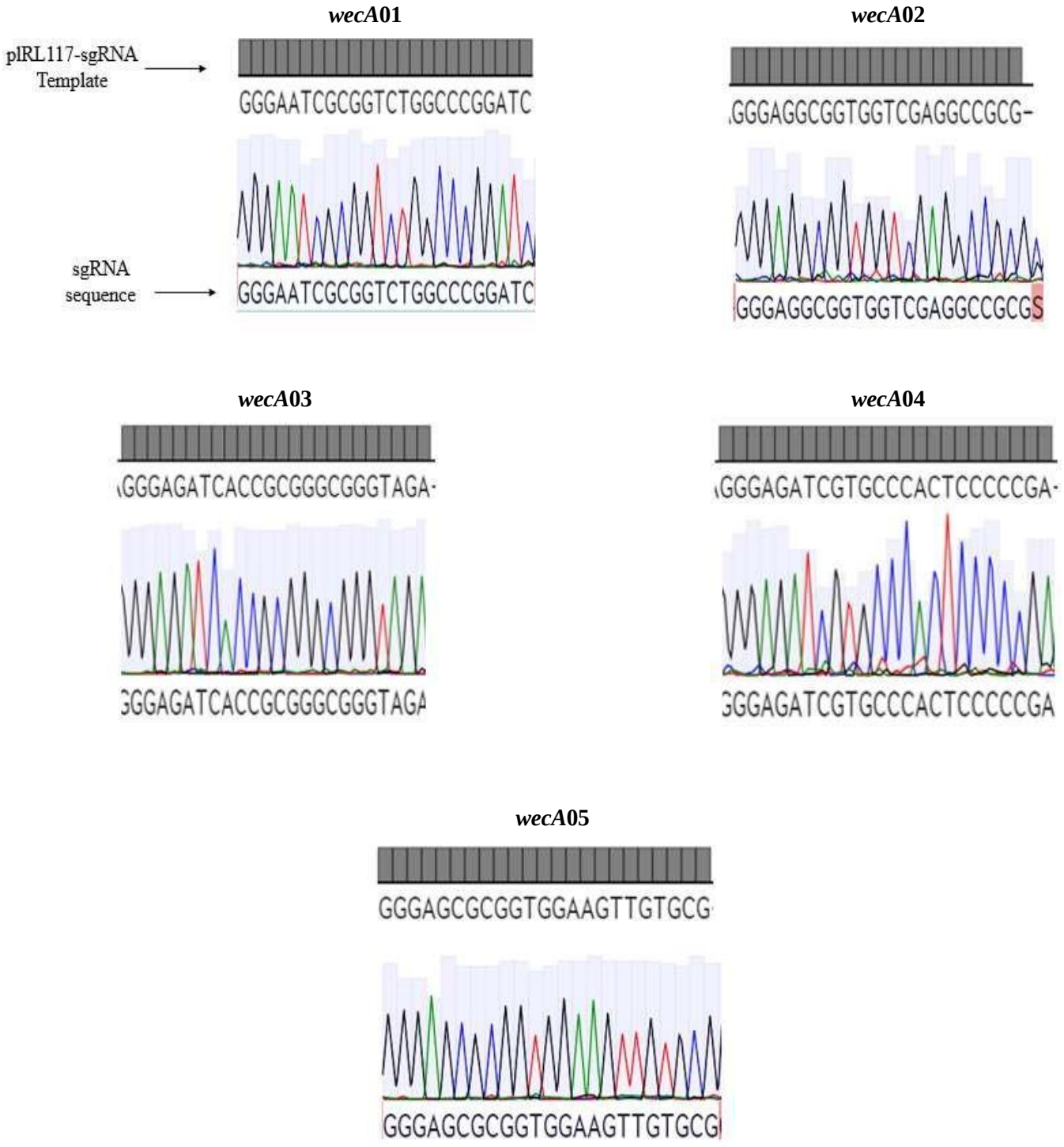

Figure S2. Sequence alignments of expected *wecA* sgRNA guide oligo insert with *M. smegmatis* recombinant plasmid DNA sequences obtained by sanger sequencing. The red base represents mismatches. Data analysed using the Benchling software Sequence Alignment Tool and the relevant sequence region of interest extracted.

***rfbD*01**

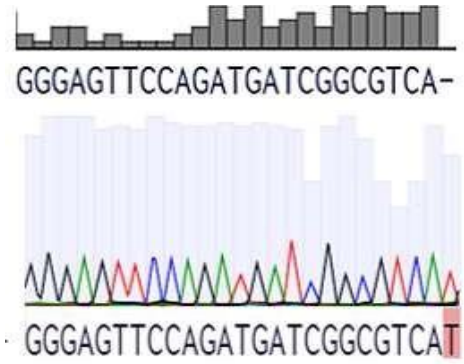

***rfbD*02**

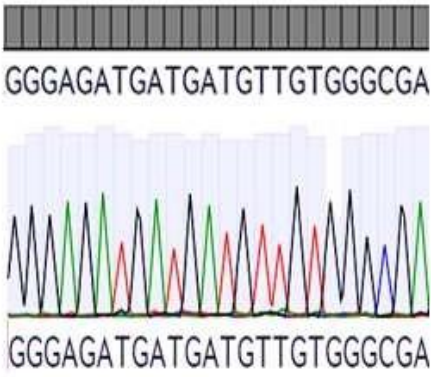

***rfbD*03**

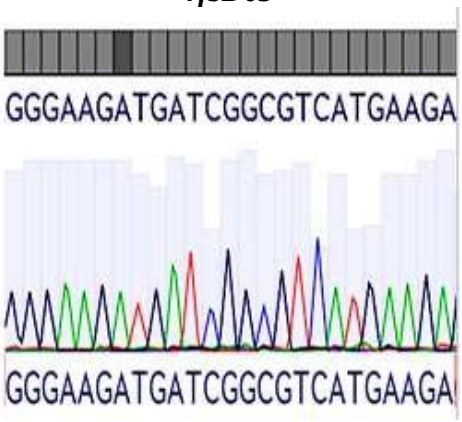

***rfbD*04**

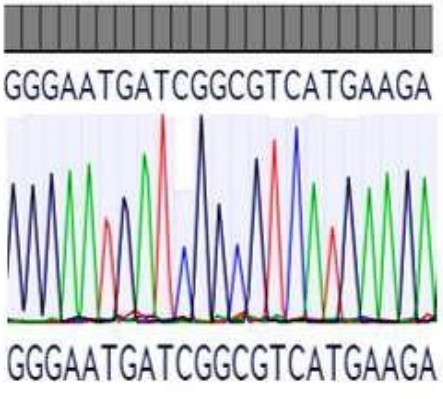

***rfbD*05**

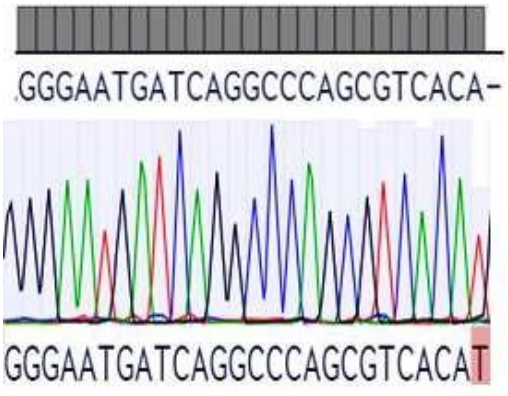

Figure S3. **Sequence alignments of expected *rfbD* sgRNA guide oligo insert with *M. smegmatis* recombinant plasmid DNA sequences obtained by sanger sequencing.** The red base represents mismatches. Data analysed using the Benchling Sequence Alignment Tool and the relevant sequence region of interest extracted.

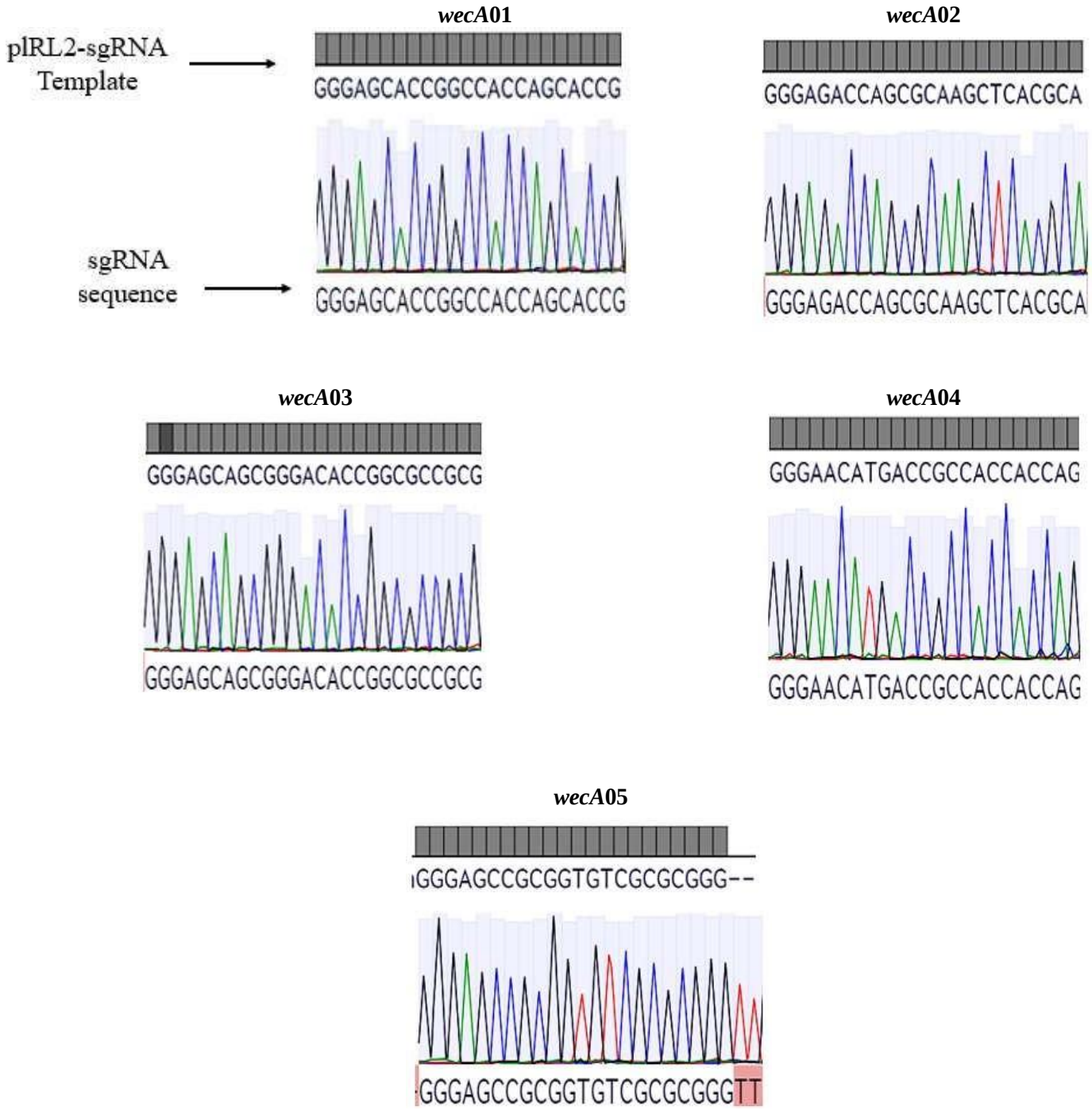

Figure S4. Sequence alignments of expected *wecA* sgRNA guide oligo insert with *M. tuberculosis* recombinant plasmid DNA sequences obtained by sanger sequencing. The red base represents mismatches. Data analysed using the Benchling software Sequence Alignment Tool and the relevant sequence region of interest extracted.

7.2. Growth analysis of *M. smegmatis* hypomorphs in liquid media

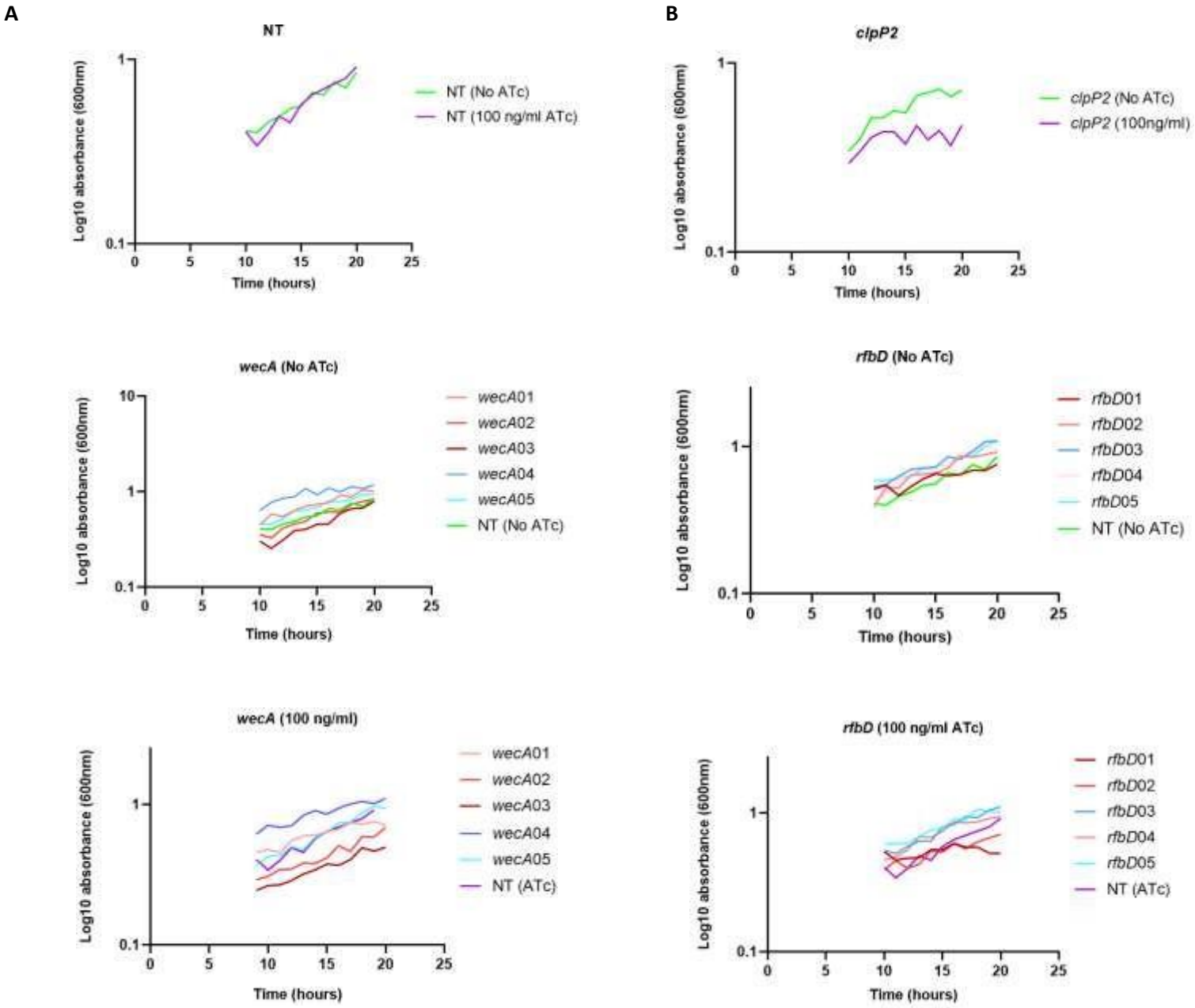

Figure S5. Logged graphs showing the growth of our *Msm* CRISPRi controls and hypomorph strains. The graphs showing the growth trajectory of the control strains present the growth in the absence and presence of 100 ng/ml ATc. The graphs showing the growth trajectory of the hypomorph strains present the growth in the presence of 100 ng/ml ATc. Growth attenuation is ranges from strong (dark red), intermediate (light pink/dark blue) to weak (light blue).

7.3. Antimycobacterial drug susceptibility assays

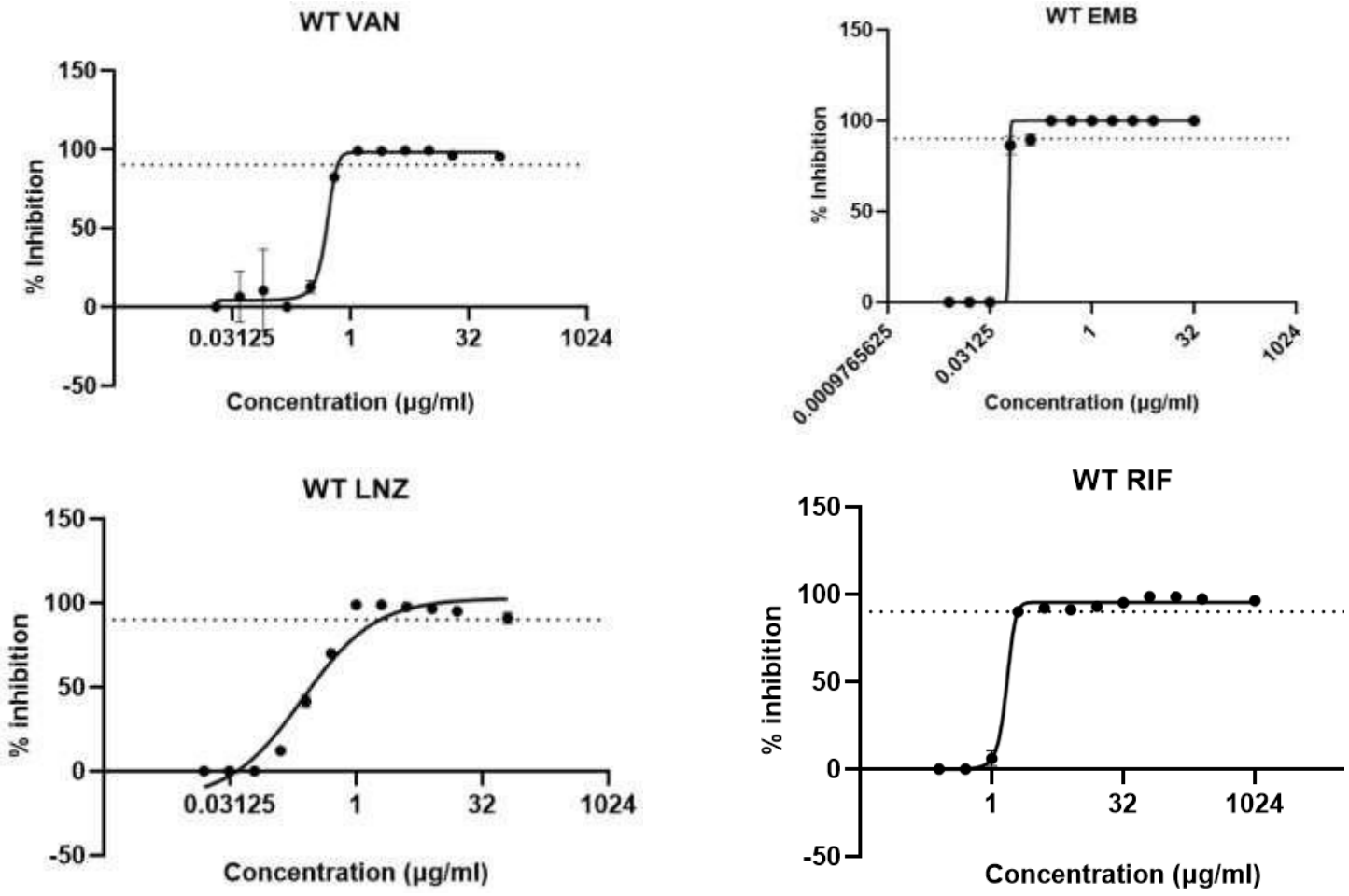

Figure S6. Repeats of the determination of reference MIC_{90} of MSM_WT strains

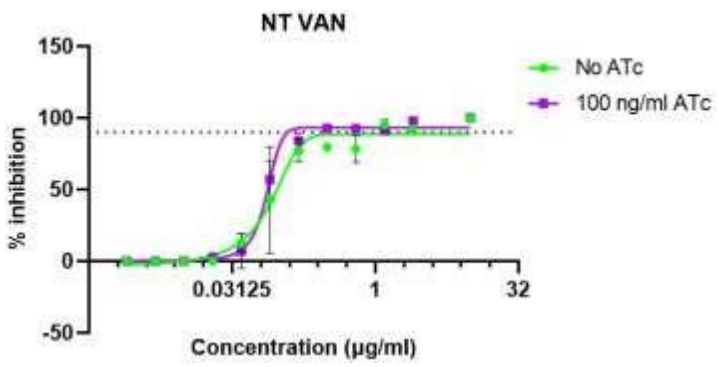

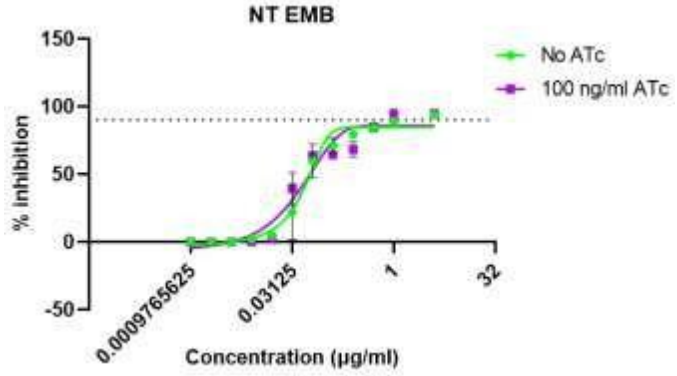

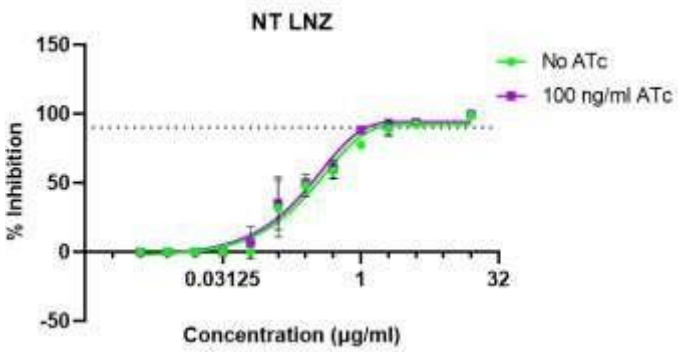

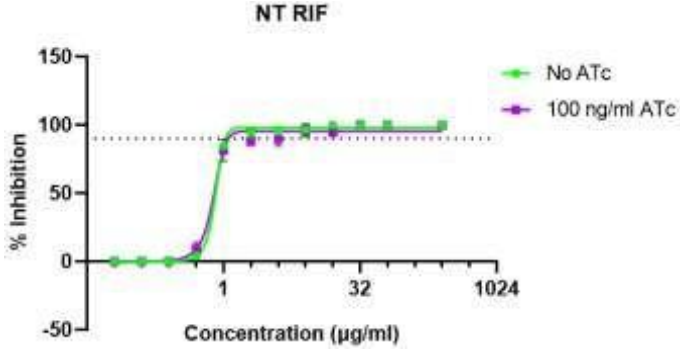

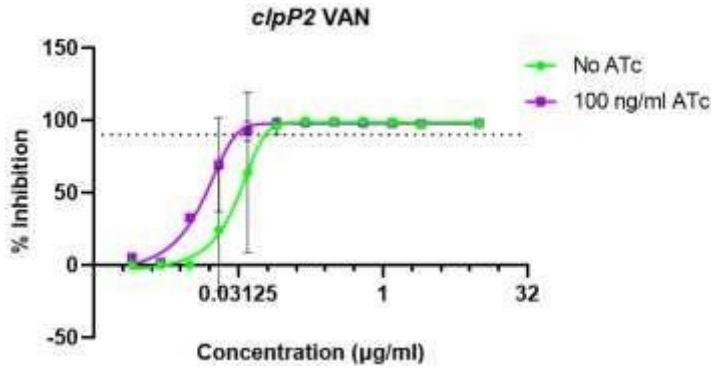

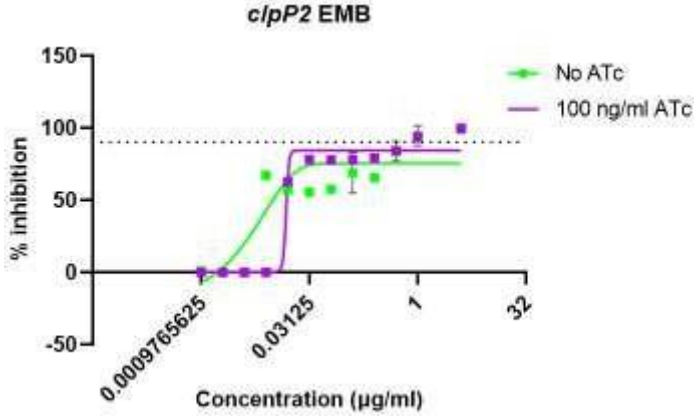

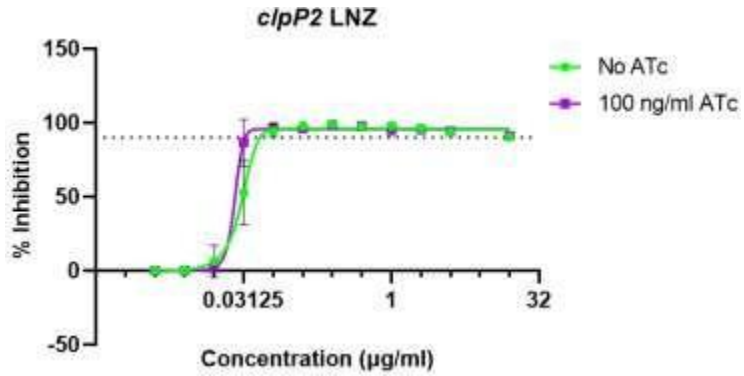

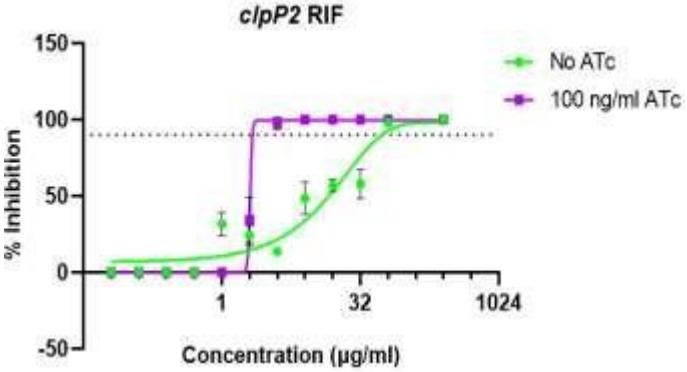

Figure S7. Repeats for the determination of MIC_{90} in *Msm* control.

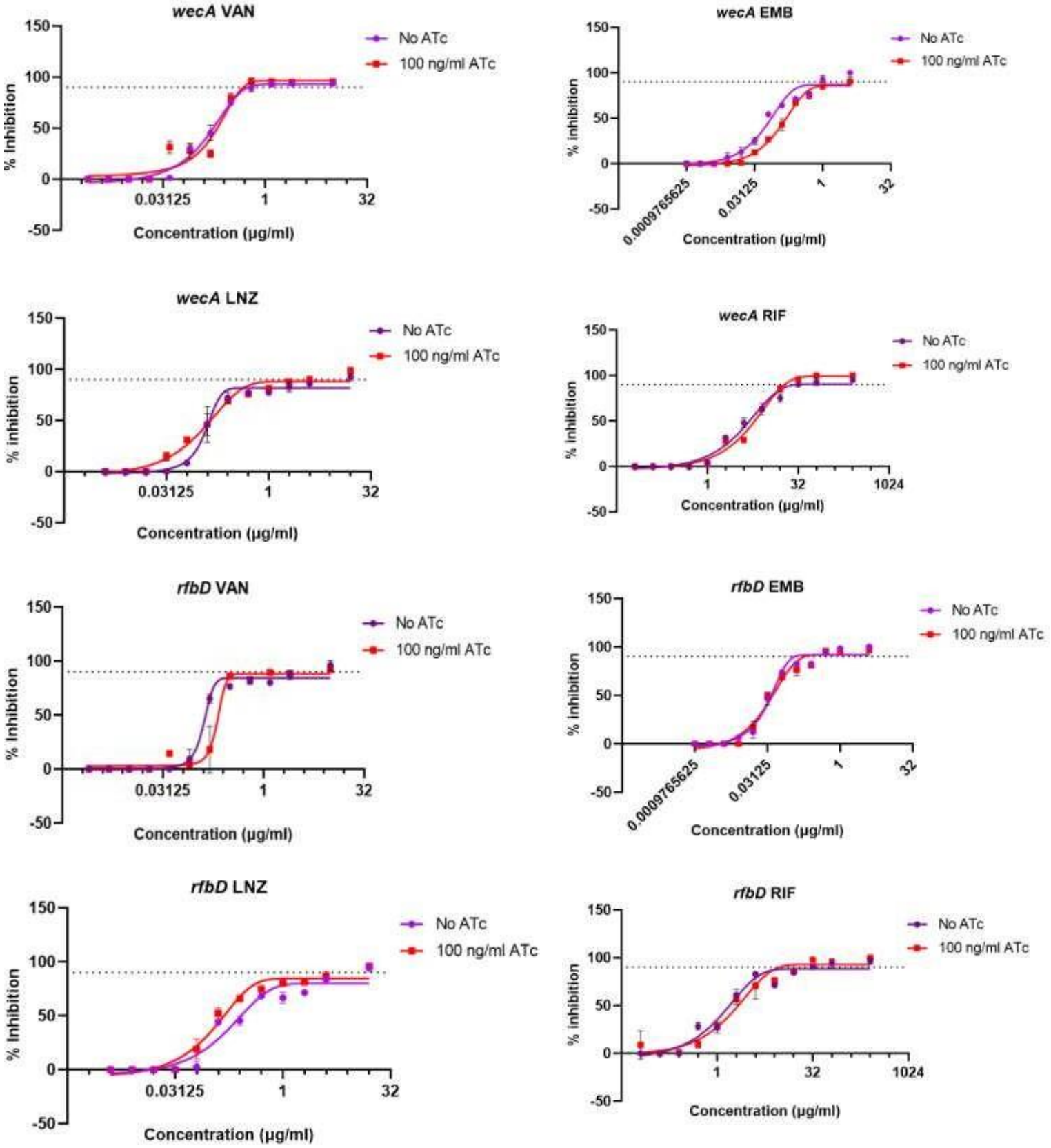

Figure S8. Repeats for the determination of MIC_{90} in *Msm* hypomorphs

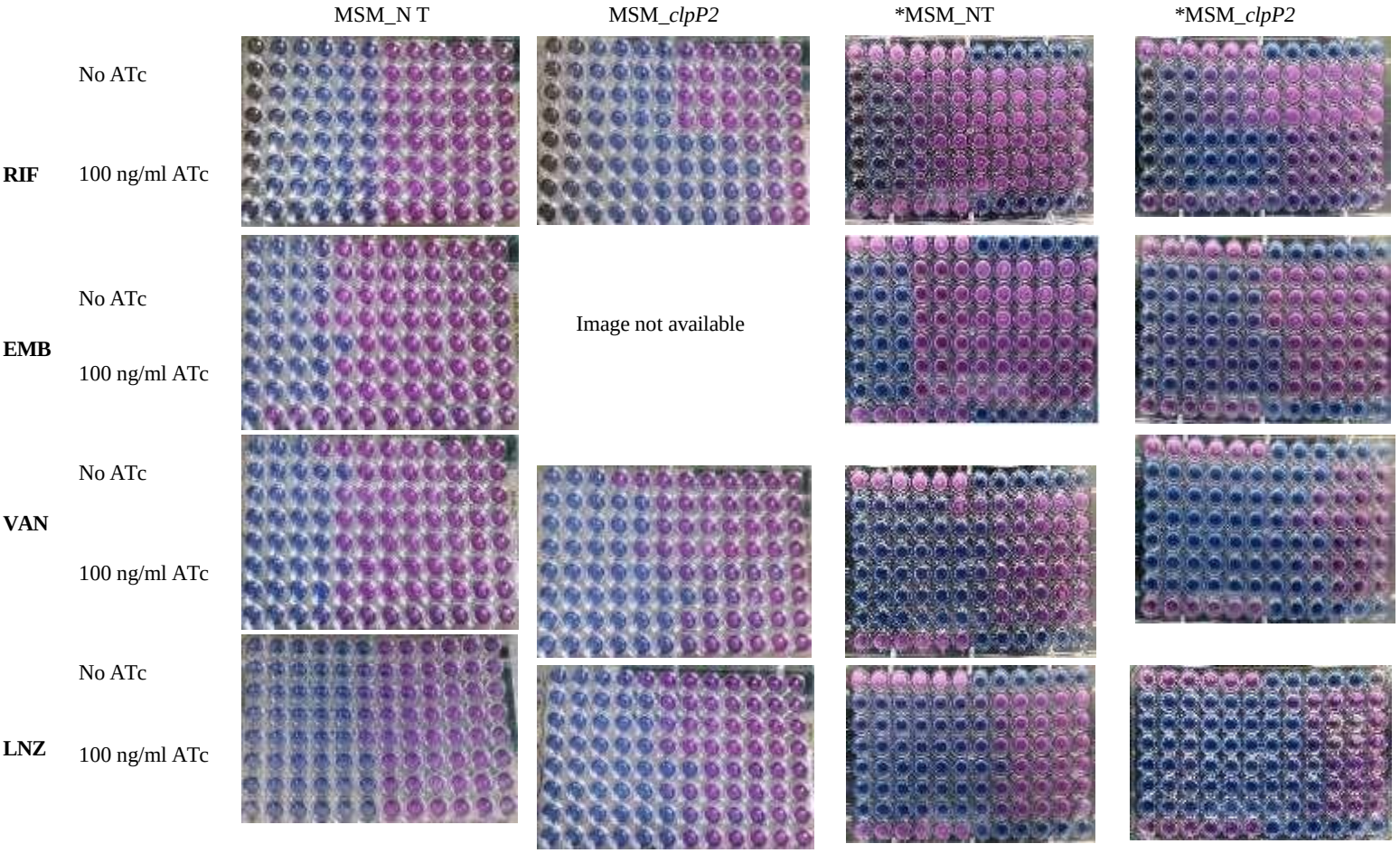

Figure S9. Colorimetric resazurin analysis of shift in MIC_{90} of *M. smegmatis* hypomorph controls. Shift in MIC_{90} compared between No ATc and 100 ng/ml ATc treatment. Wells A1-6 & H1-6 contain minimum growth (no growth control), wells A7-12 & H7-12 contain full growth (100% growth control). Blue wells indicate low density of cells and higher inhibition; pink wells indicate high density of cells and lower inhibition. Red dotted line separates the no ATc and 100 ng/ml ATc conditions.

*Repeat experiment images. Wells A1-6 & H1-6 contain full growth (100% growth control). Wells A7-12 & H7-12 contain minimum growth (no growth control).

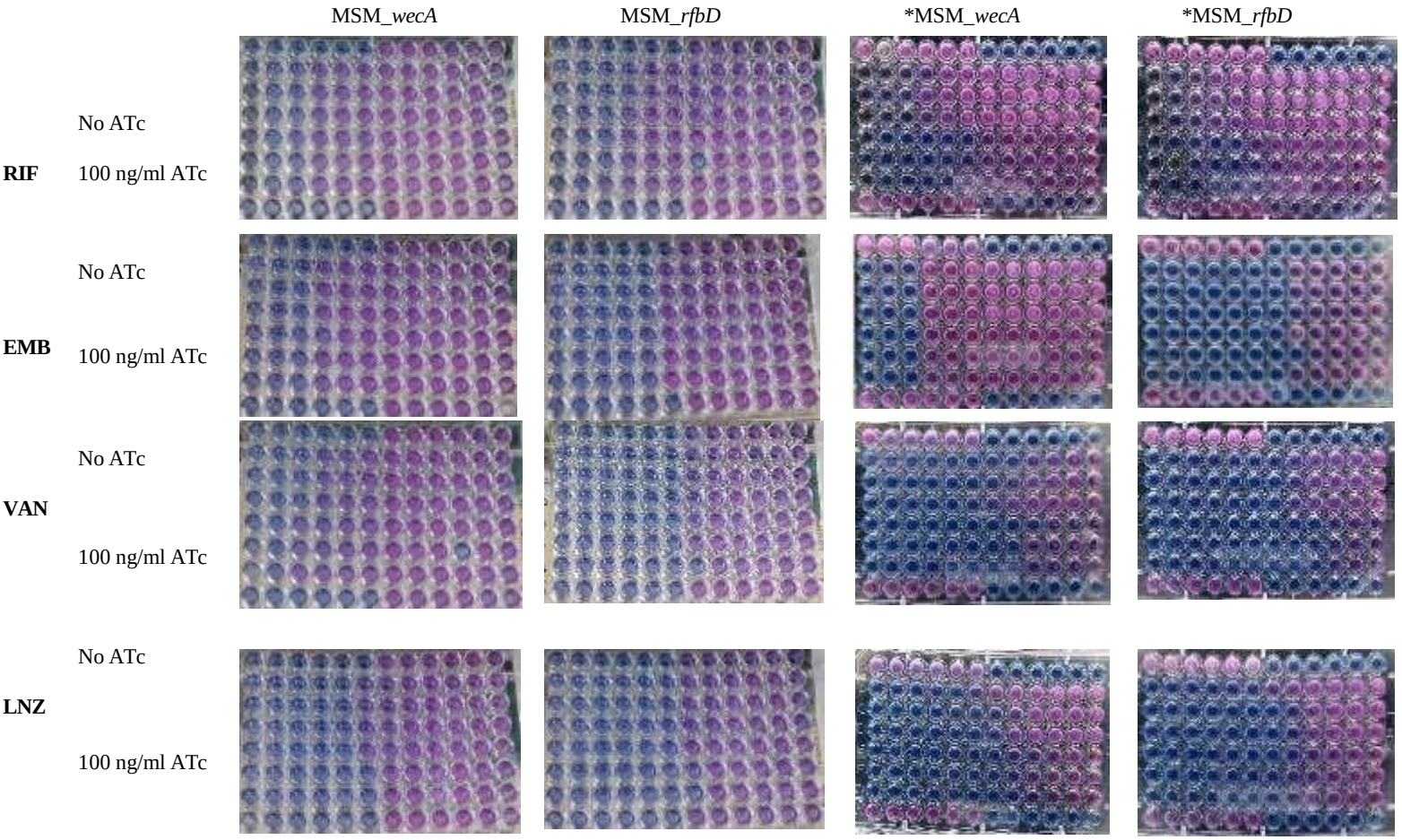

Figure S9. Colorimetric resazurin analysis of shift in MIC_{90} of *M. smegmatis* hypomorph controls. Shift in MIC_{90} compared between No ATc and 100 ng/ml ATc treatment. Wells A1-6 & H1-6 contain minimum growth (no growth control), wells A7-12 & H7-12 contain full growth (100% growth control). Blue inhibition. Red dotted line separates the no ATc and 100 ng/ml ATc conditions.

*Repeat experiment images. Wells A1-6 & H1-6 contain full growth (100% growth control). Wells A7-12 & H7-12 contain minimum growth (no growth control).

Table S2. Susceptibility data showing EC_{50} of hypomorphs for each antibiotic tested. EC_{50} values obtained using non-linear regression analysis.

Drug	Strain	No ATc	ATc (100 ng/ml)	Fold decrease
Vancomycin (VAN)	**MSM_NT**	0.2479	0.2202	1.13
	MSM_clpP2	0.5703	0.4497	1.27
	MSM_wecA	0.8346	0.4486	1.86
	MSM_rfbD	1.264	0.9507	1.33
Ethambutol (EMB)	**MSM_NT**	1.770	1.534	1.53
	MSM_clpP2	1.827	1.834	0.99
	MSM_wecA	1.869	1.037	1.80
	MSM_rfbD	1.523	1.073	1.42
Linezolid (LNZ)	**MSM_NT**	0.4872	0.4531	1,08
	MSM_clpP2	0.3741	0.1328	2.82
	MSM_wecA	0.3670	0.2122	1.73
	MSM_rfbD	0.1713	0.1327	1.29
Rifampicin (RIF)	**MSM_NT**	1.001	0.9865	1.01
	MSM_clpP2	0.2928	0.007508	38.99
	MSM_wecA	0.4867	0.2428	2.00
	MSM_rfbD	0.6525	0.8424	0.77

7.4. Morphological analyses and comparison of *M. smegmatis* CRISPRi strains

Table S3. MicrobeJ plugin settings

Data	**Settings**
Channel 1	Default bright
Morphology	Smooth
Attributes	Area: 0.5-50 Length: 3-10 Width: 0.2-1 Angularity: 0-0.7 Range: 0.2-1 Amplitude: 0-0.5

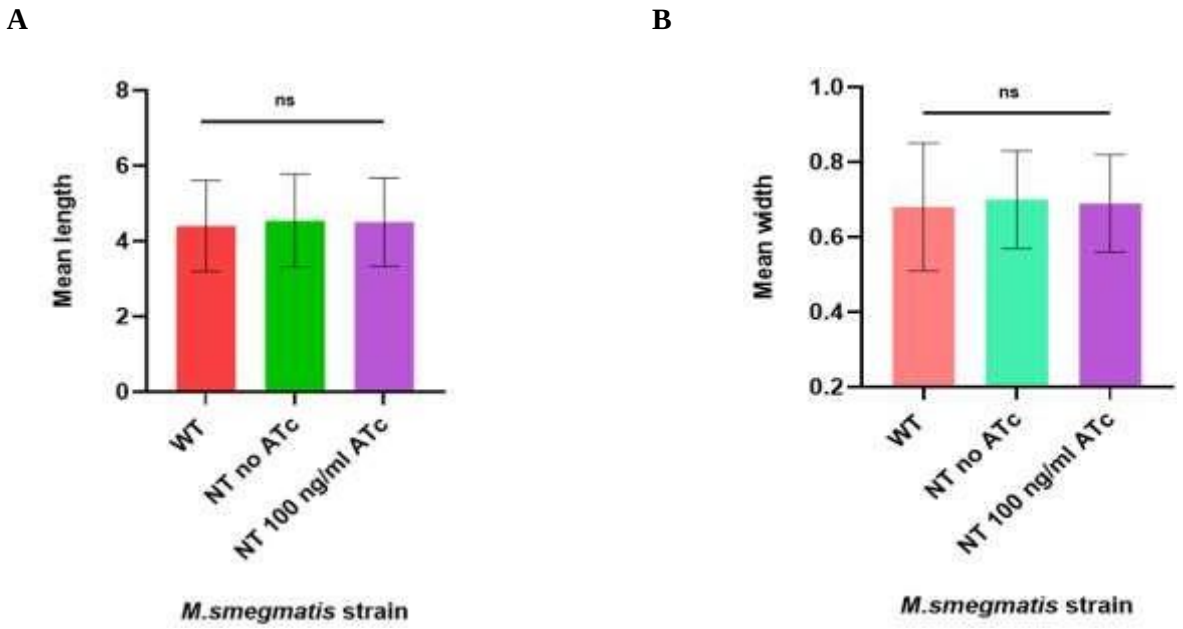

Figure S11. Quantitation of MSM_WT and MSM_NT cellular dimensions. Comparison of **A,** cell lengths (in µm) and **B,** cell widths (in µm) of MSM_WT (reds) and MSM_NT strains before (greens) and after (purple) induction of the CRISPRi system. Between 100 to 150 cells were analysed per strain. Error bars represent standard deviation. Ns= not significant. Cellular dimensions compared using a paired t-test. P>0.05.

A

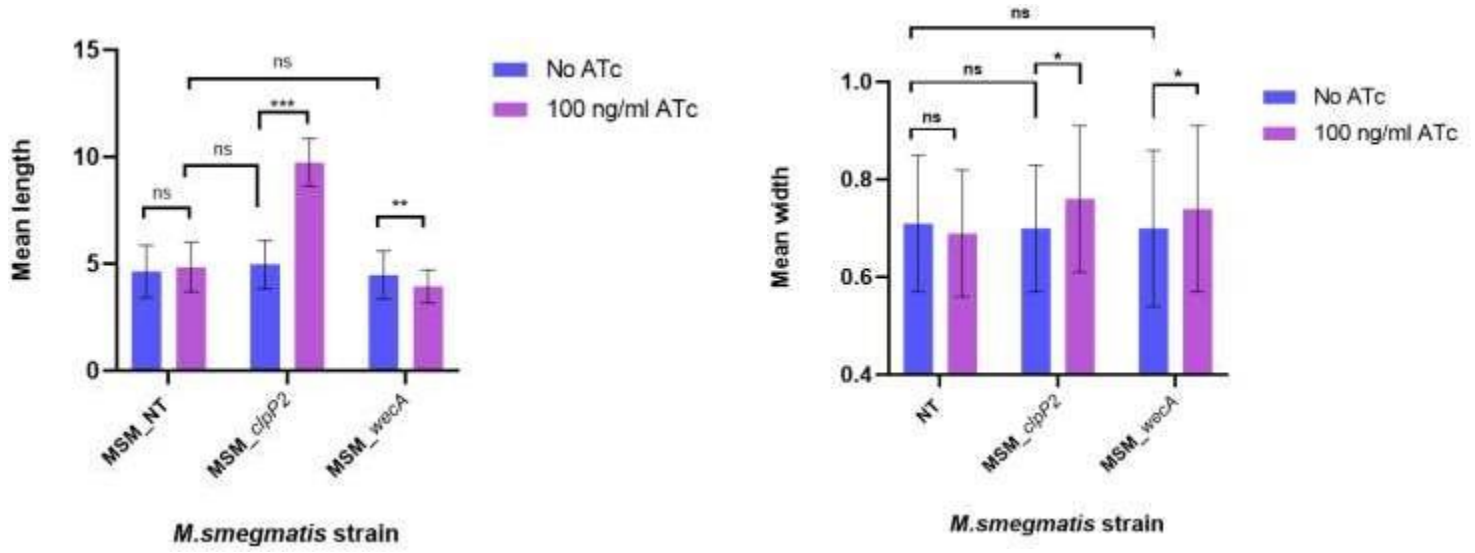

B

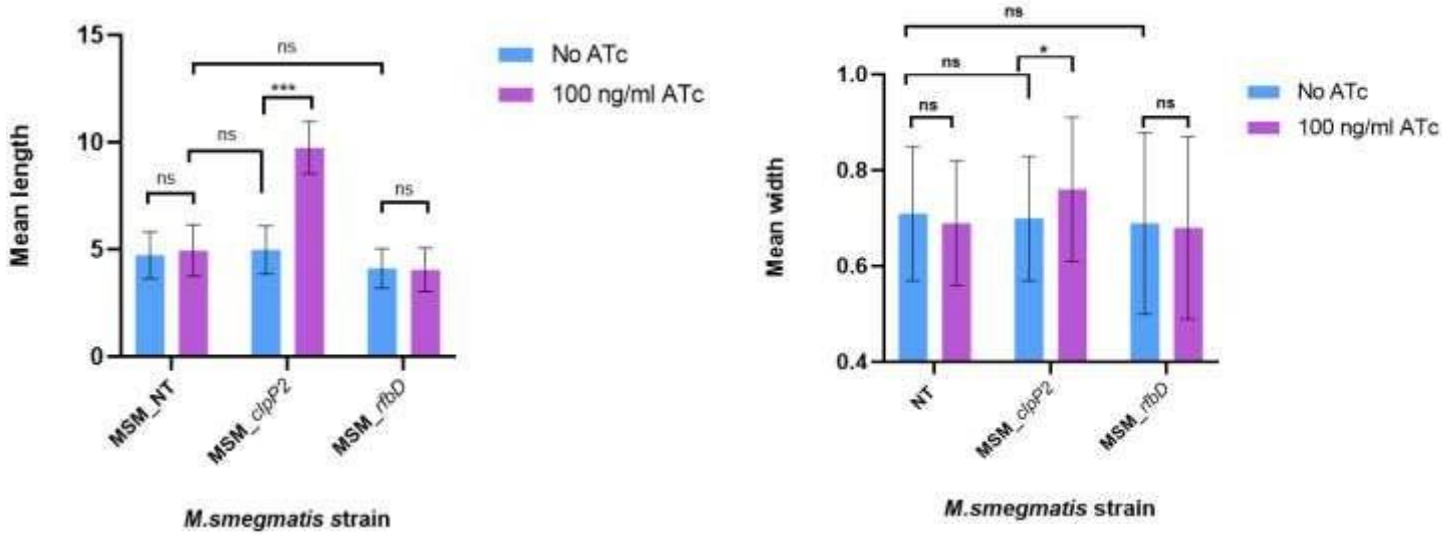

Figure S12. Quantitation of the *M. smegmatis* CRISPRi hypomorph cellular dimensions. Comparison of mean cell lengths (in µm) and mean cell widths (in µm) of ***A,*** MSM_*wecA* and ***B,*** MSM_*rfbD* strains in the absence (blue) and presence (purple) of 100 ng/ml ATc. Approximately 100 to 150 cells were analysed per strain. Error bars represent standard deviations. Cellular dimensions compared using a paired t-test. P>0.05.

6.5. Caseinolytic protease in mycobacteria

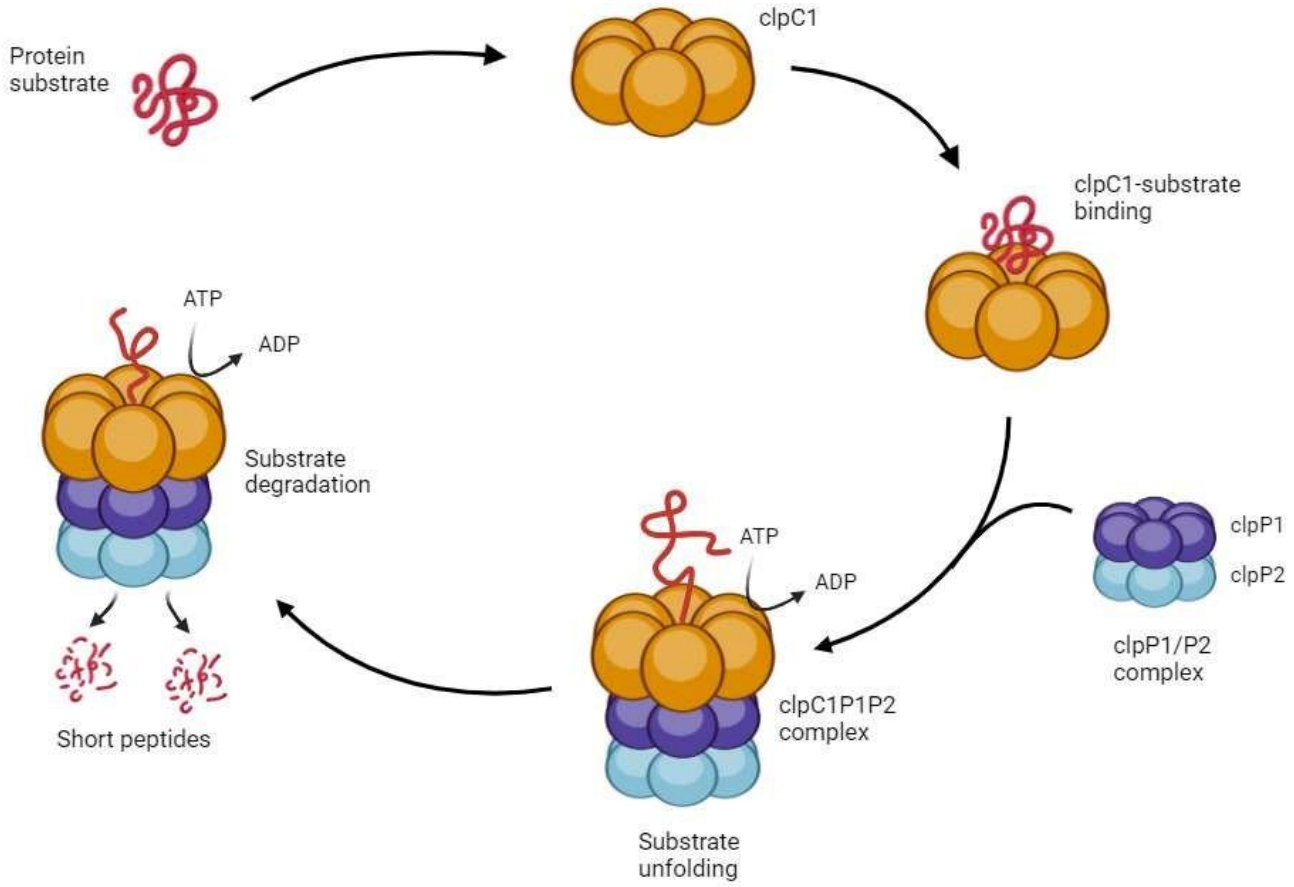

Figure S13. Activity of clp proteases to regulate protein homeostasis in mycobacteria. ClpC1 (indicated in orange) recognises and binds the misfolded/dysfunctional protein (in red) as a substrate and binds to the clpP1/P2 complex (in purple and blue). The peptidase activity of clpP1 unfolds and breaks down the substrate in an ATP-dependent manner, Finally, the clpP1/P2 complex degrades the substrate into short peptides. G*enerated using Biorender (2025).*

7.6. Investigation of the morphology of CRISPRi *M. tuberculosis* H37Rv by fluorescence microscopy

7.6.1. Metabolic labelling of *Mycobacterium tuberculosis* H37Rv with DMN-Trehalose and RADA fluorescent probes

To inoculate strains, 100 µl of stationary phase glycerol stocks of *Mtb* H37Rv hypomorph strains were added to 5 ml 7H9/OADC supplemented with Kan25 and incubated for 7 days at 37°C while stationary. Following the incubation period, the cells were passaged into 5 ml 7H9/OADC supplemented with Kan25 and incubated for an additional 3 days until they reached an expected OD_{600} of 0.6-0.8. The cultures were then passaged in 5 ml 7H9/OADC without antibiotic supplementation and incubated for 5 days while stationary. Each culture was inoculated as pairs; one without and one with 100 ng/ml ATc. The endpoint OD_{600} of the cultures were determined and presented in **Table S2**. The endpoint OD_{600} serves as an indication of growth attenuation in liquid media.

Next, 100 µl of the exponentially replicating bacterial cells were mixed with 1 µl DMN-Tre (10 µM) and 1 µl RADA (2.5 µM) and incubated at 37°C while shaking for 18 hours. The cells were then centrifuged at 6 000 *rcf* for 10 mins and resuspended in 100 µl PBST. 100 µl of fresh 8% paraformaldehyde (PFA) was added to these cells and the samples incubated at room temperature for 24 hours. Post fixation samples were centrifuged at 6 000 *rcf* for 10 mins and resuspended in 100 µl PBST. The cells were prepped and visualised by microscopy as described in **section 2.9.2**.

7.6.2. *In vitro* characterization and validation of CRISPRi strains

Table S4. End-point OD_{600} of the MTB_Rv control and hypomorph strains

	OD_{600} (No ATc)	**OD_{600} (100 ng/ml ATc)**	**Fold Difference (No ATc / ATc)**
MTB_Rv_NT	3.3	3.4	1.0
MTB_Rv_*wecA*	3.8	3.7	1.0
MTB_Rv_*rfbD*	3.8	2.0	1.9

7.6.3. Morphological analyses of *M. tuberculosis* H37Rv CRISPRi control strains

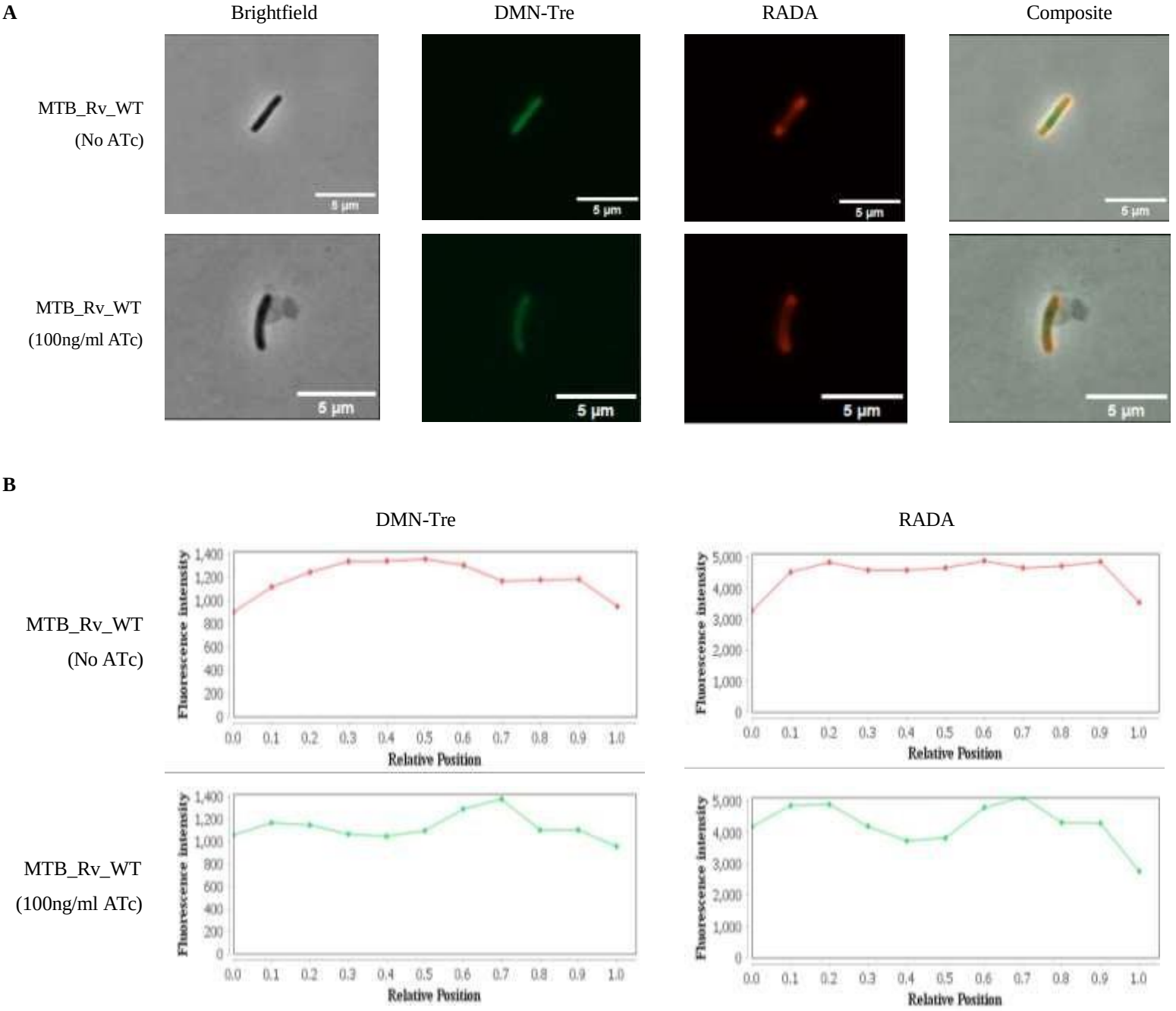

Figure S14. MTB_Rv_WT microscopy data. ***A,*** Visualisation of MTB_Rv_WT strains and localisation of DMN-Tre and RADA. Untreated MTB_Rv_WT are shown on the top row, while treated MTB_Rv_WT are shown on the bottom row. First panel shows bacilli under brightfield channel; second panel shows bacilli under DMN-Tre Green fluorescent channel; third panel shows bacilli under RADA red fluorescent channel; last panel shows bacilli under composite of DMN-Tre and RADA channels. ***B,*** Intensity distribution of the DMN-Tre and RADA stains across MTB_Rv_WT in the untreated (top row) and treated (bottom row). The X-axis represents the relative position along the cell body where 0.5 represents the mid-cell (septum) and 0 or 1.0 represent the cell poles. The Y-axis represents the average fluorescence intensity of the DMN-Tre stain. Approximately 100 cells analysed under both untreated and ATc treated strains.

A

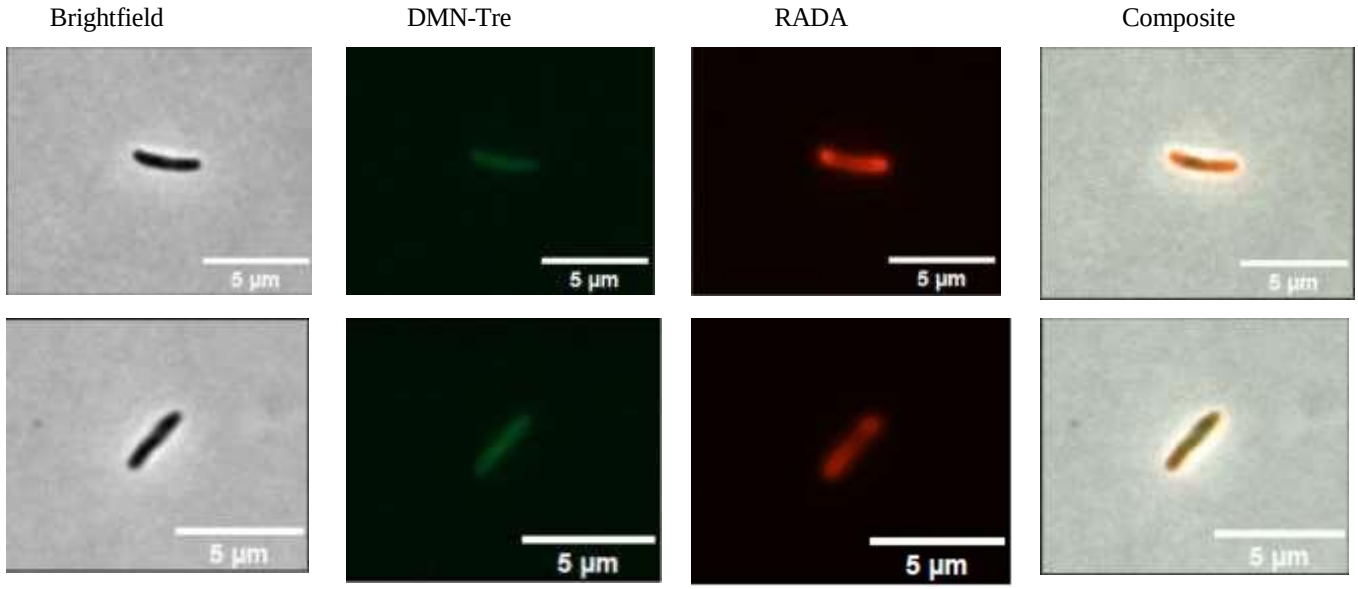

B

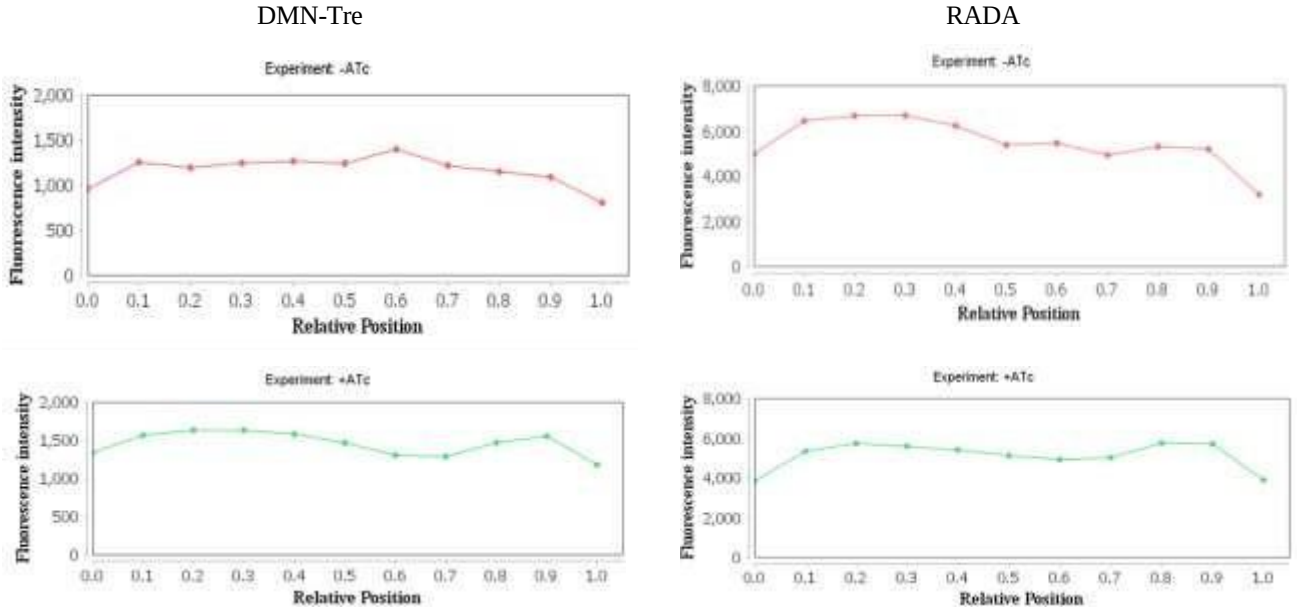

Figure S15. MTB_Rv_NT microscopy data. ***A,*** Visualisation of MTB_Rv_NT strains and localisation of DMN-Tre and RADA. Untreated MTB_Rv_NT are shown on the top row, while treated MTB_Rv_NT are shown on the bottom row. First panel shows bacilli under brightfield channel; second panel shows bacilli under DMN-Tre Green fluorescent channel; third panel shows bacilli under RADA red fluorescent channel; last panel shows bacilli under composite of DMN-Tre and RADA channels. ***B,*** Intensity distribution of the DMN-Tre and RADA stains across MTB_Rv_NT in the untreated (top row) and treated (bottom row). The X-axis represents the relative position along the cell body where 0.5 represents the mid-cell (septum) and 0 or 1.0 represent the cell poles. The Y-axis represents the average fluorescence intensity of the DMN-Tre stain.. Approximately 100 cells analysed under both untreated and ATc treated strains.

7.6.4. Morphological analyses of *M. tuberculosis* H37Rv CRISPRi *wecA* hypomorph strains

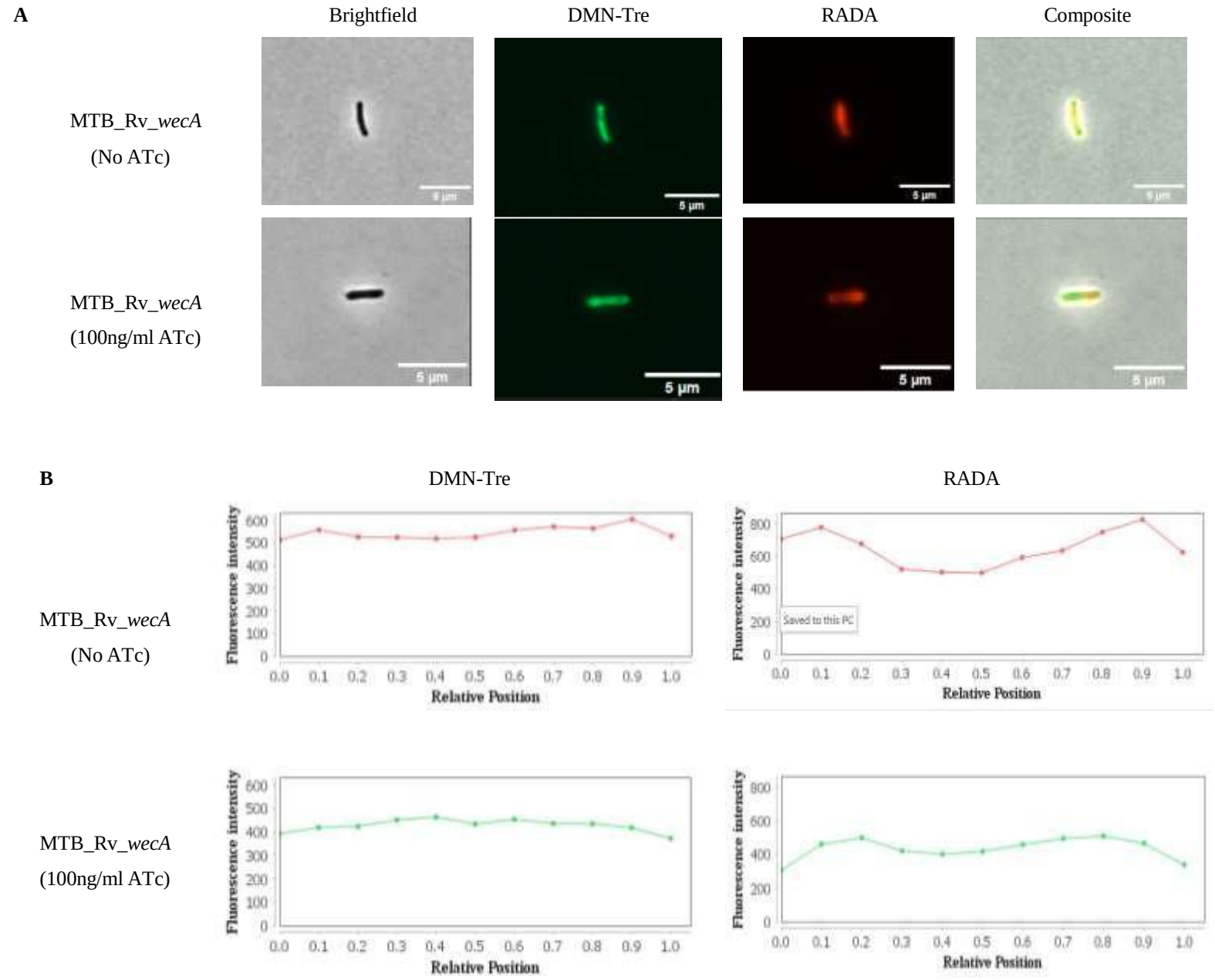

Figure S16. MTB_Rv_*wecA* microscopy data. ***A,*** Visualisation of MTB_Rv_*wecA* strains and localisation of DMN-Tre and RADA. Untreated MTB_Rv_*wecA* are shown on the top row, while treated MTB_Rv_*wecA* are shown on the bottom row. First panel shows bacilli under brightfield channel; second panel shows bacilli under DMN-Tre Green fluorescent channel; third panel shows bacilli under RADA red fluorescent channel; last panel shows bacilli under composite of DMN-Tre and RADA channels. ***B,*** Intensity distribution of the DMN-Tre and RADA stains across MTB_Rv_*wecA* in the untreated (top row) and treated (bottom row). The X-axis represents the relative position along the cell body where 0.5 represents the mid-cell (septum) and 0 or 1.0 represent the cell poles. The Y-axis represents the average fluorescence intensity of the DMN-Tre stain.. Approximately 150 cells analysed under both untreated and ATc treated strains.

7.6.5. Morphological analyses of *M. tuberculosis* H37Ra CRISPRi *rfbD* hypomorph strains

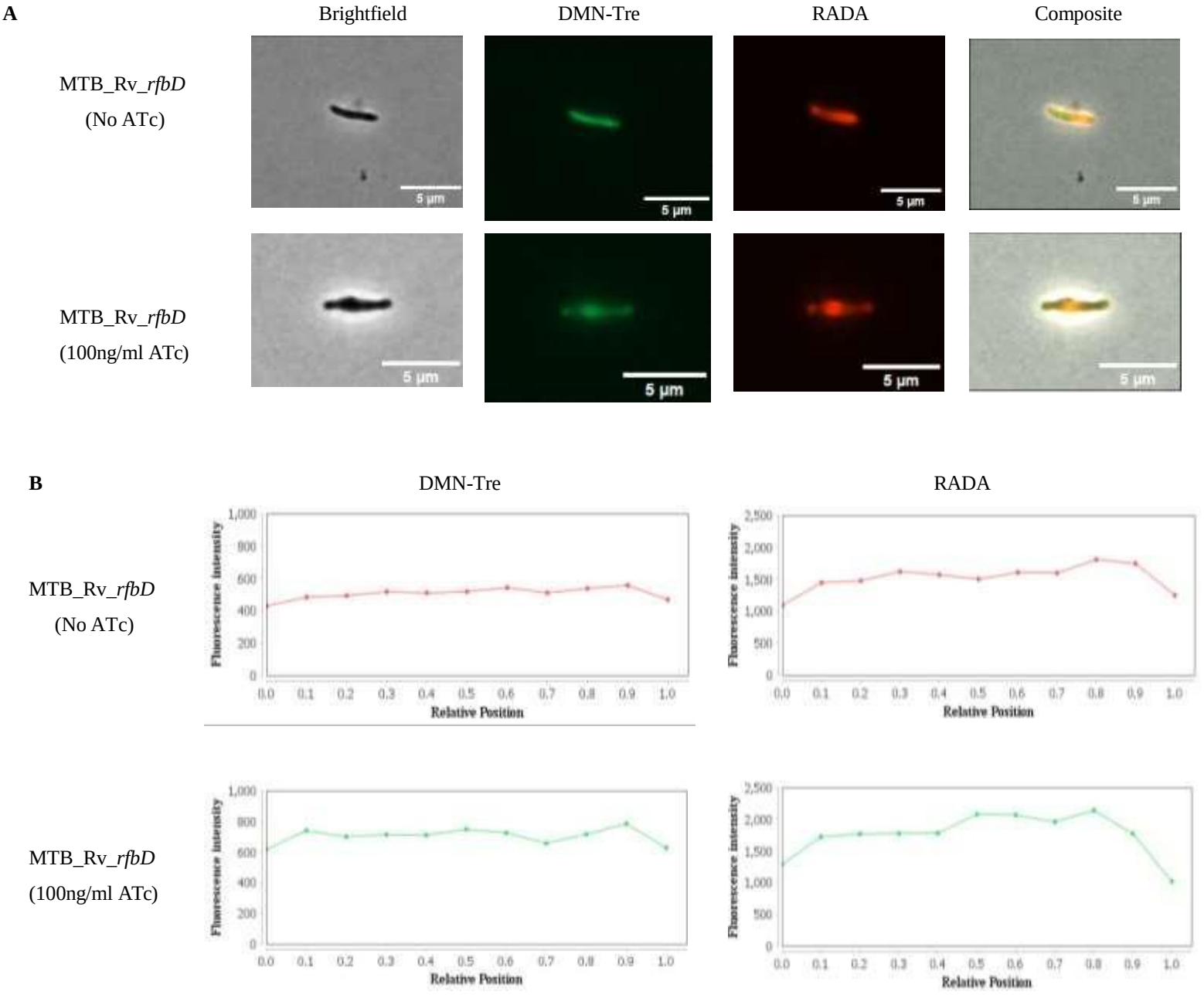

Figure S17. MTB_Rv_*rfbD* microscopy data. ***A,*** Visualisation of MTB_Rv_*rfbD* strains and localisation of DMN-Tre and RADA. Untreated MTB_Rv_*rfbD* are shown on the top row, while treated MTB_Rv_*rfbD* are shown on the bottom row. First panel shows bacilli under brightfield channel; second panel shows bacilli under DMN-Tre Green fluorescent channel; third panel shows bacilli under RADA red fluorescent channel; last panel shows bacilli under composite of DMN-Tre and RADA channels. ***B,*** Intensity distribution of the DMN-Tre and RADA stains across MTB_Rv_*rfbD* in the untreated (top row) and treated (bottom row). The X-axis represents the relative position along the cell body where 0.5 represents the mid-cell (septum) and 0 or 1.0 represent the cell poles. The Y-axis represents the average fluorescence intensity of the DMN-Tre stain.. Approximately 100 cells analysed under both untreated and ATc treated strains.

Chapter 8: Appendix

A

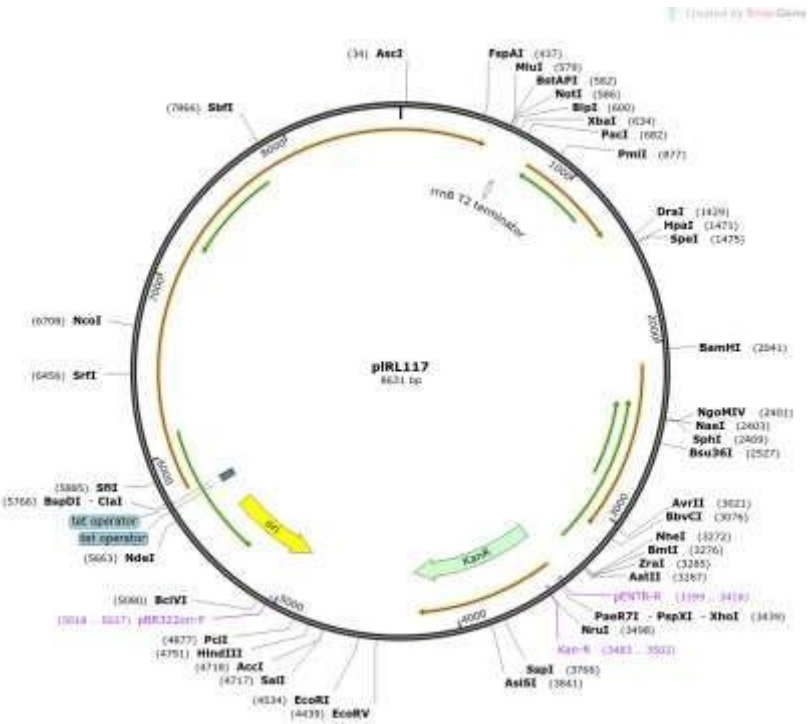

B

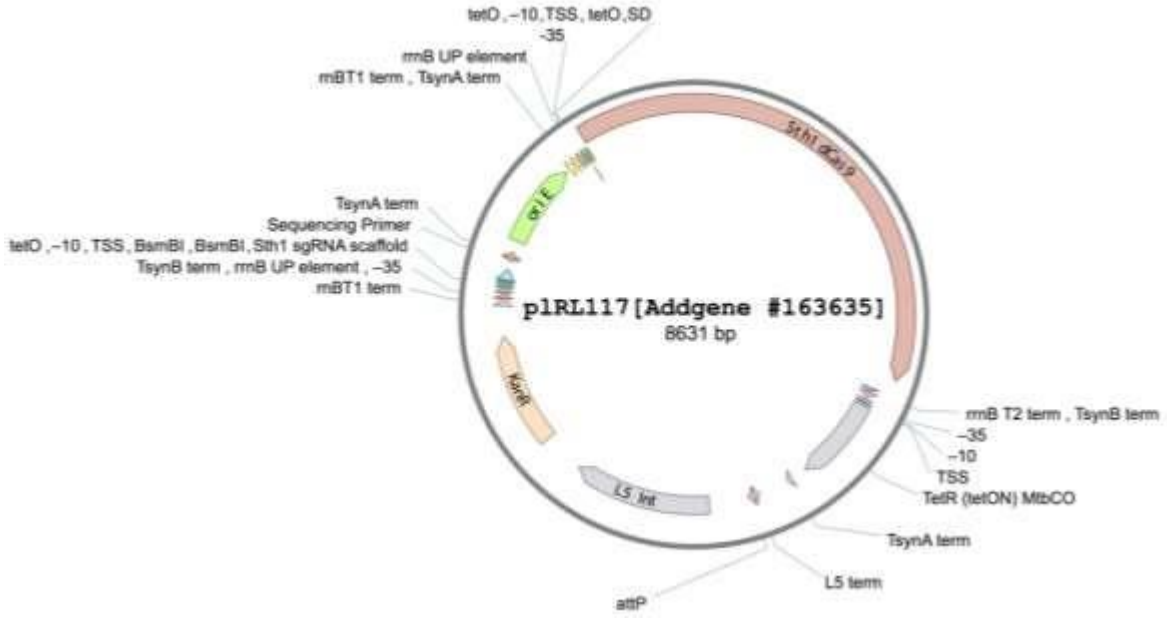

Figure 1. Diagram of the plRL117 plasmid used in this study for *M. smegmatis* work. *A*, Fully annotated plasmid and *B*, plasmid containing CRISPRi features of interest. Retrieved from Bosch et al. (2021) and addgene.

A

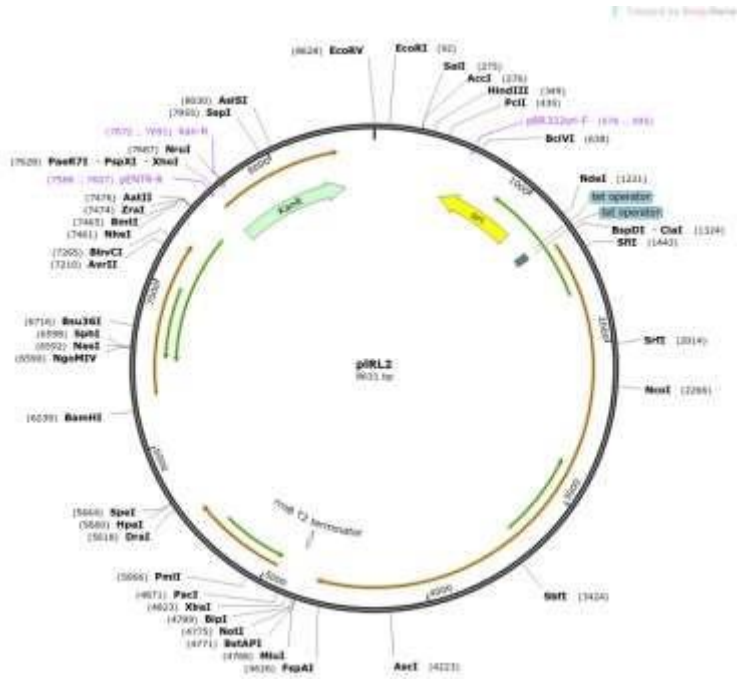

B

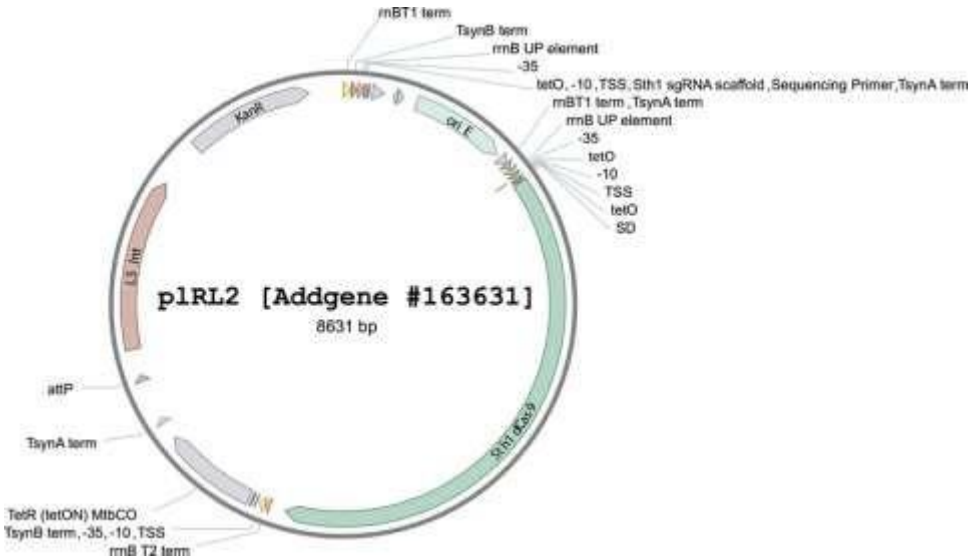

Figure 2. Diagram of the plRL2 plasmid used in this study for *M. tuberculosis* work. ***A,*** Fully annotated plasmid and ***B*** plasmid containing CRISPRi features of interest Retrieved from Bosch et al. (2021) and addgene.

A

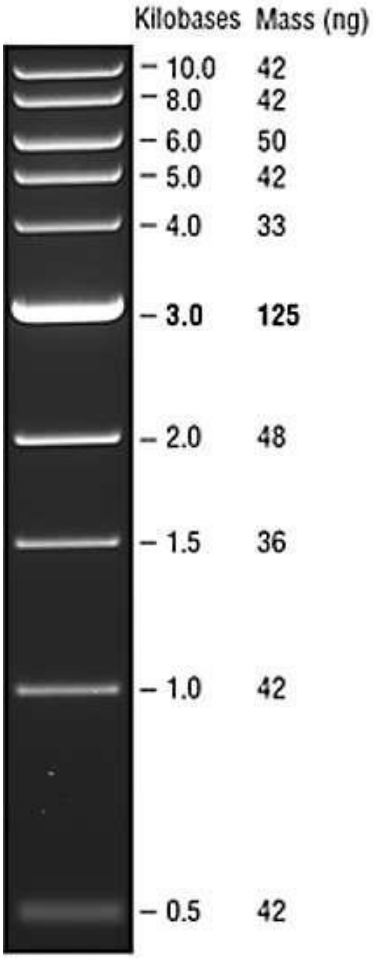

B

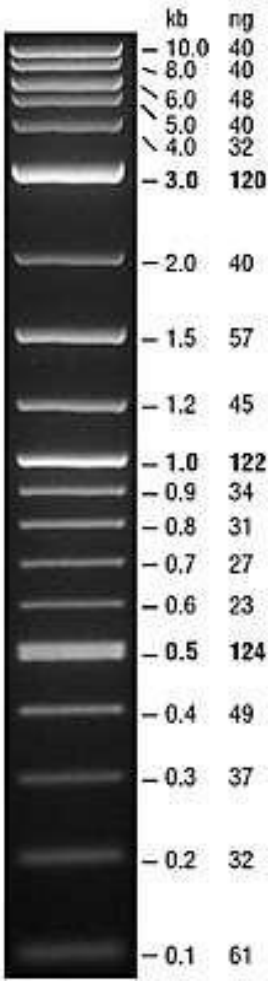

Figure 3. Agarose gel electrophoresis image of DNA Ladders used in this study. ***A,*** Quick-Load 1 kb DNA Ladder (size range: 500 bp to 10 kb) and ***B,*** Quick-Load 1 kb Plus Ladder (size range: (100 bp to 10 kb). Ladders are formulated with bromophenol blue dye. *Retrieved from New England Biolabs (NEB).*